

# **PHOTOCATALYTIC DEGRADATION OF WATER POLLUTANTS USING ACTIVATED CARBON- TiO<sub>2</sub>/METAL DOPED TiO<sub>2</sub> BASED NANOCOMPOSITE**

*by*

**MRIDUSHMITA BARUAH**



*Submitted to*

**NAGALAND UNIVERSITY**

*In Partial Fulfillment of the Requirements for Award of the Degree*

*of*

**DOCTOR OF PHILOSOPHY IN CHEMISTRY**

**DEPARTEMENT OF CHEMISTRY**

**NAGALAND UNIVERSITY**

**LUMAMI-798627**

**NAGALAND, INDIA**

**2021**

**DEDICATED**

*To those who believe in **hard**  
Work and never-give-up on their  
**DREAMS...***

# NAGALAND



# UNIVERSITY

(A Central University Estd. By the Act of Parliament No. 35 of 1989)

Headquarters: Lumami-798627, Nagaland, India

## Department of Chemistry

### DECLARATION

I, **Ms. Mridushmita Baruah** bearing Ph.D. Registration No. **Ph.D./CHE/00001** with effect from **30<sup>th</sup> August 2016**, hereby declare that the subject matter of my Ph.D. thesis entitled **“Photocatalytic degradation of water pollutants using activated carbon-TiO<sub>2</sub>/metal doped TiO<sub>2</sub> based nanocomposite”** is the record of work done by me, and that the contents of this thesis did not form the basis for award of any previous degree to me or to anybody else known to the best of my knowledge. This thesis has not been submitted by me for any other Research Degree in any other University/Institute.

This Ph. D. thesis is submitted in compliance with the UGC Regulation 2016 dated May 05, 2016 (Minimum Standard and Procedure for Award of M. Phil. /Ph. D. Degree) to the Nagaland University for the degree of Doctor of Philosophy in Chemistry.

*Mridushmita Baruah*  
**Mridushmita Baruah** 19/12/2021

*[Signature]*  
**Head** 19/12/21  
Department of Chemistry  
Nagaland University

विभागाध्यक्ष / Head  
रसायन विज्ञान विभाग / Department of Chemistry  
नागालैण्ड विश्वविद्यालय / Nagaland University  
लुमाँमी / Lumami- 798 627

*[Signature]*  
**Supervisor**  
Prof. Dipak Sinha  
Department of Chemistry  
Nagaland University

# NAGALAND



# UNIVERSITY

*(A Central University Estd. By the Act of Parliament No. 35 of 1989)*

*Headquarters: Lumami-798627, Nagaland, India*

Prof. Dipak Sinha  
Department of Chemistry

e-mail: [dipaksinha@gmail.com](mailto:dipaksinha@gmail.com)  
[dipaksinha@nagalanduniversity.ac.in](mailto:dipaksinha@nagalanduniversity.ac.in)

## CERTIFICATE

This is to certify that **Ms. Mridushmita Baruah**, a registered Research Scholar for Ph.D. degree in Chemistry under Nagaland University has carried out his research work under my guidance. Her thesis entitled “**Photocatalytic degradation of water pollutants using activated carbon-TiO<sub>2</sub>/metal doped TiO<sub>2</sub> based nanocomposite**” embodies the original research work and has fulfilled all the requirements according to the rules of this University regarding investigations.

Further, to the best of my knowledge, the research work has not been submitted to any university for the award of any degree or diploma to any other University/Institution.

**(Dipak Sinha)**

**Supervisor**

Prof. Dipak Sinha  
Department of Chemistry  
Nagaland University



## Acknowledgements

Alone we can do so little, together we can do so much.

I take this moment to extend my appreciation and gratitude to every individual for their help and support through the course of my Ph.D. journey. THANK YOU.

Firstly I would like to thank our almighty God for blessings me with wisdom, good health, and guidance throughout my research journey.

I extend my heartfelt and profound gratitude to **Prof. Dipak Sinha**, my research supervisor, for allowing me to work under him in the first place. His constant and patient guidance, enthusiastic motivation, and encouragement have always been the fuel to move one step further. His valuable and constructive critiques have always been the pillar, without which the completion of this work would not have been possible. The years spent under his guidance have been a worthy experience that has molded me into the person I am today. His consistency in discussing creative and brilliant ideas has been a catalyze which has elevated my interest and confidence in science more than ever before.

I would also like to thank **Prof. Upasana Bora Sinha**, Department of Chemistry, Nagaland University, for her thoughtful advice and constructive recommendations. Her ever-ready attitude and excellent caliber to proofread my manuscripts whenever I approach, despite her busy schedule have contributed significantly to the success of my research work.

I also would acknowledge a deep sense of gratitude to all the teaching faculties of the Chemistry department, Nagaland University: **Prof. M. Indira Devi** (Head of Department), **Dr. I. Tavishe Phucho**, **Dr. M. Prabhakar**, **Dr. Nurul Alam Choudhury**, and **Dr. Seram Dushila Devi**, for their useful suggestions and assistance that helped me to keep my progress on track.

My sincere gratitude to **Nagaland University**, for providing the basic facilities to conduct my research. I am also grateful to the University Grant Commission (PF/RDC/NNF-41/2017-1521) for providing financial assistance.

I owe my sincere thanks to **Dr. R.L Goswamee**, CSIR-NEIST, **Dr. Khemnath Patir**, Guahati University, and **Dr. Arundhuti Devi**, IASST, Guwahati for allowing me to use their instruments during characterization of my samples.

I extend my sincere gratitude to **Prof. Nikhil Guchhait**, Department of Chemistry, Calcutta University for extending computational facility.

My gratitude and thanks to the non-teaching staffs **Mr. S. Bendangtemsu**, **Ms. Sunepjungla**, **Ms. Temsuienla Amer**, **Mr. Johnny Yanthan**, **Mr. Phyoemo Patton** for their immense support throughout my research period.

My greatest indebtedness goes to my labmates **Dr. Parimal Chandra Bhomick**, **Dr. Chubaakum Pongener**, **Dr. Champa Gogoi**, **Ms. Aola Supong**, **Mr. Supongtoshi Jamir**,

**Mr. Suraj Kumar, Mr. Soremo L Ezung, and Mr. Shisak Sharma** for their unwavering support and encouragements.

Special thanks to my research scholar friends from other laboratories and department for their wonderful friendship and encouragement.

On my personal note, I would like to acknowledge my family members and friends whose love, support, guidance, and prayers have encouraged and pushed me to achieve where I have reached now.

Last but not the least, I want to acknowledge everyone who have directly or indirectly influence and contributed in furnishing to complete this research work.

*Mridushmita Baruah*  
**Mridushmita Baruah** 14/12/202

# NAGALAND UNIVERSITY

Sl. No. : 16- 59079

## STATEMENT OF MARKS Ph. D COURSE WORK EXAMINATION, 2017

DEPARTMENT OF CHEMISTRY

The following are the marks secured by Mridushmita Baruah  
Roll No. 06/16 of Ph.D Course Work Examination held in 2017

Subject(s)/Paper(s)	Max. Marks	Minimum Qualifying Marks	Marks Secured
Paper No. Chem-601 Research Methodology	100	35	72
Paper No. Chem-602 (D) Advance in Chemistry	100	35	64
Paper No. Chem-603 Literature Review, Report Writing and Presentation	100	35	84
<b>Total Aggregate Marks</b>			<b>220</b>
Average Pass Mark – 55 %			

Result	Division	Percentage
Passed	I Division	73 %

Marks compared by:



COE/Dy. Reg./AR (Exams)

*[Signature]*

# NAGALAND UNIVERSITY

HEAD QUARTERS : LUMAMI

## Ph. D COURSE WORK EXAMINATION

This is to certify that Mr/Ms. **Mridushmita Baruah**  
of Nagaland University bearing Roll No. **6/16** is qualified in the Ph.D Course Work Examination  
in the Department of **Chemistry** Nagaland University held in the Year 20**17**

*[Signature]*  
Head of Department

**Department of Chemistry**  
Nagaland University

Dean

*[Signature]*  
Dean

School of

School of Sciences  
Nagaland University  
Hqs. Lumami Nagaland



## CONTENTS

<i>List of figures</i>	<i>i-v</i>
<i>List of tables</i>	<i>i-ii</i>

### CHAPTER 1: Introduction

1.1 Introduction	1-2
1.2 Photocatalysis	2
1.3 Mechanism of heterogeneous photocatalysis	3-4
1.4 Semiconductor materials as photocatalyst	4-5
1.5 Titanium dioxide (TiO <sub>2</sub> ) as a photocatalyst	5-7
1.6 Difficulties in TiO <sub>2</sub> photocatalysis	7-9
1.7 Modification of TiO <sub>2</sub> photocatalyst	9-10
1.8 Applications of TiO <sub>2</sub> photocatalysis	11-13
1.9 Present study	13-14
1.10 Aims and objectives of the work	14-16
References	17-24

### CHAPTER 2: Materials and methods

2.1 Materials and methods	25
2.2 Synthesis of photocatalyst and supporting material	25-27
2.2.1 Synthesis of TiO <sub>2</sub> nanoparticles and TiO <sub>2</sub> /activated carbon nanocomposite	25-27
2.2.2 Synthesis of activated carbon	27
2.3 Instruments coupled with this work	27-32
2.4 Photocatalytic activity of the TiO <sub>2</sub> /activated carbon nanocomposite	32-35
2.4.1 Application of Gas Chromatography-Mass Spectrometry (GC-MS) for identification of end products	34
2.4.2 Photocatalytic reactor	34-35
2.5 Description of water pollutants mentioned in this work	35-37
2.6 Kinetic equations	37-38
2.6.1 Langmuir Hinshelwood kinetic model	37-38
2.6.2 Half-life time reaction	38
2.7 Thermodynamic studies	38
2.8 Energy consumption and cost analysis	39
2.8.1 Electrical energy determination	39
2.8.2 Total operating cost	39
2.9 Density functional theory (DFT) studies	40-41
References	41-47

### CHAPTER 3: Photocatalytic degradation of alizarin red S dye using TiO<sub>2</sub>-activated carbon nanocomposite

3.1 Introduction	48-50
3.2 Materials and methods	51-55

3.2.1 Materials	51
3.2.2 Synthesis of TiO <sub>2</sub> supported on activated carbon (TiO <sub>2</sub> -NP/PAC) nanocomposite	51
3.2.2.1 Activated carbon preparation	51
3.2.2.2 Sol-gel method of TiO <sub>2</sub> synthesis	51-52
3.2.2.3 TiO <sub>2</sub> supported on activated carbon (TiO <sub>2</sub> -NP/PAC) nanocomposite synthesis	52
3.2.3 Characterization of TiO <sub>2</sub> -NP/PAC nanocomposite	52
3.2.4 Photocatalysis	53
3.2.5 Phytotoxicity assessment	54
3.2.6 Computational studies	54-55
3.3 Results and discussions	55-76
3.3.1 Characterization of TiO <sub>2</sub> -NP/PAC nanocomposite	55-60
3.3.2 Photocatalytic reactions	60-63
3.3.3 Kinetic studies	63-64
3.3.4 Thermodynamic studies	64-65
3.3.5 Effect of interfering ions on ARS photocatalytic degradation	65-66
3.3.6 Catalyst reusability and photostability	66-67
3.3.7 GC-MS analysis	67-68
3.3.8 Mechanism for photodegradation	68-69
3.3.9 Toxicity assessment of ARS and its effluent after degradation	69-70
3.3.10 Energy consumption and cost analysis	70-72
3.3.11 Results computational studies	72-75
3.3.12 Comparison with other composites	76
3.4 Conclusion	76-77
References	78-82

## **CHAPTER 4: Photocatalytic degradation of congo red dye using Fe-doped TiO<sub>2</sub>/activated carbon nanocomposite and its antimicrobial activity towards *E. coli* and *S. aureus***

4.1 Introduction	83-85
4.2 Materials and methods	86-88
4.2.1 Materials	86
4.2.2 Synthesis of FDT/PAC nanocomposite	86
4.2.3 Characterization of FDT/PAC nanocomposite	86-87
4.2.4 Photocatalytic degradation experiment	87-88
4.2.5 Antibacterial activity experiment	88
4.2.5.1 Photocatalytic inactivation procedure	88
4.3 Results and discussion	88-111
4.3.1 Characterization of FDT/PAC nanocomposite	88-95
4.3.2 Photocatalytic activity	95-98
4.3.3 Kinetic studies	98-99
4.3.4 Thermodynamic studies	99-100

4.3.5 Effect of interfering ions on CR photocatalytic degradation	100-101
4.3.6 Reusability and photostability of the nanocomposite	101-102
4.3.7 GC-Mass analysis	102-104
4.3.8 Photocatalytic inactivation	105-108
4.3.9 Energy consumption and cost analysis	109-110
4.3.10 Comparison studies	110
4.4 Conclusion	111
References	112-118

## **CHAPTER 5: Photocatalytic degradation of anthracene using Ni-doped TiO<sub>2</sub>/activated carbon nanocomposite**

5.1 Introduction	119-120
5.2 Materials and methods	121-122
5.2.1 Materials	121
5.2.2 Synthesis of NDT/PAC nanocomposite	121
5.2.3 Characterization	121-122
5.2.4 Photocatalytic degradation experiment	122
5.3 Results and discussion	123-138
5.3.1 Characterization of NDT/PAC nanocomposite	123-127
5.3.2 Photocatalytic activity	127-130
5.3.3 Kinetic studies	131
5.3.4 Thermodynamic studies	131-132
5.3.5 Effect of interfering ions on ANT photocatalytic degradation	132-133
5.3.6 Nanocomposite reusability and photostability	133-134
5.3.7 GC-Mass analysis	134-135
5.3.8 Energy consumption and cost analysis	136-137
5.3.9 Comparison studies	137-138
5.4 Conclusion	138-139
References	140-143

## **CHAPTER 6: Photocatalytic degradation of phenol using Co-doped TiO<sub>2</sub>/activated carbon nanocomposite**

6.1 Introduction	144-145
6.2 Materials and methods	146-147
6.2.1 Materials	146
6.2.2 Synthesis of CDT/PAC nanocomposite	146
6.2.3 Characterization of CDT/PAC nanocomposite	146-147
6.2.4 Photocatalytic degradation experiment	147
6.3 Results and discussion	148-164
6.3.1 Characterization of CDT/PAC nanocomposite	148-152
6.3.2 Photocatalytic activity	152-155
6.3.3 Kinetic studies	155-156

6.3.4 Thermodynamic studies	156-157
6.3.5 Effect of interfering ions on photocatalytic degradation of phenol	157-158
6.3.6 Nanocomposite reusability and photostability	158-159
6.3.7 GC-Mass analysis	160-161
6.3.8 Energy consumption and cost analysis	161-163
6.3.9 Comparison studies	163-164
6.4 Conclusion	164-165
References	166-171

<b>Chapter 7: Summary and conclusions</b>	172-175
---	---------

<b><i>Appendix 1 Ph.D. Thesis Certificate on Plagiarism check</i></b>
---





## *List of Figures*

<b>Figure 1.1</b>	Conventional wastewater treatment methods	1
<b>Figure 1.2</b>	Mechanism of photocatalytic degradation	4
<b>Figure 1.3</b>	Different crystals forms of TiO <sub>2</sub>	6
<b>Figure 1.4</b>	Principle of TiO <sub>2</sub> supported on activated carbon nanocomposite	8
<b>Figure 1.5</b>	Schematic diagram showing the mechanism of metal-doped TiO <sub>2</sub> -NP	10
<b>Figure 1.6</b>	Scheme of the present study	14
<b>Figure 1.7</b>	Outline of the thesis	16
<b>Figure 2.1</b>	A schematic illustration of a XRD system	28
<b>Figure 2.2</b>	A schematic diagram of a SEM	29
<b>Figure 2.3</b>	A schematic illustration of a FT-IR system	30
<b>Figure 2.4</b>	A schematic illustration of a PL system	30
<b>Figure 2.5</b>	Schematic illustration of a DRS system	31
<b>Figure 2.6</b>	Schematic illustration of a BET analyzer	31
<b>Figure 2.7</b>	A schematic illustration of a GC-MS analyzer	34
<b>Figure 2.8</b>	Schematic experimental setup for UV light photocatalytic device	34
<b>Figure 2.9</b>	Molecular structure of Alizarin red S dye	35
<b>Figure 2.10</b>	Molecular structure of Congo red dye	36
<b>Figure 2.11</b>	Molecular structure of Anthracene	36
<b>Figure 2.12</b>	Molecular structure of Phenol	36
<b>Figure 3.1</b>	Schematic illustration of photodegradation of alizarin red S dye using TiO <sub>2</sub> -NP/PAC nanocomposite	50
<b>Figure 3.2</b>	Different reaction steps associated with the synthesis of TiO <sub>2</sub>	52
<b>Figure 3.3</b>	X-ray Diffractogram of TiO <sub>2</sub> -NP/PAC nanocomposite	55
<b>Figure 3.4</b>	SEM images of (a) TiO <sub>2</sub> nanoparticles and (b) TiO <sub>2</sub> -NP/PAC nanocomposite	56
<b>Figure 3.5</b>	EDX spectra of TiO <sub>2</sub> -NP/PAC nanocomposite	56
<b>Figure 3.6</b>	XPS spectra of TiO <sub>2</sub> -NP/PAC nanocomposite: (a) survey, (b) Ti 2p, (c) C 1s, and (d) O 1s	57
<b>Figure 3.7</b>	FT-IR spectra of TiO <sub>2</sub> -NP/PAC nanocomposite	58
<b>Figure 3.8</b>	(a) UV-visible DRS spectra and (b) Tauc's plot for calculating bandgap of TiO <sub>2</sub> -NP/PAC nanocomposite	59
<b>Figure 3.9</b>	Photoluminescence spectra of TiO <sub>2</sub> , and TiO <sub>2</sub> -NP/PAC nanocomposite	59
<b>Figure 3.10</b>	Zero-point charge plot for TiO <sub>2</sub> -NP/PAC nanocomposite	60
<b>Figure 3.11</b>	Snapshot showing aqueous deep red color ARS and the colorless end products obtained after degradation by TiO <sub>2</sub> -NP/PAC nanocomposite	61
<b>Figure 3.12</b>	Effect of nanocomposite loading in the degradation of ARS solution	61
<b>Figure 3.13</b>	Effect of initial pH in the degradation of ARS solution	62

<b>Figure 3.14</b>	Effect of initial dye concentration on the photocatalytic degradation of ARS solution	63
<b>Figure 3.15</b>	Pseudo first-order model of ARS photodegradation onto the TiO <sub>2</sub> -NP/PAC nanocomposite	64
<b>Figure 3.16</b>	lnK <sub>d</sub> as a function of 1/T (ARS = 20 ppm, pH 2, catalyst dose = 0.05 g, and irradiation time = 80 minutes)	64
<b>Figure 3.17</b>	Photocatalytic degradation of ARS in the presence of interfering ions using TiO <sub>2</sub> -NP/PAC nanocomposite	66
<b>Figure 3.18</b>	ARS degradation efficiency of TiO <sub>2</sub> -NP/PAC nanocomposite up to five cycles	66
<b>Figure 3.19</b>	FT-IR spectra of TiO <sub>2</sub> -NP/PAC before and after ARS degradation	67
<b>Figure 3.20</b>	Mass spectra of degradation products of ARS aqueous solution	67
<b>Figure 3.21</b>	Proposed degradation pathway for the degradation of ARS over TiO <sub>2</sub> -NP/PAC nanocomposite	68
<b>Figure 3.22</b>	Growth of the <i>Cicer arietinum</i> (Gram), <i>Solanum lycopersicum</i> (Tomato), <i>Pisum sativum</i> (Garden pea), <i>Vigna radiate</i> (Mung bean) seeds on treatment with (a) ARS, (b) ARS extract, and (c) Distilled H <sub>2</sub> O	69
<b>Figure 3.23</b>	HOMO and LUMO molecular orbital of PAC, TiO <sub>2</sub> , ARS, TiO <sub>2</sub> -NP/PAC, and interaction of TiO <sub>2</sub> , and TiO <sub>2</sub> -NP/PAC with ARS	73
<b>Figure 4.1</b>	Schematic illustration of photodegradation of congo red and photocatalytic inactivation of bacteria over FDT/PAC nanocomposite	85
<b>Figure 4.2</b>	X-ray Diffraction pattern of FDT/PAC nanocomposite and a comparison with TiO <sub>2</sub> , TiO <sub>2</sub> -NP/PAC	89
<b>Figure 4.3</b>	(a) SEM image of FDT/PAC nanocomposite, (b) EDX spectra of FDT/PAC nanocomposite	90
<b>Figure 4.4</b>	Survey scan spectra for FDT/PAC nanocomposite	90
<b>Figure 4.5</b>	High resolution core level XPS spectrum of (a) Ti 2p, (b) O 1s, and (c) C 1s	91
<b>Figure 4.6</b>	FT-IR spectra of TiO <sub>2</sub> and FDT/PAC nanocomposite	92
<b>Figure 4.7</b>	(a) UV-Visible DRS spectra and (b) Tauc's plot for the determination of optical bandgap for TiO <sub>2</sub> , TiO <sub>2</sub> -NP/PAC, and FDT/PAC nanocomposite	93
<b>Figure 4.8</b>	Photoluminescence spectra of TiO <sub>2</sub> and FDT/PAC nanocomposite	94
<b>Figure 4.7</b>	Zero-point charge plot for FDT/PAC nanocomposite	95
<b>Figure 4.10</b>	Effect of FDT/PAC nanocomposite loading in the degradation of CR solution	96
<b>Figure 4.11</b>	Effect of pH in the degradation of CR solution	96
<b>Figure 4.12</b>	Effect of degradation of CR dye solutions by (a) FDT/PAC, (b) TiO <sub>2</sub> -NP/PAC, and (c) TiO <sub>2</sub> catalyst for degradation of different	98

concentrations of dye solutions for different contact times under visible light (520 nm)

<b>Figure 4.13</b>	Pseudo-first-order rate kinetics of CR degradation loaded on FDT/PAC nanocomposite	99
<b>Figure 4.14</b>	$\ln K_d$ as a function of $1/T$ (CR concentration = 20 ppm, pH = 1, Nanocomposite dose = 0.06 g and Contact time = 60 minutes)	99
<b>Figure 4.15</b>	Photocatalytic degradation of CR in the presence of interfering ions using FDT/PAC nanocomposite	101
<b>Figure 4.16</b>	CR degradation efficiency of FDT/PAC nanocomposite up to five cycles	101
<b>Figure 4.17</b>	FT-IR spectra of FDT/PAC before and after CR degradation	102
<b>Figure 4.18</b>	Mass spectra of the metabolite of CR dye	102
<b>Figure 4.19</b>	Proposed degradation pathway for the degradation of CR over FDT/PAC nanocomposite	104
<b>Figure 4.20</b>	Photocatalytic inactivation of (a) <i>E. coli</i> , (b) <i>S. aureus</i> as a function of time	105
<b>Figure 4.21</b>	Photographs of photocatalytic inactivation of <i>E. coli</i> at different light exposure times	106
<b>Figure 4.22</b>	Photographs of photocatalytic inactivation of <i>S. aureus</i> at different light exposure times	106
<b>Figure 4.23</b>	A schematic diagram showing the mechanism of photocatalytic inactivation of bacteria using FDT/PAC nanocomposite	107
<b>Figure 5.1</b>	A schematic representation of photocatalytic degradation of anthracene using NDT/PAC nanocomposite	120
<b>Figure 5.2</b>	XRD patterns of NDT/PAC nanocomposite in contrast with $\text{TiO}_2$ , $\text{TiO}_2\text{-NP/PAC}$	123
<b>Figure 5.3</b>	(a) SEM image and (b) EDX pattern of NDT/PAC nanocomposite	124
<b>Figure 5.4</b>	FT-IR spectra of NDT/PAC nanocomposite	125
<b>Figure 5.5</b>	(a) UV-Visible DRS spectra and (b) Tauc's plot for the determination of optical band gap for $\text{TiO}_2$ , $\text{TiO}_2\text{-NP/PAC}$ , and NDT/PAC nanocomposite	126
<b>Figure 5.6</b>	Photoluminescence spectra of $\text{TiO}_2$ , and NDT/PAC nanocomposite	126
<b>Figure 5.7</b>	Zero-point charge plot for NDT/PAC nanocomposite	127
<b>Figure 5.8</b>	Effect of NDT/PAC (0.05 g) with irradiation time in the degradation of ANT solution under UV light (325 nm)	128
<b>Figure 5.9</b>	Effect of nanocomposite (a) NDT/PAC, (b) $\text{TiO}_2\text{-NP/PAC}$ , and (c) $\text{TiO}_2$ amount in the degradation of ANT solution under visible light	129
<b>Figure 5.10</b>	Effect of (a) NDT/PAC, (b) $\text{TiO}_2\text{-NP/PAC}$ , and (c) $\text{TiO}_2$ (0.05 g) with pH in the degradation of ANT solution under visible light	130

<b>Figure 5.11</b>	Effect of (a) NDT/PAC, (b) TiO <sub>2</sub> -NP/PAC, and (c) TiO <sub>2</sub> (0.05 g) with contact time in the degradation of ANT solution under visible light	130
<b>Figure 5.12</b>	Pseudo-first-order rate kinetics of ANT degradation loaded on NDT/PAC nanocomposite	131
<b>Figure 5.13</b>	lnK <sub>d</sub> as a function of 1/T (Using 20 ppm ANT concentration, 0.05 g NDT/PAC, pH 2, and 50 minutes visible light irradiation)	132
<b>Figure 5.14</b>	Photocatalytic degradation of ANT in the presence of interfering ions using NDT/PAC nanocomposite	133
<b>Figure 5.15</b>	ANT degradation efficiency of NDT/PAC nanocomposite upto five cycles	134
<b>Figure 5.16</b>	FT-IR spectra of NDT/PAC before and after ANT degradation	134
<b>Figure 5.17</b>	Mass spectra of degradation products of ANT aqueous solution	135
<b>Figure 5.18</b>	Proposed degradation pathway for the degradation of ANT over NDT/PAC nanocomposite	135
<b>Figure 6.1</b>	Schematic illustration of photodegradation of phenol over CDT/PAC nanocomposite	145
<b>Figure 6.2</b>	X-ray Diffraction pattern of CDT/PAC nanocomposite and a comparison with TiO <sub>2</sub> , TiO <sub>2</sub> -NP/PAC	148
<b>Figure 6.3</b>	SEM image of (a) CDT/PAC nanocomposite, (b) EDX spectra of CDT/PAC nanocomposite	149
<b>Figure 6.4</b>	FT-IR spectra of CDT/PAC nanocomposite	149
<b>Figure 6.5</b>	(a) UV-Visible DRS spectra and (b) Tauc plot for the determination of optical bandgap for TiO <sub>2</sub> and CDT/PAC nanocomposite (plot for TiO <sub>2</sub> -NP/PAC is shown for comparison only)	150
<b>Figure 6.6</b>	Photoluminescence spectra of TiO <sub>2</sub> , and CDT/PAC nanocomposite	151
<b>Figure 6.7</b>	Zero-point charge plot for CDT/PAC nanocomposite	152
<b>Figure 6.8</b>	Effect of CDT/PAC (0.35 g) with irradiation time in the degradation of phenol solution under UV light (325 nm)	153
<b>Figure 6.9</b>	Effect of nanocomposite (a) CDT/PAC, (b) TiO <sub>2</sub> -NP/PAC, and (c) TiO <sub>2</sub> amount in the degradation of phenol solution under visible light	154
<b>Figure 6.10</b>	Effect of (a) CDT/PAC, (b) TiO <sub>2</sub> -NP/PAC, and (c) TiO <sub>2</sub> (0.35 g) with pH in the degradation of phenol solution under visible light	154
<b>Figure 6.11</b>	Effect of (a) CDT/PAC, (b) TiO <sub>2</sub> -NP/PAC, and (c) TiO <sub>2</sub> (0.35 g) with contact time in the degradation of phenol solution under visible light	155
<b>Figure 6.12</b>	Pseudo-first-order rate kinetics of phenol degradation loaded on CDT/PAC nanocomposite	156
<b>Figure 6.13</b>	lnK <sub>d</sub> as a function of 1/T (phenol concentration = 20 ppm, pH = 2, Nanocomposite dose = 0.35 g and Contact time = 60 minutes)	157

<b>Figure 6.14</b>	Photocatalytic degradation of phenol in the presence of interfering ions using CDT/PAC nanocomposite	158
<b>Figure 6.15</b>	Phenol degradation efficiency of CDT/PAC nanocomposite upto five cycles	159
<b>Figure 6.16</b>	FT-IR spectra of CDT/PAC before and after ANT degradation	159
<b>Figure 6.17</b>	FT-IR spectra of CDT/PAC before and after ANT degradation	160
<b>Figure 6.18</b>	Proposed degradation pathway for the degradation of phenol over CDT/PAC nanocomposite	161





## *List of Tables*

<b>Table 1.1</b>	Bandgap energy and wavelength of photocatalysts	5
<b>Table 1.2</b>	Physical and chemical properties of anatase TiO <sub>2</sub>	7
<b>Table 3.1</b>	Values of various thermodynamics parameters for the degradation of ARS using TiO <sub>2</sub> -NP/PAC	65
<b>Table 3.2</b>	Phytotoxicity of ARS and metabolites formed after its degradation	70
<b>Table 3.3</b>	Effect of ARS concentration on electrical energy consumption	71
<b>Table 3.4</b>	Cost analysis of ARS degradation in the photocatalytic reactor under different operating conditions	72
<b>Table 3.5</b>	Calculated molecular properties of PAC and TiO <sub>2</sub> -NP/PAC nanocomposite	74
<b>Table 3.6</b>	Molecular chemical descriptors of PAC and TiO <sub>2</sub> -NP/PAC nanocomposite	74
<b>Table 3.7</b>	Adsorption energy and bond length of TiO <sub>2</sub> -ARS and TiO <sub>2</sub> -NP/PAC-ARS system	75
<b>Table 3.8</b>	Comparison of catalytic activity of other work in the literature with TiO <sub>2</sub> /pine cone activated carbon nanocomposite	76
<b>Table 4.1</b>	BET surface area and pore size of TiO <sub>2</sub> , FDT/PAC nanocomposite	94
<b>Table 4.2</b>	Thermodynamic parameters calculated for the degradation of CR dye using FDT/PAC nanocomposite	100
<b>Table 4.3</b>	Rate constant of bacterial photocatalytic inactivation of <i>E. coli</i> and <i>S. aureus</i>	108
<b>Table 4.4</b>	Effect of CR dye concentration on electrical energy consumption	109
<b>Table 4.5</b>	Cost analysis of CR degradation in the photocatalytic reactor under different operating conditions	110
<b>Table 4.6</b>	Comparison of catalytic activity of previous works in the literature with FDT/PAC nanocomposite	110
<b>Table 5.1</b>	BET surface area and pore size of TiO <sub>2</sub> , PAC, and, NDT/PAC nanocomposite	127
<b>Table 5.2</b>	Values of enthalpy ( $\Delta H^\circ$ ), entropy ( $\Delta S^\circ$ ), and Gibbs free energy ( $\Delta G^\circ$ ) calculated for the photocatalytic degradation of ANT using NDT/PAC nanocomposite	132
<b>Table 5.3</b>	Effect of ANT concentration on electrical energy consumption	136
<b>Table 5.4</b>	Cost analysis of ANT degradation in the photocatalytic reactor under different operating conditions	137
<b>Table 5.5</b>	Comparison of catalytic activity of previous work in the literature with NDT/PAC nanocomposite	138
<b>Table 6.1</b>	BET surface area and pore size of TiO <sub>2</sub> , CDT/PAC nanocomposite	152
<b>Table 6.2</b>	Thermodynamic parameters calculated for the degradation of phenol using CDT/PAC nanocomposite	157
<b>Table 6.3</b>	Effect of phenol concentration on electrical energy consumption	162
<b>Table 6.4</b>	Cost analysis of phenol degradation in the photocatalytic reactor under different operating conditions	163

**Table 6.5** Comparison of catalytic activity of other work in the literature with CDT/PAC nanocomposite

# **CHAPTER 1**

## **INTRODUCTION**

---

This chapter presents a brief introduction to the titanium dioxide photocatalytic oxidation process which is utilized as an efficient novel method for wastewater treatment. The structures, unique properties, and mechanisms involved in titanium dioxide photocatalysis are presented. An overview of the strategies for the enhancement of the activity by dispersing titanium dioxide nanoparticles in suitable support is also included. Methodologies for the utilization of the titanium dioxide nanoparticles in visible light by doping with different metals/non-metals are also discussed. Finally, the use of modified titanium dioxide nanocomposite for wastewater remediation is also presented.

## 1.1 Introduction

Water pollution is a major concern as it causes damaging effects on aquatic biota and also on human health [1]. Water is mostly polluted due to the release of organic and inorganic pollutants from textile, chemical, and pharmaceutical industries [2–5]. The use of toxic chemicals during different processes in industries pollutes water which poses a major threat to the environment [6]. While some of the toxic organic chemicals are easily biodegradable by the microorganisms present in the water however synthetic chemicals cannot be removed from water by natural processes [7]. Chemicals such as synthetic dyes from the textile industry, nitroaromatics, polycyclic aromatic hydrocarbons, organochlorines, polychlorinated biphenyls, polymers, and pesticides, etc. are considered as the major environmental pollutants as these are highly persistent [8]. In addition to chemical contaminants, the presence of infectious bacteria's *Staphylococcus aureus* (*S. aureus*) and *Escherichia coli* (*E. coli*) are also of serious concern to the environment as these pollute water and are causes of serious water-borne diseases [9]. Therefore, the degradation of such hazardous pollutants from water is of great concern for everyone [10].

In present times, numerous techniques such as biological treatments, conventional physicochemical methods, microbial and enzymatic decomposition are available for the treatment of the pollutants in wastewater [11]. The development of an appropriate method for the removal of water pollutants depends upon several factors such as treatment efficiency, economic efficiency, pollutants type, the concentration of pollutants, and environmental compatibility [12]. Some of the conventional physicochemical methods used for the treatment of wastewater are shown in Figure 1.1



**Figure 1.1** Conventional wastewater treatment methods

Conventional methods of wastewater treatment have limitations not only in terms of rate but also in terms of feasibility, operational difficulties, reliability, efficiency, pre-treatment necessities, practicability, environmental impact, sludge production [13]. Furthermore, the requirement of toxic chemicals in many of these treatment processes leads to an additional requirement of managing and treating their residuals products can further append to the problems of contamination in freshwater sources [14]. The commonly used wastewater purification methods such as chemical precipitation, coagulation, flotation, adsorption, ion exchange on resins, membrane filtration, etc., convert pollutants to toxic by-products and generate sludges, the removal of which requires additional cost and steps [15]. Therefore, in order to resolve the shortcomings of conventional wastewater treatment, it becomes necessary to innovate efficient wastewater treatment technologies by adopting or combining other new advanced methods. One such method which is expected to hold promise is photocatalysis. This advanced method is gaining more attention due to its ability to degrade organic pollutants to less harmful carbon dioxide and water, without producing any sludges, and its cost-effectiveness and sustainability properties make it a highly efficient technique [16], and therefore it was proposed to apply photocatalysis as an eco-friendly technology for complete degradation of pollutants to less harmful products.

## 1.2 Photocatalysis

Photocatalysis is a process by which the rate of a chemical reaction is altered in presence of a photocatalyst under the influence of ultraviolet, visible, or infrared radiation [17]. During photocatalysis, highly reactive hydroxyl radicals ( $\cdot\text{OH}$ ; electrochemical potential 2.80 V) are generated from the photocatalyst upon exposure light [18]. These powerful hydroxyl radicals can easily oxidize pollutants and mineralize them to  $\text{CO}_2$ , and  $\text{H}_2\text{O}$  [19]. The photocatalysis can be classified into two types, *viz.*, homogenous photocatalysis and heterogeneous photocatalysis based on the photocatalyst phase with respect to the reactants [20].

During homogenous photocatalysis, the photocatalyst and the reactant molecules present in the same phase are irradiated with light to generate the reactive hydroxyl radicals. Some of the most used homogeneous photocatalysis methods include photo-Fenton ( $\text{UV}/\text{Fe}^{2+}/\text{H}_2\text{O}_2$ ) systems and ozone ( $\text{UV}/\text{O}_3/\text{H}_2\text{O}_2$ ) photolysis [21].

In heterogeneous photocatalysis, the photocatalyst and the reactants exist in either solid-liquid or solid-gas phases [22]. This method is an effective destructive technology for the photocatalytic degradation of pollutants due to its simplicity of separation from the reaction mixture, lower operating cost, and reusability properties [23]. This method uses semiconductor

metal oxides for the degradation of pollutants using easily available solar light and atmospheric oxygen ( $O_2$ ) as the source of energy and oxidant, respectively [24]. Therefore our present work mainly describes the synthesis of heterogeneous catalysts of semiconductor metal oxide and their application in pollutants degradation.

### 1.3. Mechanism of heterogeneous photocatalysis

The mechanism of heterogeneous photocatalysis used for degradation of highly concentrated toxic and harmful pollutants to carbon dioxide and water involve different steps which are discussed below [25]:

#### (i) Excitation of the semiconductor

A Semiconductor metal oxide has a valence band (VB) and conduction band (CB) in its structure and the valence band is populated with electrons [26]. The energy between the two bands is called bandgap energy. When the semiconductor metal oxide is irradiated with light of energy equal to or higher than the bandgap energy, electrons ( $e^-$ ) present in the VB excited to the CB leaving a hole ( $h^+$ ) in the VB (equation 1.1). The photo-induced electrons at the bottom of the CB are involved in the reduction processes, while the holes at the top of the VB are involved in the oxidation processes [27].

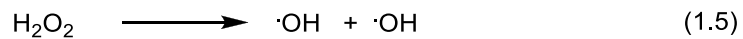
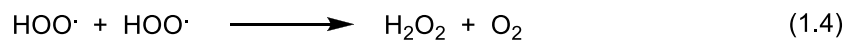
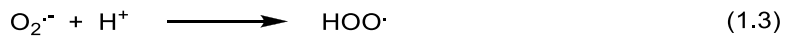


#### (ii) Formation of hydroxyl radical

The as generated excited electron ( $e^-_{CB}$ ) can react with the adsorbed oxygen ( $O_2$ ) on the  $TiO_2$  surface (photoreduction) to form reactive superoxide radical ( $O_2^{\cdot-}$ ) (equation 1.2).



The  $O_2^{\cdot-}$  radical further react with water molecules to form  $H_2O_2$  which eventually decomposes with the liberation of  $\cdot OH$  radical (equation 1.5) [28].



The hole ( $h^+_{VB}$ ) can react with water (photooxidation) to form reactive hydroxyl radical ( $\cdot OH$ ) (equation 1.6) [29].

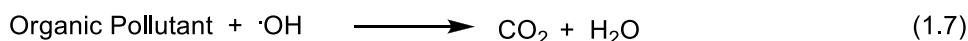


**(iii) Recombination reaction**

The as generated electron ( $e_{CB}^-$ ) and hole ( $h_{VB}^+$ ) can also recombine without participating in photoreaction while discharging the absorbed light energy in the form of heat [30].

**(iv) Degradation of organic pollutants**

Organic pollutants adsorbed on semiconductor surfaces are oxidized by the generated  $\cdot OH$  radical. This highly reactive  $\cdot OH$  radical has a similar oxidation potential similar to the normal hydrogen electrode (2.8 V), thus it can oxidize organic pollutants to the mineralized products, yielding  $CO_2$  and  $H_2O$  [31].



The schematic representation of the photocatalysis mechanism is shown in Figure 1.2:

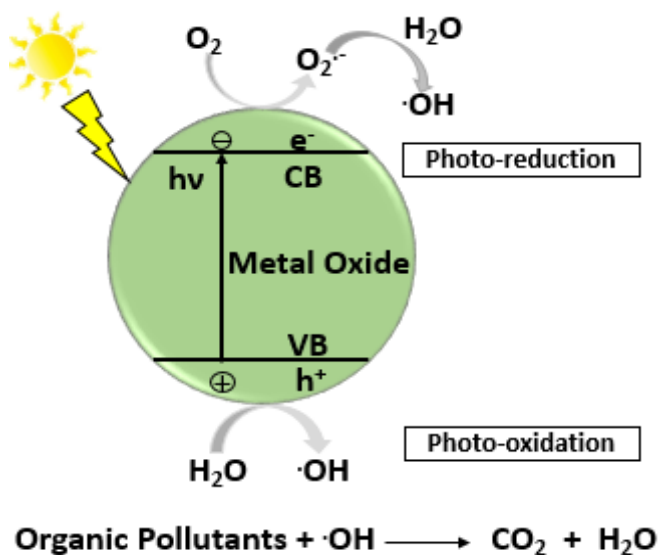


**Figure 1.2** Mechanism of photocatalytic degradation

**1.4 Semiconductor materials as photocatalyst**

In recent years, several semiconductor photocatalysts and their properties have been investigated. Ideally, a semiconductor photocatalyst should be photostable, chemically and biologically inert, should not undergo photo corrosion, low cost, non-toxic, suitable for both UV and visible light energy harnessing, and have appropriate bandgap energies for catalyzing reactions [29,32].

The most common semiconductors used as photocatalysts with their bandgap energies ( $E_g$ ) and respective wavelength are summarized in Table 1.1 [33].



<b>Table 1.1</b> Bandgap energy and wavelength of photocatalysts		
<b>Semiconductor</b>	<b>Bandgap (eV)</b>	<b>Wavelength (nm)</b>
TiO <sub>2</sub> (anatase)	3.20	388
TiO <sub>2</sub> (rutile)	3.00	413
ZnO	3.20	388
WO <sub>3</sub>	2.80	443
Bi <sub>2</sub> O <sub>3</sub>	2.80	400
Fe <sub>2</sub> O <sub>3</sub>	2.20	539
CdS	2.40	514
CuS	2.20	570
ZnS	3.60	344
CuO	2.00	570
BiVO <sub>4</sub>	2.40	500
Ag <sub>3</sub> PO <sub>4</sub>	2.45	365
g-C <sub>3</sub> N <sub>4</sub>	2.70	450
TaON	2.3	532
Ta <sub>3</sub> N <sub>5</sub>	2.10	473

For a semiconductor to act as an efficient photocatalyst it must absorb photons, generate electron-hole pairs, have minimum recombination of the electron-hole pairs, be stable over a prolonged period, and have oxidation-reduction potential of the  $\cdot\text{OH}$  and  $\text{H}_2\text{O}$  pairs within the bandgap domain of the semiconductor material [34].

Photocatalysis mainly used different semiconductor metal oxides (TiO<sub>2</sub>, SnO<sub>2</sub>, Bi<sub>2</sub>O<sub>3</sub>, ZrO<sub>2</sub>, ZnO, etc.) or metal sulphides (ZnS, PbS, CdS) for degradation of pollutants using easily available solar light and atmospheric oxygen (O<sub>2</sub>) as the source of energy and oxidant, respectively [35]. Among all the metal oxides used in photocatalysis, titanium dioxide (TiO<sub>2</sub>) is considered to be a benchmark photocatalyst which is superior to others due to its good photoactivity, low cost, strong oxidizing power, non-toxic nature, active at ambient temperature, and also not requires secondary disposal [36]. Therefore, in our present work, we used TiO<sub>2</sub> as the photocatalyst for photodegradation studies, a brief account of its properties, structures, etc. are described in the following section.

### 1.5 Titanium dioxide (TiO<sub>2</sub>) as a photocatalyst

TiO<sub>2</sub> was first discovered by Fujishima and Honda in 1972 and reported to have been used for water photolysis [37]. TiO<sub>2</sub> has been widely used as a photocatalyst due to its low cost, biological, and chemical inertness, photochemical stability, non-toxic, stability in ambient conditions, recyclability, and, wide bandgap energy of 3.2 eV for anatase and 3.0 eV for the rutile phase [38]. It can degrade toxic organic pollutants such as dyes, polyaromatic hydrocarbons, phenols, etc., and also has the ability to inactivate microbes present in water [39].

TiO<sub>2</sub> nanoparticles (TiO<sub>2</sub>-NP) exist in four main crystal forms: the stable rutile (tetragonal), metastable anatase (tetragonal), most stable brookite (rhombohedral), and TiO<sub>2</sub>-B (monoclinic) [40]. The metastable anatase can transform to stable rutile form by calcination within the temperature range of 600-1100°C [41]. These reaction temperatures can vary from 400 to 1100°C depending upon the type and amount of additives, reaction conditions, particle size, methods of preparation, degree of agglomeration, morphology, and so on. The anatase form of TiO<sub>2</sub>-NP connected through the corners, rutile form through the edges, and in the brookite form, connected through both the corners and edges [42] (Figure 1.3). In anatase form, each Ti<sup>4+</sup> ion in the structure is encircled by an octahedron of six oxygen atoms [37].

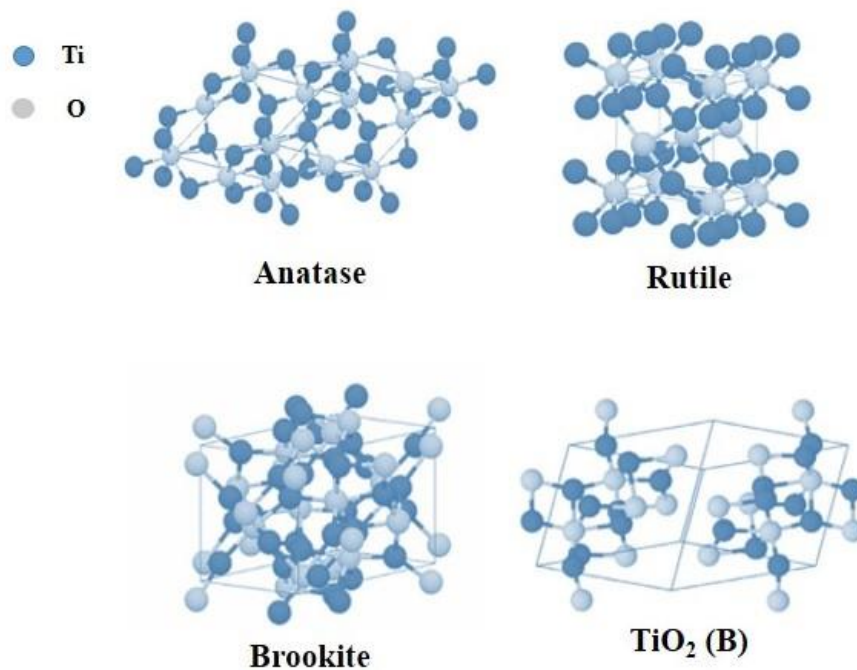


**Figure 1.3** Different crystals forms of TiO<sub>2</sub> [39]

The anatase phase gives better photocatalytic activity than the rutile phase. The properties of anatase TiO<sub>2</sub> are given in Table 1.2 [37]. The better activity of the anatase phase can be attributed to various factors, some of which are (i) the bandgap energy of rutile is lower (3.0 eV) than that of anatase (3.2 eV) which is due to the minor variations in the conduction band energies, (ii) the reducing ability of the rutile is lower than that of anatase which is due to the more positive conduction band potential of rutile as compared to the anatase by 0.2 V, (iii) the lower photocatalytic activity of rutile as compared to anatase due to the lower specific areas, larger particle size, and weak surface adsorption behaviour, (iv) anatase phase has the lowest recombination of photoexcited e<sup>-</sup>-h<sup>+</sup> pairs as compared to rutile phase due to the fastest migration of low effective mass e<sup>-</sup>-h<sup>+</sup> pairs in the anatase phase [43].

<b>Table 1.2</b> Physical and chemical properties of anatase TiO <sub>2</sub>	
<b>Properties</b>	<b>TiO<sub>2</sub> nanoparticles</b>
Molar mass ( g mol <sup>-1</sup> )	79.866
Light absorption (nm)	<390
Atoms per unit cell (Z)	4
Lattice parameters	a = 0.3785, c = 0.9514
Color	White
Odor	Odorless
Density (gcm <sup>-3</sup> )	3.78
Melting point (K)	2116
Boiling point (K)	3245
Solubility	Insoluble in water
Refractive index	2.488
Ti-O bond length (Å)	1.94 (4) 1.97 (2)
Thermal Conductivity (W m <sup>-1</sup> K <sup>-1</sup> )	4.8-11.8

### 1.6 Difficulties in TiO<sub>2</sub> photocatalysis

Due to the efficient photostability, TiO<sub>2</sub> is used in different applications such as in water treatment, air-purification, destruction of microorganisms, smell elimination, anti-mist, and self-cleaning [44]. However, there are some problems associated with the use of TiO<sub>2</sub>-NP as a photocatalyst. Since TiO<sub>2</sub>-NP is prone to agglomeration, difficulties are created while separating it from the solution [45]. Therefore, in order to decrease the agglomeration of TiO<sub>2</sub>-NP different supports have been used which helps in separating photocatalyst from the reaction solution.

Various matrixes have been used as support for the photocatalyst. For example, various glass, clay, activated carbon, silica gel, and polymeric materials, zeolites, cellulose, stainless steel, quartz, pumice stone, alumina, etc. have been reported by several workers as support for TiO<sub>2</sub>-NP [46]. The criteria for the selection of optimal catalyst support are:

- (i) The matrix should bond properly with the TiO<sub>2</sub> either chemically or physically without decreasing the reactivity of TiO<sub>2</sub> [47].
- (ii) The matrix should have a large surface area and a strong adsorption ability towards the pollutants to be degraded. This decreases the intermediates formed during photocatalytic degradation [48].
- (iii) The matrix should be transparent so that it allows light to go through it and be chemically inert so that it does not react with the contaminant molecules, intermediates, and the neighboring aqueous system [49].

- (iv) The matrix should allow easy and fast recovery of photocatalyst and re-use the photocatalyst with or without regeneration [50].

### Supporting material

Among the different supports available, activated carbon is commonly used in water remediation processes due to its good adsorption capacity, high surface area, inert, and suitable pore structure [35]. Activated carbon (AC) is a highly porous material having hydrophilic surface functional groups as well as a hydrophobic graphene layer used for both sorption and catalytic applications [51]. It has a high degree of porosity, an extensive surface area (500–2000  $\text{m}^2\text{g}^{-1}$ ), and a high degree of surface reactivity [52]. Therefore, in the present work nanocomposite of  $\text{TiO}_2$  with activated carbon as a support system has been used for the photocatalytic degradation of pollutants.

The nanocomposite of  $\text{TiO}_2$  with activated carbon as a support system helps in increasing the photocatalytic degradation rate by gradually facilitating pollutant molecules to come in contact with the  $\text{TiO}_2$  through the process of adsorption [53]. Thus hydroxyl radicals generated during the photocatalysis of  $\text{TiO}_2$  are easily able to trap pollutant molecules and this allows the degradation of pollutants at a faster rate with a lower electron-hole recombination rate [54] (Figure 1.4).

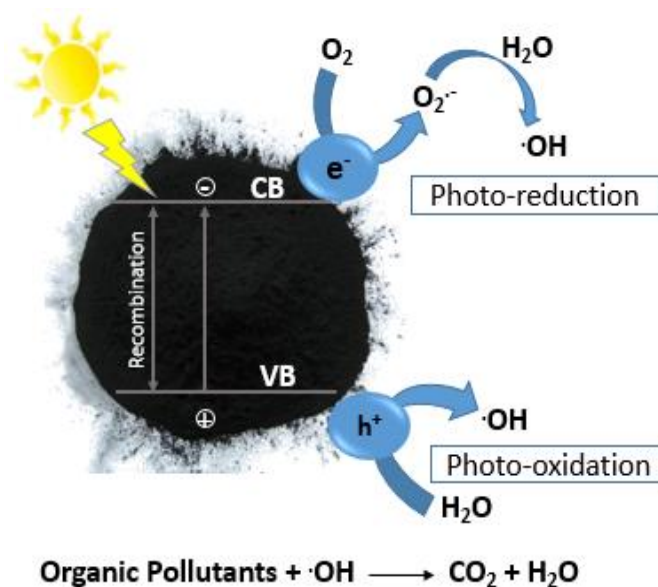


**Figure 1.4** Principle of  $\text{TiO}_2$  supported on activated carbon nanocomposite

The added advantages of using activated carbon are that AC-supported  $\text{TiO}_2$  exhibits synergism effects based on the adsorption property of AC and the photoactivity of  $\text{TiO}_2$ , which enhances

the overall removal efficiency of pollutants [55]. The main advantages of using AC for TiO<sub>2</sub> support are:

- (i) The high surface area of AC endows the nanocomposite photocatalysts with a good ability to adsorb or capture pollutant molecules in water, thus ensuring a high concentration of organic compounds around the surface of the photocatalysts, and thereby improving the photocatalytic reaction rates [56].
- (ii) The intermediates generated after photocatalysis can be effectively adsorbed by AC for the subsequent degradation cycle so that the availability of the photocatalyst can be improved [57].
- (iii) The combination of AC with semiconductors can partially suppress the combination of photogenerated electron-hole pairs so that the photocatalytic activity of nanocomposite will be improved [58].
- (iv) TiO<sub>2</sub> particles are hydrophilic when exposed to direct light whereas organic pollutants are hydrophobic. Because of this, the interaction between the pollutant molecules and TiO<sub>2</sub> becomes hampered. Therefore the use of AC as support allows the molecules of pollutants to come closer to the active site of TiO<sub>2</sub> leading to a quick and effective photodegradation process [59].

### 1.7 Modification of TiO<sub>2</sub> photocatalyst

TiO<sub>2</sub> has some properties that are very essential to accelerate light-driven chemical reactions in the ultraviolet region due to its larger bandgap energy (3.2 eV) [60]. However, the high electron-hole recombination and wide bandgap energy limit the use of TiO<sub>2</sub> in the highly available solar light or visible light region (400-750 nm) [61,62]. In order to make the photodegradation possible in the visible light region, it is essential to reduce the bandgap energy and that is possible by modifying the band energy of the TiO<sub>2</sub> either by doping metal/non-metal elements or by dye photosensitization and hydrogen treatment [61]. One of the ways to shift the light absorbance to the visible light region is by doping TiO<sub>2</sub> with metal dopant [63]. This path stimulates the usage of visible light and also helps the photogenerated electron-hole pair to keep separate [64]. In the present work, TiO<sub>2</sub> has been doped with metal ions having incomplete d subshell with an aim to increase the light absorbance in the visible light region.

#### Metal-doped TiO<sub>2</sub>

Doping has been proved to be a significant strategy in bandgap engineering in order to change the optical properties of semiconductor photocatalysts which are active in the visible light

region [65]. The insertion of a metal ions dopant in the crystal lattice modified the band edge positions of the crystal [66]. Cations that have been used for doping include rare earth metals (Th, Sc, Y) [67,68], transition metals (Fe, Co, Ni) [64,69], noble metals (Pd, Os, Ru) [70], poor metals (Al, Ga, Sn) [71], non-metals (C, N, S) [72,73], and halogens (F, Cl, Br) [25].

Metal ions are inserted into the crystal lattice of  $\text{TiO}_2$ , therefore impurity energy levels are formed in the bandgap of  $\text{TiO}_2$  [74]. Electron transfer from these levels to the conduction band of  $\text{TiO}_2$  reduces the bandgap energy and helps the doped  $\text{TiO}_2$ -NP to absorb in the visible light region [75]. The mechanism of visible light photocatalysis using transition metal-doped  $\text{TiO}_2$  supported on activated carbon is shown in Figure 1.5.

The photocatalytic degradation of pollutants using metal-doped photocatalyst under visible light irradiation is dependent on the type of the dopant (oxidation state, size), concentration, and the morphological and microstructural properties of the metal-et photocatalyst [76]. Doping transition metals (Fe, Ni, Co) in  $\text{TiO}_2$  can trap both electrons and holes, and thereby penetrating impurity energy levels near the conduction and also near the valence band of  $\text{TiO}_2$  [77–79]. Therefore, using transition metals as dopant material enhances the photocatalytic activity of  $\text{TiO}_2$  [80]. In the present study, different transition metals (Fe, Co, Ni) have been used as a dopant for  $\text{TiO}_2$  in order to enhance its photocatalytic activity in the visible light region.

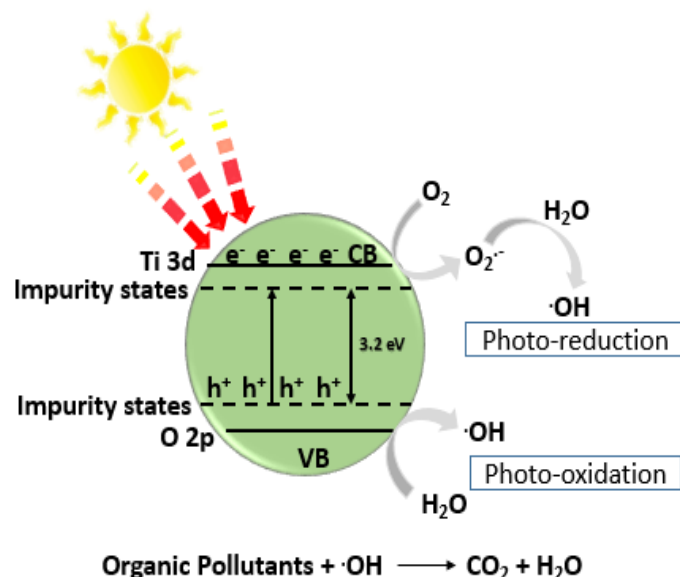


**Figure 1.5** Schematic diagram showing the mechanism of metal-doped  $\text{TiO}_2$ -NP [36]

### 1.8 Applications of $\text{TiO}_2$ photocatalysis

In the present study, the photocatalytic degradation of various organic pollutants like dyes, phenols, polyaromatic hydrocarbons (PAH), and also photocatalytic inactivation of bacterial pathogens are studied. Synthetic compounds like dyes, phenols, and polyaromatic hydrocarbons

pollute water sources and pose a severe threat to human health even at trace amounts. The presence of pathogenic microbes such as *Escherichia coli* (*E. coli*) and *Staphylococcus aureus* (*S. aureus*) in ambient water is also a major concern throughout the world because they cause water-borne diseases. Therefore, the elimination of these pollutants from water sources has become a prime concern for researchers. A brief description of the water pollutants studied in this thesis is given below:

### Degradation of dyes

In the present study, synthetic dyes alizarin red S and congo red are taken as the target pollutant molecule as these are highly used as coloring agents in the textile industry. The anthraquinone dye, alizarin red S (ARS) [1, 2-dihydroxy-9, 10-anthraquinone-sulfonic acid sodium salt] is an anionic dye and easily soluble in water [81]. It is extensively used in clothing industries from early times for coloring wool and nylon due to its vivid and durable properties. This class of dye is biologically active, which can damage genetic materials, and also can prevent the functioning of cytochrome P450 isozymes in the human body [82]. Alizarin red S cannot be completely removed by usual wastewater treatment processes due to the presence of aromatic rings in its structure. The aromatics rings have high optical, thermal, physical, and chemical stability [81]. Alizarin red S containing wastewater can cause many health problems to live organisms as it is highly toxic, carcinogenic, and mutagenic in nature [83]. Therefore, this is one of the major tasks to remove it from wastewater without being discharged into natural water bodies such as rivers and lakes. The present study planned to use titanium dioxide supported on activated carbon nanocomposite to degrade alizarin red S dye from wastewater. Various literature has been reported the use of TiO<sub>2</sub>-NP for the degradation of alizarin red S dye such as Souza *et al.* [84] reported the degradation of alizarin red S dye using Ag nanoparticles immobilized on TiO<sub>2</sub> surface with a maximum degradation percentage of 80% in 180 minutes. Sood *et al.* [85] also studied the degradation of alizarin red S dye using sol-gel prepared Bi-doped TiO<sub>2</sub> nanoparticles with a maximum degradation of 82% in 90 minutes.

The azo dye, congo red (CR) (disodium 4-amino-3-[4-[4-(1-amino-4-sulfonato-naphthalen-2-yl)diazenyl]phenyl]phenyl]diazenyl-naphthalene-1-sulfonate) is a benzidine-based anionic diazo dye [86]. It is most commonly used in fabric production and is highly carcinogenic and mutagenic. Using congo red-containing water can cause serious irritation to the eyes, skin, gastrointestinal gland, respiratory system, and reproductive system [87]. The present study planned to use Fe-doped TiO<sub>2</sub> supported on activated carbon nanocomposite for the degradation



of congo red dye from water. Mayoufi *et al.* [88] also studied the degradation of congo red dye using W-doped TiO<sub>2</sub> and they have reported a maximum degradation of 60% in 180 minutes.

### **Degradation of polyaromatic hydrocarbons (PAH)**

The presence of polyaromatic aromatic compounds in water is also a major concern due to the high toxicity, carcinogenic, teratogenetic, genotoxic, and mutagenic properties [89]. These are mainly released through the burning of fossil fuels, oil hydrolysis, forest firing, coking plants, and petroleum industries [90]. These are highly toxic as they have low aqueous solubility, high volatility, high stability, and slow biodegradation capability. In drinking water, one of the most highly concentrated PAHs is anthracene which is one of the low molecular weight tricyclic aromatic hydrocarbons [91]. Anthracene is a very toxic and allergenic, mutagenic, carcinogenic substance easily found in water. On exposure to anthracene into our body, it can directly affect the blood, intestines, stomach, skin, and lymph system, and swell the stomach and intestine [92]. Thus, the removal of this hazardous substance from water is a high concern in the environment. The present study planned to utilize Ni-doped TiO<sub>2</sub> supported on activated carbon nanocomposite for the degradation of anthracene from water and the result are discussed in the Chapter 5.

### **Degradation of phenol**

From the pharmaceuticals industries, plastic plants, oil refiners, textile industries, and coal conversion industries, phenols are mainly discharged as waste products that largely contaminate water resources [93]. The bioaccumulative, persistent, widespread occurrence, and poor biodegradability cause phenolic compounds highly concern to the environment [94]. Upon ingestion of phenol different health-related problems can arise such as metabolic acidosis, respiratory distress, renal failure, cardiovascular effects, metabolic acidosis, neurological effects, coma, and shock, necrosis of the skin, nausea, gastrointestinal irritation, vomiting, diarrhoea, muscle weakness, skin burns, abdominal pain, and paralysis [95]. Phenol retains its toxicity effects on our body even at a concentration lower than 10 ng l<sup>-1</sup> [91]. Hence, the elimination of this toxic substance is a major challenge for the research community before it releases into the environment. In this piece of work, Co-doped TiO<sub>2</sub> supported on activated carbon nanocomposite has been planned to use for the degradation of phenol from water and are discussed in Chapter 6.

## Degradation of bacterial pathogens

Water-containing bacteria are highly toxic and harmful to human health [96]. The commercial and industrial wastewater systems are highly affected by gram-negative and gram-positive bacteria. These bacteria are the most common cause of sepsis [97]. The gram-positive bacteria *Staphylococcus aureus* (*S. aureus*), is one of the most common causes of foodstuff poisoning, skin infections such as abscesses, respiratory infections such as sinusitis, and also the principal cause of hospital-acquired infections in developed countries [98]. It is a member of the *Firmicutes* family, and is a round-shaped bacterium and often found in the nose, respiratory tract, and skin [99]. The gram-negative rod-shaped bacteria *Escherichia coli* (*E. coli*) is one of the members of the family *Enterobacteriaceae* [100]. It is mainly found in drinking water and drinking this contaminated water can cause several diseases such as diarrhea, and kidney damage [101]. Therefore, the present study planned to utilize Fe-doped TiO<sub>2</sub> supported on activated carbon nanocomposite for the inactivation of *E. coli* and *S. aureus* in water. Visible light-driven photocatalytic inactivation of microbes by metal-doped TiO<sub>2</sub> photocatalyst activated carbon-supported metal oxide nanocomposite, and metal co-doped TiO<sub>2</sub> was investigated by many researchers in the last decades. Veréb *et al.* [102] have performed bare and doped rutile and anatase TiO<sub>2</sub> photocatalyst for photocatalytic inactivation of *E. coli* in water under visible light irradiation. Yadav *et al.* [103] introduced a photocatalytic inactivation of *E. coli* and *S. aureus* using Cu-doped TiO<sub>2</sub> under visible light irradiation. Hence, metal-modified TiO<sub>2</sub> has shown much attention due to its extended visible light absorption efficacy.

## 1.9 Present study

The present study is focused on the preparation of activated carbon-supported titanium dioxide nanocomposite using the hydrothermal synthesis method. The activated carbon was prepared from locally available pine cones (*Pinus kesiya*) using ZnCl<sub>2</sub> as an activating agent and the titanium dioxide was prepared using the sol-gel method. The physicochemical characterization was done using various analytical techniques. The prepared nanocomposite was then applied for the degradation of the alizarin red S dye from wastewater.

To achieve visible light response photocatalysis, bandgap energy narrowing and lowering electron-hole recombination rate are the most important factors. Narrowing bandgap energy and lowering electron-hole recombination are the most important factors to achieve visible light active photocatalysis. Therefore, modification of nanocomposite by doping with different transition metals was done to increase the visible light photocatalytic efficiency of nanocomposite towards the degradation of water pollutants. The modification of the prepared

nanocomposite was done by doping different transition metals (Fe, Ni, and Co) through the hydrothermal synthesis method. The Fe-doped  $\text{TiO}_2$  supported on activated carbon nanocomposite was applied for the degradation of the congo red dye aqueous solution and the photocatalytic inactivation of the nanocomposite was also examined against *E. coli* and *S. aureus* bacteria. The Ni-doped  $\text{TiO}_2$  supported on activated carbon nanocomposite was applied for the degradation of the anthracene from water and also Co-doped  $\text{TiO}_2$  supported on activated carbon nanocomposite was applied for the degradation of phenol from water. The mechanism of degradation of water pollutants was studied using GC-MS analysis. The effect of different interfering ions in the degradation of pollutant molecules was also studied. The reusability of the nanocomposite for the photocatalytic degradation of pollutant molecules was also studied up to the fifth cycle. The outline of the work undertaken in this thesis is shown in Figure 1.6.

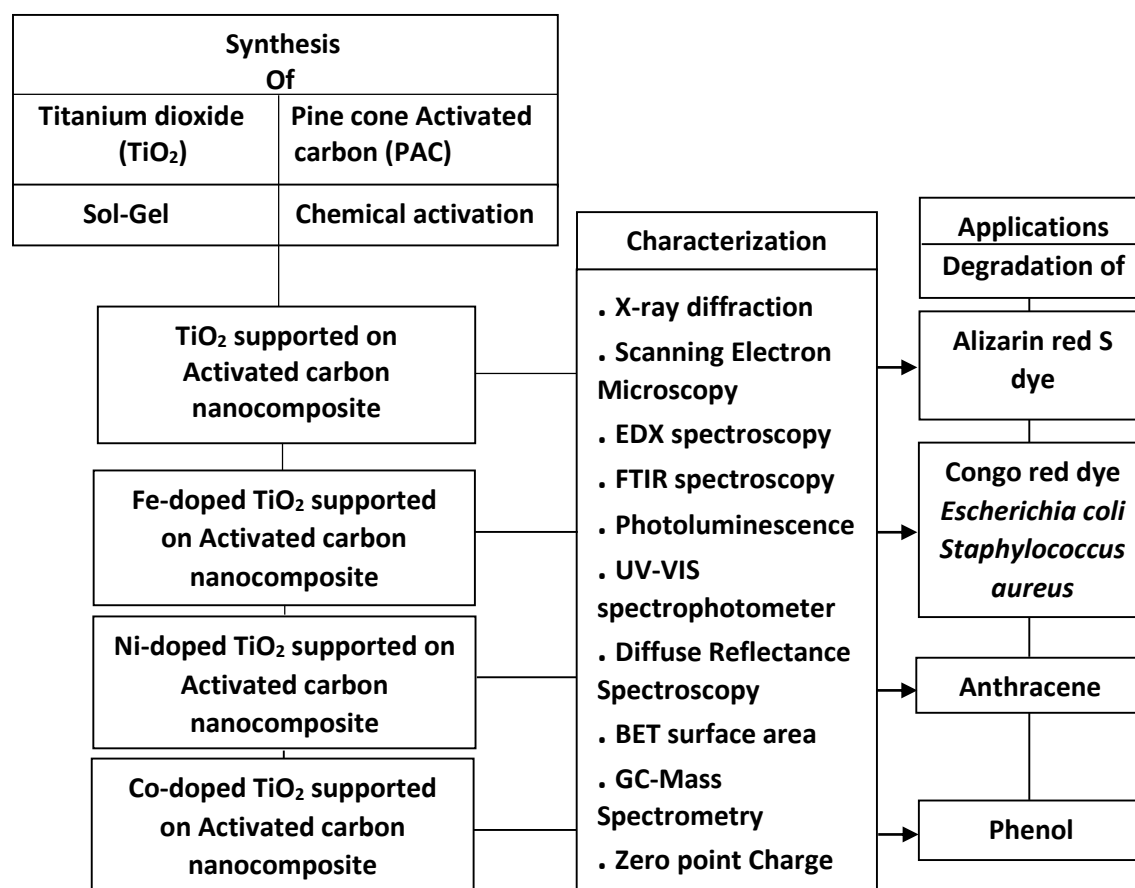


Figure 1.6 Scheme of the present study

### 1.10 Aims and objectives of the work

The aims and objectives of the present work are as follows:

- (i) To synthesis activated carbon-supported TiO<sub>2</sub> nanocomposite using hydrothermal method.
- (ii) Application of the activated carbon-supported TiO<sub>2</sub> nanocomposite for the degradation of alizarin red S dye from aqueous solution.
- (iii) To modify the activated carbon-supported TiO<sub>2</sub> nanocomposite by doping with different transition metals (Fe, Ni, and Co) using the ultrasonic-hydrothermal method.
- (iv) Application of Fe-doped activated carbon-supported TiO<sub>2</sub> nanocomposite for the degradation of congo red dye from aqueous solution and the photocatalytic inactivation of two bacteria pathogens *Escherichia coli* and *Staphylococcus aureus* from wastewater.
- (v) Application of Ni-doped activated carbon-supported TiO<sub>2</sub> nanocomposite for the degradation of anthracene from aqueous solution.
- (vi) Application of Co-doped activated carbon-supported TiO<sub>2</sub> nanocomposite for the degradation of phenol from aqueous solution.
- (vii) To evaluate the adsorption and degradation process, using different adsorption isotherms, catalytic kinetics model, and thermodynamics studies respectively.
- (viii) To study the effect of different interfering ions on photocatalytic degradation of pollutants and analysis of end products of pollutant degradation using GC-MS spectra.
- (ix) Theoretical studies to understand the mechanism of formation of the nanocomposite.

The outline of the thesis is presented in Figure 1.7.

<b>Chapter 1</b>	<b>Introduction</b>
<b>Chapter 2</b>	<b>Materials and methods</b>
<b>Chapter 3</b>	<b>Photocatalytic degradation of alizarin red S dye using TiO<sub>2</sub>/Activated carbon nanocomposite</b>
<b>Chapter 4</b>	<b>Photocatalytic degradation of congo red dye using Fe-doped TiO<sub>2</sub>/Activated carbon nanocomposite and its antimicrobial activity towards <i>E. coli</i> and <i>S. aureus</i></b>
<b>Chapter 5</b>	<b>Photocatalytic degradation of anthracene using Ni-doped TiO<sub>2</sub>/Activated carbon nanocomposite</b>
<b>Chapter 6</b>	<b>Photocatalytic degradation of phenol using Co-doped TiO<sub>2</sub>/Activated carbon nanocomposite</b>
<b>Chapter 7</b>	<b>Summary and Conclusion</b>

**Figure 1.7** Outline of the thesis

**References**

- [1] P. O. Ukaogo, U. Ewuzie, C. V. Onwuka, Environmental pollution: causes, effects, and the remedies, in: *Microorg. Sustain. Environ. Heal.*, 2020: pp. 419–430. doi:10.1016/B978-0-12-819001-2.00021-8.
- [2] D. Noel S, R. MR, Impact of Dyeing Industry Effluent on Groundwater Quality by Water Quality Index and Correlation Analysis, *J. Pollut. Eff. Control.* 2 (2014) 2–5. doi:10.4172/2375-4397.1000126.
- [3] M. El Khames Saad, R. Khiari, E. Elaloui, Y. Moussaoui, Adsorption of anthracene using activated carbon and *Posidonia oceanica*, *Arab. J. Chem.* 7 (2014) 109–113. doi:10.1016/j.arabjc.2013.11.002.
- [4] J. Yan, L. Wang, P.P. Fu, H. Yu, Photomutagenicity of 16 polycyclic aromatic hydrocarbons from the USEPA priority pollutant list, *Mutat. Res. Genet. Toxicol. Environmetal Mutagen.* 557 (2004) 99–108. doi:10.1016/j.mrgentox.2003.10.004.
- [5] WHO (World Health Organisation), Polynuclear aromatic hydrocarbons in Drinking-water, in: *Guidel. Drink. Qual.*, 1998: pp. 1–27.
- [6] A. Segun Ayangbenro, O. Oluranti Babalola, A New Strategy for Heavy Metal Polluted Environments: A Review of Microbial Biosorbents, *Int. J. Environmetal Res. Public Heal.* 14 (2017) 1–16. doi:10.3390/ijerph14010094.
- [7] F. R. Deleo, H. F. Chambers, Reemergence of antibiotic-resistant *Staphylococcus aureus* in the genomics era, *J. Clin. Investig.* 119 (2009) 2464–2474. doi:10.1172/JCI38226.2464.
- [8] H. Harms, D. Schlosser, L. Y. Wick, Untapped potential: exploiting fungi in bioremediation of hazardous chemicals, *Nat. Rev. Microbiol.* 9 (2011) 177–192. doi:10.1038/nrmicro2519.
- [9] P. K. Pandey, P. H Kass, M. L Soupir, S. Biswas, V. P Singh, Contamination of water resources by pathogenic bacteria, *AMB Express.* 4 (2014) 1–16. doi:10.1186/s13568-014-0051-x.
- [10] S. Sharma, A. Bhattacharya, Drinking water contamination and treatment techniques, *Appl. Water Sci.* 7 (2017) 1043–1067. doi:10.1007/s13201-016-0455-7.
- [11] P. Rajasulochana, V. Preethy, Comparison on efficiency of various techniques in treatment of waste and sewage water-A comprehensive review, *Resour. Technol.* 2 (2016) 175–184. doi:10.1016/j.reffit.2016.09.004.
- [12] M. T. Amin, A. A. Alazba, U. Manzoor, A Review of Removal of Pollutants from Water/Wastewater Using Different Types of Nanomaterials, *Adv. Mater. Sci. Eng.* 2014 (2014) 1–24. doi:10.1155/2014/825910.
- [13] G. Crini, E. Lichtfouse, Wastewater treatment: an overview, in: *Green Adsorbents Pollut. Remov.*, 2018: pp. 1–22. doi:10.1007/978-3-319-92111-2\_1.
- [14] N. Sasakova, G. Gregova, D. Takacova, J. Mojzisova, I. Papajova, J. Venglovsky, T.

- Szaboova, S. Kovacova, Pollution of Surface and Ground Water by Sources Related to Agricultural Activities, *Front. Sustain. Food Syst.* 2 (2018) 1–11. doi:10.3389/fsufs.2018.00042.
- [15] R. Ahmad, A. Mirza, Green synthesis of Xanthan gum/Methionine-bentonite nanocomposite for sequestering toxic anionic dye, *Surf. Interfaces.* 2 (2013) 65–72. doi:10.1016/B978-0-08-096984-8.00029-X.
- [16] C. Byrne, G. Subramanian, S.C. Pillai, Recent advances in photocatalysis for environmental applications, *J. Environ. Chem. Eng.* 6 (2018) 3531–3555. doi:10.1016/j.jece.2017.07.080.
- [17] S. W. Verbruggen, TiO<sub>2</sub> photocatalysis for the degradation of pollutants in gas phase: from morphological design to plasmonic enhancement, *J. Photochem. Photobiol. C Photochem.* 24 (2015) 64–82. doi:10.1016/j.jphotochemrev.2015.07.001.
- [18] A. Buthiyappan, A. Raman Abdul Aziz, W. Mohd Ashri Wan Daud, Recent advances and prospects of catalytic advanced oxidation process in treating textile effluents, *Rev. Chem. Eng.* 32 (2016) 1–47. doi:10.1515/revce-2015-0034.
- [19] L. Lin, W. Jiang, L. Chen, P. Xu, H. Wang, Treatment of Produced Water with Photocatalysis: Recent Advances, Affecting Factors and Future Research Prospects, *Catalysts.* 10 (2020) 1–18. doi:10.3390/catal10080924.
- [20] A. Kumar, G. Pandey, A review on the factors affecting the photocatalytic degradation of hazardous materials, *Mater. Sci. Eng. Int. J.* 1 (2017) 106–114. doi:10.15406/mseij.2017.01.00018.
- [21] M. Muruganandham, R.P.S. Suri, S. Jafari, M. Sillanpää, G. Lee, J.J. Wu, M. Swaminathan, Recent Developments in Homogeneous Advanced Oxidation Processes for Water and Wastewater Treatment, *Int. J. Photoenergy.* 2014 (2014) 1–21. doi:10.1155/2014/821674.
- [22] D. Chen, M. Sivakumar, A.K. Ray, Heterogeneous photocatalysis in environmental remediation, *Dev. Chem. Eng. Miner. Process.* 8 (2000) 505–550. doi:10.1002/apj.5500080507.
- [23] O. Carp, C. L. Huisman, A. Reller, Photoinduced reactivity of titanium dioxide, *Prog. Solid State Chem.* 32 (2004) 33–177. doi:10.1016/j.progsolidstchem.2004.08.001.
- [24] A. Omo Ibadon, P. Fitzpatrick, Heterogeneous Photocatalysis: Recent Advances and Applications, *Catalysts.* 3 (2013) 189–218. doi:10.3390/catal3010189.
- [25] M. M. Mahlambi, C. J. Ngila, B. B. Mamba, Recent Developments in Environmental Photocatalytic Degradation of Organic Pollutants: The Case of Titanium Dioxide Nanoparticles—A Review, *J. Nanomater.* 2015 (2015) 1–29. doi:10.1155/2015/790173.
- [26] W. Wang, J. C. Yu, P. Keung Wong, Photocatalysts for Solar-Induced Water Disinfection: New Developments and Opportunities, *Mater. Sci. Forum.* 734 (2013) 63–89. doi:10.4028/www.scientific.net/MSF.734.63.

- [27] O. Legrini, E. Oliveros, A.M. Braun, Photochemical Processes for Water Treatment, *Chem. Rev.* 93 (1993) 671–698. doi:10.1021/cr00018a003.
- [28] W. H. Glaze, J.-W. Kang, Advanced Oxidation Processes. Description of a Kinetic Model for the Oxidation of Hazardous Materials in Aqueous Media with Ozone and Hydrogen Peroxide in a Semibatch Reactor, *Ind. Eng. Chem. Res.* 28 (1989) 1573–1580. doi:10.1021/ie00095a001.
- [29] J. Carlos Colmenares, R. Luque, Heterogeneous photocatalytic nanomaterials: prospect and challenges in selective transformations of biomass-derived compounds, *Chem Soc Rev.* 43 (2014) 765–778. doi:10.1039/c3cs60262a.
- [30] R. Daghrir, P. Drogui, D. Robert, Modified TiO<sub>2</sub> For Environmental Photocatalytic Applications: A Review, *Ind. Eng. Chem. Res.* 52 (2013) 3581–3599. doi:10.1021/ie303468t.
- [31] E.M. Cuerda-correa, M.F. Alexandre-franco, C. Fernández-González, Advanced Oxidation Processes for the Removal of Antibiotics from Water. An Overview, *Water.* 12 (2020) 1–51. doi:10.3390/w12010102.
- [32] R. Ameta, S. C. Ameta, Binary Semiconductors, in: *Photocatal. Princ. Appl.*, 2021: pp. 17–33. doi:10.1201/9781315372396-4.
- [33] G. Mamba, A. K. Mishra, Graphitic carbon nitride (g-C<sub>3</sub>N<sub>4</sub>) nanocomposites: A new and exciting generation of visible light driven photocatalysts for environmental pollution remediation, *Appl. Catal. B Environ.* 198 (2016) 347–377. doi:10.1016/j.apcatb.2016.05.052.
- [34] L. Yang, H. Zhou, T. Fan, D. Zhang, Semiconductor photocatalysts for water oxidation: current status and challenges, *Phys. Chem. Chem. Phys.* 16 (2014) 6810–6826. doi:10.1039/b000000xc.
- [35] M. Baruah, A. Supong, P. Chandra, B. Rituparna, K. Chubaakum, Batch sorption-photodegradation of Alizarin Red S using synthesized TiO<sub>2</sub>/activated carbon nanocomposite: an experimental study and computer modelling, *Nanotechnol. Environ. Eng.* 3 (2020) 1–13. doi:10.1007/s41204-020-00071-3.
- [36] V. Kumaravel, S. Mathew, J. Bartlett, S.C. Pillai, Photocatalytic hydrogen production using metal doped TiO<sub>2</sub>: A review of recent advances, *Appl. Catal. B Environ.* 244 (2019) 1021–1064. doi:10.1016/j.apcatb.2018.11.080.
- [37] W. Qi Fang, X. Gong, H. Gui Yang, On the Unusual Properties of Anatase TiO<sub>2</sub> Exposed by Highly Reactive Facets, *Phys. Chem. Lett.* 2 (2011) 725–734. doi:10.1021/jz200117r.
- [38] K. Hashimoto, H. Irie, A. Fujishima, TiO<sub>2</sub> photocatalysis: A historical overview and future prospects, *Jpn. J. Appl. Phys.* 44 (2005) 8269–8285. doi:10.1143/JJAP.44.8269.
- [39] S. Reghunath, D. Pinheiro, S. Devi Kr, A review of hierarchical nanostructures of TiO<sub>2</sub>: Advances and applications, *Appl. Surf. Sci. Adv.* 3 (2021) 1–34. doi:10.1016/j.apsadv.2021.100063.



- [40] R. Verma, J. Gangwar, A. K. Srivastava, Multiphase TiO<sub>2</sub> nanostructures: a review of efficient synthesis, growth mechanism, probing capabilities, and applications in bio-safety and health, *RSC Adv.* 7 (2017) 44199–44224. doi:10.1039/c7ra06925a.
- [41] Q. Zhang, C. Li, High temperature stable anatase phase titanium dioxide films synthesized by mist chemical vapor deposition, *Nanomaterials.* 10 (2020) 1–8. doi:10.3390/nano10050911.
- [42] W. Hu, L. Li, G. Li, Y. Liu, R. L. Withers, Atomic-scale control of TiO<sub>6</sub> octahedra through solution chemistry towards giant dielectric response, *Sci. Rep.* 4 (2014) 1–9. doi:10.1038/srep06582.
- [43] J. Zhang, P. Zhou, J. Liu, J. Yu, New understanding of the difference of photocatalytic activity among anatase, rutile and brookite TiO<sub>2</sub>, *Phys.Chem.Chem.Phys.* 16 (2014) 20382–20386. doi:10.1039/c4cp02201g.
- [44] Y. Paz, Application of TiO<sub>2</sub> photocatalysis for air treatment: Patents’ overview, *Appl. Catal. B Environ.* 99 (2010) 448–460. doi:10.1016/j.apcatb.2010.05.011.
- [45] M. Ouzzine, A. J. Romero-Anaya, M. A. Lillo-Ródenas, A. Linares-Solano, Spherical activated carbon as an enhanced support for TiO<sub>2</sub>/AC photocatalysts, *Carbon N. Y.* 67 (2014) 104–118. doi:10.1016/j.carbon.2013.09.069.
- [46] W. Zhou, P. Zhang, W. Liu, Anatase TiO<sub>2</sub> nanospindle/activated carbon (AC) composite photocatalysts with enhanced activity in removal of organic contaminant, *Int. J. Photoenergy.* 2012 (2012) 28–30. doi:10.1155/2012/325902.
- [47] L. Giraldo, J.C. Moreno-Pirajan, Activated Carbon Prepared from Orange Peels Coated with Titanium Oxide Nanoparticles: Characterization and Applications in the Decomposition of NO<sub>x</sub>, *Orient. J. Chem.* 30 (2014) 451–461. doi:10.13005/ojc/300207.
- [48] B. Ghasemi, B. Anvaripour, S. Jorfi, N. Jaafarzadeh, Enhanced Photocatalytic Degradation and Mineralization of Furfural Using UVC/TiO<sub>2</sub>/GAC Composite in Aqueous Solution, *Int. J. Photoenergy.* 2016 (2016) 1–10. doi:10.1155/2016/2782607.
- [49] A. Ying Shan, T. Idaty Mohd Ghazi, S. Abdul Rashid, Immobilisation of titanium dioxide onto supporting materials in heterogeneous photocatalysis: A review, *Appl. Catal. A, Gen.* 389 (2010) 1–8. doi:10.1016/j.apcata.2010.08.053.
- [50] L. F. Velasco, J. B. Parra, C. O. Ania, Role of activated carbon features on the photocatalytic degradation of phenol, *Appl. Surf. Sci.* 256 (2010) 5254–5258. doi:10.1016/j.apsusc.2009.12.113.
- [51] M. J. Sweetman, S. May, N. Mebberson, P. Pendleton, K. Vasilev, S. E. Plush, J. D. Hayball, Activated Carbon, Carbon Nanotubes and Graphene: Materials and Composites for Advanced Water Purification, *J. Carbon Res.* 3 (2017) 1–29. doi:10.3390/c3020018.
- [52] A. O. Dieng, R. Z. Wang, Literature review on solar adsorption technologies for ice-making and air conditioning purposes and recent developments in solar technology, *Renew. Sustain. Energy Rev.* 5 (2001) 313–342. doi:10.1016/S1364-0321(01)00004-1.

- [53] P. Muthirulan, C. Nirmala Devi, M. Meenakshi Sundaram, Synchronous role of coupled adsorption and photocatalytic degradation on CAC–TiO<sub>2</sub> composite generating excellent mineralization of alizarin cyanine green dye in aqueous solution, *Arab. J. Chem.* 10 (2013) 1477–1483. doi:10.1016/j.arabjc.2013.04.028.
- [54] A. Di Paola, E. García-lópez, G. Marcì, L. Palmisano, A survey of photocatalytic materials for environmental remediation, *J. Hazard. Mater.* 211–212 (2012) 3–29. doi:10.1016/j.jhazmat.2011.11.050.
- [55] J. Matos, J. Laine, J. Marie Herrmann, Effect of the type of activated carbons on the photocatalytic degradation of aqueous organic pollutants by UV-irradiated titania, *J. Catal.* 200 (2001) 10–20. doi:10.1006/jcat.2001.3191.
- [56] B. Xing, C. Shi, C. Zhang, G. Yi, L. Chen, H. Guo, G. Huang, J. Cao, Preparation of TiO<sub>2</sub>/Activated Carbon Composites for Photocatalytic Degradation of RhB under UV Light Irradiation, *J. Nanomater.* 2016 (2016) 1–10. doi:10.1155/2016/8393648.
- [57] J. Ge, Y. Zhang, S.-J. Park, Recent advances in carbonaceous photocatalysts with enhanced photocatalytic performances: A mini review, *Materials (Basel)*. 12 (2019) 1–26. doi:10.3390/ma12121916.
- [58] F. Khan, M.S. Kahan, S. Kamal, M. Arshad, S.I. Ahmad, S.A.A. Nami, Recent advances on Graphene oxide and Reduced Graphene oxide based Nanocomposites for photodegradation of dyes, *J. Materials Chem. C*. 8 (2020) 15940–15955. doi:10.1039/D0TC03684F.
- [59] S. Bagheri, N. Muhd Julkapli, S. Bee Abd Hamid, Functionalized Activated Carbon Derived from Biomass for Photocatalysis Applications Perspective, *Int. J. Photoenergy*. 2015 (2015) 1–30. doi:10.1155/2015/218743.
- [60] J. Zhou, B. Zhu, L. Wang, Y. Li, Q. Qiao, Enhanced photocatalytic activity of Fe- doped TiO<sub>2</sub> coated on N-doped activated carbon composites for photocatalytic degradation of dyeing wastewater, *Resour. Environ. Eng.* 1890 (2017) 1–10. doi:10.1063/1.5005187.
- [61] J. Ma, H. He, F. Liu, Effect of Fe on the photocatalytic removal of NO<sub>x</sub> over visible light responsive Fe/TiO<sub>2</sub> catalysts, *Appl. Catal. B Environ.* 179 (2015) 21–28. doi:10.1016/j.apcatb.2015.05.003.
- [62] C. Dette, M. A. Perez-Osorio, C. S. Kley, P. Punke, C. E. Patrick, P. Jacobson, F. Giustino, S. Jung Jung, K. Kern, TiO<sub>2</sub> Anatase with a Bandgap in the Visible Region, *Nano Lett.* 14 (2014) 6533–6538. doi:10.1021/nl503131s.
- [63] M. Khairy, W. Zakaria, Effect of metal-doping of TiO<sub>2</sub> nanoparticles on their photocatalytic activities toward removal of organic dyes, *Egypt. J. Pet.* 23 (2014) 419–426. doi:10.1016/j.ejpe.2014.09.010.
- [64] W. Kweku Darkwah, M. Kody Christelle Sandrine, B. Beryl Adormaa, G. Kwesi Teye, J. Buer Puplampu, Solar light harvest: modified d-block metals in photocatalysis, *Catal. Sci. Technol.* 10 (2020) 5321–5344. doi:10.1039/c9cy02435b.
- [65] A. Mittal, B. Mari, S. Sharma, V. Kumari, S. Maken, K. Kumari, N. Kumar, Non-metal

- modified TiO<sub>2</sub>: a step towards visible light photocatalysis, *J. Mater. Sci. Mater. Electron.* 30 (2019) 3186–3207. doi:10.1007/s10854-018-00651-9.
- [66] A. Zaleska, Doped-TiO<sub>2</sub>: a review, *Recent Patents Eng.* 2 (2008) 157–164. doi:10.2174/187221208786306289.
- [67] Y. Yaoguang, C. Gang, Z. Yansong, H. Zhonghui, Recent advances in rare-earth elements modification of inorganic semiconductor-based photocatalysts for efficient solar energy conversion: A review, *J. Rare Earths.* 33 (2015) 453–462. doi:10.1016/S1002-0721(14)60440-3.
- [68] H. Liu, L. Yu, W. Chen, Y. Li, The Progress of TiO<sub>2</sub> Nanocrystals Doped with Rare Earth Ions, *J. Nanomater.* 2012 (2012) 1–9. doi:10.1155/2012/235879.
- [69] V. Etacheri, C. Di Valentin, J. Schneider, D. Bahnemann, S. C. Pillai, Visible-light activation of TiO<sub>2</sub> photocatalysts: Advances in theory and experiments, *J. Reprod. Immunol.* 25 (2015) 1–29. doi:10.1016/j.jphotochemrev.2015.08.003.
- [70] Y. Lin, Y. Cao, Q. Yao, O. Jin Huang Chai, J. Xie, Engineering Noble Metal Nanomaterials for Pollutant Decomposition, *Ind. Eng. Chem. Res.* 59 (2020) 20561–20581. doi:10.1021/acs.iecr.0c04258.
- [71] M. Vittoria Dozzi, E. Selli, Doping TiO<sub>2</sub> with p-block elements: Effects on photocatalytic activity, *J. Photochem. Photobiol. C Photochem. Rev.* 14 (2013) 13–28. doi:10.1016/j.jphotochemrev.2012.09.002.
- [72] R. Marschall, L. Wang, Non-metal doping of transition metal oxides for visible-light photocatalysis, *Catal. Today.* 225 (2014) 111–135. doi:10.1016/j.cattod.2013.10.088.
- [73] M. Li, S. Zhang, Y. Peng, L. Lv, B. Pan, Enhanced visible light responsive photocatalytic activity of TiO<sub>2</sub>-based nanocrystallites: impact of doping sequence, *RSC Adv.* 5 (2015) 7363–7369. doi:10.1039/C4RA10604K.
- [74] Z. Li, D. Ding, Q. Liu, C. Ning, Hydrogen Sensing with Ni-Doped TiO<sub>2</sub> Nanotubes, *Sensors.* 13 (2013) 8393–8402. doi:10.3390/s130708393.
- [75] S. Ali Ansari, M. Hwan Cho, Highly Visible Light Responsive, Narrow Band gap TiO<sub>2</sub> Nanoparticles Modified by Elemental Red Phosphorus for Photocatalysis and Photoelectrochemical Applications, *Sci. Rep.* 6 (2016) 1–10. doi:10.1038/srep25405.
- [76] V. Binas, D. Venieri, D. Kotzias, G. Kiriakidis, Modified TiO<sub>2</sub> based photocatalysts for improved air and health quality, *J Mater.* 3 (2017) 3–16. doi:10.1016/j.jmat.2016.11.002.
- [77] E. B. Butler, C.-C. Chen, Y.-T. Hung, M. Suleiman Al Ahmad, Y.-P. Fu, Effect of Fe-doped TiO<sub>2</sub> photocatalysts on the degradation of acid orange 7, *Integr. Ferroelectr.* 168 (2016) 1–9. doi:10.1080/10584587.2016.1157779.
- [78] A. Ranjitha, N. Muthukumarasamy, M. Thambidurai, D. Velauthapillai, R. Balasundaraprabhu, S. Agilan, Fabrication of Ni-doped TiO<sub>2</sub> thin film photoelectrode for solar cells, *Sol. Energy.* 3 (2014) 159–165. doi:10.1016/j.solener.2014.02.034.
- [79] M. H. Mangrola, V. G. Joshi, B. H. Parmar, A. S. Pillai, Optical and dielectric properties

- of the Cobalt doped TiO<sub>2</sub> nanoparticles, *Int. J. Mod. Phys. Conf. Ser.* 22 (2013) 332–335. doi:10.1142/S2010194513010313.
- [80] K.S. Siddhapara, D.V. Shah, Study of photocatalytic activity and properties of transition metal ions doped nanocrystalline TiO<sub>2</sub> prepared by sol-gel method, *Adv. Mater. Sci. Eng.* 2014 (2014) 1–5. doi:10.1155/2014/462198.
- [81] P. Zucca, C. Vinci, F. Sollai, A. Rescigno, E. Sanjust, Degradation of Alizarin Red S under mild experimental conditions by immobilized 5,10,15,20-tetrakis(4-sulfonatophenyl)porphine-Mn (III) as a biomimetic peroxidase-like catalyst, *J. Mol. Catal. A Chem.* 288 (2008) 97–102. doi:10.1016/j.molcata.2008.04.001.
- [82] E. Routoula, S. V. Patwardhan, Degradation of Anthraquinone Dyes from Effluents: A Review Focusing on Enzymatic Dye Degradation with Industrial Potential, *Environ. Sci. Technol.* 54 (2020) 647–664. doi:10.1021/acs.est.9b03737.
- [83] V. Katheresan, J. Kansedo, S. Yon Lau, Efficiency of various recent wastewater dye removal methods: A review, *J. Environ. Chem. Eng.* 6 (2018) 4676–4697. doi:10.1016/j.jece.2018.06.060.
- [84] M. L. de Souza, P. Corio, Effect of silver nanoparticles on TiO<sub>2</sub>-mediated photodegradation of Alizarin Red S, *Appl. Catal. B Environ.* 136–137 (2013) 325–333. doi:10.1016/j.apcatb.2013.02.012.
- [85] S. Sood, S. Kumar Mehta, Aa. Umar, S. Kumar Kansal, The visible light-driven photocatalytic degradation of Alizarin red S using Bi-doped TiO<sub>2</sub> nanoparticles, *New J. Chem.* 38 (2014) 3127–3136. doi:10.1039/c4nj00179f.
- [86] M. Baruah, S.L. Ezung, A. Supong, P.C. Bhomick, S. Kumar, D. Sinha, Synthesis, characterization of novel Fe-doped TiO<sub>2</sub> activated carbon nanocomposite towards photocatalytic degradation of Congo red, *E. coli*, and *S. aureus*, *Korean J. Chem. Eng.* 38 (2021) 1277–1290. doi:10.1007/s11814-021-0830-4.
- [87] B. Lellis, C. Zani Fávaro-polonio, J. Alencar Pamphile, J. Cesar Polonio, Effects of textile dyes on health and the environment and bioremediation potential of living organisms, *Biotechnol. Res. Innov.* 3 (2019) 275–290. doi:10.1016/j.biori.2019.09.001.
- [88] A. Mayoufi, M. Faouzi Nsib, A. Houas, Doping level effect on visible-light irradiation W-doped TiO<sub>2</sub>-anatase photocatalysts for Congo red photodegradation, *Comptes Rendus Chim.* 17 (2014) 818–823. doi:10.1016/j.crci.2014.01.019.
- [89] Sakshi, A. K. Haritash, A comprehensive review of metabolic and genomic aspects of PAH-degradation, *Arch. Microbiol.* 202 (2020) 2033–2058. doi:10.1007/s00203-020-01929-5.
- [90] A. T. Lawal, Polycyclic aromatic hydrocarbons. A review, *Cogent Environ. Sci.* 71 (2017) 1–89. doi:10.1080/23311843.2017.1339841.
- [91] H. Karyab, M. Yunesian, S. Nasser, A. Hosein Mahvi, R. Ahmadkhaniha, N. Rastkari, R. Nabizadeh, Polycyclic Aromatic Hydrocarbons in drinking water of Tehran, Iran, *J. Environ. Heal. Sci. Eng.* 12 (2013) 1–7. doi:10.1186/2052-336X-11-25.

- [92] A. Tarafdar, A. Sinha, R. E. Masto, Biodegradation of anthracene by a newly isolated bacterial strain, *Bacillus thuringiensis* AT.ISM.1, isolated from a fly ash deposition site, *Appl. Microbiol.* 65 (2017) 327–334. doi:10.1111/lam.12785.
- [93] H. I. Abdel-Shafy, M. S.M. Mansour, A review on polycyclic aromatic hydrocarbons: Source, environmental impact, effect on human health and remediation, *Egypt. J. Pet.* 25 (2016) 107–123. doi:10.1016/j.ejpe.2015.03.011.
- [94] C. Indu Nair, K. Jayachandran, S. Shashidhar, Biodegradation of phenol, *African J. Biotechnol.* 7 (2008) 4951–4958. doi:10.4018/978-1-5225-8903-7.ch045.
- [95] W. W. Anku, M. A. Mamo, P. P. Govender, Phenolic Compounds in Water: Sources, Reactivity, Toxicity and Treatment Methods, in: *Phenolic Compd. Sources, Importance Appl.*, 2017: pp. 419–443. doi:10.5772/66927 443.
- [96] J. P.S. Cabral, Water microbiology. Bacterial pathogens and water, *Int. J. Environ. Res. Public Health.* 7 (2010) 3657–3703. doi:10.3390/ijerph7103657.
- [97] G. Ramachandran, Gram-positive and gram-negative bacterial toxins in sepsis, *Virulence.* 5 (2014) 213–218. doi:10.4161/viru.27024.
- [98] S. Y. C. Tong, J. S. Davis, E. Eichenberger, T.L. Holland, V. G. Fowler, Jr., *Staphylococcus aureus* Infections: Epidemiology, Pathophysiology, Clinical Manifestations, and Management, *Clin. Microbiol. Rev.* 28 (2015) 603–661. doi:10.1128/CMR.00134-14.
- [99] L. G. Harris, S. J. Foster, R. G. Richards, An introduction to *Staphylococcus aureus*, and techniques for identifying and quantifying *S. aureus* adhering in relation to adhesion to biomaterials: Review, *Eur. Cells Mater.* 4 (2002) 39–60. doi:10.22203/eCM.v004a04.
- [100] J. Jang, H.-G. Hur, M. J. Sadowsky, M. N. Byappanahalli, T. Yan, S. Ishii, Environmental *Escherichia coli*: ecology and public health implications—a review, *J. Appl. Microbiol.* 123 (2017) 570–581. doi:10.1111/jam.13468.
- [101] T. A. Russo, J. R. Johnson, Medical and economic impact of extraintestinal infections due to *Escherichia coli*: focus on an increasingly important endemic problem, *Microbes Infect.* 5 (2003) 449–456. doi:10.1016/S1286-4579(03)00049-2.
- [102] G. Veréb, L. Manczinger, G. Bozsó, A. Sienkiewicz, L. Forró, K. Mogyorósi, K. Hernádi, A. Dombi, Comparison of the photocatalytic efficiencies of bare and doped rutile and anatase TiO<sub>2</sub> photocatalysts under visible light for phenol degradation and *E. coli* inactivation, *Appl. Catal. B Environ.* 129 (2013) 566–574. doi:10.1016/j.apcatb.2012.09.045.
- [103] H. M. Yadav, S. V. Otari, V. B. Koli, S. S. Mali, C. Kook Hong, S. H. Pawar, S. D. Delekar, Preparation and characterization of copper-doped anatase TiO<sub>2</sub> nanoparticles with visible light photocatalytic antibacterial activity, *J. Photochem. Photobiol. A Chem.* 280 (2014) 32–38. doi:10.1016/j.jphotochem.2014.02.006.

## CHAPTER 2

### MATERIALS AND METHODS

---

This chapter gives an outline of the materials and methods used in the current research work. A brief discussion on the various analytical techniques used for this study and details regarding the photocatalytic device used for running the experiments is presented in this chapter. The procedure used for photocatalysis using  $\text{TiO}_2$  nanoparticles is also highlighted in this chapter. A brief explanation of the photocatalytic kinetic model and the thermodynamic parameters used for understanding the photocatalytic degradation process are also discussed in detail.

## 2.1 Materials and methods

For the present study, titanium dioxide ( $\text{TiO}_2$ ) and its nanocomposite were synthesized using different analytical grade chemicals. Chemicals such as titanium tetrachloride ( $\text{TiCl}_4$ ), nickel nitrate ( $\text{Ni}(\text{NO}_3)_2 \cdot 6\text{H}_2\text{O}$ ), hydrochloric acid ( $\text{HCl}$ ), ferric nitrate ( $\text{Fe}(\text{NO}_3)_3 \cdot 9\text{H}_2\text{O}$ ), zinc chloride ( $\text{ZnCl}_2$ ), cobalt nitrate ( $\text{Co}(\text{NO}_3)_2 \cdot 6\text{H}_2\text{O}$ ), ammonia ( $\text{NH}_3$ ), sodium hydroxide ( $\text{NaOH}$ ), and sulphuric acid ( $\text{H}_2\text{SO}_4$ ) were obtained from Sigma-Aldrich. Co., India. Sulphuric acid ( $\text{H}_2\text{SO}_4$ ), silver nitrate ( $\text{AgNO}_3$ ), ethylenediaminetetraacetic acid ( $\text{C}_{10}\text{H}_{16}\text{N}_2\text{O}_8$ ), sodium nitrate ( $\text{NaNO}_3$ ), sodium chloride ( $\text{NaCl}$ ), copper sulphate ( $\text{CuSO}_4$ ), glycine ( $\text{C}_2\text{H}_5\text{NO}_2$ ), oxalic acid ( $\text{C}_2\text{H}_2\text{O}_4$ ), and cadmium nitrate ( $\text{Cd}(\text{NO}_3)_2 \cdot 4\text{H}_2\text{O}$ ) were obtained from Himedia, India. Chemicals and dyes such as alizarin red S (ARS), congo red (CR), anthracene ( $\text{C}_{14}\text{H}_{10}$ ), and phenol ( $\text{C}_6\text{H}_6\text{O}$ ) were purchased from Merck, India. Luria-Bertain (LB) nutrient broth, nutrient agar, ethanol ( $\text{C}_2\text{H}_5\text{OH}$ ) were purchased from Himedia, India. Double distilled water (DDW) was used during the experiments.

## 2.2 Synthesis of photocatalyst and supporting material

The synthesizing process and the processing conditions are the main aspects upon which the structure, particle size, electronic, optical properties, and stoichiometry of any nanomaterial depends [1]. Hence, the selection of a suitable method is an essential requirement for the synthesis of a highly active photocatalyst. In the current study, photocatalyst titanium dioxide ( $\text{TiO}_2$ ), and titanium dioxide/activated carbon nanocomposite have been used for photocatalytic degradation studies. The following section describes the synthesis of  $\text{TiO}_2$  nanoparticles, supporting material (activated carbon), and  $\text{TiO}_2$ /activated carbon nanocomposite.

### 2.2.1 Synthesis of $\text{TiO}_2$ nanoparticles and $\text{TiO}_2$ /activated carbon nanocomposite

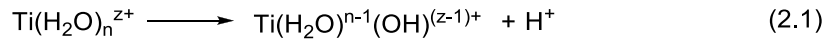
There are different methods available for the synthesis of  $\text{TiO}_2$  and its nanocomposites, such as the microemulsion method [2], co-precipitation [3], reverse micelle method [4], and polyol method [5]. However, these methods have low efficiency, extensive agglomeration, poor crystallinity, and particle size distribution [6]. Therefore, in the present study sol-gel and hydrothermal synthesis have been used as the appropriate technique to synthesize highly pure, homogeneous, and narrow particle size distribution  $\text{TiO}_2$  nanoparticles. A brief introduction to the methods of synthesis used for the synthesis of  $\text{TiO}_2$  nanoparticles and their nanocomposite is given in the following sections.



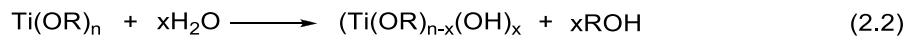
### Sol-gel method for TiO<sub>2</sub> nanoparticles synthesis

Sol-gel is an outstanding route for the synthesis of highly pure TiO<sub>2</sub> nanoparticles [7]. The formation of nanoparticles using the sol-gel process involves the following steps [8,9]:

**Solvation:** The metal cation, Ti<sup>z+</sup> of the raw material was first dispersed in a solvent to form the solvent unit Ti(H<sub>2</sub>O)<sup>z+</sup> with the release of H<sup>+</sup> ions to maintain the coordination number.

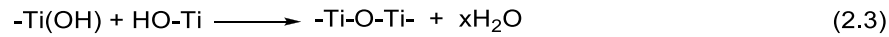


**Hydrolysis:** Non-ionizing metal alkoxide, Ti(OR)<sub>n</sub>, (R = alkyl group) react with water to form an active monomer.

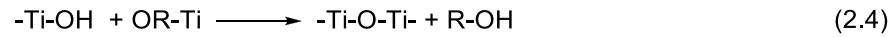


**Polycondensation:** The active monomer is then polymerized to form a sol. The monomer can polymerize in two different ways depending upon its type.

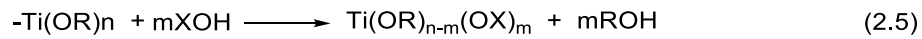
#### Dehydration polycondensation:



#### Dealcoholization polycondensation:



Lastly, polymerization of sol particles in between the as-formed colloidal particles occurs, which leads to gel formation.



The as-formed gel is then dried, sintered, and solidified to prepare molecular nanomaterial. The sol-gel method is used for the preparation of porous, film, composite, powder, fiber materials, and bulk materials for load-bearing, thermal insulation, enclosure, thermal, sound, and heat insulation, partition, and wind protection [10].

In this study, TiO<sub>2</sub> nanoparticles were synthesized using the sol-gel method in which titanium tetrachloride (TiCl<sub>4</sub>) was used as the starting material. The details regarding the sol-gel synthesized TiO<sub>2</sub> nanoparticles are presented in Chapter 3.

### (b) Hydrothermal method for TiO<sub>2</sub>/activated carbon and metal-doped TiO<sub>2</sub>/activated carbon nanocomposite synthesis

Hydrothermal synthesis is one of the most commonly used techniques for the preparation of nanocomposites [11]. In hydrothermal synthesis, high pressure and temperature are generated



inside the hydrothermal autoclave which modifies the physicochemical properties of water and thus changes the mobility and solubility of reactant molecules to undergo crystallization reactions [12]. The easy handling, low-temperature reaction condition, and one-step reaction processing make hydrothermal synthesis a suitable method for the preparation of nanomaterial [13].

In this work, TiO<sub>2</sub>/activated carbon and metal-doped TiO<sub>2</sub>/activated carbon nanocomposite were synthesized using the hydrothermal method using sol-gel synthesized TiO<sub>2</sub> nanoparticles and chemically activated pine-cone activated carbon. Details regarding TiO<sub>2</sub>/activated carbon and metal-doped TiO<sub>2</sub>/activated carbon nanocomposite synthesis are presented in Chapters 3, 4, 5, and 6.

### 2.2.2 Synthesis of activated carbon

Activated carbons are mainly synthesized through physical and chemical activation methods. During physical activation, the raw materials are carbonized using CO<sub>2</sub>, O<sub>2</sub>, or steam in an inert atmosphere and heated at temperatures around 600-1200°C. During the process of chemical activation, raw materials are activated by using chemical activating agents such as acids (HCl, H<sub>2</sub>SO<sub>4</sub>, H<sub>3</sub>PO<sub>4</sub>), alkali metals (KOH, NaOH, Na<sub>2</sub>CO<sub>3</sub>), metal salts (ZnCl<sub>2</sub>, AlCl<sub>3</sub>, FeCl<sub>3</sub>), and heating the materials at 400-900°C.

In the present study, pine-cone activated carbon was prepared using the chemical activation method by applying activating agent ZnCl<sub>2</sub> as this method gives a more porous structure, higher yield, and more surface area material. The details of the activated carbon synthesis are given in Chapter 3.

## 2.3 Instruments coupled with this work

The synthesized TiO<sub>2</sub> nanoparticles and their nanocomposite were characterized by XRD (X-ray diffractometer), SEM-EDX (Scanning electron microscopy-Energy dispersive X-ray spectroscopy), X-ray photoelectron spectroscopy (XPS), FT-IR (Fourier transform Infra-red spectroscopy), PL (Photoluminescence), UV-DRS (UV-visible diffuse reflectance spectroscopy), BET (Brunauer-Emmett-Teller) surface area analyser, and pH<sub>zpc</sub> (Zero-point charge) at different pH values.

### X-ray diffractometer (XRD)

X-ray diffraction is an instrumentation method applied for the rapid and powerful identification of crystalline phases and crystal structures of all kinds of materials, including catalysts,

minerals, solar cells, pharmaceuticals, polymers, fluids, metals, ceramics, plastics, thin-film coatings, and semiconductors [14].

The average value of the crystal sizes was determined by using Debye-Scherrer's equation [15]:

$$D = \frac{\kappa\lambda}{\beta \cos\theta} \quad (2.6)$$

where  $\kappa$  = Scherer constant (0.9),  $\lambda$  = wavelength of the Cu  $K_\alpha$  X-ray radiation (0.15418 nm),  $\theta$  = diffraction angle, and  $\beta$  = full-width at half-maximum (FWHM) of highest intensity peak [14].

In this study, the crystalline structure of the photocatalyst was obtained using powder X-ray diffraction spectrum using PANalytical X'Pert PRO Diffractometer (Rigaku-Ultima IV, Japan). The source of XRD was Cu  $K_\alpha$  radiation operated at an energy of 40 eV and electrical current 40 mA. The diffractometer configuration is schematically shown in Figure 2.1.

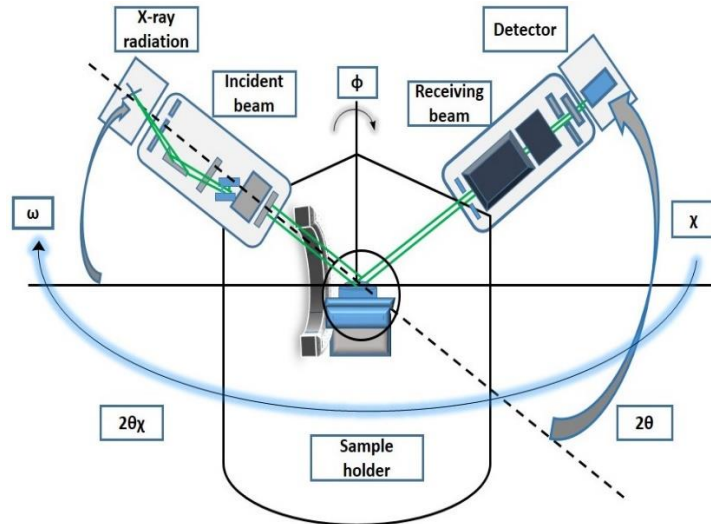


**Figure 2.1** Schematic illustration of XRD instrument [16]

### Scanning electron microscopy (SEM)

Scanning electron microscopy is an important instrument for observing the surface structure, composition, topography, and crystallographic details of any sample. SEM can identify and analyse surface contaminations, surface fractures, crystal structures, and, chemical compositions [17]. In the present work, the surface morphology and surface texture of the photocatalyst were analysed using a scanning electron microscope (Zeiss, Gemini, Sigma-300). The internal configuration of SEM is shown in Figure 2.2.

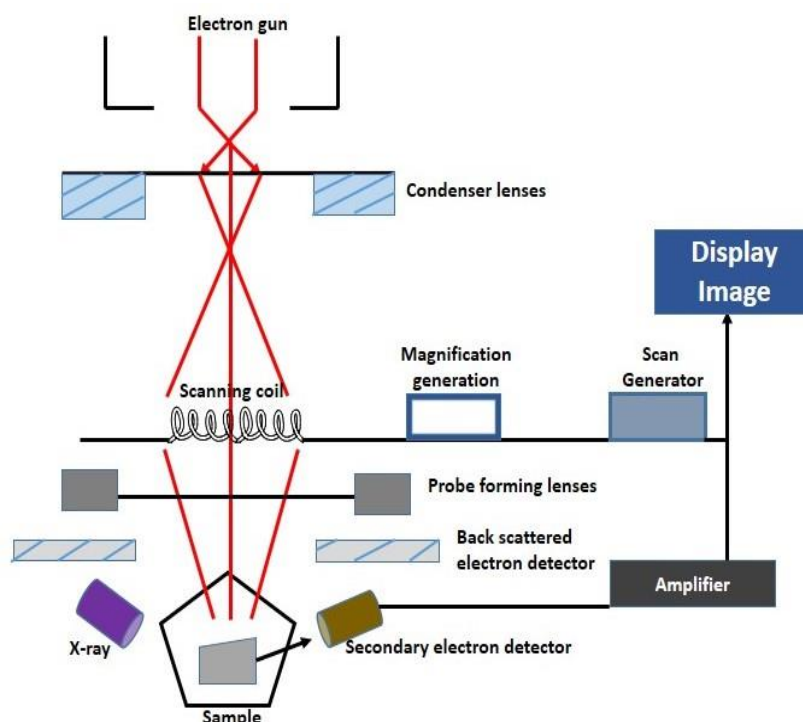


**Figure 2.2** A schematic diagram of an SEM [18]

### Energy-dispersive X-ray spectroscopy (EDX)

Energy-dispersive X-ray spectroscopy is an efficient analytical method for analysing the elemental composition of the desired sample and is used along with scanning electron microscopy (SEM) [19]. The spectra generated with EDX are easy to interpret and also give a high spatial resolution. In the present study, the elemental composition of the photocatalyst was analysed using energy-dispersive X-ray spectroscopy (EDX) along with scanning electron microscopy (SEM).

### X-ray photoelectron spectroscopy (XPS)

X-ray photoelectron spectroscopy is a surface characterization technique used to determine the elemental composition, electrical/chemical states, and stoichiometry of material using their binding energies. The XPS spectra are generated when a high-energy photon (X-ray) ejects an electron from the core orbital of an atom. In the present work, X-ray photoelectron spectroscopy (XPS) (Model: ESCALAB Xi+ Make: Thermo Fisher Scientific Pvt. Ltd., UK) was used to determine the valence state and elemental composition of the photocatalyst.

### Fourier transform Infra-red spectroscopy (FT-IR)

Fourier transform Infra-red spectroscopy is an essential analytical tool for identifying surface chemical functional groups in any material [20]. The infrared spectrum is obtained by

irradiating a sample with infrared radiation, and the fraction of the incident infrared radiation absorbed at given energy determines the maximum intensity of the sample molecule [21]. The functional groups present in the photocatalyst were identified using Fourier transform Infra-red (FT-IR) spectrometer (Model: Spectrum Two, Made: Perkin Elmer, 1:100 ratio of photocatalyst pellet and KBr). The internal configuration of FT-IR is shown below in Figure 2.3.

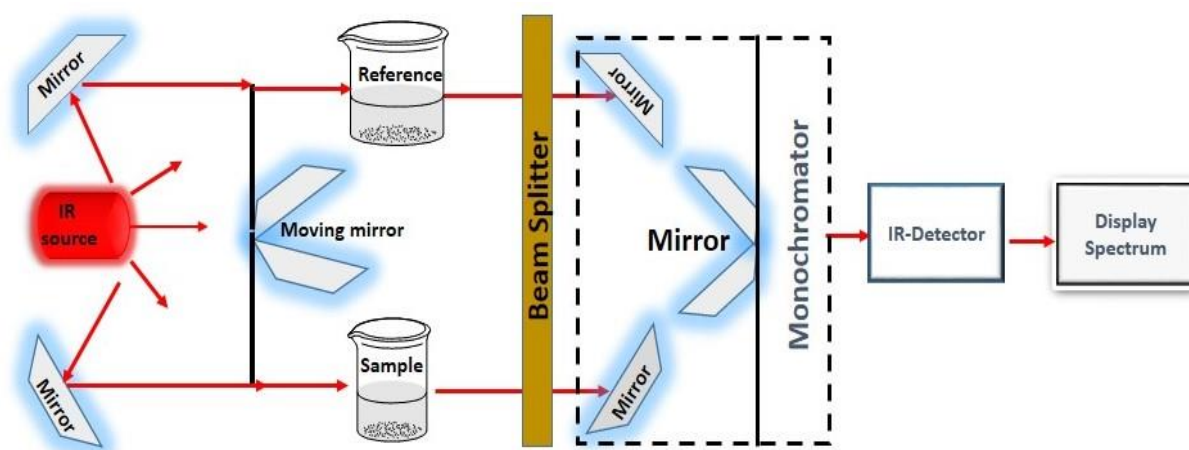


**Figure 2.3** A schematic illustration of an FT-IR system [22]

### Photoluminescence (PL)

Photoluminescence is a non-destructive analytical technique in which when light is absorbed by a material, and its electron is transferred from the ground state to a higher energy level within femto second and returns to the ground state upon emission of photons [23]. In this study, this technique was used for the bandgap determination of the photocatalyst and to analyze the recombination mechanism of the electron-hole pair of semiconductor material [24]. The photoluminescence (PL) spectra of the photocatalyst were obtained using a photoluminescence spectrophotometer (Horiba Fluoromax-4CP spectrofluorometer, 150 W Xenon Lamp). The experimental setup of PL is shown below in Figure 2.4.

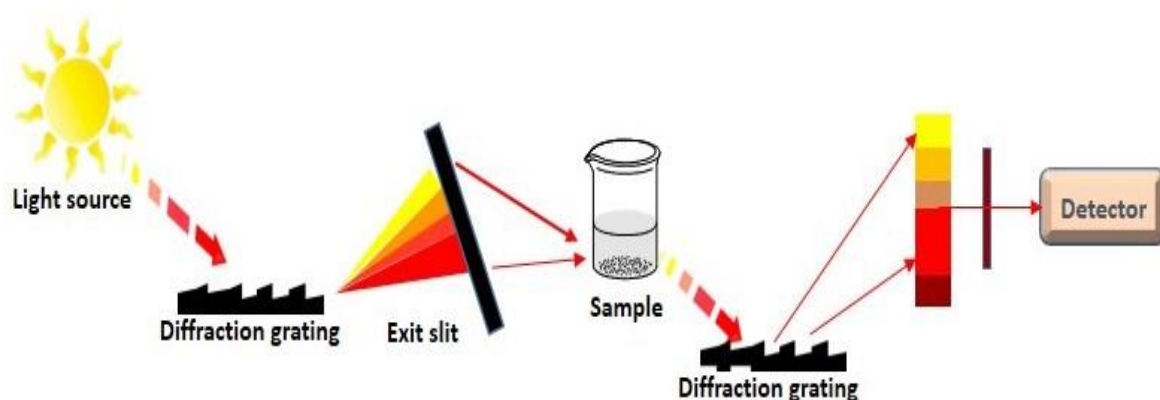


**Figure 2.4** A schematic illustration of a PL system [23]

**UV-visible diffuse reflectance spectroscopy (DRS)**

UV-visible diffuse reflectance spectroscopy is the most versatile technique for studying the bandgap energy of any photocatalyst. It depends on the reflection of electromagnetic radiation by a powder sample [25]. The bandgap energy of the photocatalysts was studied using a UV-visible diffuse reflectance spectrophotometer (Shimadzu UV-2600, and wavelength 200-600 nm). The experimental setup of the DRS is shown below in Figure 2.5.

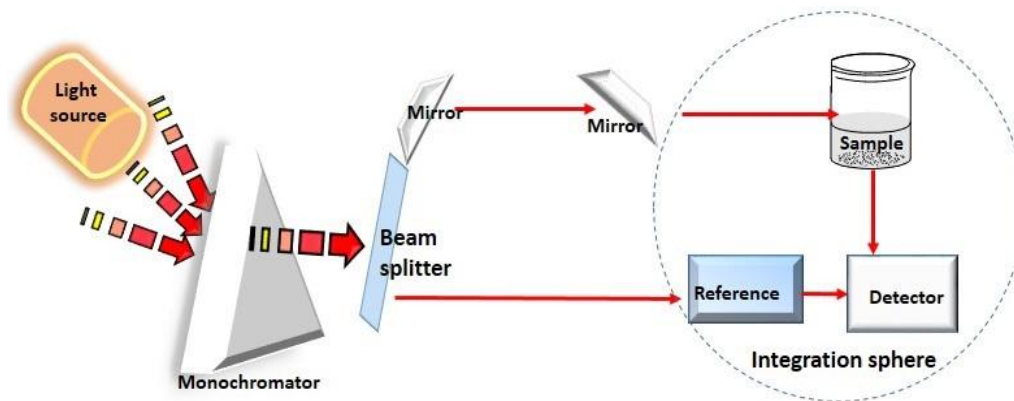


**Figure 2.5** Schematic illustration of a DRS system [26]

**Brunauer-Emmett-Teller analysis (BET analysis)**

Brunauer-Emmett-Teller analysis is a commonly used technique to determine the surface areas, and total pore volume, and pore radius of materials [27]. Nitrogen ( $N_2$ ) gas is usually used in BET surface area analysis because of its ability to interact with other solids and its existence in high purity [28]. In this study, the surface areas of the photocatalyst were measured by the  $N_2$  adsorption-desorption isotherm with a Quantachrome instrument (Autosorb iQ station 1, 77K) based on the Brunauer–Emmett–Teller (BET) model. The experimental setup of the BET analyser is shown below in Figure 2.6.

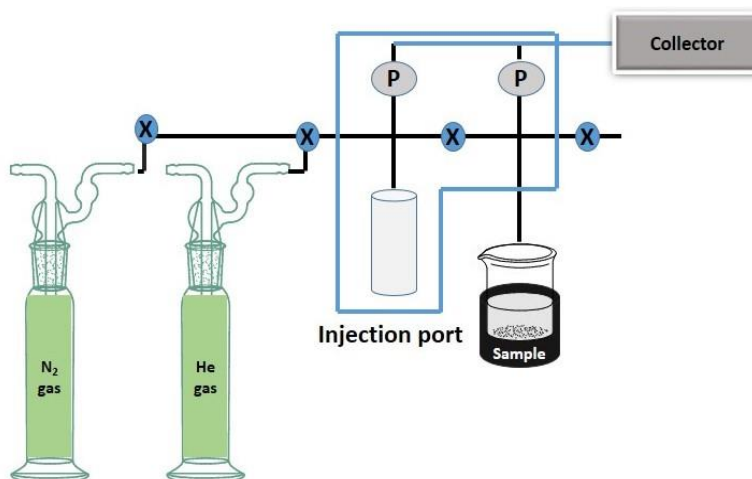


**Figure 2.6** Schematic illustration of a BET analyzer [29]

### Zero-point Charge

Zero-point charge (pHzpc) is the pH at which the net electrostatic surface charge of the photocatalyst is equal to zero [30]. The net surface charge of the photocatalyst is such that it displays acidic behaviour at pH below its pHzpc and pH above its pHzpc, it will behave as basic. Hence, in an acidic medium, the  $H^+$  ions on the surface of the photocatalyst increase ( $pH < pHzpc$ ) which results in the attraction of positively charged pollutant molecules. On the other hand, in a basic medium the availability of  $OH^-$  anion on the surface of the photocatalyst increases ( $pH > pHzpc$ ) leading to more attraction towards positively charged pollutant molecules [31].

For zero-point charge pH measurement, the pH of 0.1 M  $NaNO_3$  (50 ml) was adjusted to a value between 2 to 10 by adding either 0.1M HCl or 0.1 M NaOH solutions. The pH of each solution was recorded as the initial pH ( $pH_{initial}$ ). Thereafter, 0.1 g of the photocatalyst was added and the solution was stirred for 24 hours in a rotary shaker at room temperature. The final pH of each solution was recorded and a graph of initial pH versus final pH was plotted [32].

### 2.4 Photocatalytic activity of the $TiO_2$ /activated carbon nanocomposite

In the present study, the synthesized nanocomposite was used for the photodegradation of water pollutants such as dyes, pharmaceutical compounds, and biological pollutants from water. The dyes under study were Alizarin red S, Congo red, and pharmaceutical compounds selected were anthracene and phenol. Batch mode degradation experiments were performed inside a reactor for the degradation of organic pollutants [32]. The photocatalytic experiments were conducted at 25°C using a constant flow of water inside the reaction chamber using a water pump. For this study, the  $TiO_2$  nanocomposite was mixed with the pollutant of varied concentrations by vigorously stirring the reaction mixture without exposure to light for 30 minutes so that adsorption-desorption equilibrium could be established within the reaction system. After equilibrium was established, the concentration of the pollutant was measured, and this was taken as the initial concentration so that the adsorption of the pollutant due to the nanocomposite did not hinder the study of the overall photocatalytic effect. Later, the final concentration of the centrifuged pollutant solution was measured using a UV-Vis spectrophotometer (Perkin Elmer, LAMBDA 365) at its corresponding  $\lambda_{max}$  values by taking out 3.5 ml at every 10 minutes interval. A batch mode study was conducted for photocatalytic degradation of water pollutants by varying different parameters, as given below.

### Effect of nanocomposite amount

The effect of the nanocomposite on the photocatalytic degradation of water pollutants was studied at different dosages of nanocomposite with different concentrations of pollutants solution.

### Effect of pH

In order to understand the effect of pH, a study on the photodegradation of water pollutants was conducted with a certain amount of nanocomposite and pollutant concentration within the pH range of 1.0-11.0 by addition of either HCl or NaOH (0.1 M).

### Effect of pollutant concentration and light irradiation time

The effect of pollutant concentration and time of irradiation was examined with a certain amount of nanocomposite and pH by varying the pollutant concentration with light irradiation for upto 120 minutes.

### Effect of Interfering ions

The effect of different interfering ions such as sodium chloride, zinc chloride, copper sulphate, glycine, oxalic acid, sodium nitrite, cadmium nitrate, and EDTA on photocatalytic degradation of pollutants was studied to investigate the applicability of nanocomposite in the industrial wastewater matrix.

The pollutant degradation percentage was calculated using equation 2.7 [32]:

$$\text{Degradation percentage (\%)} = \frac{C_i - C_e}{C_i} \times 100 \quad (2.7)$$

where  $C_i$  = initial concentration of pollutant, and  $C_e$  = concentration of a pollutant after the photocatalytic treatment. The detailed batch mode experiments for the degradation of dyes and pharmaceutical compounds are discussed in Chapters 3, 4, 5, and 6.

The water-borne pathogens considered for the current study were *Escherichia coli* and *Staphylococcus aureus* bacteria. The photocatalytic inactivation efficiency of bacteria was calculated using equation 2.8 [33].

$$\text{Inactivation efficiency (\%)} = \frac{\text{Number of colonies} \times \text{dilution factor}}{\text{Volume of culture plate}} \quad (2.8)$$

The detailed experimental setup for the inactivation of *Escherichia coli* and *Staphylococcus aureus* bacteria is described in Chapter 4.



### 2.4.1 Application of Gas chromatography-Mass spectrometry (GC-MS) analysis to identify end products of photocatalysis

Gas chromatography-Mass spectrometry is an instrumentation technique that couples both the properties of gas chromatography (GC) and mass spectroscopy (MS) to identify both semi-volatile and volatile organic compounds in a variety of samples [34]. Gas chromatography (GC) can separate many volatile and non-volatile compounds; on the other hand, mass spectrometry (MS) can selectively identify many compounds [35]. In this study, the degraded end products of the pollutants were confirmed using GC-MS analysis (Shimadzu GCMS-TQ8030 analyser). The experimental setup of the GC-MS is shown below in Figure 2.7.

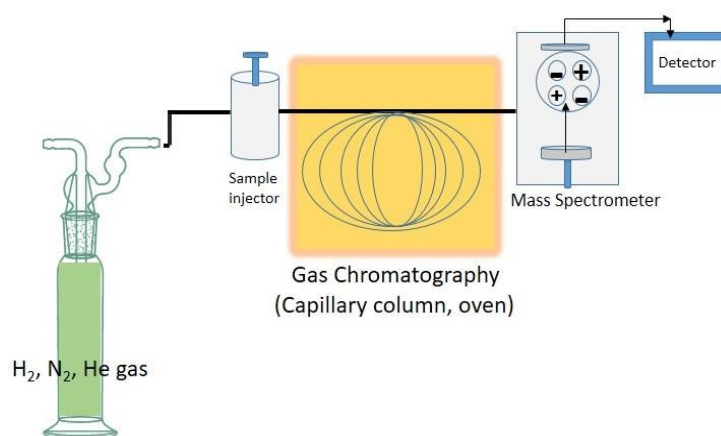


**Figure 2.7** A schematic illustration of a GC-MS analyzer [36]

### 2.4.2 Photocatalytic reactor

For the present study, photocatalytic reactions were performed inside a photocatalytic device, as described in the schematic diagram (Figure 2.8).

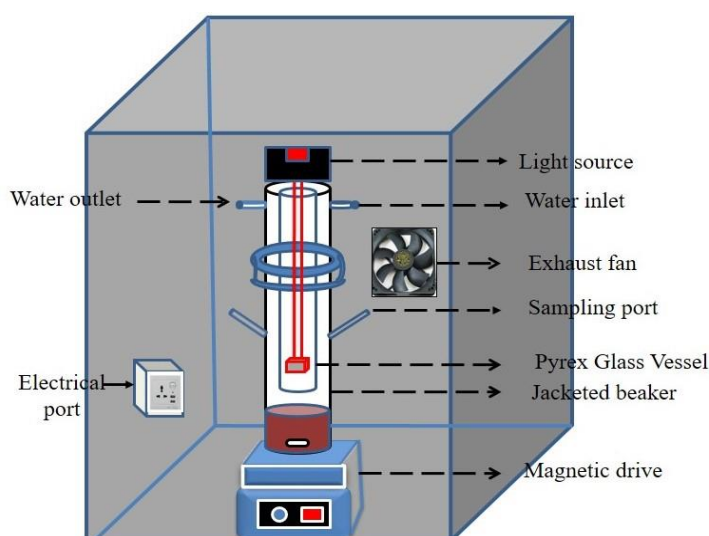


**Figure 2.8** Schematic experimental setup for UV light photocatalytic device



The reactor consists of a double jacketed glass vessel with an outer jacket made of borosilicate glass consisting of two ports, one for sample addition and another for insertion of a condenser to cool hot gases into liquids. While the inner jacket consists of a pyrex glass vessel, inside which a 450 W mercury lamp (UV source) with a wavelength of 325 nm having light power of 1500 mW/cm<sup>2</sup> was placed 5 cm away from the reaction mixture. In visible light reactions, a visible lamp having a maximum wavelength of 520 nm (High-pressure mercury lamp, 350 W) was placed 5 cm away from the reaction mixture. For proper mixing of the reaction system, a magnetic stirrer was placed just below the double jacketed glass vessel. Further, for maintaining a stable temperature, a continuous flow of water was circulated throughout the outer jacket with the help of a pump. Additionally, an exhaust fan was also placed in the wall of the reactor chamber for constant circulation of air inside the system.

### 2.5 Description of water pollutants mentioned in this work

A brief description of the different water pollutants revealed in this work is discussed below:

#### Alizarin red S

Alizarin red S (1, 2-dihydroxy-9, 10-anthraquinone-3-sulphonate, ARS, alias Mordant Red 3, C.I. no. 58005) is one of the anionic anthraquinone dyes considered to be a highly long-lasting toxic type due to its complex composition of aromatic rings [37]. This dye is highly mutagenic and carcinogenic because it is capable of inducing oxidative damages in organisms. Therefore, considering all the ill effects of ARS on humans and the ecosystem, it is very important for the degradation of vital to degrade this dye from wastewater before it is discharged into natural water bodies [32,38]. The molecular structure of the ARS dye is presented in Figure 2.9.

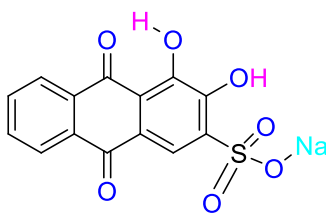


**Figure 2.9** Molecular structure of Alizarin red S dye

#### Congo red

Congo red (Sodium salt of 3,3'-([1,1'-biphenyl]-4,4'-diyl) bis(4-amino naphthalene-1-sulfonic acid), C<sub>32</sub>H<sub>22</sub>N<sub>6</sub>Na<sub>2</sub>O<sub>6</sub>S<sub>2</sub>, CR) is a highly toxic anionic dye that belongs to the direct azo group of dye [39]. It is used in various textile industries such as printing, textile, paper, pulp and in cosmetic manufacturing industries, and also in rubber and plastic industries. Congo red consists

of various benzidine groups and naphthoic acid, which are carcinogenic and mutagenic [40]. Exposure to this dye affects the reproductive systems of living beings and causes allergic reactions. Therefore, development of methods for the degradation of this dye is essential before it enters the natural water stream [33]. The molecular structure of the CR dye is presented in Figure 2.10.

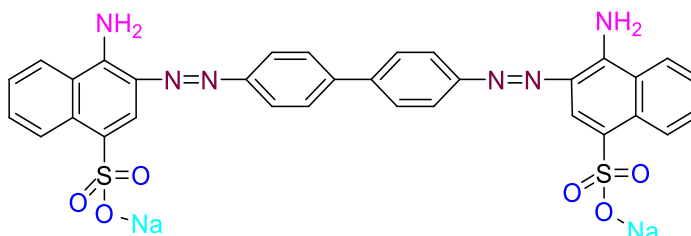


**Figure 2.10** Molecular structure of Congo red dye

### Anthracene

One of the most highly concentrated polyaromatic hydrocarbons which are found in drinking water is anthracene (ANT). It is one of the low molecular weight tricyclic aromatic hydrocarbons consisting of three fused benzene rings [41]. Anthracene is used as a preservative in wood and lumber and as an insecticide for crops. During oxidation reactions, anthracene breaks down to anthraquinone which is used as a building block for a lot of dyes. It is a very toxic and allergenic, mutagenic, carcinogenic substance easily found in water [42]. Exposure to anthracene can directly affect the blood, intestines, stomach, skin, and lymph system, and cause swelling of the stomach and intestine (USEPA Archive Data, CAS no. 120-12-7) [43]. Therefore, the development of methods for the removal of anthracene, thereby preventing its entry into our bodies is essential. The molecular structure of the anthracene is presented in Figure 2.11.

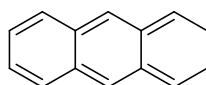


**Figure 2.11** Molecular structure of Anthracene

### Phenol

Phenol ( $C_6H_5OH$ ) is an aromatic organic compound, with a molecular weight of  $94.11 \text{ g mol}^{-1}$  and composition of carbon (76.50%), oxygen (17.00%), and hydrogen (6.43%). It is widely used as antiseptics, disinfectants, and as a starting material in industries to make plastics, drugs, etc. Upon ingestion of phenol different health-related problems can arise such as metabolic acidosis, respiratory distress, renal failure, cardiovascular effects, neurological effects, necrosis of the skin, gastrointestinal irritation, abdominal pain, and paralysis [44]. It causes harmful side

effects such as hyperemia, hyperplasia, bronchopneumonia, liver and kidney damage [45]. The molecular structure of the phenol is presented in Figure 2.12.

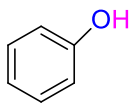


**Figure 2.12** Molecular structure of Phenol

### **Pathogenic microbes *Escherichia coli* and *Staphylococcus aureus***

*Escherichia coli* (*E. coli*) is a rod-shaped gram-negative bacterium and belongs to the *Enterobacteriaceae* family within the *Gammaproteobacteria* class [46]. Under optimal growth conditions (Temperature 37°C, pH 4.4-9.0) it multiplies very fast, replicating in ~20 minutes. It is found in the digestive tract of humans and also in the digestive tract of other warm-blooded animals. It has been used as a sign of fecal contagion in food and water due to its common occurrences in feces and water. It can infect the gastrointestinal tract, cause urinary tract infection, neonatal meningitis, and is a leading cause of enteric infections and systemic infections [47].

*Staphylococcus aureus* (*S. aureus*) is a coccus-shaped gram-positive bacterium with a diameter of between 0.7  $\mu\text{m}$  to 1.2  $\mu\text{m}$  and a member of the family *Micrococcaceae* [48]. Under optimal growth conditions (Temperature 30-37°C, pH 4.2-9.3) multiplies rapidly, replicating in ~20 minutes. It is widely distributed in the environment and human bodies, it is mostly found in skin glands, skin, and mucous membranes of humans. It can cause a wide range of infections in skin and soft tissues including abscesses, impetigo, carbuncles, etc.; deep-seated infections such as pneumonia, septic shock, bacteremia, etc.; metastatic infections; toxin-mediated diseases [49].

Therefore, the inactivation of microbes such as *Escherichia coli* (*E. coli*) and *Staphylococcus aureus* (*S. aureus*) in ambient water is also a major concern throughout the world because they are the major causes of water-borne diseases.

## **2.6 Kinetic studies**

Chemical Kinetic studies give information about the rate of a chemical reaction and also corresponding catalytic mechanism. In photocatalysis, the Langmuir-Hinshelwood equation is widely used to describe photocatalytic kinetics [50].

### **2.6.1 Langmuir Hinshelwood kinetic model**

In the heterogeneous catalytic process, Langmuir Hinshelwood kinetic is the most widely used

kinetic model applied during the photocatalytic degradation of organic pollutants in solution. According to this model, the two reacting species are chemisorbed on the catalyst surface before the reaction takes place [50]. Also, the limiting reaction rate is the rate of oxidation at a maximum coverage of catalyst. The expression of this model is as follows:

$$r = -\frac{dC}{dt} = \frac{k_{app}C}{1 + K_e C} \quad (2.9)$$

where  $C$  = concentration of the pollutant ( $\text{mg L}^{-1}$ ),  $k_e$  = equilibrium constant for the adsorption of the pollutant on the photocatalyst surface ( $\text{L mg}^{-1}$ ), and  $k_{app}$  = apparent rate coefficient ( $\text{min}^{-1}$ ) [51].

As the concentration of pollutant is generally very small for standard photocatalytic reactions,  $k_e C$  in equation 2.9 is much lower than 1, and therefore equation 2.9 changes to:

$$-\frac{dC}{dt} = k_{app}C \quad (2.10)$$

By integrating equation 2.10 from 0 to  $t$ , another form of the L-H model can be deduced:

$$\ln \frac{C_i}{C_e} = k_{app}t \quad (2.11)$$

where  $C_i$  = initial concentration of pollutant, and  $C_e$  = concentration of a pollutant at equilibrium. Equation 2.11 is used to calculate the  $k_{app}$  value of different photocatalytic reactions [52].

### 2.6.2 Half-life time reaction

A half-life time reaction is used to calculate the first-order kinetics reaction rate. The half lifetime ( $t_{1/2}$ ) is calculated using equation 2.12.

$$t_{1/2} = \frac{\ln 2}{K_{app}} = \frac{0.6931}{K_{app}} \quad (2.12)$$

where  $t_{1/2}$  is the half-life time of reactions calculated from  $k_{app}$  (minute) [52].

### 2.7 Thermodynamic studies

Thermodynamic studies were done to understand the relationship between changes in temperatures with respect to heat and energy. The thermodynamics parameters such as standard entropy ( $\Delta S^\circ$ ), enthalpy ( $\Delta H^\circ$ ), free energy ( $\Delta G^\circ$ ) of the pollutant photodegradation were related to the distribution coefficient ( $K_d$ ) by:

$$\ln K_d = \frac{\Delta S^\circ}{R} - \frac{\Delta H^\circ}{RT} \quad (2.13)$$

$$\Delta G^\circ = -RT \ln K_d \quad (2.14)$$

where T is the absolute temperature,  $K_d$  is the distribution coefficient, R ( $8.314 \text{ J mol}^{-1} \text{ K}^{-1}$ ),  $\Delta H^\circ$ , and  $\Delta S^\circ$  are obtained from the slope and intercept by plotting  $\ln K_d$  versus  $1/T$  [53].

## 2.8 Energy consumption and cost analysis

### 2.8.1 Electrical energy determination

In selecting an efficient wastewater treatment method several factors such as its regulations, operation, flexibility, cost, efficient quality goals, etc. have to be considered. Although these factors are essential, the cost involved in operating a method plays a predominant role in the overall process. Since the photocatalytic degradation process is an electric energy-driven process, the electrical energy consumed while running the experiment represents a major fraction of the total operating costs [54]. Therefore, measuring the electric energy per order ( $E_{EO}$ ) for pollutant degradation can be a useful and informative way to calculate the expenses during the reaction and it can be calculated as [55]:

$$E_{EO} = \frac{P \times t \times 1000}{V \times 60 \times \log\left(\frac{C_i}{C_e}\right)} \quad (2.15)$$

where P = Input power (kW), V = Volume of pollutant solution (L),  $C_i$  = Initial pollutant concentration,  $C_e$  = Final pollutant concentration, t = Irradiation time (minute).

By combining the Langmuir-Hinshelwood pseudo-first-order rate equation 2.11 with equation 2.15, the  $E_{EO}$  for a pseudo-first-order reaction can be written as [56]:

$$E_{EO} = \frac{38.4 \times P}{V \times K_{app}} \quad (2.16)$$

where  $K_{app}$  = pseudo-first-order rate constant ( $\text{min}^{-1}$ ). The above equation 2.16 was used to calculate the model of electric energy per order for the pseudo-first-order batch reactor.

### 2.8.2 Total operating cost

Cost estimation is an important parameter to understand the efficiency of the applied method. It can be measured by adding the total maintenance cost, operating cost, and capital cost. Since this cost depends on the concentration and nature of the pollutant and the reactor set-up, therefore the total operating cost involved was carried out using electric energy consumed while running the entire photocatalytic degradation process [57].

The total operating cost and energy consumed in pollutant degradation are calculated using the equations 2.17 and 2.18 [58]:

$$\text{Total operating cost} = \frac{\text{Energy consumed per mg of pollutant degradation (kWh)} \times \text{unit cost} \left( \frac{\text{INR}}{\text{kWh}} \right) \times 10^6}{\text{Pollutant degradation (mg)}} \quad (2.17)$$

$$\text{Energy consumed per mg of pollutant degradation} = \frac{\text{Power input(kW)} \times \text{Reaction time (min)}}{1000 \times 60} \quad (2.18)$$

## 2.9 Density functional theory (DFT) studies

Quantum chemical methods using the density functional theory calculation have now become a feasible way to provide the theoretical basis for the rapid selection of highly proficient materials, thus revealing the relationship between structures and properties of the materials.

GaussView05 suite of the program was used for building all the concerned structures which were then optimized in the Gaussian09 software [59]. The calculations were performed using Beck's three-parameter hybrid, the functional correlation of Lee-YangParr (B3LYP) hybrid functional method and the 6-31G basis set [60] to produce the more stable conformation, alter the molecular geometry, and reduce the energy of the system. Since the experiments were performed in a water solvent medium, the geometry optimizations were done employing the polarisable continuum model with the dielectric constant of water ( $\epsilon = 80$ ).

Further to understand the chemical reactivity and to get a better insight into the adsorption and degradation process, quantum chemical parameters like HOMO-LUMO energy gap (H), chemical hardness ( $\eta$ ), chemical softness (S), chemical potential ( $\mu$ ), electron-accepting power ( $\omega^+$ ), electron-donating power ( $\omega^-$ ), electrophilicity index ( $\omega$ ) and nucleophilicity index (N) were calculated using the formulas given below:

### HOMO-LUMO energy gap (H)

The energy gap of HOMO-LUMO determines the chemical reactivity of the molecule; hence a high value of the HOMO-LUMO energy gap implies that the molecules show lower reactivity and higher stability. The HOMO-LUMO energy gap is given by the equation 2.19 [61]:

$$H = E_{HOMO} - E_{LUMO} \quad (2.19)$$

where  $E_{HOMO}$  is the energy of the highest occupied molecular orbital;  $E_{LUMO}$  is the energy of the lowest unoccupied molecular orbital.

### Chemical hardness ( $\eta$ ) and Chemical softness (S)

The stability of a molecule increases with the increase of hardness which thereby decreases its reactivity. The chemical hardness of a molecule is given by the equation 2.20 [62]:

$$\eta = \frac{E_{HOMO} - E_{LUMO}}{2} \quad (2.20)$$

The stability of a molecule increases with the decrease of softness which thereby increases its reactivity. The chemical softness of a molecule is given by the equation 2.21:

$$S = \frac{1}{2\eta} \quad (2.21)$$

**Chemical potential ( $\mu$ )**

A higher value of chemical potential indicates higher reactivity of the molecule. Chemical potential is given by the equation 2.22 [63]:

$$\mu = \frac{E_{LUMO} + E_{HOMO}}{2} \quad (2.22)$$

**Electron-donating power ( $\omega^-$ ) and electron-accepting power ( $\omega^+$ )**

The electron-donating power is the tendency of a molecule to donate an electron. It is given by the equation 2.23:

$$\omega^- = \frac{(3I+A)^2}{16(I-A)} \quad (2.23)$$

The electron-accepting power of a molecule is the ability of a molecule to accept an electron, and is given as [64]:

$$\omega^+ = \frac{(I+3A)^2}{16(I-A)} \quad (2.24)$$

where A is the electron affinity of a molecule, I is the ionization potential of a molecule.

**Electrophilicity index ( $\omega$ )**

The reactivity of a molecule increases with the larger value of the electrophilicity index. Electrophilicity index ( $\omega$ ) is given by equation 2.25 [65]:

$$\omega = \frac{\mu^2}{2\eta} \quad (2.25)$$

If  $\omega > 1.5$  eV it is a strong electrophile,  $0.8 < \omega < 1.5$  eV is moderate and  $\omega < 0.8$  eV marginal [66].

**Nucleophilicity index (N)**

A good, more reactive nucleophile is characterized by the lower value of  $\omega$  [67].

$$N = \frac{1}{\omega^-} \times 10 \quad (2.26)$$

If a molecule has  $N > 3$  eV it is a strong nucleophile,  $2 < N < 3$  eV a moderate and  $N < 2$  eV marginal [68].

**References**

- [1] J. Kumar Patra, K.-H. Baek, Green Nanobiotechnology: Factors Affecting Synthesis and Characterization Techniques, *J. Nanomater.* 2014 (2014) 1–12. doi:10.1155/2014/417305.
- [2] G. S. Falk, M. Borlaf, M. J. López-Muñoz, J. C. Fariñas, J. B. Rodrigues Neto, R. Moreno, Microwave-assisted synthesis of TiO<sub>2</sub> nanoparticles: photocatalytic activity of powders and thin films, *J. Nanoparticle Res.* 20 (2018) 1–10. doi:10.1007/s11051-018-4140-7.
- [3] Y. Li, G. P. Demopoulos, Precipitation of nanosized titanium dioxide from aqueous titanium (IV) chloride solutions by neutralization with MgO, *Hydrometallurgy*. 90 (2008) 26–33. doi:10.1016/j.hydromet.2007.09.008.
- [4] T. Tatarchuk, N. Danyliuk, A. Shyichuk, W. Macyk, M. Naushad, Photocatalytic degradation of dyes using rutile TiO<sub>2</sub> synthesized by reverse micelle and low temperature methods: real-time monitoring of the degradation kinetics, *J. Mol. Liq.* 342 (2021) 1–17. doi:10.1016/j.molliq.2021.117407.
- [5] H. -Hsin Tseng, M. -Chi Wei, S. -Fan Hsiung, C. -Wei Chiou, Degradation of xylene vapor over Ni-doped TiO<sub>2</sub> photocatalysts prepared by polyol-mediated synthesis, *Chem. Eng. J.* 150 (2009) 160–167. doi:10.1016/j.cej.2008.12.015.
- [6] T. Dippong, E. Andrea Levei, O. Cadar, Recent Advances in Synthesis and Applications of MFe<sub>2</sub>O<sub>4</sub> (M = Co, Cu, Mn, Ni, Zn) Nanoparticles, *Nanomaterials*. 11 (2021) 1–33. doi:10.3390/nano11061560.
- [7] M. Hossein Nateq, R. Ceccato, Sol-Gel Synthesis of TiO<sub>2</sub> Nanocrystalline Particles with Enhanced Surface Area through the Reverse Micelle Approach, *Adv. Mater. Sci. Eng.* 2019 (2019) 1–14. doi:10.1155/2019/1567824.
- [8] A. Prince Periyasamy, M. Venkataraman, D. Kremenakova, J. Militky, Y. Zhou, Progress in Sol-Gel Technology for the Coatings of Fabrics, *Materials (Basel)*. 13 (2020) 1–34. doi:10.3390/ma13081838.
- [9] J. Bergek, B. Elgh, A. E.C. Palmqvist, L. Nordstierna, Formation of titanium dioxide core-shell microcapsules through a binary-phase spray technique, *Phys. Chem. Chem. Phys.* 19 (2017) 23878–23886. doi:10.1039/c7cp02571h.
- [10] D. R.Uhlmann, G. Teowee, Sol-gel science and technology: Current state and future prospects, *J. Sol-Gel Sci. Technol.* 13 (1998) 153–162. doi:10.1023/A:1008692430779.
- [11] Y. X. Gan, A. H. Jayatissa, Z. Yu, X. Chen, M. Li, Hydrothermal Synthesis of Nanomaterials, *J. Nanomater.* 2020 (2020) 1–3. doi:10.1155/2020/8917013.
- [12] A. Querejeta, A. Varela, M. Parras, F. del Monte, M. Garcia-Hernandez, J. M. Gonzalez-Calbet, Hydrothermal Synthesis: A Suitable Route to Elaborate Nanomanganites, *Chem. Mater.* 21 (2009) 1898–1905. doi:10.1021/cm9001306.
- [13] S. Feng, R. Xu, New Materials in Hydrothermal Synthesis, *Acc. Chem. Res.* 34 (2001)



- 239–247. doi:10.1021/ar0000105.
- [14] A.A. Bunaciu, H.Y. Aboul-enein, X-Ray Diffraction: Instrumentation and Applications, *Crit. Rev. Analytical Chem.* 45 (2015) 289–299. doi:10.1080/10408347.2014.949616.
- [15] P. Singh, M.C. Vishnu, K.K. Sharma, A. Borthakur, P. Srivastava, D.B. Pal, D. Tiwary, P.K. Mishra, Photocatalytic degradation of Acid Red dye stuff in the presence of activated carbon-TiO<sub>2</sub> composite and its kinetic enumeration, *J. Water Process Eng.* 12 (2016) 20–31. doi:10.1016/j.jwpe.2016.04.007.
- [16] K. Inaba, S. Kobayashi, K. Uehara, A. Okada, S. Lakshmi Reddy, T. Endo, High Resolution X-Ray Diffraction Analyses of (La, Sr) MnO<sub>3</sub>/ZnO/ Sapphire (0001) Double Heteroepitaxial Films, *Adv. Mater. Phys. Chem.* 3 (2013) 72–89. doi:10.4236/ampc.2013.31A010.
- [17] K. Akhtar, S. Ali Khan, S. Bahadar Khan, A. M. Asiri, Scanning Electron Microscopy: Principle and Applications in Nanomaterials Characterization, in: *Handb. Mater. Charact.*, 2018: pp. 113–145. doi:10.1007/978-3-319-92955-2\_4.
- [18] A. Salman Ali, Application of Nanomaterials in Environmental Improvement, in: *Nanotechnol. Environ.*, 2020: pp. 1–20. doi:10.5772/intechopen.91438.
- [19] P. D. Ngo, Energy Dispersive Spectroscopy, in: *Fail. Anal. Integr. Circuits*, 1999: pp. 205–215. doi:10.1007/978-1-4615-4919-2\_12.
- [20] M. Zainal Abidin, M. Paula Junqueira-Gonçalves, V. V. Khutoryanskiy, K. Niranjana, Intensifying chitin hydrolysis by adjunct treatments – an overview, *J. Chem. Technol. Biotechnol.* 92 (2017) 2787–2798. doi:10.1002/jctb.5208.
- [21] B. Stuart, Infrared spectroscopy, *Kirk-Othmer Encycl. Chem. Technol.* (2015) 1–17. doi:10.1002/0471238961.0914061810151405.a01.pub3.
- [22] R. Bhargava, S.-Q. Wang, J. L. Koenig, FTIR microspectroscopy of polymeric systems, *Adv. Polym. Sci.* 163 (2003) 137–191. doi:10.1007/b11052.
- [23] T. Aoki, Photoluminescence Spectroscopy, in: E.N. Kaufmann (Ed.), *Charact. Mater.*, 1st ed., 2012: pp. 681–688. doi:https://doi.org/10.1002/0471266965.com058.pub2.
- [24] A. Erbe, S. Nayak, Y.-H. Chen, F. Niu, M. Pander, S. Tecklenburg, C. Toparli, How to probe structure, kinetics, and dynamics at complex interfaces in situ and operando by optical spectroscopy, in: *Encycl. Interfacial Chem. Surf. Sci. Electrochem.*, Elsevier, 2018: pp. 199–219. doi:10.1016/B978-0-12-409547-2.14061-2.
- [25] G. Kortüm, W. Braun, G. Herzog, Principles and Techniques of Diffuse-Reflectance Spectroscopy, *Angew. Chemie Int. Ed. English.* 2 (1963) 333–341. doi:10.1002/anie.196303331.
- [26] B. M. Weckhuysen, R. A. Schoonheydt, Recent progress in diffuse reflectance spectroscopy of supported metal oxide catalysts, *Catal. Today.* 49 (1999) 441–451. doi:10.1016/S0920-5861(98)00458-1.
- [27] M. Naderi, Surface Area: Brunauer-Emmett-Teller (BET), in: *Prog. Filtr. Sep.*, 2015: pp.

- 585–608. doi:10.1016/B978-0-12-384746-1.00014-8.
- [28] M. Thommes, K. Kaneko, A. V. Neimark, J. P. Olivier, F. Rodriguez-Reinoso, J. Rouquerol, K. S.W. Sing, Physisorption of gases, with special reference to the evaluation of surface area and pore size distribution (IUPAC Technical Report), *Pure Appl. Chem.* 87 (2015) 1051–1069. doi:10.1515/pac-2014-1117.
- [29] S. Yurdakal, C. Garlisi, L. Özcan, M. Bellardita, G. Palmisano, (Photo) catalyst characterization techniques: Adsorption isotherms and BET, SEM, FTIR, UV-Vis, photoluminescence, and electrochemical characterizations, in: *Heterog. Photocatal.*, 2019: pp. 87–152. doi:10.1016/B978-0-444-64015-4.00004-3.
- [30] T. Mahmood, M. Tahir Saddique, A. Naeem, P. Westerho, S. Mustafa, Comparison of Different Methods for the Point of Zero Charge Determination of NiO, *Ind. Eng. Chem. Res.* 50 (2011) 10017–10023. doi:10.1021/ie200271d.
- [31] K. Roy Bhattacharyya, Priyadarshi G. Chowdhury, Synthesis and characterization of Mn/Co/Ti LDH and its utilization as a photocatalyst in visible light assisted degradation of aqueous Rhodamine B, *RSC Adv.* 6 (2016) 112016–112034. doi:10.1039/C6RA24288J.
- [32] M. Baruah, A. Supong, P. Chandra, B. Rituparna, K. Chubaakum, Batch sorption-photodegradation of Alizarin Red S using synthesized TiO<sub>2</sub>/activated carbon nanocomposite: an experimental study and computer modelling, *Nanotechnol. Environ. Eng.* 3 (2020) 1–13. doi:10.1007/s41204-020-00071-3.
- [33] M. Baruah, S.L. Ezung, A. Supong, P.C. Bhomick, S. Kumar, D. Sinha, Synthesis, characterization of novel Fe-doped TiO<sub>2</sub> activated carbon nanocomposite towards photocatalytic degradation of Congo red, *E. coli*, and *S. aureus*, *Korean J. Chem. Eng.* 38 (2021) 1277–1290. doi:10.1007/s11814-021-0830-4.
- [34] J. Sneddon, S. Masuram, J. C. Richert, Gas Chromatography-Mass Spectrometry-Basic Principles, Instrumentation and Selected Applications for Detection of Organic Compounds, *Anal. Lett.* 2719 (2007) 1003–1012. doi:10.1080/00032710701300648.
- [35] C. Lourenço, S. Bergin, J. Hodgkinson, D. Francis, S. E. Staines, J. R. Saffell, C. Walton, R. P. Tatam, Instrumentation for quantitative analysis of volatile compounds emission at elevated temperatures. Part 1: Design and implementation, *Sci. Rep.* 10 (2020) 1–11. doi:10.1038/s41598-020-65472-5.
- [36] Y. Obeidat, The Most Common Methods for Breath Acetone Concentration Detection: A Review, *IEEE Sens. J.* 21 (2021) 14540–14558. doi:10.1109/JSEN.2021.3074610.
- [37] P. Zucca, C. Vinci, F. Sollai, A. Rescigno, E. Sanjust, Degradation of Alizarin Red S under mild experimental conditions by immobilized 5,10,15,20-tetrakis(4-sulfonatophenyl)porphine-Mn (III) as a biomimetic peroxidase-like catalyst, *J. Mol. Catal. A Chem.* 288 (2008) 97–102. doi:10.1016/j.molcata.2008.04.001.
- [38] S. Hu, D. Yuan, Y. Liu, L. Zhao, H. Guo, Q. Niu, W. Zong, R. Liu, The toxic effects of alizarin red S on catalase at the molecular level, *RSC Adv.* 9 (2019) 33368–33377. doi:10.1039/c9ra02986a.

- [39] J. L. Harry-asobara, I. Kamei, Characteristics of White-rot Fungus *Phlebia brevispora* TMIC33929 and Its Growth-Promoting Bacterium *Enterobacter* sp. TN3W-14 in the Decolorization of Dye-Contaminated Water, *Appl. Biochem. Biotechnol.* 189 (2019) 1183–1194. doi:10.1007/s12010-019-03062-6.
- [40] S. Benkhaya, S. M'rabet, A. El Harfi, A review on classifications, recent synthesis and applications of textile dyes, *Inorg. Chem. Commun.* 115 (2020) 1–35. doi:10.1016/j.inoche.2020.107891.
- [41] H. I. Abdel-Shafy, M. S.M. Mansour, A review on polycyclic aromatic hydrocarbons: Source, environmental impact, effect on human health and remediation, *Egypt. J. Pet.* 25 (2016) 107–123. doi:10.1016/j.ejpe.2015.03.011.
- [42] A. Tarafdar, A. Sinha, R. E. Masto, Biodegradation of anthracene by a newly isolated bacterial strain, *Bacillus thuringiensis* AT.ISM.1, isolated from a fly ash deposition site, *Appl. Microbiol.* 65 (2017) 327–334. doi:10.1111/lam.12785.
- [43] M. Rani, Rachna, U. Shanker, Mineralization of carcinogenic anthracene and phenanthrene by sunlight active bimetallic oxides nanocomposites, *J. Colloid Interface Sci.* 555 (2019) 676–688. doi:10.1016/j.jcis.2019.08.016.
- [44] W. W. Anku, M. A. Mamo, P. P. Govender, Phenolic Compounds in Water: Sources, Reactivity, Toxicity and Treatment Methods, in: *Phenolic Compd. Sources, Importance Appl.*, 2017: pp. 419–443. doi:10.5772/66927 443.
- [45] H. Babich, D.L. Davis, Phenol: A Review of Environmental and Health Risks, *Regul. Toxicol. Pharmacol.* 1 (1981) 90–109. doi:10.1016/0273-2300(81)90071-4.
- [46] J. Jang, H. G. Hur, M. J. Sadowsky, M. N. Byappanahalli, T. Yan, S. Ishii, Environmental *Escherichia coli*: ecology and public health implications—a review, *J. Appl. Microbiol.* 123 (2017) 570–581. doi:10.1111/jam.13468.
- [47] Y. Nguyen, V. Sperandio, Enterohemorrhagic *E. coli* (EHEC) pathogenesis., *Front. Cell. Infect. Microbiol.* 2 (2012) 90. doi:10.3389/fcimb.2012.00090.
- [48] L. G. Harris, S. J. Foster, R. G. Richards, An introduction to *Staphylococcus aureus*, and techniques for identifying and quantifying *S. aureus* adhering in relation to adhesion to biomaterials: Review, *Eur. Cells Mater.* 4 (2002) 39–60. doi:10.22203/eCM.v004a04.
- [49] R. J. Gordon, F. D. Lowy, Pathogenesis of Methicillin-Resistant *Staphylococcus aureus* Infection, *Clin. Infect. Dis.* 10032 (2008) 350–359. doi:10.1086/533591.
- [50] R. J. Baxter, P. Hu, Insight into why the Langmuir–Hinshelwood mechanism is generally preferred, *J. Chem. Phys.* 116 (2002) 4379–4381. doi:10.1063/1.1458938.
- [51] N. G. Asenjo, R. Santamarí, C. Blanco, M. Granda, Pa. Alvarez, R. Menendez, Correct use of the Langmuir–Hinshelwood equation for proving the absence of a synergy effect in the photocatalytic degradation of phenol on a suspended mixture of titania and activated carbon, *Carbon N. Y.* 5 (2012) 62–69. doi:10.1016/j.carbon.2012.12.010.
- [52] N. Guettai, H.A. Amar, Photocatalytic oxidation of methyl orange in presence of

- titanium dioxide in aqueous suspension. Part II: kinetics study, *Desalination*. 185 (2005) 439–448. doi:10.1016/j.desal.2005.04.049.
- [53] B. Liu, X. Zhao, C. Terashima, A. Fujishima, K. Nakata, Thermodynamic and kinetic analysis of heterogeneous photocatalysis for semiconductor systems, *R. Soc. Chem.* 16 (2014) 8751–8760. doi:10.1039/c3cp55317e.
- [54] J. R. Bolton, K. G. Bircher, W. Tumas, C. A. Tolman, Figures-of-merit for the technical development and application of advanced oxidation technologies for both electric- and solar-driven systems, *Pure Appl. Chem.* 73 (2001) 627–637. doi:10.1351/pac200173040627.
- [55] N. Daneshvar, A. Aleboyeh, A. R. Khataee, The evaluation of electrical energy per order ( $E_{EO}$ ) for photooxidative decolorization of four textile dye solutions by the kinetic model, *Chemosphere*. 59 (2005) 761–767. doi:10.1016/j.chemosphere.2004.11.012.
- [56] S. R. Cater, M. I. Stefan, J. R. Bolton, A. Safarzadeh-Amiri, UV/H<sub>2</sub>O<sub>2</sub> Treatment of Methyl *tert*-Butyl Ether in Contaminated Waters, *Environ. Sci. Technol.* 34 (2000) 659–662. doi:10.1021/es9905750.
- [57] R. C. Asha, M. A. Vishnuganth, N. Remya, N. Selvaraju, M. Kumar, Livestock Wastewater Treatment in Batch and Continuous Photocatalytic Systems: Performance and Economic Analyses, *Water Air Soil Pollut.* 226 (2015) 1–13. doi:10.1007/s11270-015-2396-4.
- [58] M. A. Vishnuganth, N. Remya, M. Kumar, N. Selvaraju, Photocatalytic degradation of carbofuran by TiO<sub>2</sub>-coated activated carbon: Model for kinetic, electrical energy per order and economic analysis, *J. Environ. Manage.* 181 (2016) 201–207. doi:10.1016/j.jenvman.2016.06.016.
- [59] M. J. Frisch, G. W. Trucks, H. B. Schlegel, G. E. Scuseria, M. A. Robb, J. R. Cheeseman, G. Scalmani, V. Barone, B. Mennucci, G. A. Petersson, H. Nakatsuji, M. Caricato, X. Li, H. P. Hratchian, A. F. Izmaylov, J. Bloino, G. Zheng, J. L. Sonnenberg, M. Hada, M. Ehara, K. Toyota, R. Fukuda, J. Hasegawa, M. Ishida, T. Nakajima, Y. Honda, O. Kitao, H. Nakai, T. Vreven, J. A. Jr. Montgomery, J. E. Peralta, F. Ogliaro, M. Bearpark, J. J. Heyd, E. Brothers, K. N. Kudin, V. N. Staroverov, R. Kobayashi, J. Normand, K. Raghavachari, A. Rendell, J. C. Burant, S. S. Iyengar, J. Tomasi, M. Cossi, N. Rega, J. M. Millam, M. Klene, J. E. Knox, J. B. Cross, V. Bakken, C. Adamo, J. Jaramillo, R. Gomperts, R. E. Stratmann, O. Yazyev, A. J. Austin, R. Cammi, C. Pomelli, J. W. Ochterski, R. L. Martin, K. Morokuma, V. G. Zakrzewski, G. A. Voth, P. Salvador, J. J. Dannenberg, S. Dapprich, A. D. Daniels, O. Farkas, J. B. Foresman, J. V. Ortiz, J. Cioslowski, D. J. Fox, *Gaussian 09, Revision A.02-SMP*, Gaussian, Inc., Wallingford, CT. (2009).
- [60] M.J. Frisch, J.A. Pople, J.S. Binkley, Self-consistent molecular orbital methods 25. Supplementary functions for Gaussian basis sets, *J. Chem. Phys.* 80 (1984) 3265–3269. doi:10.1063/1.447079.
- [61] G. Q. Blantocas, A. S. Alaboodi, A.-B. H. Mekky, Synthesis of Chitosan-TiO<sub>2</sub> Antimicrobial Composites via a 2-Step Process of Electrospinning and Plasma Sputtering, *Arab. J. Sci. Eng.* 43 (2018) 389–398. doi:10.1007/s13369-017-2695-8.

- [62] C. Cárdenas, The Fukui potential is a measure of the chemical hardness, *Chem. Phys. Lett.* 513 (2011) 127–129. doi:10.1016/j.cplett.2011.07.059.
- [63] A. Bendjeddou, T. Abbaz, A. K. Gouasmia, D. Villemain, Molecular Structure, HOMO-LUMO, MEP and Fukui Function Analysis of Some TTF-donor Substituted Molecules Using DFT (B3LYP) Calculations, *Int. Res. J. Pure Appl. Chem.* 12 (2016) 1–9. doi:10.9734/IRJPAC/2016/27066.
- [64] J. L. Gázquez, A. Cedillo, A. Vela, Electrodonating and electroaccepting powers, *J. Phys. Chem. A*. 111 (2007) 1966–1970. doi:10.1021/jp065459f.
- [65] D. Cortés-Arriagada, L. Sanhueza, M. Santander-Nelli, Modeling the physisorption of bisphenol A on graphene and graphene oxide, *J. Mol. Model.* 19 (2013) 3569–3580. doi:10.1007/s00894-013-1872-2.
- [66] L. R. Domingo, P. Pérez, The nucleophilicity N index in organic chemistry, *Org. Biomol. Chem.* 9 (2011) 7168–7175. doi:10.1039/c1ob05856h.
- [67] S. Pratihari, S. Roy, Nucleophilicity and site selectivity of commonly used arenes and heteroarenes, *J. Org. Chem.* 75 (2010) 4957–4963. doi:10.1021/jo100425a.
- [68] P. Jaramillo, L. R. Domingo, E. Chamorro, P. Pérez, A further exploration of a nucleophilicity index based on the gas-phase ionization potentials, *J. Mol. Struct. Theochem.* 865 (2008) 68–72. doi:10.1016/j.theochem.2008.06.022.

## CHAPTER 3

### PHOTOCATALYTIC DEGRADATION OF ALIZARIN RED S DYE USING TiO<sub>2</sub>-ACTIVATED CARBON NANOCOMPOSITE<sup>1</sup>

---

This chapter deals with the preparation of titanium dioxide-activated carbon nanocomposite using the hydrothermal synthesis method. The physicochemical characterization of the nanocomposite was done by different analytical methods like SEM-EDX, XRD, XPS, FT-IR, photoluminescence (PL), pH<sub>ZPC</sub>, and UV-Visible diffuse reflectance spectroscopy (DRS). The nanocomposite was used for the photocatalytic degradation of an anionic dye, Alizarin red S (ARS) from an aqueous solution in the ultra-violet light region. The efficacy of the nanocomposite in the simultaneous adsorption and degradation of ARS aqueous solution was evaluated by varying nanocomposite dosage, contact time, ARS concentrations, and pH. The toxicity assessment of the ARS and its photocatalytic degradation products were analyzed using two phytotoxicity assays: root elongation and plant growth assay. The photodegradation mechanism of ARS was studied using GC-MS analysis. Also, theoretical Density functional theory (DFT) studies were used to understand the mechanism of formation of the nanocomposite, and different chemical descriptors such as dipole moment, ionization energy, chemical softness and hardness, and HOMO-LUMO energy were calculated to compare the efficiency and reactivity of activated carbon and nanocomposite towards ARS degradation.

---

The text of this chapter has been published as:

<sup>1</sup>**M. Baruah, A. Supong, P. C. Bhomick, R. Karmaker, C. Pongener, D. Sinha, Batch sorption-photodegradation of Alizarin Red S using synthesized TiO<sub>2</sub>/activated carbon nanocomposite: an experimental study and computer modelling, *Nanotechnology for Environmental Engineering*, 3 (2020) 1–13. <https://doi.org/10.1007/s41204-020-00071-3>.**

### 3.1 Introduction<sup>1</sup>

Dye effluents generated from industries such as textile, leather, cosmetics, rubber, plastic, etc. lead to severe water contamination and pose serious environmental hazards. The discharge of these harmful effluents into water bodies leads to damaging effects on aquatic biota and also on humans owing to their high toxicity, non-biodegradability, carcinogenicity, mutagenicity, and teratogenic effects. Pollutants such as dyes are mostly non-biodegradable and thus accumulate in sediments and surface water, impacting photosynthetic activity, thereby ultimately inhibiting the overall development of aquatic plants and animals. Today, around 700 tons of dyestuffs are produced annually from over 1,00,000 dyes used commercially. These dyes include basic dyes, acid dyes, direct dyes, azo dyes, mordant dyes, disperse dyes, reactive dyes, and sulphur dyes [1]. These dyes are mostly hazardous to health and unfortunately also have a long degradation process due to their high chemical reactivity and photostability. Among the dyes, alizarin red S (1, 2-dihydroxy-9, 10 anthraquinone-3-sulfonate, ARS) is one of the anthraquinone dyes considered to be a highly long-lasting toxic type due to its complex composition of aromatic rings [2]. Therefore, considering all the ill effects of ARS on humans and the ecosystem, it is vital to remove this dye from wastewater prior to its being discharged into natural water bodies. Considering the existing processes for wastewater treatment, many of the conventional physicochemical processes such as adsorption by activated carbon, membrane filtration, ion exchange, chemical coagulation, reverse osmosis, etc. [3] that were previously used for the removal of dyes have certain disadvantages because, during the treatment of contaminated water, these methods simply facilitate removal of pollutants from the liquid phase to the solid phase thus leading to the generation of more secondary wastes [4]. Hence, it is very important to develop new efficient wastewater treatment methods which have the capacity to degrade the toxic organic compounds and in this regard, a new advanced oxidation process using an embedded photocatalyst is presently being considered as an alternative wastewater treatment method.

---

The text of this chapter has been published as:

<sup>1</sup>**M. Baruah, A. Supong, P. C. Bhomick, R. Karmaker, C. Pongener, D. Sinha, Batch sorption-photodegradation of Alizarin Red S using synthesized TiO<sub>2</sub>/activated carbon nanocomposite: an experimental study and computer modelling, *Nanotechnology for Environmental Engineering*, 3 (2020) 1–13. <https://doi.org/10.1007/s41204-020-00071-3>.**



In the advanced oxidation process (AOP), photocatalysis can generate powerful hydroxyl radicals ( $\cdot\text{OH}$ ) in the presence of  $\text{H}_2\text{O}$  and  $\text{O}_2$  from the atmosphere by irradiating a photocatalyst with light of wavelength ( $\lambda \leq 600 \text{ nm}$ ) [5], which can reduce the photocatalyst bandgap energy. Mechanistically, the hydroxyl radical ( $\cdot\text{OH}$ ) reacts with the hole in the valence band and the excited electron in the conduction band of the photocatalyst, performing a redox reaction, thereafter degrading the organic pollutant to  $\text{CO}_2$  and  $\text{H}_2\text{O}$  [6]. Photocatalysis focuses mainly on the use of semiconductor metal oxides ( $\text{TiO}_2$ ,  $\text{ZnO}$ ,  $\text{Bi}_2\text{O}_3$ ,  $\text{ZrO}_2$ ,  $\text{SnO}_2$ , etc.) or metal sulphides ( $\text{ZnS}$ ,  $\text{CdS}$ ,  $\text{PbS}$ ) for degradation of organic pollutants present in water at ambient temperature, with the use of light as the energy source, and oxygen ( $\text{O}_2$ ) from the atmosphere as an oxidant. Among the semiconductors, titanium dioxide ( $\text{TiO}_2$ ) is a preferred photocatalyst due to its large photoactivity, biological and chemical inactivity, photostability, non-toxicity, inexpensive and environment-friendly nature. However, there are some problems associated with the use of  $\text{TiO}_2$  as a photocatalyst. The agglomerative nature of  $\text{TiO}_2$  nanoparticles creates difficulties in separating it from the solution. Again, the wide bandgap energy of  $\text{TiO}_2$  (3.2 eV for anatase and 3.02 eV for rutile  $\text{TiO}_2$ ) makes its use as a catalyst a little limited [7]. Therefore, to resolve the agglomeration nature of nano- $\text{TiO}_2$ , some supports such as zeolites, clay, alumina, carbon black, carbon nanofibres, and activated carbon have been used [8]. Among the different supports, activated carbon (AC) is used commonly in water remediation processes due to its good adsorption capacity, high surface area, inert, and suitable pore structure [9]. The added advantage of using activated carbon is that activated carbon-supported  $\text{TiO}_2$  exhibits synergism effects based on the adsorption property of AC and the photoactivity of  $\text{TiO}_2$  [10], which enhances its overall removal efficiency, especially for dyes. Understanding that cost-effectiveness is a major concern in the synthesis of activated carbon, in the present work, cones of pine (*Pinus kesiya*) have been used for the preparation of activated carbon due to their easy availability, ease of collection, and commercial non-utility. The prepared pine cone activated carbon (PAC) was thereafter impregnated with  $\text{TiO}_2$  nanoparticles *via* the hydrothermal synthesis method thereby resulting in the formation of the composite.

Quantum chemical methods have now become a feasible way to provide the theoretical basis for the rapid selection of highly proficient materials, thus revealing the relationship between structures and properties of the activated carbon and nanocomposite materials. Many researchers have succeeded in predicting the theoretical rationale of the reactivity and interaction properties of nanomaterial-based on quantum chemical methods. Some theoretical studies had also been reported in the literature, for example, Blantocas *et al.* [11] had used the



Gaussian 09W program to calculate the reactivity of pure Chitosan and Chitosan-TiO<sub>2</sub> substrate by using different molecular properties, while Souza *et al.* [12] used DFT based descriptors to study the molecular chemical reactivity of basic dye with activated carbon. Ullah *et al.* [13] presented a systematic investigation on the optical, electronic structure, surface interaction, electronegativity, and surface transfer mechanism between polypyrrole TiO<sub>2</sub> nanocomposite. Therefore, taking into account the accuracy and simplicity of quantum chemical methods in describing the reactivity and interactive properties of nanocomposite materials, the present study attempted to theoretically understand the reactivity of PAC and nanocomposite towards ARS degradation by using DFT calculations.

This piece of work presents an effort to develop a new nanocomposite material using pine cone based activated carbon (PAC) and titanium dioxide nanoparticles (TiO<sub>2</sub>-NP) to be used as photocatalyst for degradation of organic dyes, and the methodology was tested on an anionic dye namely alizarin red S. In a novel attempt, theoretical studies involving the DFT method was used to supplement the experimental results on the study of the reactivity of PAC and nanocomposite towards ARS dye degradation using water as the solvent medium. The end product of the TiO<sub>2</sub>-NP/PAC nanocomposite left after the mineralization of the ARS dye was utilized for the phytotoxicity analysis to investigate the toxicity effect of the ARS photodegraded products on different plants. The typical mechanism for the photodegradation of alizarin red S dye using TiO<sub>2</sub>-NP/PAC nanocomposite is shown in Figure 3.1.

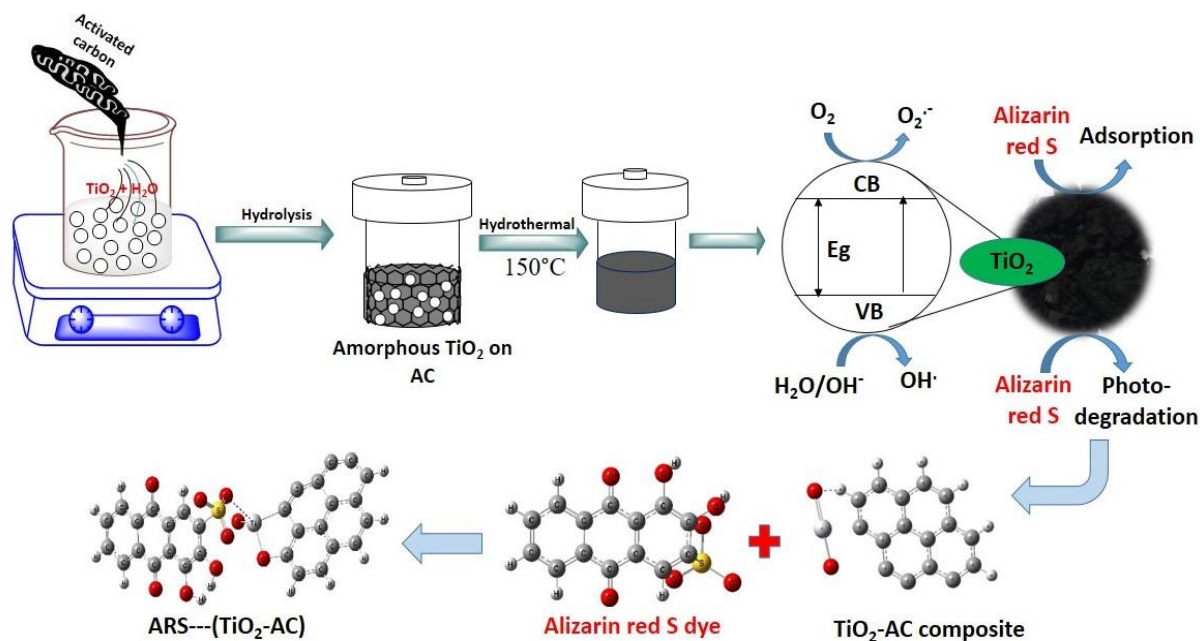


**Figure 3.1** Schematic illustration of photodegradation of alizarin red S dye using TiO<sub>2</sub>-NP/PAC nanocomposite

## 3.2 Materials and methods

### 3.2.1 Materials

Titanium tetrachloride ( $\text{TiCl}_4$ , 99.90%) and alizarin red S (ARS) used in the current study were obtained from Sigma-Aldrich. Co., India. Sulphuric acid (98%), hydrochloric acid (37%), ammonia (30%), sodium hydroxide (99%), silver nitrate, and zinc chloride (96%) were obtained from Merck India Ltd., India, and all the chemicals have been used as supplied without further purification.

### 3.2.2 Synthesis of $\text{TiO}_2$ supported on activated carbon ( $\text{TiO}_2$ -NP/PAC) nanocomposite

For the synthesis of  $\text{TiO}_2$ -NP/PAC nanocomposite,  $\text{TiO}_2$  nanoparticles and activated carbon were used as starting materials. Activated carbon was synthesized using bio-waste pine cones and  $\text{TiO}_2$  nanoparticles using the sol-gel method. The synthetic route for the preparation of activated carbon,  $\text{TiO}_2$  nanoparticles, and  $\text{TiO}_2$ -NP/PAC nanocomposite are discussed below:

#### 3.2.2.1 Activated carbon preparation

The supporting material, activated carbons are synthesized using the chemical activation method, as it is the most versatile method for the synthesis of highly porous and high surface area carbon. For the preparation of activated carbon locally available pine cones (*Pinus kesiya*) are used as the raw material. At first, pine cones were collected and washed properly with double distilled water for the removal of any adhered impurities. The washed cones were oven-dried at  $100^\circ\text{C}$  for 24 hours so that the sample becomes completely dry. The dried sample was then crushed into a fine powder using a planetary ball mill. 5.0 g of this powder sample was then mixed with 100 ml  $\text{ZnCl}_2$  solution containing 10.0 g of  $\text{ZnCl}_2$  and agitated at  $80^\circ\text{C}$  for 4 hours. The as-obtained mixture was pyrolyzed in a muffle furnace at  $500^\circ\text{C}$  for 90 minutes. The activated sample was then washed with 0.1M HCl and 0.1M NaOH to make the residual solution pH neutral and dried at  $110^\circ\text{C}$  [14].

#### 3.2.2.2 Sol-gel method of $\text{TiO}_2$ synthesis

For the synthesis of  $\text{TiO}_2$  nanoparticles by sol-gel method, 1 ml  $\text{TiCl}_4$  was gradually added to dilute sulphuric acid (10%) solution while vigorously stirring at  $0^\circ\text{C}$  in an ice-water bath. After 30 minutes of stirring, a grey-colored solution was formed after which the solution became clear upon subsequent heating at  $65^\circ\text{C}$ . The solution was then cooled to room temperature and then heated for 60 minutes at  $110^\circ\text{C}$ . Later, concentrated ammonia solution ( $\text{NH}_3\cdot\text{H}_2\text{O}$ ) was added dropwise until the pH reached 7. The as-prepared solution was cooled at room temperature and gelled for 12 hours. The gelled  $\text{TiO}_2$  solution was filtered out and washed with

double distilled water until there were no white sediments with 0.1 M  $\text{AgNO}_3$  solution which indicates that the chloride ion from  $\text{TiCl}_4$  is completely removed from the solution. It was then dried at room temperature and was further calcinated at  $500^\circ\text{C}$  for 1 hour to produce the anatase form of  $\text{TiO}_2$  [15]. The reaction steps associated with the synthesis of  $\text{TiO}_2$  are shown below:

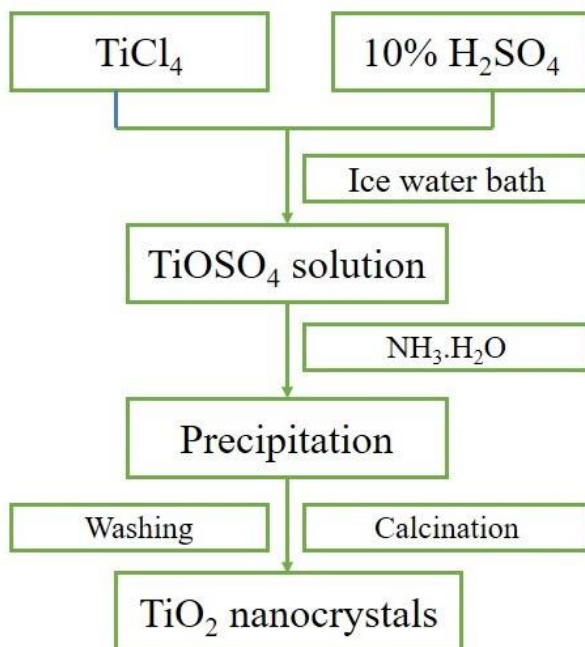


**Figure 3.2** Different reaction steps associated with the synthesis of  $\text{TiO}_2$

### 3.2.2.3 $\text{TiO}_2$ supported on activated carbon ( $\text{TiO}_2$ -NP/PAC) nanocomposite synthesis

For the synthesis of  $\text{TiO}_2$ -NP/PAC nanocomposite, 0.3 g of  $\text{TiO}_2$  nanoparticle was mixed with 20 ml double distilled water while the solution was simultaneously stirred for 20 minutes at room temperature. Afterward, 0.3 g of the prepared PAC was decanted slowly into the  $\text{TiO}_2$  solution and was sonicated for one hour. The  $\text{TiO}_2$ -NP/PAC nanocomposite was then transferred into a Teflon-lined autoclave at  $150^\circ\text{C}$  in an oven for 24 hours. Once the hydrothermal process was completed, the solution was washed with double distilled water multiple times, centrifuged, and dried in an oven at  $65^\circ\text{C}$  overnight [16].

### 3.2.3 Characterization of $\text{TiO}_2$ -NP/PAC nanocomposite

Different analytical techniques were used for the characterization of the  $\text{TiO}_2$ -NP/PAC nanocomposite. The powder X-ray diffraction (XRD) spectrum of the  $\text{TiO}_2$ -NP/PAC was attained using a Philips Xpert PRO diffractometer (Model: Rigaku-Ultima IV Japan) using monochromatic  $\text{CuK}\beta$  X-ray radiation at 40 mA at 40 kV. The surface morphology and surface texture of the  $\text{TiO}_2$ -NP/PAC nanocomposite were analyzed using Scanning Electron

Microscopy (SEM) (Model: Zeiss, Gemini, Sigma-300), together with energy-dispersive X-ray spectroscopy (EDX) analysis for investigating elemental composition. The elemental composition and valence states of the TiO<sub>2</sub>-NP/PAC nanocomposite was studied using X-ray photoelectron spectroscopy (XPS) (Model: ESCALAB Xi+, Made: Thermo Fisher Scientific). The functional groups present on the nanocomposite were identified using Fourier transform Infra-red (FT-IR) spectrometer (Model: Spectrum Two, Made: Perkin Elmer). Photoluminescence studies were investigated using Horiba Fluoromax-4CP spectrofluorometer equipped with a 150 W Xenon Lamp. UV/Vis diffuse reflectance spectrophotometer (Shimadzu UV-2600) in the range of 200-600 nm was used to understand the bandgap of TiO<sub>2</sub>-NP/PAC nanocomposite. The residual dye concentration was measured using Perkin Elmer UV/Vis  $\lambda$ -365 spectrophotometer. The zero-point charge of the prepared TiO<sub>2</sub>-NP/PAC nanocomposite was determined using the batch equilibrium method as described in Chapter 2 section 2.3.

### 3.2.4 Photocatalysis

The ultra-violet light-assisted photocatalytic degradation of ARS was performed in a specially designed photocatalytic reactor consisting of a black box (dimensions: 63×44×44cm). For this study, a 250 ml Pyrex glass vessel containing 150 ml of ARS solution was placed and an amount of TiO<sub>2</sub>-NP/PAC nanocomposite was mixed with the solution at the bottom of the reactor. A 450 W mercury ultra-violet lamp with a wavelength of 325 nm having light power of 1500 mW/cm<sup>2</sup> was located at the top of the reactor; 10 cm away from the reaction solution. The detail about the photocatalytic reactor is described in Chapter 2 section 2.4.2.

### Photocatalytic degradation experiment

The photocatalytic process was accomplished by maintaining a continuous temperature of 25°C using a continuous flow of water throughout the reaction system. At first, 1000 ppm stock solution of ARS was prepared by dissolving 1000 mg of ARS powder. To undergo photocatalytic reactions, the calculated amount of TiO<sub>2</sub>-NP/PAC nanocomposite was first dispersed in a 150 ml aqueous solution of ARS of various strengths (20 ppm, 60 ppm, and 100 ppm) by a vigorous stirring of the reaction mixture in dark conditions up to 30 minutes to establish adsorption-desorption equilibrium within the reaction system before UV irradiation. The ARS degradation percentage was calculated using equation 3.1.

$$\text{Degradation \%} = \frac{C_i - C_e}{C_i} \times 100 \quad (3.1)$$

where C<sub>i</sub> is the initial ARS concentration (ppm), C<sub>e</sub> is the ARS concentration in the solution at equilibrium (ppm).

### 3.2.5 Phytotoxicity assessment

It is essential to estimate the effect of toxicity of the dye solution before and after degradation since the effluents are mainly discharged in the natural streams, and rivers are largely used in the agricultural field [17,18]. The toxicity assessment of the ARS and its photocatalytic degradation products were analyzed using two phytotoxicity assays: root elongation and plant growth assay. For this study, seeds of *Cicer arietinum*, *Solanum lycopersicum*, *Pisum sativum*, *Vigna radiata* were collected from the local market. The experiments were conducted by feeding the seeds of each plant with ARS and also with the photodegraded products of ARS (referred as ARS extract). A control experiment was conducted by splashing the seeds with distilled water.

For this experiment, twelve plastic pots each containing 20 g of properly washed and dried sand were used to sow the seeds of the plant. The pots were divided into three sets of four pots each namely S1, S2, and S3. Each pot in the set was sowed with ten seeds each of *Cicer arietinum* (labeled as PC), *Solanum lycopersicum* (labeled as PS), *Pisum sativum* (labeled as PP), and *Vigna radiata* (labeled as PV), respectively. Subsequently, 5 ml of 500 ppm ARS was added to S1, 5 ml of 500 ppm ARS extract to S2, and 5 ml of distilled water to S3 for every 12 h at ambient temperature.

The phytotoxicity assay was examined on the basis of germination percentage, shoot, and root length. The germination percentage, the length of the shoot, and the root were measured after 15 days.

The seeds germination percentage was calculated according to the equation given shown below [19]:

$$\text{Germination \%} = \frac{\text{Seeds germinated}}{\text{Total seeds}} \times 100 \quad (3.2)$$

### 3.2.6 Computational studies

A computational study using DFT calculations was conducted to understand the chemical reactivity and to get a better insight into the adsorption and degradation process of TiO<sub>2</sub>-NP/PAC nanocomposite. GaussView 05 suite of the program was employed to build all the concerned structures. Optimization was performed on Gaussian09 software at basis set 6-31g level and B3LYP hybrid functional in a dielectric medium of  $\epsilon = 80$  (corresponding to water). The different quantum chemical parameters like HOMO-LUMO energy gap (H), chemical hardness ( $\eta$ ), chemical softness (S), chemical potential ( $\mu$ ), electron-accepting power ( $\omega^+$ ), electron-donating power ( $\omega^-$ ), electrophilicity index ( $\omega$ ), and nucleophilicity index (N) were calculated using equations 2.19-2.26 as described in Chapter 2.

For the calculation of adsorption energies of alizarin red S (ARS) on the TiO<sub>2</sub> and TiO<sub>2</sub>-NP/PAC nanocomposite, the following equation was used [20]:

$$\Delta E_{\text{adsorp}} = E_{xy} - (E_x + E_y) \quad (3.3)$$

where  $\Delta E_{\text{adsorp}}$  = adsorption energy of ARS on the TiO<sub>2</sub> and TiO<sub>2</sub>-NP/PAC nanocomposite,  $E_{xy}$  = total energy of the TiO<sub>2</sub>-ARS and TiO<sub>2</sub>-NP/PAC-ARS nanocomposite in an equilibrium state,  $E_x$  = energy of the TiO<sub>2</sub> and TiO<sub>2</sub>-NP/PAC nanocomposite, and  $E_y$  = energy of the ARS molecule.

### 3.3 Results and discussion

#### 3.3.1 Characterization of TiO<sub>2</sub>-NP/PAC nanocomposite

##### (a) XRD analysis

X-ray diffraction phase patterns of the TiO<sub>2</sub> and TiO<sub>2</sub>-NP/PAC nanocomposite powder are shown in Figure 3.3. The appearance of XRD peaks at  $2\theta = 25.32^\circ$ ,  $37.80^\circ$ ,  $48.10^\circ$ ,  $55.10^\circ$  and  $62.36^\circ$  corresponds to (1 0 1), (0 0 4), (2 0 0), (1 0 5), and (2 0 4) planes which confirmed the formation of pure nanocrystalline anatase phase of TiO<sub>2</sub> [JCPDS card No. 21-1272]. Even in the case of TiO<sub>2</sub>-NP/PAC nanocomposite, the presence of these peaks confirmed that the presence of crystalline structure of TiO<sub>2</sub> in the carbon matrix along with XRD pattern at  $\sim 23^\circ$  and  $\sim 43^\circ$ , corresponding to (0 0 2) and (1 0 0) plane, confirming the presence of graphite-like microcrystalline structure of activated carbon [21]. The average size of the TiO<sub>2</sub>-NP/PAC nanocomposite calculated using the Debye-Scherrer equation [22] was found to be 2.35 nm.

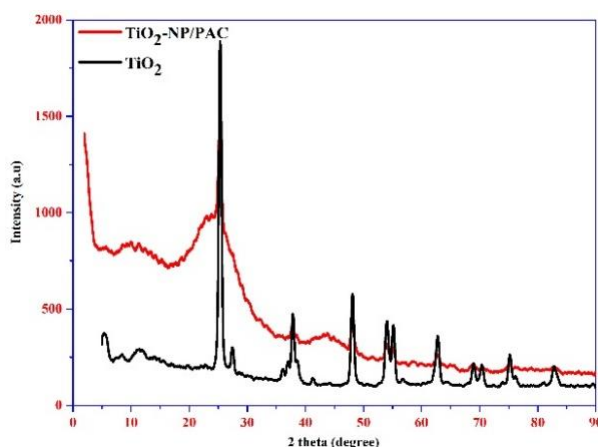


**Figure 3.3** X-ray Diffractogram of TiO<sub>2</sub>-NP/PAC nanocomposite

##### (b) SEM/EDX analysis

The surface morphologies of the synthesized TiO<sub>2</sub> and TiO<sub>2</sub>-NP/PAC nanocomposite were characterized by SEM and their micrographs are shown in Figure 3.4 (a) and (b). The SEM image of TiO<sub>2</sub> shows particle agglomeration with spherical particles varying in size from 6-100



nm. However, after the impregnation process using activated carbon as the substrate, it was observed that the  $\text{TiO}_2$  are placed inside the PAC pores and on the surface of the adsorbent. This hinders the agglomeration of  $\text{TiO}_2$  nanoparticles which aids in an efficient photocatalytic process.

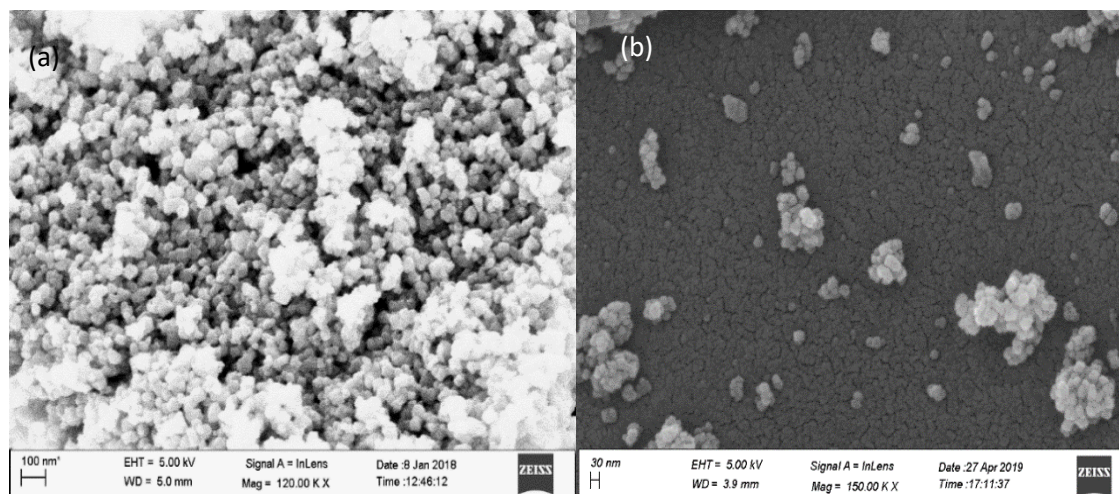


**Figure 3.4** SEM images of (a)  $\text{TiO}_2$  nanoparticles and (b)  $\text{TiO}_2$ -NP/PAC nanocomposite

The elemental compositions of the prepared  $\text{TiO}_2$ -NP/PAC nanocomposite were further investigated by employing EDX (Figure 3.5).

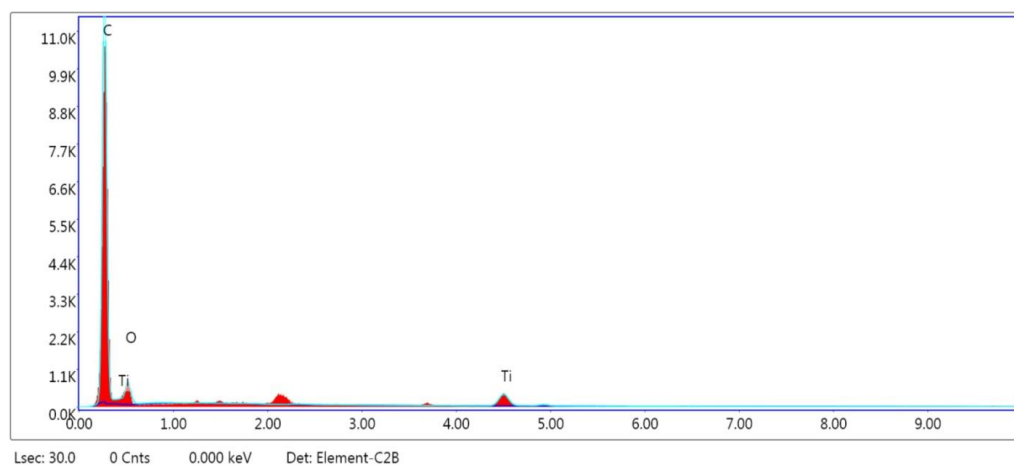


**Figure 3.5** EDX spectra of  $\text{TiO}_2$ -NP/PAC nanocomposite

The EDX graph revealed that the prepared  $\text{TiO}_2$ -NP/PAC nanocomposite has a carbon content of 78.27%, oxygen of 12.18%, and Ti of 9.55%. In the EDX graph, the presence of C, O, and Ti peaks is due to the use of carbon and  $\text{TiCl}_4$  while preparing the  $\text{TiO}_2$ -NP/PAC nanocomposite.

### (c) XPS analysis

To study the chemical composition and elemental states of the  $\text{TiO}_2$ -NP/PAC nanocomposite,

X-ray photoelectron spectroscopy (XPS) analysis was executed and are shown in Figure 3.6. The full scan XPS spectra of the nanocomposite (Figure 3.6 (a)) indicates the presence of elements such as Ti, O, and C at their corresponding chemical states. The detail XPS core level spectra of Ti 2p, and C 1s, and O 1s for TiO<sub>2</sub>-NP/PAC nanocomposite are shown in Figure 3.6 (b), 3.6 (c), 3.6 (d), respectively. The core level spectrum of Ti 2p displayed two peaks: the first major one at 459.4 eV corresponds to the binding energy of Ti 2p<sub>3/2</sub> state and the second one at 465.12 eV refers to the binding energy of Ti 2p<sub>1/2</sub> state [23]. The XPS spectrum of C 1s showed a strong peak at 284.83 eV, and it deconvoluted into 284.77, 285.58, and 288.68 eV, which are attributed to the C=C bonds, C-OH, and C=O bonds activated carbon [24]. The XPS spectrum of O 1s showed a strong peak at 531.58 eV, it deconvoluted into three peaks at 531.33, 533.36, and 533.47 eV, which were ascribed to the surface oxygen species of hydroxyl groups, lattice oxygen of TiO<sub>2</sub>, and oxygen vacancies, respectively [25]. Thus, the XPS results confirm the formation the TiO<sub>2</sub>-NP/PAC nanocomposite.

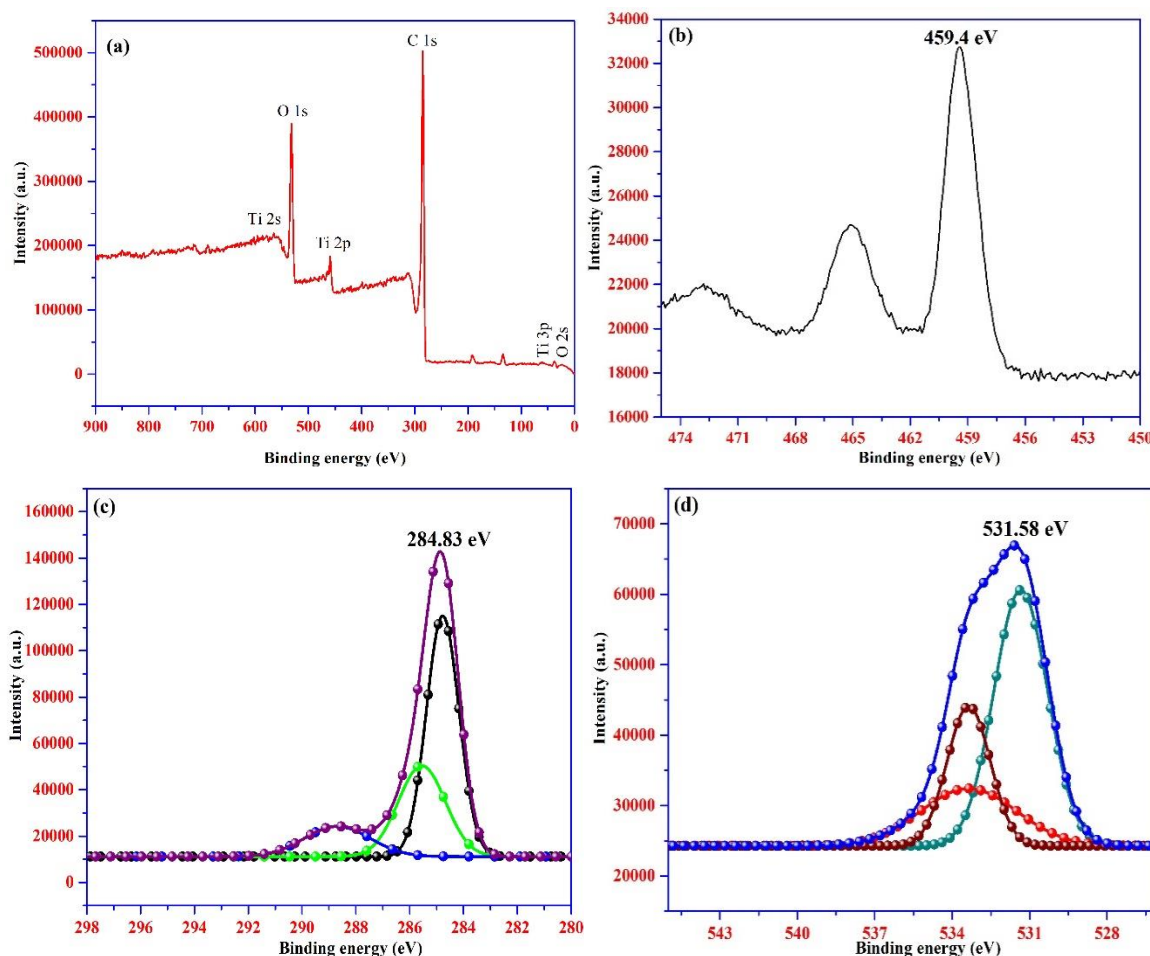


**Figure 3.6** XPS spectra of TiO<sub>2</sub>-NP/PAC nanocomposite: (a) survey, (b) Ti 2p, (c) C 1s, and (d) O 1s



**(d) FT-IR analysis**

FT-IR spectra of TiO<sub>2</sub>-NP/PAC nanocomposite showed the presence of 833.96, 715.32, and 505.68 cm<sup>-1</sup> peaks corresponding to Ti-O-C and Ti-O stretching vibrations, which confirmed the formation of bonds between TiO<sub>2</sub> and carbon material (Figure 3.7) [26].

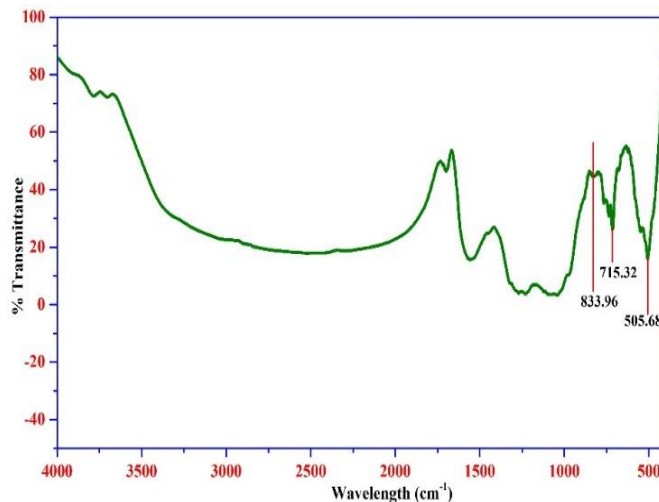


**Figure 3.7** FT-IR spectra of TiO<sub>2</sub>-NP/PAC nanocomposite

**(d) UV-Vis DRS analysis**

UV-Vis DRS measurements were done in the range of 200-600 nm and the spectra are presented in Figure 3.8 (a) and (b). The TiO<sub>2</sub>-NP/PAC nanocomposite showed a hump having an absorption edge at ~230 nm which lies in the UV range.

The optical bandgap energy of the TiO<sub>2</sub>-NP/PAC nanocomposite was followed by classical Tauc's equation given below [27]:

$$\alpha h\nu = K (h\nu - E_g)^n \quad (3.4)$$

where  $E_g$  represents the optical bandgap,  $h\nu$  is the photon energy,  $K$  is a constant, and  $n$  depends on the nature of the transition. In fact,  $n$  assumes a value of 1/2, 3/2, 2, and 3 for direct allowed, direct forbidden, indirect allowed, and indirect forbidden transitions respectively. In the case of TiO<sub>2</sub>-NP/PAC nanocomposite, the best fit of  $(\alpha h\nu)^2$  versus  $h\nu$  was attained for  $n = 1/2$ , which signifies a direct allowed transition across the bandgap energy. The absorption bandgap energy equivalent to  $E_g = 3.2$  eV was observed for the TiO<sub>2</sub>-NP/PAC nanocomposite, satisfying the bandgap energy of the anatase phase of TiO<sub>2</sub>.

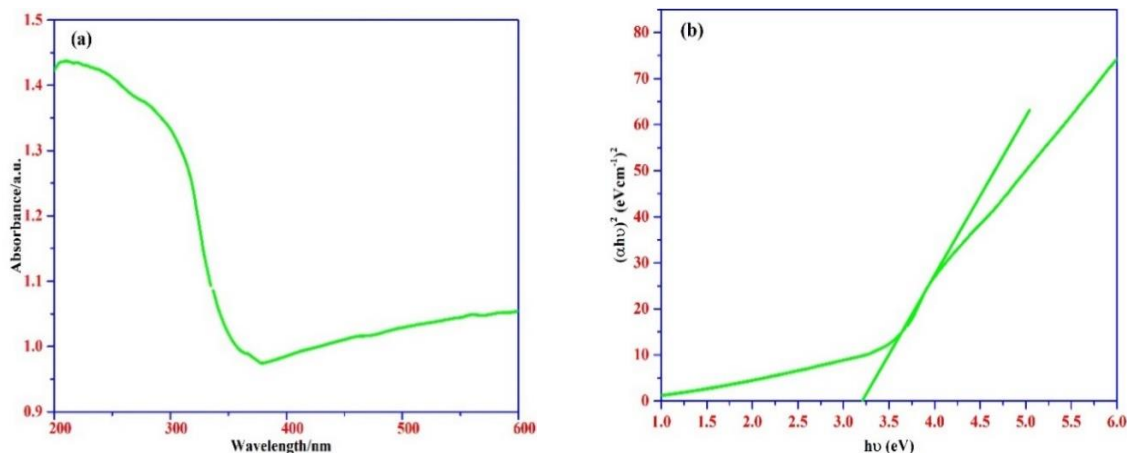


**Figure 3.8** (a) UV-visible DRS spectra and (b) Tauc's plot for calculating bandgap of TiO<sub>2</sub>-NP/PAC nanocomposite

### (e) PL analysis

Photoluminescence (PL) was applied to determine the fate of photogenerated species. When a photocatalyst is irradiated by a photon, an electron and a hole are produced on the surface of the catalyst and the produced electron-hole pair can recombine by emission of photons resulting in a photoluminescence effect [28]. Therefore, the lower the PL intensity lower is the recombination rate of electron-hole pairs and the higher will be the photocatalytic activity of the photocatalyst [29]. The PL spectrum in Figure 3.9 shows that the peak intensity of TiO<sub>2</sub> nanoparticles was high hence the recombination of electron-hole pairs was more. The lower peak intensity of TiO<sub>2</sub>-NP/PAC signifies that the recombination of electron-hole was lesser; hence, the photocatalytic reaction was expected to be more effective. Hence, the presence of PAC as support for TiO<sub>2</sub> decreases the electron-hole recombination by increasing the lifetime of the charge carrier and thus improves the photocatalytic activity.

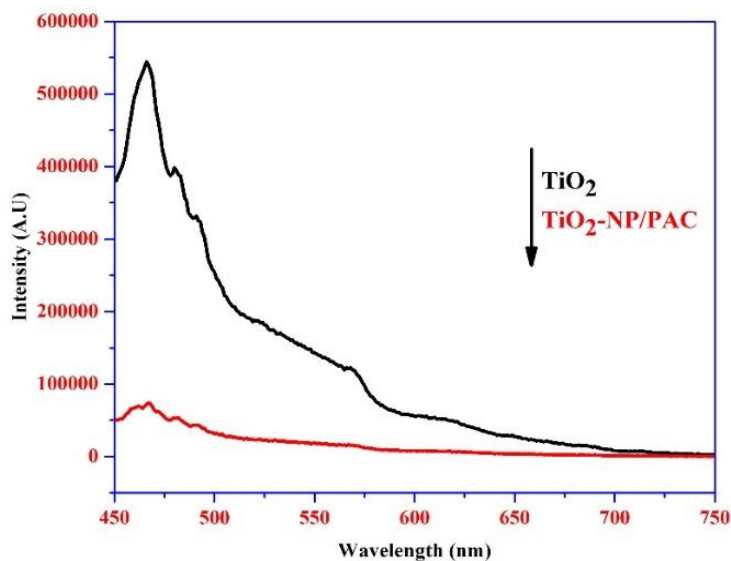


**Figure 3.9** Photoluminescence spectra of TiO<sub>2</sub>, and TiO<sub>2</sub>-NP/PAC nanocomposite

**(f) pH<sub>zpc</sub> analysis**

For zero-point charge pH (pH<sub>zpc</sub>) measurement, the pH of 0.1 M NaNO<sub>3</sub> (50 ml) was adjusted to a value between 2 to 10 by adding either 0.1M HCl or 0.1 M NaOH solutions. The pH of each solution was recorded as the initial pH (pH<sub>initial</sub>). Then 0.1 g of TiO<sub>2</sub>-NP/PAC composite was added and stirred for 24 hours in a rotary shaker at room temperature. The final pH of each solution was recorded and a graph of initial pH versus final pH was plotted and is given in Figure 3.10. The zero-point charge pH (pH<sub>zpc</sub>) of the nanocomposite was found to be 6.45.

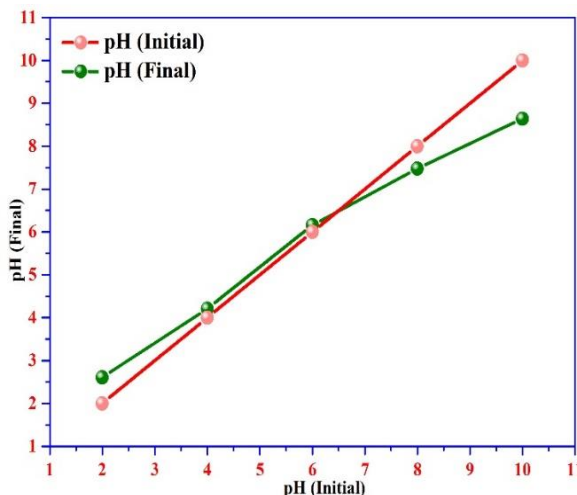


**Figure 3.10** Zero-point charge plot for TiO<sub>2</sub>-NP/PAC nanocomposite

**3.3.2 Photocatalytic reactions**

Prior to photocatalysis, the adsorption efficiency of the nanocomposite was first determined by Batch mode adsorption study, and the optimum adsorption parameters such as adsorption dose, pH, initial concentration of ARS, and contact time were determined.

The adsorption behavior of the TiO<sub>2</sub>-NP/PAC nanocomposite was studied by stirring 150 ml of the reaction mixture in a magnetic stirrer for 30 minutes in a dark condition. Once the dye concentration became constant, that concentration was taken as the initial concentration for all the photocatalytic reactions, thus ensuring that the adsorption of dye, due to the nanocomposite material does not interfere in the analysis of the overall photocatalytic degradation process. After reaching the adsorption-desorption equilibrium, the solution mixture was irradiated with UV light and after every 10 minutes time period, 3.5 ml of aliquots were taken out and centrifuged at 3500 rpm. Later, the final concentration of ARS was analysed at  $\lambda_{\text{max}}$  of 424 nm in a UV/Vis spectrophotometer. The absorbance of aliquots at different time intervals decreased from 1.0 to almost zero after 80 minutes of UV exposure, indicating a complete degradation of the dye. Furthermore, the solution color also changes from initial deep red color to a nearly transparent which also supplements the degradation of the ARS dye (Figure 3.11).



**Figure 3.11** Snapshot showing aqueous deep red color ARS and the colorless end products obtained after degradation by  $\text{TiO}_2\text{-NP/PAC}$  nanocomposite

**(a) Effects of  $\text{TiO}_2\text{-NP/PAC}$  nanocomposite amount**

The effect of  $\text{TiO}_2\text{-NP/PAC}$  loading on decolorization of ARS dye solution was studied by varying the nanocomposite dosages ranging from 0.01-0.09 g at different ARS concentrations and degradation percentage vs. adsorbent doses was plotted (Figure 3.12). The degradation efficiency was found to increase with the increase of dosages of  $\text{TiO}_2\text{-NP/PAC}$  until an amount of 0.05 g. This increase in degradation percentage can be attributed to the addition of PAC which increases the available surface area of the nanocomposite, resulting in more ARS molecules gathering around  $\text{TiO}_2\text{-NP/PAC}$  nanocomposite and also results in the generation of more photo-generated electron-hole pairs at the active sites of the nanocomposite [30]. On further increasing the dosages above 0.05 g, the photocatalytic degradation of ARS was decreased, which might probably be because of the adverse scattering of ultra-violet light through the reaction mixture which results in the decreasing of ultra-violet light penetration into the reaction mixture [31]. Thus 0.05 g of the photocatalyst was considered as the optimum dose for ARS degradation for further experiments.

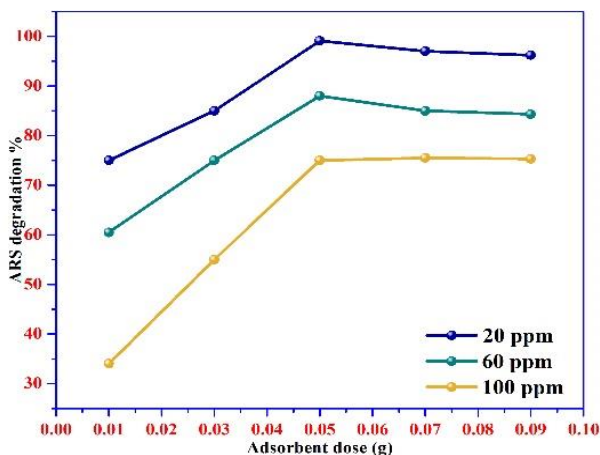


**Figure 3.12** Effect of nanocomposite loading in the degradation of ARS solution

### (b) Effects of pH

To understand the effect of pH, a study on the degradation of ARS was conducted using 0.05 g of TiO<sub>2</sub>-NP/PAC in 150 ml of dye solution (20 ppm) within the pH range of 2.0-11.0 by addition of either HCl or NaOH (0.1 M). It was observed that the degradation of the dye solution was more at lower pH (acidic condition) and less at higher pH (basic condition) (Figure 3.13). The zero-point charge (pHzpc) of the composite was found to be 6.45. It was seen that below this pHzpc, the surface of the composite behaves as acidic, and above its pHzpc, it behaves as basic [14]. Hence, in an acidic medium, the H<sup>+</sup> ions on the surface of the nanocomposite increase (pH < pHzpc) which attracts the negatively charged molecule of ARS resulting in the increased degradation of the ARS. However, in a basic medium, the availability of OH<sup>-</sup> anion on the surface of the nanocomposite increases (pH > pHzpc) leading to electrostatic repulsion between the negatively charged surface of the nanocomposite and the anionic ARS, thereby decreasing the degradation efficiency of ARS [27].

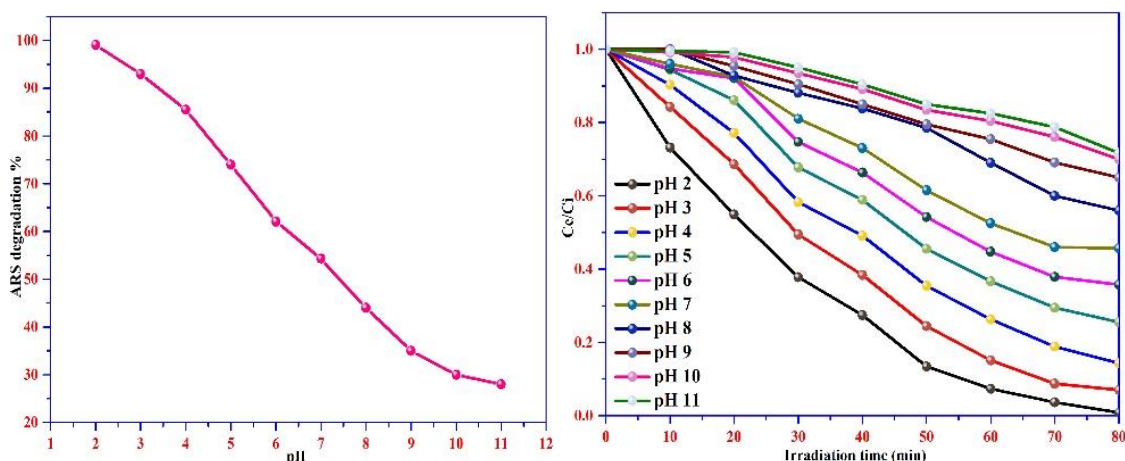


**Figure 3.13** Effect of initial pH in the degradation of ARS solution

### (c) Effects of initial dye concentration

The photocatalytic degradation of ARS was accomplished at pH = 2 with 0.05 g of TiO<sub>2</sub>-NP/PAC nanocomposite and 150 ml of different ARS concentrations of 20 ppm, 60 ppm, and 100 ppm at 25°C. The effect of initial dye concentration on the photocatalytic degradation of ARS is shown in Figure 3.14. Around 99.10% degradation of ARS was achieved with a 20 ppm ARS solution. For the 60 ppm and 100 ppm concentrations of ARS, the degradation percentage was decreased to 88% and 75%, respectively. A decrease in the degradation percentage with increasing dye concentration might be due to the inhibition of direct connection between the holes, hydroxyl radicals, and superoxide radicals generated as a result of photolysis on the TiO<sub>2</sub>-NP/PAC nanocomposite surface [32]. A higher concentration of dye functions as an inner filter

and pushes the light particles away from the photocatalyst [33]. After the adsorption process, the dye molecules are adsorbed on the surface of the photocatalyst thus blocking the active surface sites on the photocatalyst [34].

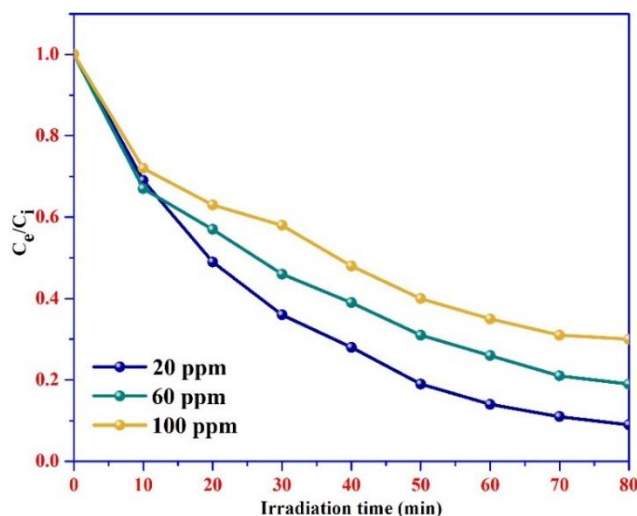


**Figure 3.14** Effect of initial dye concentration on the photocatalytic degradation of ARS solution

### 3.3.3 Kinetic studies

The kinetics of ARS photodegradation was evaluated using the Langmuir-Hinshelwood model (L-H) [26]. The kinetic studies were accomplished under the optimum condition of 20 ppm dye solutions (150 ml), pH 2, and 0.05 g of TiO<sub>2</sub>-NP/PAC nanocomposite. The pseudo-first-order kinetics and the half-life time for ARS were determined using equations 3.5 and 3.6.

$$\ln\left(\frac{C_i}{C_e}\right) = K_{app}t \quad (3.5)$$

$$t_{1/2} = \frac{\ln 2}{K_{app}} \quad (3.6)$$

where  $C_i$  is the initial concentration of the ARS,  $C_e$  is the concentration at time  $t$ ,  $K_{app}$  is the apparent rate constant, and  $t_{1/2}$  is the half-life time.

A plot of  $\ln(C_0/C_e)$  vs. irradiation time was plotted to understand the process of photocatalytic degradation of ARS by TiO<sub>2</sub>-NP/PAC nanocomposite. From Figure 3.15, it can be seen that the plot of  $\ln(C_0/C_e)$  vs. irradiation time is close to linearity, signifying that ARS degradation follows pseudo-first-order kinetic model. The  $K_{app}$  was calculated to be 0.02372 min<sup>-1</sup> and the half-life time for ARS was found to be 29.3 minutes. The pseudo-first-order signifies that the photocatalytic degradation is primarily dependent on light intensity [35] and the photoactivity of TiO<sub>2</sub>-NP/PAC nanocomposite is enhanced under UV light.

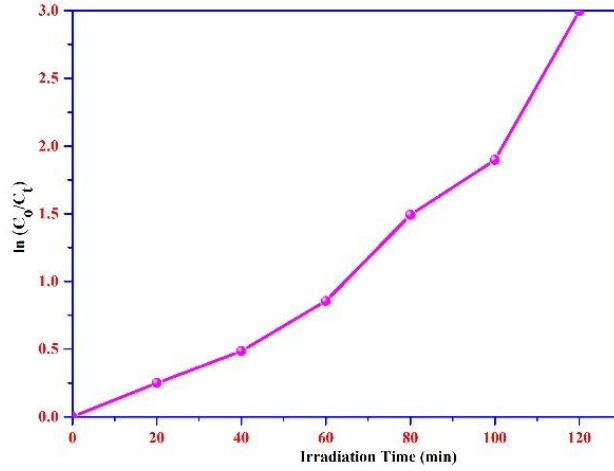


**Figure 3.15** Pseudo first-order model of ARS photodegradation onto the TiO<sub>2</sub>-NP/PAC nanocomposite

### 3.3.4 Thermodynamic studies

For this study, the standard enthalpy ( $\Delta H^\circ$ ), entropy ( $\Delta S^\circ$ ), and free energy ( $\Delta G^\circ$ ) were calculated using the Van't Hoff equation [36].

$$\ln K_c = \frac{\Delta S^\circ}{R} - \frac{\Delta H^\circ}{RT} \quad (3.7)$$

$$\Delta G^\circ = -RT \ln K_c \quad (3.8)$$

where R is the universal gas constant, T is the absolute temperature,  $K_c$  is the distribution coefficient. The values of  $\Delta H^\circ$  and  $\Delta S^\circ$  were obtained from the slope and intercept of the  $\ln K_d$  versus  $1/T$  plot (Figure 3.16).

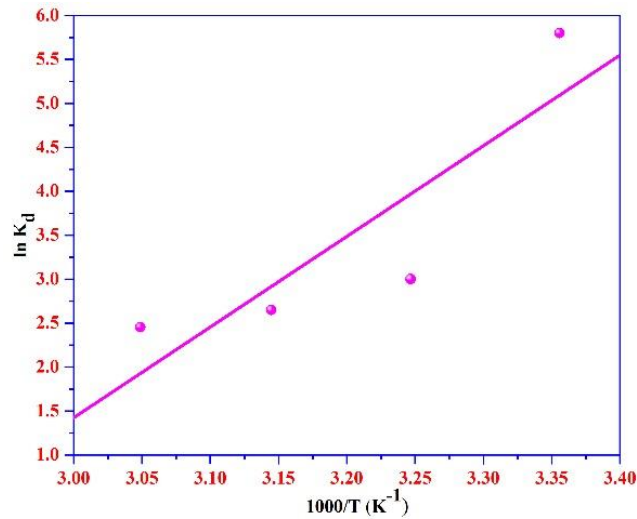


**Figure 3.16**  $\ln K_d$  as a function of  $1/T$  (ARS = 20 ppm, pH 2, catalyst dose = 0.05 g, and irradiation time = 80 minutes)

Table 3.1 represents the thermodynamic parameters at various temperatures. The negative value of  $\Delta S^\circ$  (-0.24) and  $\Delta H^\circ$  (-85.73) indicates that the ARS degradation is an exothermic and



spontaneous process. The bending of the curve is explained due to the saturation of photocatalytic sites in the nanocomposite and the competitive hydrogen evolution [37].

**Table 3.1** Values of various thermodynamics parameters for the degradation of ARS using TiO<sub>2</sub>-NP/PAC

T (K)	Thermodynamic parameters		
	$\Delta G^\circ$ (kJ mol <sup>-1</sup> )	$\Delta H^\circ$ (kJ mol <sup>-1</sup> )	$\Delta S^\circ$ (kJ mol <sup>-1</sup> K)
298	-12.61	-85.73	-0.24
308	-10.16		
318	-7.70		
328	-5.25		

### 3.3.5 Effect of interfering ions on ARS photocatalytic degradation

The main reactive species that drive a photocatalytic reaction are mainly hydroxyl radical ( $\cdot\text{OH}$ ), superoxide radical ( $\text{O}_2^-$ ), electron ( $e^-$ ), and holes ( $h^+$ ). To determine the effect of these reactive species in photocatalytic degradation process, different interfering ions were added to the reaction solution before running the ARS degradation process. In this study, 20 ppm of the scavenger was added to the ARS solution at optimum operating conditions. The percent degradation of the ARS as a function of different interfering ions is presented in Figure 3.17. From the figure it can be seen that the degradation decreases from 99.10% to 52.0% (Glycine), 75.5% (EDTA), 61.0% ( $\text{CuSO}_4$ ), 79.0% ( $\text{NaNO}_3$ ), 71.0% ( $\text{ZnCl}_2$ ), 72.5% ( $\text{NaCl}$ ), 61.0% ( $\text{Cd}(\text{NO}_3)_2$ ), 82.0% (oxalic acid). A significant decrease of ARS degradation was observed in presence of glycine as it can scavenge hydroxyl ( $\cdot\text{OH}$ ) ions [34]. The presence of nitrate ion in  $\text{Cd}(\text{NO}_3)_2$  also decreases the ARS degradation as it absorbs in the UV and visible light region [38]. Chloride ions present in both  $\text{ZnCl}_2$  and  $\text{NaCl}$  can scavenge both the  $\cdot\text{OH}$  radical and hole, hence these present also decreases the degradation of ARS [39]. The presence of EDTA in the solution act as a hole scavenger,  $\text{SO}_4^{2-}$  ion in  $\text{CuSO}_4$  as an electron scavenger [40]. However, the presence of other interfering ions (oxalic acid,  $\text{NaNO}_3$ ) has reduced the effects of the photocatalytic degradation process as they act as hole interfering ions [41]. From this result, it can observe that the photocatalytic degradation of ARS in the presence of interfering ions follows the order:

Oxalic acid <  $\text{NaNO}_3$  < EDTA <  $\text{NaCl}$  <  $\text{ZnCl}_2$  <  $\text{Cd}(\text{NO}_3)_2$  <  $\text{CuSO}_4$  < Glycine.



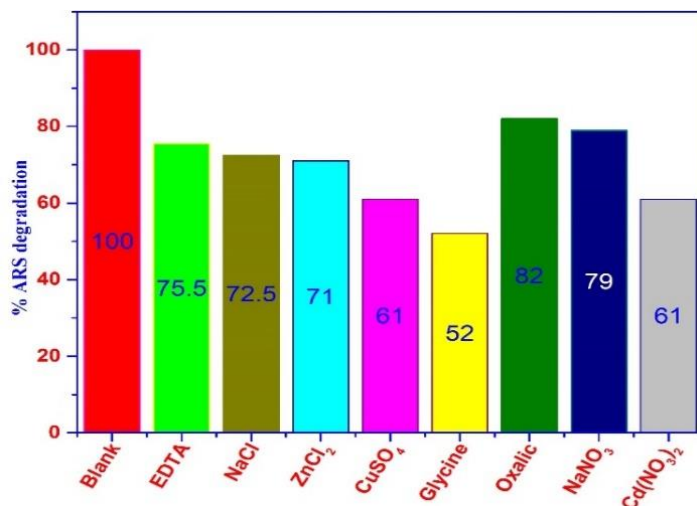


**Figure 3.17** Photocatalytic degradation of ARS in the presence of interfering ions using TiO<sub>2</sub>-NP/PAC nanocomposite

### 3.3.6 Catalyst reusability and photostability

The reusability of the TiO<sub>2</sub>-NP/PAC nanocomposite for the photocatalytic degradation of ARS dye was carried out for five cycles of usages (Figure 3.18). In the first cycle, 99.1% of ARS degradation was observed. Thereafter, it degraded to 92.5%, 89%, 85%, and 82% in the respective cycles. These results indicate that TiO<sub>2</sub>-NP/PAC nanocomposite is an excellent photocatalyst that can be used and reused several times in the photocatalytic degradation process.

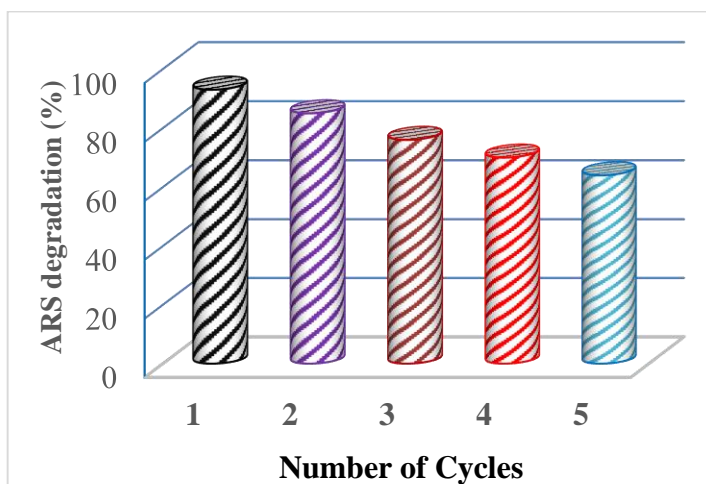


**Figure 3.18** ARS degradation efficiency of TiO<sub>2</sub>-NP/PAC nanocomposite up to five cycles

In order to understand whether any structural changes occurred after repeated reuse of the nanocomposite, infra-red (IR) spectra of the fresh nanocomposite were compared with the reused nanocomposite. From Figure 3.19, it can be perceived that all the specific peaks of the nanocomposite were present and remained in the same position for the used nanocomposite.

This confirms the fact that no structural change happened to the  $\text{TiO}_2\text{-NP/PAC}$  nanocomposite even after reusing for the fifth time also.

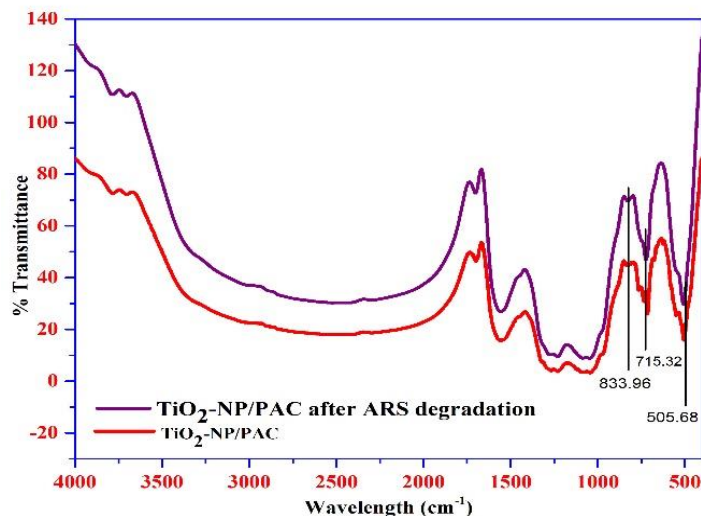


**Figure 3.19** FT-IR spectra of  $\text{TiO}_2\text{-NP/PAC}$  before and after ARS degradation

### 3.3.7 GC-MS analysis

The identification of end-products of the ARS photodegradation was confirmed through GC-MS analysis and the result is presented in Figure 3.20.

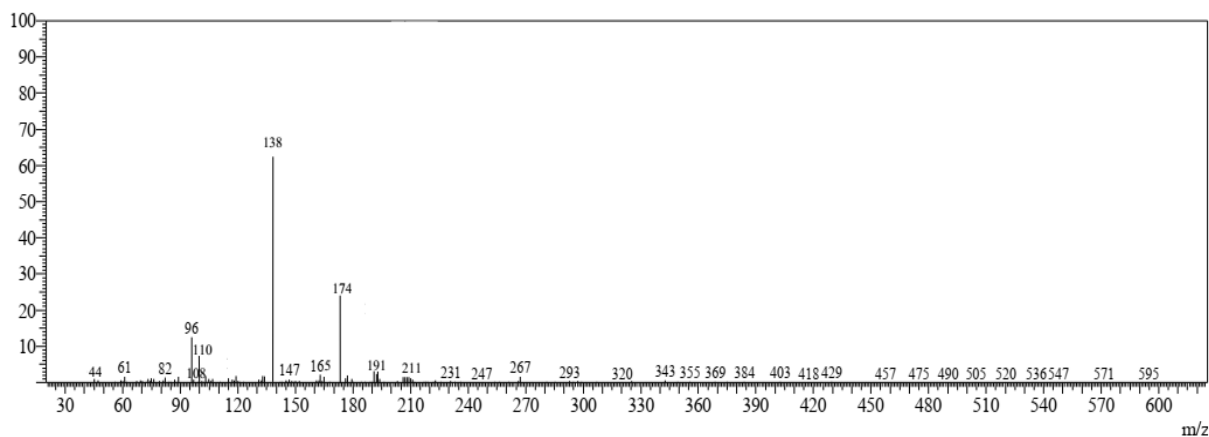


**Figure 3.20** Mass spectra of degradation products of ARS aqueous solution

The major degraded products obtained were o-hydroxy sulfonic acid at  $m/z = 174$ , phthalic acid at  $m/z = 165$ , salicylic acid at  $m/z = 138$ , catechol at  $m/z = 110$ , and cyclo 3,5-hexadiene 1,2-dienone at  $m/z = 108$ . The probable mechanism for degradation is reflected in Figure 3.21. ARS is initially degraded by an attack of hydroxyl radicals produced in the reaction medium generating three different fragments o-hydroxy sulfonic acid, phthalic acid, and salicylic acid. These further oxidize to form catechol and ring-opening of catechol resulted in the formation

of smaller products like cyclo 3,5-hexadiene 1,2-dienone, carbon dioxide ( $m/z = 44$ ), and water, etc [42].

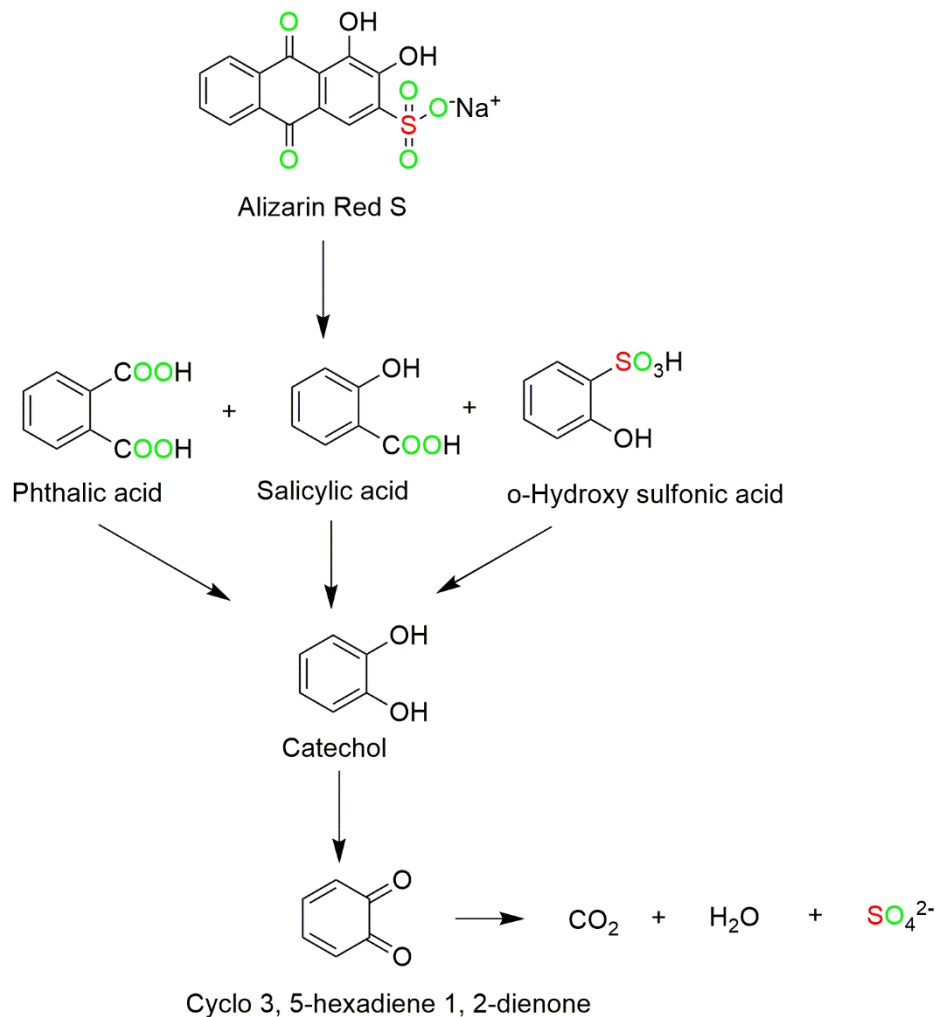


**Figure 3.21** Proposed degradation pathway for the degradation of ARS over TiO<sub>2</sub>-NP/PAC nanocomposite [43]

### 3.3.8 Mechanism for photodegradation

When a photocatalyst is illuminated by a source of light having energy equal to or higher than the bandgap energy of the photocatalyst, holes ( $h^+$ ), and electrons ( $e^-$ ) are formed on the catalyst surface. These photogenerated electrons ( $e^-_{CB}$ ) species react with the oxygen molecules adsorbed on the catalyst surface to form superoxide anion radicals ( $\cdot O_2^-$ ). The photogenerated hole ( $h^+_{VB}$ ) in the VB of semiconductors can cause dissociation of water molecules in the aqueous solution, generating highly reactive hydroxyl radicals ( $\cdot OH$ ). The  $\cdot OH$  radicals and  $\cdot O_2^-$  radicals interact with the adsorbed ARS molecule to degrade it to smaller products like cyclo 3,5-hexadiene 1,2-dienone, carbon dioxide, and water. The processes involved in the degradation of ARS are given below:



### 3.3.9 Toxicity assessment of ARS and its effluent after degradation

The phytotoxicity of the plants was measured based on seed germination percentage, length of roots, and shoots, as these are all sensitive to the presence of phytotoxic compounds. The phytotoxicity of the photodegraded products of ARS, ARS extract, and distilled water was analyzed against *Cicer arietinum* (Gram), *Solanum lycopersicum* (Tomato), *Pisum sativum* (Garden pea), *Vigna radiata* (mung bean) seeds after 15 days. Figure 3.22 shows the growth of the seeds after 15 days of treatment with ARS, ARS extract, and distilled water.

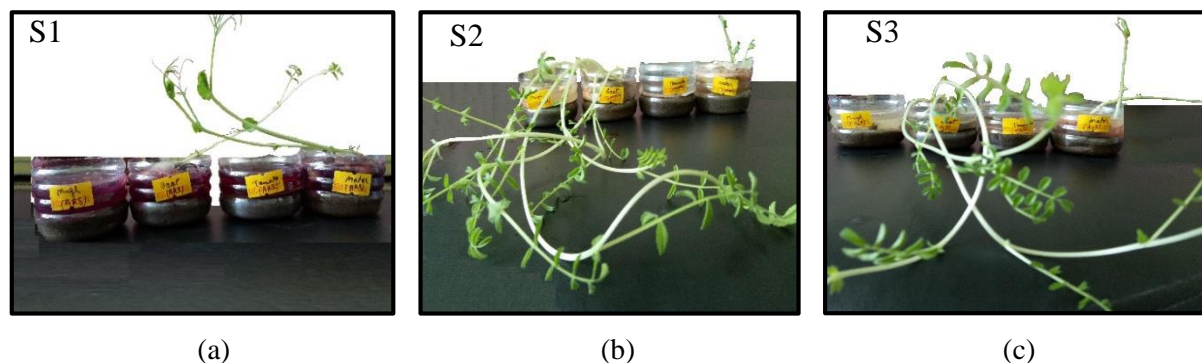


**Figure 3.22** Growth of the *Cicer arietinum* (Gram), *Solanum lycopersicum* (Tomato), *Pisum sativum* (Garden pea), *Vigna radiata* (Mung bean) seeds on treatment with (a) ARS, (b) ARS extract, and (c) Distilled H<sub>2</sub>O

Table 3.2 represents the results obtained from phytotoxic studies. In root elongation assay, ARS (500 ppm) significantly reduced the growth of all the plants as compared to distilled water and seeds treated with ARS extract. The length of shoots and roots were reduced with ARS treatment in all four plants whereas the shoots and roots lengths showed considerable growth in both distilled water and ARS extract. There was no growth in the plant's *Solanum lycopersicum* and *Vigna radiata* after the treatment of ARS (500 ppm). Other authors have also reported similar phytotoxic studies of plants against crystal violet and alizarin red S dye and their photodegraded products and they found that plants showed more sensitivity towards the dye while the products obtained after the decolorization of dye have less inhibitory effects [44,45].

Analysis of Variance (ANOVA) using the Tukey-Kramer multiple comparison test was applied to analyze the differences in shoot and root elongation of the four plants challenged with

distilled water, ARS, ARS extract. The statistical analyses were carried out using Microsoft excel 2010 and data were compared at the significance level ( $P < 0.05, 0.01$ ).

<b>Table 3.2</b> Phytotoxicity of ARS and metabolites formed after its degradation												
Observation	<i>Cicer arietinum</i>			<i>Solanum lycopersicum</i>			<i>Pisum sativum</i>			<i>Vigna radiata</i>		
	P1-C	P2-C	P3-C	P1-S	P2-S	P3-S	P1-P	P2-P	P3-P	P1-V	P2-V	P3-V
Germination (%)	40	20	50	20	0	25	33.4	26.6	33.4	36.6	0	36.6
Shoot length (cm)	3.90 ±0.04*	0.80 ±0.5	3.77 ±0.07*	2.42 ±3.49*	0	0.90 ±0.6	2.40 ±1.04**	0.61 ±0.50	3.32 ±0.39*	2.91 ±0.45*	0	2.95 ±0.76*
Root length (cm)	2.82 ±1.12*	0.90 ±0.18	2.59 ±1.17*	2.82 ±3.09*	0	0.95 ±0.2	1.72 ±1.73**	0.88 ±0.45	1.82 ±1.89*	2.49 ±0.87*	0	1.61 ±1.76*
P1: seeds treated with distilled water, P2: seeds treated with ARS (500 ppm), P3: Seeds treated with end products of ARS degradation (500 ppm), ( $P$ = alpha value, * $P < 0.05$ , ** $P < 0.01$ ), Values of the shoot and root length were mean of three experiments (Standard error of the mean, $\pm$ ).												

From the ANOVA, seeds of *Cicer arietinum*, *Pisum sativum*, and *Vigna radiata* treated with distilled water, and with end products of ARS emerged significance at the 0.05 and 0.01 probability level. The maximum value of germination percentage was recorded in P3-C (50%), P1-C (40%), P3-V (36.6%), and P1-V (36.6). Results suggested that the end products of ARS after degradation showed a good germination rate and, significant root and shoot growth for all four plants as compared to ARS. This study validates the less toxic nature of end products ARS as compared to the ARS effluents.

### 3.3.10 Energy consumption and cost analysis

#### (a) Electrical energy determination

The electrical energy consumed in running the experiments is one of the major factors to determine the total operating cost involved in the photocatalytic degradation process. Therefore, measuring the electric energy per order ( $E_{EO}$ ) for ARS degradation can be a useful and informative way to calculate the expenses during the reaction and it can be calculated as [46]:

$$E_{EO} = \frac{P \times t \times 1000}{V \times 60 \times \log\left(\frac{C_i}{C_e}\right)} \quad (3.14)$$

where  $P$  = Input power (kW),  $V$  = Volume of pollutant solution (L),  $C_i$  = Initial pollutant concentration,  $C_e$  = Final pollutant concentration,  $t$  = Irradiation time (minute).

By combining the Langmuir-Hinshelwood pseudo-first-order rate equation 3.5 with equation 2.15, the  $E_{EO}$  for a pseudo-first-order reaction can be written as [47]:

$$E_{EO} = \frac{38.4 \times P}{V \times K_{app}} \quad (3.15)$$

where  $K_{app}$  = pseudo-first-order rate constant ( $\text{min}^{-1}$ ). The above equation 3.15 was used to calculate the model of electric energy per order for the pseudo-first-order batch reactor.

In Table 3.3 the calculated  $E_{EO}$  (experimental) and  $E_{EO}$  (model) values for ARS degradation were represented and it can be seen that the electrical energy consumption was more for higher ARS concentration which could be due to the absorption of ultra-violet light at higher concentrations [48]. This increase in electrical energy consumption is also associated with the fact that the degradation rate will be low when the ARS concentration is high in wastewater. In addition, the experimental  $E_{EO}$  value accurately coincides with the kinetic model  $E_{EO}$  value which confirms that the photocatalytic degradation of ARS follows pseudo-first-order rate kinetics.

Experimental conditions			Apparent rate Constant ( $K_{app}$ ) ( $\text{min}^{-1}$ )	$R^2$	$E_{EO}$ experimental ( $\text{kWh m}^{-3}\text{order}^{-1}$ )	$E_{EO}$ model ( $\text{kWh m}^{-3}\text{order}^{-1}$ )
Initial Conc. (ppm)	$\text{TiO}_2\text{-NP/PAC}$ Conc. ( $\text{g L}^{-1}$ )	pH				
20	0.05	2	0.0237	0.99	2607.02	6475.54
60	0.05	2	0.0229	0.98	5791.94	6701.57
100	0.05	2	0.0219	0.95	8858.47	6988.17

### (b) Total Operating Cost

The total operating cost involved in running an experiment is an important aspect of choosing a wastewater treatment method. In the photocatalytic degradation process, the operating cost involved mainly depends on the design of the photocatalytic device, the concentration of pollutants, and the nanocomposite amount [49]. The total operating cost and energy consumed in the ARS degradation were calculated using the following equations [48]:

$$\text{Total operating cost} = \frac{\text{Energy consumed per mg of ARS degradation (kWh)} \times \text{unit cost} \left( \frac{\text{INR}}{\text{kWh}} \right) \times 10^6}{\text{ARS degradation (mg)}} \quad (3.16)$$

$$\text{Energy consumed per mg of ARS degradation} = \frac{\text{Poer input(kW)} \times \text{Reaction time (min)}}{1000 \times 60} \quad (3.17)$$

The results obtained were represented in Table 3.4 and it can be noticed that a total of 672.72, 240.24, and 156.86 INR (Indian rupee) were utilized for 20 ppm, 60 ppm, and 100 ppm ARS degradation using 0.05 g of  $\text{TiO}_2\text{-NP/PAC}$  nanocomposite. Furthermore, the operating cost

value decreases from 672.72 to 156.86 INR, with an increase in the initial ARS concentration [46].

**Table 3.4** Cost analysis of ARS degradation in the photocatalytic reactor under different operating conditions

ARS Conc. (ppm) $C_1$	TiO <sub>2</sub> -NP/PAC Conc. (g L <sup>-1</sup> ) $C_2$	ARS degradation Efficiency (%) $C_4$	ARS degradation (mg) $C_5 = [(C_1 \times C_4/100) \times \text{working volume}]$	Reaction time (minute) $C_6$	Energy consumed per mg of ARS degradation (kWh) $C_7 = [(P \times C_6)/(1000 \times 60)]$	Total operating cost (INR/kg of ARS degradation) $C_8 = [(C_7 \times \text{unit cost} \times 10^6)/C_5]$
20	0.05	99.10	2.97	80	0.0008	672.72
60	0.05	92.50	8.32	80	0.0008	240.24
100	0.05	85.00	12.75	80	0.0008	156.86

(a) Total energy consumed (P) 0.6 kW [includes energy for electronic magnetic stirrer (50W), water pump (50W), exhaust fan (50W) and Visible lamp (450 W)] (b) Working volume of reactor 0.15 L and (d) Unit cost of power 2.5 INR (kWh)<sup>-1</sup>.

### 3.3.11 Results of computational studies

Computational studies had been employed to get an insight into the mechanism of formation and reactivity of the prepared nanocomposite. For the current work, four fused benzene ring structures were considered for PAC and TiO<sub>2</sub>-NP/PAC nanocomposite. PAC was linked with the nano TiO<sub>2</sub> through weak hydrocarbon bonding *via* O-linkage of the O-Ti-O bond. Figure 3.23 shows the optimized molecular structures of PAC, TiO<sub>2</sub>, ARS, TiO<sub>2</sub>-NP/PAC, TiO<sub>2</sub>-ARS, and TiO<sub>2</sub>-NP/PAC-ARS respectively along with their highest occupied molecular orbital (HOMO) and lowest unoccupied molecular orbital (LUMO) structures. HOMO and LUMO perform a significant role in the chemical reaction [20]. In a chemical reaction, HOMO has the character of an electron donor with a relaxing effect on its electron, and LUMO has the property of accepting electrons with a strong affinity for electrons [50].



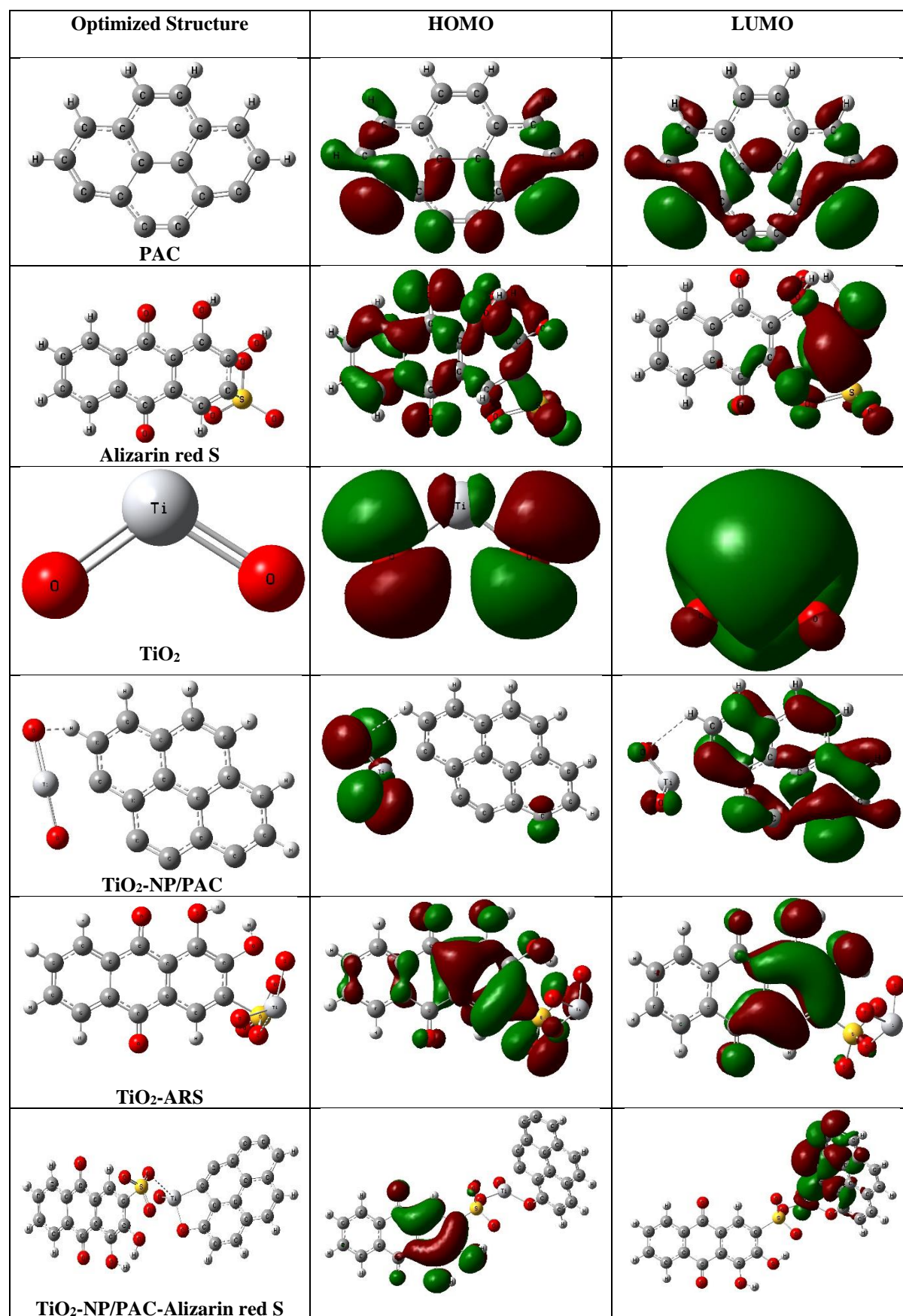


**Figure 3.23** HOMO and LUMO molecular orbital of PAC, TiO<sub>2</sub>, ARS, TiO<sub>2</sub>-NP/PAC, and interaction of TiO<sub>2</sub>, and TiO<sub>2</sub>-NP/PAC with ARS



Table 3.5 summarizes different molecular properties such as dipole moment, ionization potentials, and HOMO-LUMO bandgap energies of  $\text{TiO}_2$ , and  $\text{TiO}_2$ -NP/PAC nanocomposite. From Table 3.5, it is seen that by binding  $\text{TiO}_2$  with the PAC the dipole moment changes from 9.2448 to 25.194 debye and bandgap energy from 0.24332 to 0.02501 eV. These changes indicate that the resultant nanocomposite material is highly reactive which favors catalytic degradation.

<b>Table 3.5</b> Calculated molecular properties of PAC and $\text{TiO}_2$ -NP/PAC nanocomposite								
Molecule	Dipole moment				Ionisation Potential (eV)	Frontier orbital & Energy gap		
	x	y	z	Total dipole moment (Debye)		HOMO (eV)	LUMO (eV)	Energy gap (eV)
$\text{TiO}_2$	0	0	9.244	9.244	0.419	-0.419	-0.176	0.243
$\text{TiO}_2$ -NP/PAC	24.406	0.425	-5.968	25.194	0.207	-0.207	-0.182	0.025

Table 3.6 represents the different molecular properties of  $\text{TiO}_2$  and  $\text{TiO}_2$ -NP/PAC nanocomposite. From the table, it can be seen that the chemical hardness ( $\eta$ ) of  $\text{TiO}_2$ -NP/PAC was found to be lower than the  $\text{TiO}_2$  which signifies that the reactivity of  $\text{TiO}_2$ -NP/PAC was more than  $\text{TiO}_2$  [24]. The higher reactivity of  $\text{TiO}_2$ -NP/PAC indicates that the ability of binding PAC to the  $\text{TiO}_2$  was favorable. The chemical softness ( $S$ ) of  $\text{TiO}_2$  was found to be 4.109 eV while that of the nanocomposite  $\text{TiO}_2$ -NP/PAC was 39.98 eV, indicating that the nanocomposite  $\text{TiO}_2$ -NP/PAC was more reactive than PAC since soft molecules tend to react more than the hard molecule.

<b>Table 3.6</b> Molecular chemical descriptors of PAC and $\text{TiO}_2$ -NP/PAC nanocomposite							
Molecule	$\eta$ (eV)	$S$ (eV)	$\mu$ (eV)	$\omega$ (eV)	$N$ (eV)	$\omega^+$ (eV)	$\omega^-$ (eV)
$\text{TiO}_2$	0.121	4.109	-0.297	0.364	18.939	0.230	0.528
$\text{TiO}_2$ -NP/PAC	0.012	39.984	-0.194	1.518	6.183	1.422	1.617

The electrophilicity index of  $\text{TiO}_2$  shows value 0.364 i.e.  $0.8 < \omega < 1.5$  eV which implies that it is a marginal electrophile [28] while for the  $\text{TiO}_2$ -NP/PAC electrophilicity index value was 1.51 i.e.  $\omega > 1.5$  eV which indicates that the nanocomposite is a strong electrophile. Hence,  $\text{TiO}_2$ -NP/PAC is much more reactive than  $\text{TiO}_2$  alone. It can be seen that if a molecule has  $N > 3$  eV it is a strong nucleophile,  $2 < N < 3$  eV a moderate nucleophile and  $N < 2$  eV marginal nucleophile. Hence from the table,  $\text{TiO}_2$  is found to be a stronger nucleophile than the

nanocomposite since it has larger electron-donating groups than the nanocomposite material [30].

The increase in electron-accepting power of  $\text{TiO}_2\text{-NP/PAC}$  ( $\omega^+ = 1.42$ ) than the  $\text{TiO}_2$  alone ( $\omega^+ = 0.23$ ) suggests that the nanocomposite has the lowest electron-donating ability. The electron-accepting ability of the molecules decreases in the order:  $\text{TiO}_2\text{-NP/PAC} > \text{TiO}_2$  and the electron-donating ability of the molecule in the order:  $\text{TiO}_2 > \text{TiO}_2\text{-NP/PAC}$ . The chemical potential value of nanocomposite is more than the  $\text{TiO}_2$  which indicates that the escaping tendency of electrons is more in the case of the nanocomposite material. Thus, from this computational study, it can be seen that the binding  $\text{TiO}_2$  with PAC increases its reactivity which thereby enhances its efficiency for ARS degradation. Such theoretical studies not only provide a theoretical understanding of the reactivity of the materials but also help in the selection of highly efficient materials for pollutant degradation.

### 3.3.11.1 Adsorption of ARS onto $\text{TiO}_2$ and $\text{TiO}_2\text{-NP/PAC}$ nanocomposite

To understand the theoretical basis of ARS adsorption on the  $\text{TiO}_2$  and  $\text{TiO}_2\text{-NP/PAC}$ , Density Functional Theory (DFT) was used (Figure 3.23). The interaction of ARS on  $\text{TiO}_2$  took place *via* O atom of ARS sulfonate group and Ti atom of  $\text{TiO}_2$  ( $\text{O}_2\text{SO} \cdots \text{O}_2\text{Ti}$  interaction) and for  $\text{TiO}_2\text{-NP/PAC}$  *via* O atom of sulfonate group of ARS and Ti atom of  $\text{TiO}_2\text{-NP/PAC}$  ( $\text{O}_2\text{SO} \cdots \text{TiO}_2\text{-NP/PAC}$  interaction).

From Figure 3.23, we can see that in the ARS adsorption on the  $\text{TiO}_2\text{-NP/PAC}$  nanocomposite, the amplitude of HOMO is spread over the ARS whereas LUMO is delocalized away from the ARS and spread over the  $\text{TiO}_2\text{-NP/PAC}$ . This indicates that the charge transfer taking place from HOMO to LUMO and  $\text{TiO}_2\text{-NP/PAC}$  has positive activation of ARS.

**Table 3.7** Adsorption energy and bond length of  $\text{TiO}_2\text{-ARS}$  and  $\text{TiO}_2\text{-NP/PAC-ARS}$  system

System	Adsorption energy ( $\text{kJmol}^{-1}$ )	Bond length ( $\text{\AA}$ )
$\text{TiO}_2\text{-ARS}$	-155.41	1.94
$\text{TiO}_2\text{-NP/PAC-ARS}$	-181.49	1.92

The adsorption energies and bond distance obtained for the ARS adsorption are listed in Table 3.7. The adsorption energies of  $\text{TiO}_2\text{-NP/PAC-ARS}$  and  $\text{TiO}_2\text{-ARS}$  interactions were found to be -155.41 and -181.49  $\text{kJmol}^{-1}$  respectively. The bond length of  $\text{TiO}_2\text{-ARS}$  and  $\text{TiO}_2\text{-NP/PAC-ARS}$  corresponded to 1.94 and 1.92  $\text{\AA}$ . The shorter bond length and the higher negative adsorption energy value of the  $\text{TiO}_2\text{-NP/PAC-ARS}$  system implies that the adsorptive interaction between  $\text{TiO}_2\text{-NP/PAC}$  and ARS is more favorable than  $\text{TiO}_2\text{-ARS}$  interaction.

### 3.3.12 Comparison with other composites

The efficiency of the TiO<sub>2</sub>-NP/PAC nanocomposite obtained in the present work for the degradation of ARS dye was compared with other composites which have been reported in the literature (Table 3.8). The amount of composite taken, contact time, and the degradation capacity of the nanocomposite is used as a parameter for comparison. The TiO<sub>2</sub>-NP/PAC nanocomposite shows very effective degradation efficiency of dye in contrast with other reported literature and hence may be considered as an efficient alternative for wastewater treatment.

<b>Table 3.8</b> Comparison of catalytic activity of other work in the literature with TiO <sub>2</sub> /pine cone activated carbon nanocomposite							
<b>Composite</b>	<b>Pollutant</b>	<b>Mass (g)</b>	<b>Volume (ml)</b>	<b>C<sub>i</sub></b>	<b>Time (minute)</b>	<b>% degradation</b>	<b>Source</b>
TiO <sub>2</sub> /commercial AC	Methylene blue	0.40	500	20 ppm	180	49.80	[51]
TiO <sub>2</sub> /Grape marc AC	RB-5 Azo dye	2.00	-	20 µmol L <sup>-1</sup>	60	98.93	[26]
TiO <sub>2</sub> /commercial AC	Acid Red 131 dye	0.05	100	25 ppm	200	99.00	[52]
TiO <sub>2</sub> /bituminous coal AC	Rhodamine B	0.02	400	2 x 10 <sup>-5</sup> mol L <sup>-1</sup>	120	93.20	[53]
TiO <sub>2</sub> /commercial AC	Indigo carmine	0.03	50	5 x 10 <sup>-5</sup> M	240	90.00	[54]
TiO <sub>2</sub> /coconut shell AC	Rhodamine B	0.07	50	30 ppm	20	96.00	[55]
TiO <sub>2</sub> /coconut shell AC	Methylene blue	0.10	100	50 ppm	100	99.00	[56]
TiO <sub>2</sub> /commercial AC	Azo dye	0.50	100	0.1 g L <sup>-1</sup>	180	96.00	[57]
<b>TiO<sub>2</sub>/pine cone activated carbon</b>	<b>Alizarin red S</b>	<b>0.05</b>	<b>150</b>	<b>20 ppm</b>	<b>80</b>	<b>99.10</b>	<b>Present study</b>

### 3.4 Conclusion

TiO<sub>2</sub> photocatalyst was successfully immobilized on PAC using the hydrothermal method in order to develop new composite material. From the physicochemical characterization data of the composite, it was found that TiO<sub>2</sub> nanoparticles supported on PAC are in anatase form and mainly in the crystal size of 2.35 nm. The photocatalytic test performed with TiO<sub>2</sub>-NP/PAC nanocomposite showed that the presence of UV light significantly enhanced the ARS degradation achieving the complete degradation of 20 ppm ARS after 80 minutes of light exposure with 0.05 g optimum dose. Additionally, it was found that photocatalytic degradation of the dye follows Langmuir-Hinshelwood pseudo-first-order rate kinetics with an apparent rate

constant of  $0.02372 \text{ min}^{-1}$  and a half-life time of 29.30 minutes. The negative enthalpy and free energy indicate an exothermic and spontaneous process. The presence of interfering ions such as glycine, copper sulphate, cadmium nitrate, and zinc chloride mostly affect the degradation of ARS by  $\text{TiO}_2\text{-NP/PAC}$ , indicating that hydroxyl radicals are the dominant reactive species in the ARS degradation process. The reusability study suggests that the successful rejuvenation of  $\text{TiO}_2\text{-NP/PAC}$  nanocomposite even after fifth cycles of usages and also no structural changes were found in the FT-IR spectra of the fresh nanocomposite and reused nanocomposite, signifying remarkable photostability of the nanocomposite. The GC-MS analysis showed the formation of low molecular weight less harmful and green products such as cyclo 3,5-hexadiene 1,2-dienone, carbon dioxide, and water by the attack of hydroxyl radical on highly carcinogenic ARS. The percentage of seed germination and the length of roots and shoots of *Cicer arietinum*, *Solanum lycopersicum*, *Pisum sativum*, and *Vigna radiate* plants were used as indicators for the toxicity study. The phytotoxicity of the ARS photo-degraded products showed a considerable growth of roots and shoots and also excellent germination percentage of the four plants compared to the ARS, which suggests that the toxicity of the ARS photo-degraded products is considerably reduced compared to ARS. The cost analysis was performed by computing the electrical energy per order (experimental and model) and total operating costs associated, and it was found that 672.72, 240.24, and 156.86 INR were utilized for 20 ppm, 60 ppm, and 100 ppm of ARS degradation. The DFT results confirmed that the binding  $\text{TiO}_2$  with PAC increases the chemical reactivity of the  $\text{TiO}_2\text{-NP/PAC}$  nanocomposite as compared to  $\text{TiO}_2$  nanoparticles and also indicated favorable adsorption of the ARS in the  $\text{TiO}_2\text{-NP/PAC}$  nanocomposite than adsorption of ARS in the  $\text{TiO}_2$ . Thus, the  $\text{TiO}_2\text{-NP/PAC}$  nanocomposite has a very good activity to use as an effective and promising photocatalyst for dye degradation to innocuous components in future environmental wastewater applications.

### References

- [1] K. Vijayaraghavan, T.T. Teo, R. Balasubramanian, U.M. Joshi, Application of Sargassum biomass to remove heavy metal ions from synthetic multi-metal solutions and urban storm water runoff, *J. Hazard. Mater.* 164 (2009) 1019–1023. doi:10.1016/j.jhazmat.2008.08.105.
- [2] P. Zucca, C. Vinci, F. Sollai, A. Rescigno, E. Sanjust, Degradation of Alizarin Red S under mild experimental conditions by immobilized 5,10,15,20-tetrakis(4-sulfonatophenyl)porphine-Mn (III) as a biomimetic peroxidase-like catalyst, *J. Mol. Catal. A Chem.* 288 (2008) 97–102. doi:10.1016/j.molcata.2008.04.001.
- [3] R. Ahmad, A. Mirza, Green synthesis of Xanthan gum/Methionine-bentonite nanocomposite for sequestering toxic anionic dye, *Surf. Interfaces.* 2 (2013) 65–72. doi:10.1016/B978-0-08-096984-8.00029-X.
- [4] P. C. Vandevivere, R. Bianchi, W. Verstraete, Treatment and reuse of wastewater from the textile wet-processing industry: Review of emerging technologies, *J. Chem. Technol. Biotechnol.* 72 (1998) 289–302. doi:10.1002/CHIN.199843337.
- [5] M. Petrovic, J. Radjenovic, D. Barcelo, Advanced oxidation processes (AOPs) applied for wastewater and drinking water treatment. Elimination of pharmaceuticals, *Holist. Approach to Environ.* 1 (2011) 63–74. doi:10.33765/thate.
- [6] N.N. Bahrudin, M.A. Nawawi, Immobilized titanium dioxide/powdered activated carbon system for the photocatalytic adsorptive removal of phenol, *Korean J. Chem. Eng.* 35 (2018) 1532–1541. doi:10.1007/s11814-018-0062-4.
- [7] M. Ouzzine, A. J. Romero-Anaya, M. A. Lillo-Ródenas, A. Linares-Solano, Spherical activated carbon as an enhanced support for TiO<sub>2</sub>/AC photocatalysts, *Carbon N. Y.* 67 (2014) 104–118. doi:10.1016/j.carbon.2013.09.069.
- [8] W. Zhou, P. Zhang, W. Liu, Anatase TiO<sub>2</sub> nanospindle/activated carbon (AC) composite photocatalysts with enhanced activity in removal of organic contaminant, *Int. J. Photoenergy.* 2012 (2012) 28–30. doi:10.1155/2012/325902.
- [9] C. Anyika, N. Asilayana Mohd Asri, Z. Abdul Majid, A. Yahya, J. Jaafar, Synthesis and characterization of magnetic activated carbon developed from palm kernel shells, *Nanotechnol. Environ. Eng.* 2 (2017) 1–25. doi:10.1007/s41204-017-0027-6.
- [10] J. Matos, J. Laine, J. Marie Herrmann, Effect of the type of activated carbons on the photocatalytic degradation of aqueous organic pollutants by UV-irradiated titania, *J. Catal.* 200 (2001) 10–20. doi:10.1006/jcat.2001.3191.
- [11] G. Q. Blantocas, A. S. Alaboodi, A.-B. H. Mekky, Synthesis of Chitosan-TiO<sub>2</sub> Antimicrobial Composites via a 2-Step Process of Electrospinning and Plasma Sputtering, *Arab. J. Sci. Eng.* 43 (2018) 389–398. doi:10.1007/s13369-017-2695-8.
- [12] T. Nayara Vieira de Souza, S. Maria Leão de Carvalho, M. Gurgel Adeodato Vieira, M. Gurgel Carlos da Silva, D. do Socorro Barros Brasil, Adsorption of basic dyes onto activated carbon: Experimental and theoretical investigation of chemical reactivity of

- basic dyes using DFT-based descriptors, Appl. Surf. Sci. 448 (2018) 662–670. doi:10.1016/j.apsusc.2018.04.087.
- [13] H. Ullah, A. Ali Tahir, T. K Mallick, Polypyrrole/TiO<sub>2</sub> composites for the application of photocatalysis, Sensors Actuators B Chem. 241 (2016) 1161–1169. doi:10.1016/j.snb.2016.10.019.
- [14] P.C. Bhomick, A. Supong, M. Baruah, C. Pongener, Pine Cone biomass as an effecient precursor for the synthesis of activated biocarbon for adsorption of anionic dye from aqueous solution : Isotherm, kinetic, thermodynamic and regeneration studies, Sustain. Chem. Pharm. 10 (2018) 41–49. doi:10.1016/j.scp.2018.09.001.
- [15] W. Li, T. Zeng, Preparation of TiO<sub>2</sub> anatase nanocrystals by TiCl<sub>4</sub> hydrolysis with additive H<sub>2</sub>SO<sub>4</sub>, PLoS One. 6 (2011) 2–7. doi:10.1371/journal.pone.0021082.
- [16] M. Asiltürk, Ş. Şener, TiO<sub>2</sub>-activated carbon photocatalysts: Preparation, characterization and photocatalytic activities, Chem. Eng. J. 180 (2012) 354–363. doi:10.1016/j.cej.2011.11.045.
- [17] D. Baena-Baldiris, A. Montes-Robledo, R. Baldiris-Avila, *Franconibacter sp.*, IMS: A New Strain in Decolorization and Degradation of Azo Dyes Ponceau S Red and Methyl Orange, ACS Omega. 5 (2020) 28146–28157. doi:10.1021/acsomega.0c03786.
- [18] S. Chattaraj, J. Johnson, D. Madamwar, Biotransformation of mixture of dyes by enriched bacterial consortium ASD, Desalin. Water Treat. 57 (2015) 21585–21597. doi:10.1080/19443994.2015.1124345.
- [19] A. Birara, M. Muthuswamy, M. Andargie, Effect of chemical mutation by sodium azide on quantitaive traits variations in *Sesamum indicum L.*, Asian J. Biol. Sci. 6 (2013) 356–362. doi:10.3923/ajbs.2013.356.362.
- [20] N. Sharotri, D. Sharma, D. Sud, Experimental and theoretical investigations of Mn-N-co-doped TiO<sub>2</sub> photocatalyst for visible light, J. Mater. Res. Technol. 8 (2019) 3995–4009. doi:10.1016/j.jmrt.2019.07.008.
- [21] S. Li, K. Han, J. Li, M. Li, C. Lu, Preparation and characterization of super activated carbon produced from gulfweed by KOH activation, Microporous Mesoporous Mater. 243 (2017) 291–300. doi:10.1016/j.micromeso.2017.02.052.
- [22] P. Singh, M. C. Vishnu, K. Kumar Sharma, A. Borthakur, P. Srivastava, D. B Pal, D. Tiwary, P. Kumar Mishra, Photocatalytic degradation of Acid Red dye stuff in the presence of activated carbon-TiO<sub>2</sub> composite and its kinetic enumeration, J. Water Process Eng. 12 (2016) 20–31. doi:10.1016/j.jwpe.2016.04.007.
- [23] N. Ramesh Reddy, U. Bharagav, M. Mamatha Kumari, K. K. Cheralathan, P. K. Ojha, M. V. Shankar, S. Woo Joo, Inclusion of low cost activated carbon for improving hydrogen production performance of TiO<sub>2</sub> nanoparticles under natural solar light irradiation, Ceram. Int. 47 (2021) 10216–10225. doi:10.1016/j.ceramint.2020.10.187.
- [24] J. Shi, G. Chen, G. Zeng, A. Chen, K. He, Z. Huang, L. Hu, J. Zeng, J. Wu, W. Liu, Hydrothermal synthesis of graphene wrapped Fe-doped TiO<sub>2</sub> nanospheres with high

- photocatalysis performance, *Ceram. Int.* 44 (2018) 7473–7480. doi:10.1016/j.ceramint.2018.01.124.
- [25] C. Bathula, I. Rabani, S. Sekar, H.-K. Youi, J.-Y. Choy, A. Kadam, N.K. Shretha, Y.-S. Seo, H.-S. Kim, Enhanced removal of organic dye by activated carbon decorated TiO<sub>2</sub> nanoparticles from *Mentha Aquatica* leaves via ultrasonic approach, *Ceram. Int.* 47 (2021) 8732–8739. doi:10.1016/j.ceramint.2020.12.282.
- [26] H. Belayachi, B. Bestani, N. Benderdouche, M. Belhakem, The use of TiO<sub>2</sub> immobilized into grape marc-based activated carbon for RB-5 Azo dye photocatalytic degradation, *Arab. J. Chem.* 12 (2015) 3018–3027. doi:10.1016/j.arabjc.2015.06.040.
- [27] P.R. Chowdhury, K.G. Bhattacharyya, Synthesis and characterization of Mn/Co/Ti LDH and its utilization as a photocatalyst in visible light assisted degradation of aqueous Rhodamine B, *RSC Adv.* 6 (2016) 112016–112034. doi:10.1039/c6ra24288j.
- [28] A. Omo Ibhaddon, P. Fitzpatrick, Heterogeneous Photocatalysis: Recent Advances and Applications, *Catalysts.* 3 (2013) 189–218. doi:10.3390/catal3010189.
- [29] Y. Zhao, B. Li, Q. Wang, W. Gao, C.J. Wang, M. Wei, D.G. Evans, X. Duan, D. O'Hare, NiTi-Layered double hydroxides nanosheets as efficient photocatalysts for oxygen evolution from water using visible light, *Chem. Sci.* 5 (2014) 951–958. doi:10.1039/c3sc52546e.
- [30] L. Mohapatra, K. Parida, A review on the recent progress, challenges and perspective of layered double hydroxides as promising photocatalysts, *J. Mater. Chem. A.* 4 (2016) 10744–10766. doi:10.1039/c6ta01668e.
- [31] N. Zhang, M. -Quan Yang, S. Liu, Y. Sun, Y. -Jun Xu, Waltzing with the Versatile Platform of Graphene to Synthesize Composite Photocatalysts, *Chem. Rev.* 115 (2015) 10307–10377. doi:10.1021/acs.chemrev.5b00267.
- [32] Z. Noorimotlagh, I. Kazeminezhad, N. Jaafarzadeh, M. Ahmadi, Z. Ramezani, S.S. Martinez, The visible-light photodegradation of Nonylphenol in the presence of carbon-doped TiO<sub>2</sub> with Rutile/Anatase ratio coated on GAC: Effect of parameters and degradation mechanism, *J. Hazard. Mater.* 350 (2018) 108–120. doi:10.1016/j.jhazmat.2018.02.022.
- [33] N. Modirshahla, M.A. Behnajady, Photooxidative degradation of Malachite Green ( MG ) by UV/H<sub>2</sub>O<sub>2</sub>: Influence of operational parameters and kinetic modeling, *Dye. Pigment.* 70 (2006) 54–59. doi:10.1016/j.dyepig.2005.04.012.
- [34] P. Zheng, Z. Pan, H. Li, B. Bai, W. Guan, Effect of different type of scavengers on the photocatalytic removal of copper and cyanide in the presence of TiO<sub>2</sub>@yeast hybrids, *J. Mater. Sci. Mater. Electron.* 26 (2015) 6399–6410. doi:10.1007/s10854-015-3229-3.
- [35] H. C Yatmaz, A. Akyol, M. Bayramoglu, Kinetics of the Photocatalytic Decolorization of an Azo Reactive Dye in Aqueous ZnO Suspensions, *Ind. Eng. Chem. Res.* 43 (2004) 6035–6039. doi:10.1021/ie049921z.
- [36] R. Ahmad, Studies on adsorption of crystal violet dye from aqueous solution onto



- coniferous pinus bark powder (CPBP), J. Hazard. Mater. 171 (2009) 767–773. doi:10.1016/j.jhazmat.2009.06.060.
- [37] S. Xu, D. Delai Sun, Significant improvement of photocatalytic hydrogen generation rate over TiO<sub>2</sub> with deposited CuO, Int. J. Hydrogen Energy. 34 (2009) 6096–6104. doi:10.1016/j.ijhydene.2009.05.119.
- [38] S. Jothivel, R. Velmurugan, K. Selvam, B. Krishnakumar, M. Swaminathan, Preparation, characterization and photocatalytic activity of acidic sulfated nano titania for the degradation of Reactive Orange 4 under UV light, Sep. Purif. Technol. 77 (2011) 245–250. doi:10.1016/j.seppur.2010.12.014.
- [39] N. Zhang, G. Liu, H. Liu, Y. Wang, Z. He, G. Wang, Diclofenac photodegradation under simulated sunlight: Effect of different forms of nitrogen and Kinetics, J. Hazard. Mater. 192 (2011) 411–418. doi:10.1016/j.jhazmat.2011.05.038.
- [40] Gunture, A. Singh, A. Bhati, P. Khare, K. Malika Tripathi, S. Kumar Sankar, Soluble Graphene Nanosheets for the Sunlight-Induced Photodegradation of the Mixture of Dyes and its Environmental Assessment, Sci. Rep. 9 (2019) 1–12. doi:10.1038/s41598-019-38717-1.
- [41] J. A. Anderson, Simultaneous photocatalytic degradation of nitrate and oxalic acid over gold promoted titania, Catal. Today. 181 (2012) 171–176. doi:10.1016/j.cattod.2011.05.027.
- [42] Y. Rao, Y. Zhang, A. Li, T. Zhang, T. Jiao, Photocatalytic activity of G-TiO<sub>2</sub>@Fe<sub>3</sub>O<sub>4</sub> with persulfate for degradation of alizarin red S under visible light, Chemosphere. 266 (2021) 1–9. doi:10.1016/j.chemosphere.2020.129236.
- [43] L.G. Devi, C. Munikrishnappa, B. Nagaraj, K.E. Rajashekhar, Effect of chloride and sulfate ions on the advanced photo Fenton and modified photo Fenton degradation process of Alizarin Red S, J. Mol. Catal. A. Chem. 374 (2013) 125–131. doi:10.1016/j.molcata.2013.03.023.
- [44] G. K. Parshetti, S. G. Parshetti, A. A. Telke, D. C. Kalyani, R. A. Doong, S. P. Govindwar, Biodegradation of Crystal Violet by Agrobacterium radiobacter, J. Environ. Sci. 23 (2011) 1384–1393. doi:10.1016/S1001-0742(10)60547-5.
- [45] D.C. Kalyani, P.S. Patil, J.P. Jadhav, S.P. Govindwar, Biodegradation of reactive textile dye Red BLI by an isolated bacterium *Pseudomonas* sp. SUK1, Bioresour. Technol. 99 (2008) 4635–4641. doi:10.1016/j.biortech.2007.06.058.
- [46] N. Daneshvar, A. Aleboyeh, A. R Khataee, The evaluation of electrical energy per order (E<sub>EO</sub>) for photooxidative decolorization of four textile dye solutions by the kinetic model, Chemosphere. 59 (2005) 761–767. doi:10.1016/j.chemosphere.2004.11.012.
- [47] S. R. Cater, M. I. Stefan, J. R. Bolton, A. Safarzadeh-Amiri, UV/H<sub>2</sub>O<sub>2</sub> Treatment of Methyl *tert*-Butyl Ether in Contaminated Waters, Environ. Sci. Technol. 34 (2000) 659–662. doi:10.1021/es9905750.
- [48] M. A Vishnuganth, N. Remya, M. Kumar, N. Selvaraju, Photocatalytic degradation of

- carbofuran by TiO<sub>2</sub>-coated activated carbon: Model for kinetic, electrical energy per order and economic analysis, *J. Environ. Manage.* 181 (2016) 201–207. doi:10.1016/j.jenvman.2016.06.016.
- [49] R. C. Asha, M. A. Vishnuganth, N. Remya, N. Selvaraju, M. Kumar, Livestock Wastewater Treatment in Batch and Continuous Photocatalytic Systems: Performance and Economic Analyses, *Water Air Soil Pollut.* 226 (2015) 1–13. doi:10.1007/s11270-015-2396-4.
- [50] Q. Chen, W. Zhu, X. Hou, K. Xu, Density functional theory study of the adsorption of acetone on the pure and transition metal doped (TiO<sub>2</sub>)<sub>38</sub> clusters, *Vacuum.* 119 (2015) 123–130. doi:10.1016/j.vacuum.2015.05.003.
- [51] H. Atout, A. Bouguettoucha, D. Chebli, J.M. Gatica, H. Vidal, M.P. Yeste, A. Amrane, Integration of Adsorption and Photocatalytic Degradation of Methylene Blue Using TiO<sub>2</sub> Supported on Granular Activated Carbon, *Arab. J. Sci. Eng.* 42 (2017) 1475–1486. doi:10.1007/s13369-016-2369-y.
- [52] P. Singh, M.C. Vishnu, K.K. Sharma, A. Borthakur, P. Srivastava, D.B. Pal, D. Tiwary, P.K. Mishra, Photocatalytic degradation of Acid Red dye stuff in the presence of activated carbon-TiO<sub>2</sub> composite and its kinetic enumeration, *J. Water Process Eng.* 12 (2016) 20–31. doi:10.1016/j.jwpe.2016.04.007.
- [53] B. Xing, C. Shi, C. Zhang, G. Yi, L. Chen, H. Guo, G. Huang, J. Cao, Preparation of TiO<sub>2</sub>/Activated Carbon Composites for Photocatalytic Degradation of RhB under UV Light Irradiation, *J. Nanomater.* 2016 (2016) 1–10. doi:10.1155/2016/8393648.
- [54] A. K Subramani, K. Byrappa, S. Ananda, K. M Lokanatha Rai, C. Ranganathaiah, M. Yoshimura, Photocatalytic degradation of indigo carmine dye using TiO<sub>2</sub> impregnated activated carbon, *Bull. Mater. Sci.* 30 (2007) 37–41. doi:10.1007/s12034-007-0007-8.
- [55] H. Zhong, Y. Shaogui, J. Yongming, S. Cheng, Microwave photocatalytic degradation of Rhodamine B using TiO<sub>2</sub> supported on activated carbon: Mechanism implication, *J. Environ. Sci.* 21 (2009) 268–272. doi:10.1016/S1001-0742(08)62262-7.
- [56] H. Anh Le, L. Thuy Linh, S. Chin, J. Jurng, Photocatalytic degradation of methylene blue by a combination of TiO<sub>2</sub>-anatase and coconut shell activated carbon, *Powder Technol.* 225 (2012) 167–175. doi:10.1016/j.powtec.2012.04.004.
- [57] C. Andriantsiferana, E.F. Mohamed, H. Delmas, Photocatalytic degradation of an azo-dye on TiO<sub>2</sub>/activated carbon composite material, *Environ. Technol. (United Kingdom).* 35 (2014) 355–363. doi:10.1080/09593330.2013.828094.

## CHAPTER 4

### PHOTOCATALYTIC DEGRADATION OF CONGO RED DYE USING Fe-DOPED TiO<sub>2</sub>/ACTIVATED CARBON NANOCOMPOSITE AND ITS ANTIMICROBIAL ACTIVITY TOWARDS *E. coli* AND *S. aureus*<sup>1</sup>

---

This chapter deals with the preparation of Fe-doped titanium dioxide nanocomposite supported on activated carbon. The nanocomposite was synthesized by hydrothermal method and the physicochemical characterization of the nanocomposite was done by different analytical methods like SEM-EDX, XRD, FT-IR, XPS, photoluminescence (PL), pH<sub>ZPC</sub>, and UV-Visible diffuse reflectance spectroscopy (DRS). The photocatalyst was used for the degradation of an anionic dye, Congo red (CR) from an aqueous solution through the visible light irradiation. The degradation efficacy of the catalyst was studied by varying catalyst dosages, contact time, CR concentrations, and pH of the solution. The end products of degradation were analysed using GC-MS analysis. The effect of different interfering ions on photocatalytic degradation of CR and also the reusability of the nanocomposite were studied. The nanocomposite was also employed to inactivate pathogenic microbes such as *Escherichia coli* (*E. coli*) and *Staphylococcus aureus* (*S. aureus*) from water.

---

The text of this chapter has been published as:

<sup>1</sup>**M. Baruah, S. L. Ezung, A. Supong, P. C. Bhomick, S. Kumar, D. Sinha, Synthesis, characterization of novel Fe-doped TiO<sub>2</sub> activated carbon nanocomposite towards photocatalytic degradation of Congo red, *E. coli*, and *S. aureus*, Korean J. Chem. Eng., 38 (2021), 1277-1290. <https://doi.org/10.1007/s11814-021-0830-4>.**

### 4.1 Introduction<sup>1</sup>

The impact of nanotechnology has become increasingly evident in different areas of science and technology, including the field of environmental remediation and disinfection. Several environmentally beneficial technologies such as heterogeneous photocatalysis (HP) and solar disinfection (SODIS) using metal oxide semiconductor photocatalysts have been developed and applied extensively for air purification, wastewater treatment, and environmental regulations [1–3]. Among all the metal oxides used,  $\text{TiO}_2$  is the photocatalyst with most potential due to its chemical constancy, low cost, relatively benign nature, photochemical stability, and no further requirements of secondary disposal and expensive oxidizing chemicals. However, a high quantity recombination rate between electron and hole pairs limits the use of  $\text{TiO}_2$  in the visible region (400–750 nm), which accounts for 43% of solar light [4]. Therefore, to overcome this problem, it is desired to alter the band structure of the anatase  $\text{TiO}_2$  and in this regard, different methodologies like metal/non-metal elements doping, dye photosensitization, hydrogen treatment have been developed to enhance the  $\text{TiO}_2$  photoactivity in the visible light region [4]. Amongst different alternatives available, transition metal doping is a simple and efficient approach to widen the wavelength region of  $\text{TiO}_2$  to the visible light range [5]. The use of dopant in the metal oxide creates an intermediate level in the lattice which constrains the electron-hole pair from recombination, thereby leading to enhancement of the photocatalytic activity of  $\text{TiO}_2$  [6]. Among the different metal dopants,  $\text{Fe}^{3+}$  has garnered more attention due to its ionic radius of 0.64 Å which is identical to the ionic radius of  $\text{Ti}^{4+}$  (0.68 Å); therefore making it easier to incorporate  $\text{Fe}^{3+}$  into the crystal structure of  $\text{TiO}_2$ . Application of Fe-doped in  $\text{TiO}_2$  has been widely reported for the degradation of environmental pollutants [7–9],  $\text{NO}_x$  degradation [4],  $\text{CO}_2$  reduction [10], and water splitting for hydrogen production [11]. Literature reports have shown that the incorporation of  $\text{Fe}^{3+}$  ions in the  $\text{TiO}_2$  lattice reduces the electron-hole recombination rate, narrows the  $\text{TiO}_2$  bandgap, and thus increases the photocatalytic activity of  $\text{TiO}_2$ . However, powdered  $\text{TiO}_2$  has low exchange efficacy and is difficult to split after the photocatalytic reaction [7].

---

The text of this chapter has been published as:

<sup>1</sup>**M. Baruah, S. L. Ezung, A. Supong, P. C. Bhomick, S. Kumar, D. Sinha, Synthesis, characterization of novel Fe-doped  $\text{TiO}_2$  activated carbon nanocomposite towards photocatalytic degradation of Congo red, *E. coli*, and *S. aureus*, *Korean J. Chem. Eng.*, 38 (2021), 1277–1290. <https://doi.org/10.1007/s11814-021-0830-4>.**

Hence, to achieve quick and easy degradation of organic pollutants and also for simple management of the photocatalyst, it is desired that  $\text{TiO}_2$  is loaded onto an appropriate adsorbent. In this regard, different adsorbents such as zeolites, perlite, clay, silica, and activated carbon have been used as support systems for  $\text{TiO}_2$  [12].

Activated carbon with its good adsorption capacity is more appropriate as an adsorbent support system for the photocatalyst in any wastewater treatment process, as it can significantly gather pollutant molecules near the photocatalytic sites during the adsorption-degradation process. Additionally, the synergistic effect between activated carbon and  $\text{TiO}_2$  will separate the photo-induced electrons and electrons-holes, and inhibit their rapid recombination which extends the electron's life-time and a likelihood of increase in the photocatalytic efficiency.

Wide use of toxic dyes in fabric production can cause ecological degradation and human illness [13]. Dyes in wastewater are a major cause of water contamination and interfere with the oxygen transport system at the water-air interface [14]. Among the toxic dyes, congo red is the most commonly used dye in fabric production, and it consists of various benzidine groups, which are carcinogenic and mutagenic [15]. Therefore through this work, an effort has been made to remove this dye through photocatalytic degradation with Fe-doped  $\text{TiO}_2$  activated carbon nanocomposite.

The presence of pathogenic microbes such as *Escherichia coli* (*E. coli*) and *Staphylococcus aureus* (*S. aureus*) in ambient water is also a major concern throughout the world because they cause water-borne diseases. Different methods that have been employed to control microbes are pasteurization, ultra-high pressure/temperature treated sterilization, and, microwave sanitization [16]. However, most of the methodologies require heat treatment and thus have their limitations. Hence an alternative method using metal oxide nanoparticles has been studied for the inactivation of microbes. Thus, the present photocatalyst is employed not only for the degradation of organic contaminants but also for inactivating different microbes in wastewater. The main reason for using photocatalysis is that the reactive oxygen species, produced during photocatalysis can kill the microbes through the nucleic acid attack, co-enzyme oxidation, and dis-organizing cell membrane [17]. Visible light-driven photocatalytic inactivation of microbes by metal-doped  $\text{TiO}_2$  photocatalyst [18], carbon-supported metal oxide nanocomposite [19], and metal co-doped  $\text{TiO}_2$  [17] have been investigated by many researchers in the last decades. Veréb *et al.* [20] reported the bare and doped rutile and anatase  $\text{TiO}_2$  photocatalyst for photocatalytic inactivation of *E. coli* in water under visible light irradiation. Mathew *et al.* [21] introduced a photocatalytic inactivation of *E. coli* and *S. aureus* in water using Cu-doped  $\text{TiO}_2$

under visible light irradiation. Hence, metal-modified  $\text{TiO}_2$  has been receiving much attention due to its extended visible light absorption efficacy.

Therefore, for the present study, we have prepared visible light active FDT/PAC nanocomposite via a combination of ultrasonic-hydrothermal treatment to ensure good dispersion of Fe-doped  $\text{TiO}_2$  on activated carbon surface to generate a high photocatalytic activity. Standard characterization protocols were employed to understand the basis of the improved activity of the nanocomposite. The photocatalytic inactivation property of the nanocomposite was also explored against gram-positive and gram-negative bacteria. The typical mechanism for the photodegradation of congo red and photocatalytic inactivation of bacteria is shown in Figure 4.1. This could be one of the first reports to highlight the use of FDT/PAC nanocomposite for degradation of anionic congo red dye from wastewater using less amount of nanocomposite, reduced reaction time, and further, this nanocomposite was also used as an antimicrobial for the inactivation of microbes. The operating cost and electrical energy consumed while running the experiments were calculated and found to be minimal.

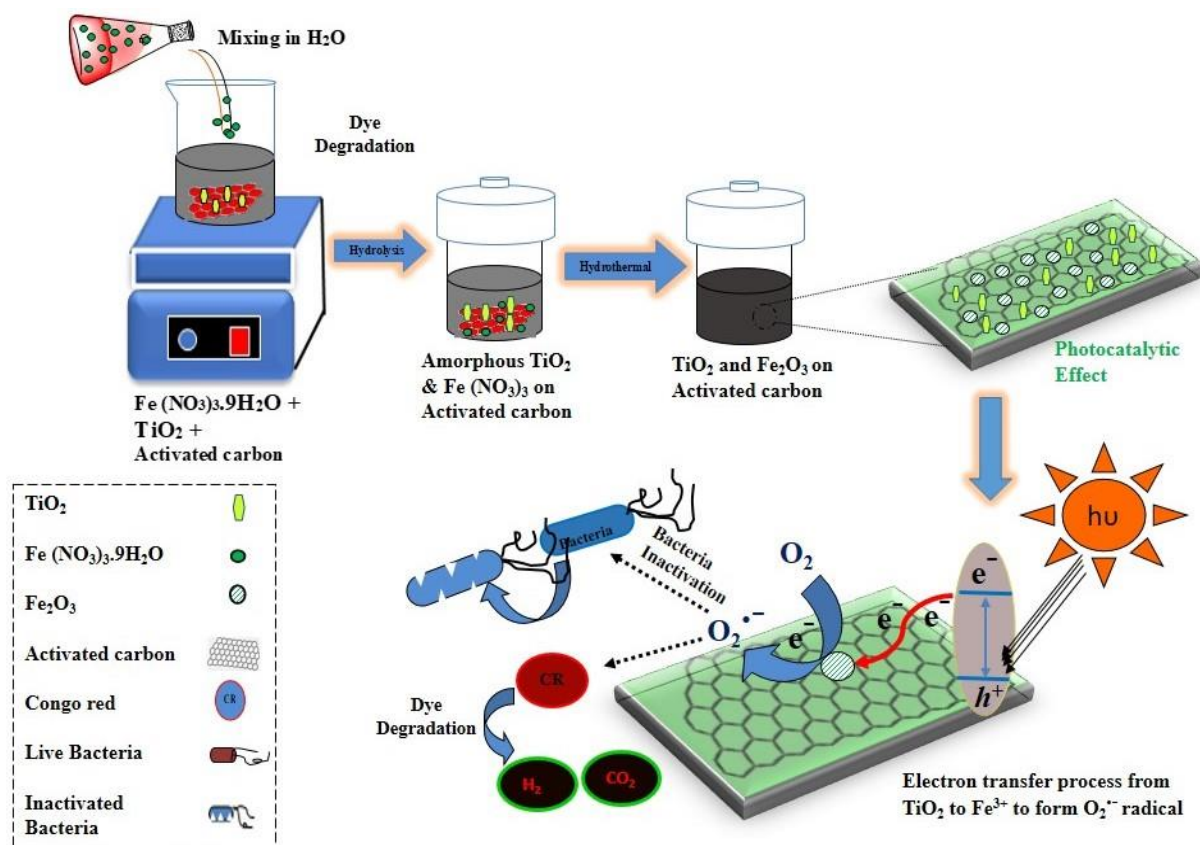


**Figure 4.1** Schematic illustration of photodegradation of congo red and photocatalytic inactivation of bacteria over FDT/PAC nanocomposite



## 4.2 Materials and methods

### 4.2.1 Materials

Titanium tetrachloride (99.10%), congo red (CR), ferric nitrate hexahydrate (98%), zinc chloride (99%), sulphuric acid (98%), and ammonia (25%) were procured from Sigma-Aldrich. Co., India. All chemicals utilized were of pure scientific grade and used without further purifications.

### 4.2.2 Synthesis of FDT/PAC nanocomposite

For the synthesis of FDT/PAC nanocomposite, activated carbon and  $\text{TiO}_2$  were used as precursors. Bio-waste pine cones were utilized for activated carbon preparation and the sol-gel method was used for the synthesis of  $\text{TiO}_2$  nanoparticles. The synthetic routes for AC and  $\text{TiO}_2$  synthesis were described in sections 3.2.2.1 and 3.2.2.2 of Chapter 3. The synthetic methods for the preparation of pine cone activated carbon (PAC) with photocatalyst  $\text{TiO}_2$  have been described in detail in section 3.2.2.3 of Chapter 3.

For the synthesis of FDT/PAC nanocomposite, 0.15 g of the as-prepared sol-gel  $\text{TiO}_2$  nanoparticle was slowly added to 1 g of 100 ml ferric nitrate solution and the solution was simultaneously stirred for 30 minutes. Thereafter, 0.3 g of the as-prepared PAC was poured slowly into the above mixture and the obtained solution was ultrasonicated for 1 h. Later, the sonicated mixture was shifted into a hydrothermal autoclave and kept at  $150^\circ\text{C}$  inside the oven for 24 h. After the hydrothermal treatment, the solution was washed appropriately with double refined water using a centrifuge machine so that the solution pH becomes neutral and finally the solution was dried at  $65^\circ\text{C}$  for 12 h [22].

### 4.2.3 Characterization of FDT/PAC nanocomposite

The synthesized FDT/PAC nanocomposite was characterized by several analytical techniques. The crystal structure of the FDT/PAC nanocomposite was obtained using an X-ray diffractometer (Model: X'pert PRO, Philips, Japan,  $\text{CuK}\alpha$  radiation). The surface structure of the FDT/PAC nanocomposite was studied using scanning electron microscopy (SEM) (Model: Zeiss, Sigma-300, Made: Carl Zeiss Microscopy, Germany). The elemental analysis was done using energy-dispersive X-ray spectroscopy (EDX). The elemental composition and valence states of the FDT/PAC nanocomposite was studied using X-ray photoelectron spectroscopy (XPS) (Model: ESCALAB Xi+, Made: Thermo Fisher Scientific). The functional groups present on the FDT/PAC nanocomposite were identified using Fourier transform Infra-red (FT-IR) spectrometer (Model: Spectrum Two, Made: Perkin Elmer). The bandgap energy was



studied using a diffuse reflectance spectrophotometer (DRS) (Model: Shimadzu UV-2600, and wavelength 200-600 nm). Photoluminescence spectrophotometer (Horiba Fluoromax-4CP spectrofluorometer, 150 W Xenon Lamp) was used to obtain the photoluminescence (PL) spectra. Surface areas of the samples were measured by the N<sub>2</sub> adsorption-desorption isotherm with a Quantachrome instrument (Autosorb iQ Station 1, 77 K) based on the Brunauer–Emmett–Teller (BET) model. The total pore volume and pore radii were estimated from the consequent N<sub>2</sub> adsorption volume *via* the Barrett–Joyner–Halenda (BJH, at relative pressure 0.09) theory. The batch equilibrium method was used to determine the zero-point charge (pHzpc) of the FDT/PAC nanocomposite [23] and the method has been described in Chapter 2 section 2.3.

#### 4.2.4 Photocatalytic degradation experiment

A photocatalytic reactor, which consists of a black box (dimension: 63 × 44 × 44 cm) was used to perform the photocatalytic reaction of CR. A 250 ml Pyrex glass vessel containing 200 ml of CR solution was placed above a magnetic stirrer and an amount of FDT/PAC was mixed with the solution at the bottom of the reactor. A visible lamp having a maximum wavelength of 520 nm (High-pressure mercury lamp, 350 W) was located at the top of the reactor, 10 cm away from the reaction solution. The photocatalytic reaction was caused by the use of visible radiation which reached the FDT/PAC photocatalyst through the pollutant solution. The reactor temperature was maintained at 25°C using a constant flow of water inside the reaction scheme using a water pump. Also, an exhaust fan was used inside the reactor for the continuous circulation of air.

For the degradation of CR dye, a stock solution of CR (1000 ppm) was first prepared using 1 g of CR in 1000 ml double distilled water. Further, the required concentration was obtained by the dilution of stock solution to various concentrations 20 ppm, 60 ppm, and 100 ppm. For this study, FDT/PAC nanocomposite was mixed in a 200 ml CR dye solution of varying concentrations (20 ppm, 60 ppm, and 100 ppm) by vigorously stirring the reaction mixture without exposure to light till 30 minutes so that adsorption-desorption equilibrium could be established within the reaction system. After equilibrium was established, the concentration of the dye was measured and this was taken as the initial concentration so that the adsorption of CR due to the nanocomposite does not hinder the study of the overall photocatalytic effect. Later, the final concentration of the dye solution was measured using a UV-Vis spectrophotometer at  $\lambda_{\text{max}}$  of 497 nm by taking out 3.5 ml at every 10 minutes interval.

The CR degradation percentage was calculated by equation 4.1.

$$\text{CR degradation (\%)} = \frac{C_i - C_e}{C_i} \times 100 \quad (4.1)$$

where  $C_i$  and  $C_e$  are the concentrations of CR before and after the photocatalytic treatment.

#### 4.2.5 Antibacterial activity experiment

For the photocatalytic antimicrobial test of FDT/PAC nanocomposite, gram-negative bacteria *Escherichia coli* (*E. coli*) and gram-positive bacteria *Staphylococcus aureus* (*S. aureus*) were used as test bacterium. *E. coli* and *S. aureus* were cultured using Luria-Bertain (LB) nutrient broth and the solution was incubated for 6 h at 37°C overnight. The bacterial pellet was assembled by centrifuging the culture medium at 2500 rpm for 15 minutes and suspended in the autoclaved distilled water. The initial concentration was adjusted to  $10^5$  CFU (colony forming unit)  $\text{ml}^{-1}$ . The nutrient agar and broth media, and all plating equipment were autoclaved before starting the experiments.

##### 4.2.5.1 Photocatalytic inactivation procedure

At first, autoclaved nutrient agar was poured into Petri plates for solidification. Then, 70 ml of bacterial suspension ( $10^5$  CFU  $\text{ml}^{-1}$ ) was added to the sterile Pyrex glass vessel and was stirred using a magnetic stirrer (150 rpm) throughout the experiments. Thereafter 0.05 g of the nanocomposite was added and the resultant mixture was exposed to visible light. At a specified time interval, 0.01 ml of the suspension was collected from the reactor and spread on the nutrient agar plates. To cultivate the bacteria, the agar Petri plates were placed inside an incubator at 37°C for 24 h. After incubation, the bacteria residual colonies were quantified using a digital colony counter.

The photocatalytic inactivation efficiency of bacteria was calculated using equation 4.2 [24]:

$$\text{Inactivation efficiency (\%)} = \frac{\text{no. of colonies} \times \text{dilution factor}}{\text{volume of culture plate}} \quad (4.2)$$

### 4.3 Results and discussion

#### 4.3.1 Characterization of FDT/PAC nanocomposite

##### (a) XRD analysis

XRD peaks of FDT/PAC nanocomposite are shown in Figure 4.2 and a comparison has been made with the XRD peaks of  $\text{TiO}_2$ ,  $\text{TiO}_2$  supported on pine-cone activated carbon ( $\text{TiO}_2$ -NP/PAC) nanocomposite [25]. The XRD peaks at  $2\theta = 25.281, 38.576, 48.050, 53.891, 55.062, 62.690, 68.762, 70.311$  and  $75.032$  correspond to (1 0 1), (1 1 2), (2 0 0), (1 0 5), (2 1 1), (2 0 4), (1 1 6), (2 2 0), and (2 1 5) planes which confirms that the samples have anatase crystalline

form of  $\text{TiO}_2$  (JCPDS 21-1272). The peaks related to Fe ions are not found in the XRD pattern of FDT/PAC nanocomposite. This observation can be ascribed because Fe ions were incorporated into the crystal lattice of titania due to the similar radius of  $\text{Ti}^{4+}$  (0.068 nm) and  $\text{Fe}^{3+}$  (0.064 nm) [8]. It is believed that  $\text{Fe}^{3+}$  inserts into the interior matrix of the Fe-doped  $\text{TiO}_2$  nanoparticles instead of the exterior surface [26]. Similar patterns of results i.e. absence of Fe signal in XRD spectra for Fe-doped  $\text{TiO}_2$  was also observed by several other authors [6,27–29]. Furthermore, no XRD phase is found for activated carbon due to its amorphous structure. The crystalline size calculated for the FDT/PAC nanocomposite using the Debye-Scherrer equation was found to be 4.36 nm.

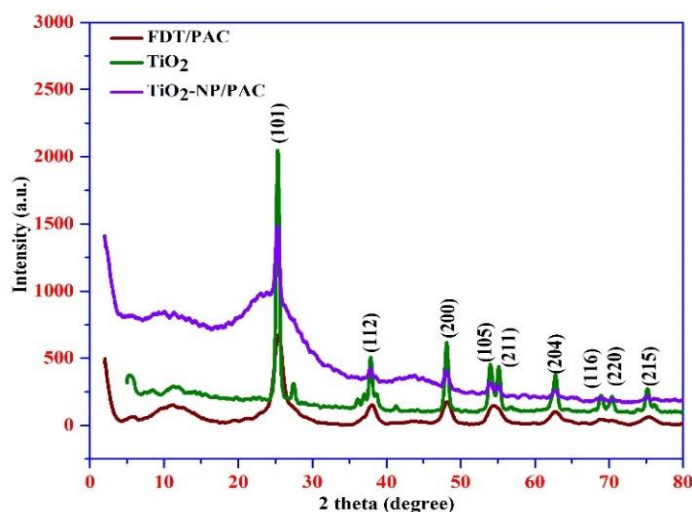


**Figure 4.2** X-ray Diffraction pattern of FDT/PAC nanocomposite and a comparison with  $\text{TiO}_2$ ,  $\text{TiO}_2$ -NP/PAC [25]

#### (b) SEM and EDX analysis

The SEM micrograph of the FDT/PAC nanocomposite is shown in Figure 4.3 (a). From the SEM image of FDT/PAC nanocomposite, it can be observed that white spherical particles of  $\text{TiO}_2$  with different sizes were irregularly agglomerated on the surface of the PAC, and there were fine Fe ions accumulated or attached to the surface of the  $\text{TiO}_2$ . The presence of Fe ions on the surface of the PAC is expected to increase the absorption of light in the visible light region thus enhancing the photocatalytic activity. Furthermore, it is observed that the Fe-doped  $\text{TiO}_2$  nanoparticles are well dispersed on the PAC surface and have an average 2-20 nm particle size distribution.

The purity and elemental compositions of the FDT/PAC nanocomposite were analysed by EDX analysis (Figure 4.3 (b)). The EDX spectrum revealed that the FDT/PAC nanocomposite has a Fe content of 29.27%, Ti of 28.69%, C of 2.52%, and O of 28.22% which confirms the equal distribution of Fe, Ti, and O over the C surface.

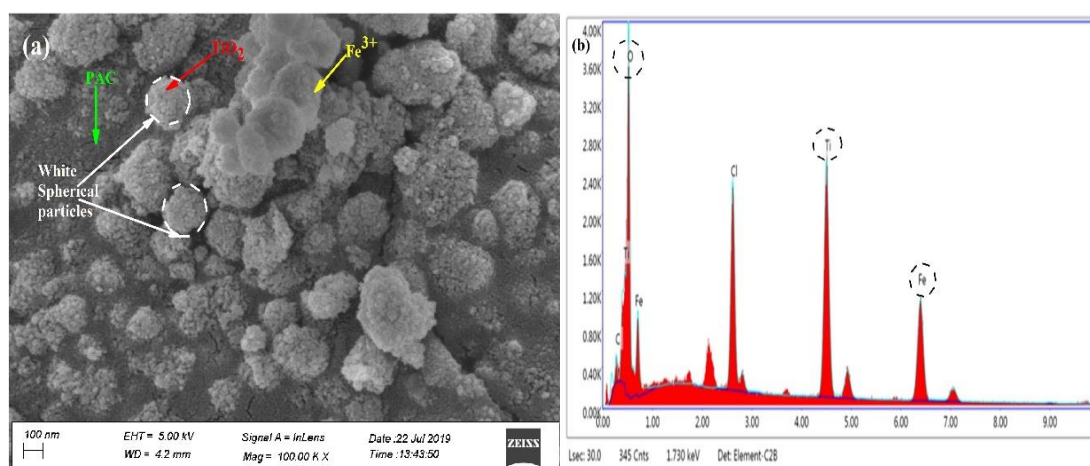


**Figure 4.3** (a) SEM image of FDT/PAC nanocomposite, (b) EDX spectra of FDT/PAC nanocomposite  
(c) XPS analysis

The chemical composition and valence band of the elements in the FDT/PAC nanocomposite was analysed using XPS analysis. The full scan XPS survey of the nanocomposite is shown in Figure 4.4. The presence of elements such as Ti, O, C, and Fe at their corresponding chemical states confirm the formation of the FDT/PAC nanocomposite. Figure 4.4 illustrates that the Fe-doped  $\text{TiO}_2$  nanoparticles has two chemical states of  $\text{Fe}^{3+}$  and  $\text{Fe}^{2+}$ . The major Fe  $2p_{3/2}$  peak at 710.62 is the main signature peak for  $\text{Fe}^{3+}$  ion. The small Fe  $2p_{1/2}$  peak corresponding at 725.34 eV is attributed to the  $\text{Fe}^{2+}$  ion, which might form during the hydrothermal process for the high temperature and pressure [30]. The detail XPS core level spectra for other elements such as Ti 2p, O 1s, C 1s, and Fe 2p are shown in Figure 4.5(a), (b), and (c).

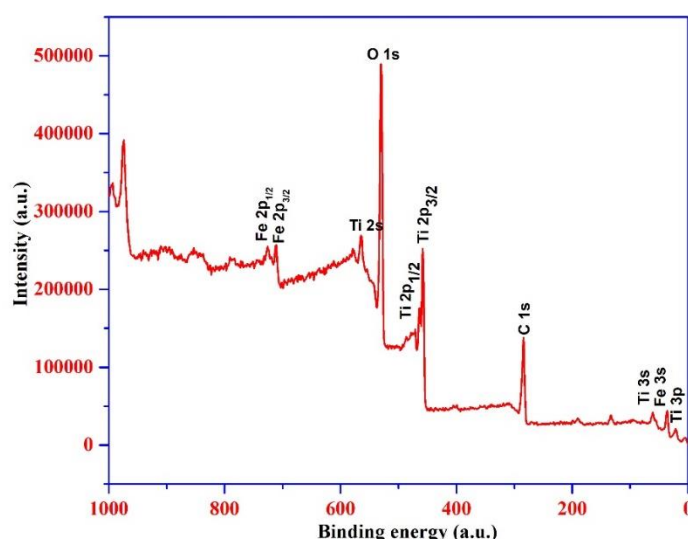


**Figure 4.4** Survey scan spectra for FDT/PAC nanocomposite

The core level spectra of Ti 2p (Figure 4.5 (a)) displays two peaks at binding energy 458.76 and 464.45 eV, respectively, which can be attributed to the spin orbital splitting of  $2p_{3/2}$  and  $2p_{1/2}$

states [31]. The major peak at 458.76 eV corresponds to the Ti ions with valence state 4+ ( $\text{Ti}^{4+}$ ), while the peak at lower binding energy of 464.45 eV refers to the Ti ions with a reduced valence state 3+ ( $\text{Ti}^{3+}$ ). The XPS spectra of O 1s (Figure 4.5 (b)) exhibited a strong peak at 530.52 eV, it deconvoluted into three peaks at 530.38, 531.38, and 532.72 eV, which were ascribed to the surface oxygen species of hydroxyl groups, lattice oxygen of  $\text{TiO}_2$ , and oxygen vacancies, respectively [32]. The XPS spectrum of C 1s (Figure 4.5 (c)) showed a strong peak at 284.66 eV, and it deconvoluted into 284.48, 285.85, and 288.39 eV, which are attributed to the C=C bonds, C-OH, and C=O bonds activated carbon [33]. Thus, the XPS results confirm the formation of the FDT/PAC nanocomposite.

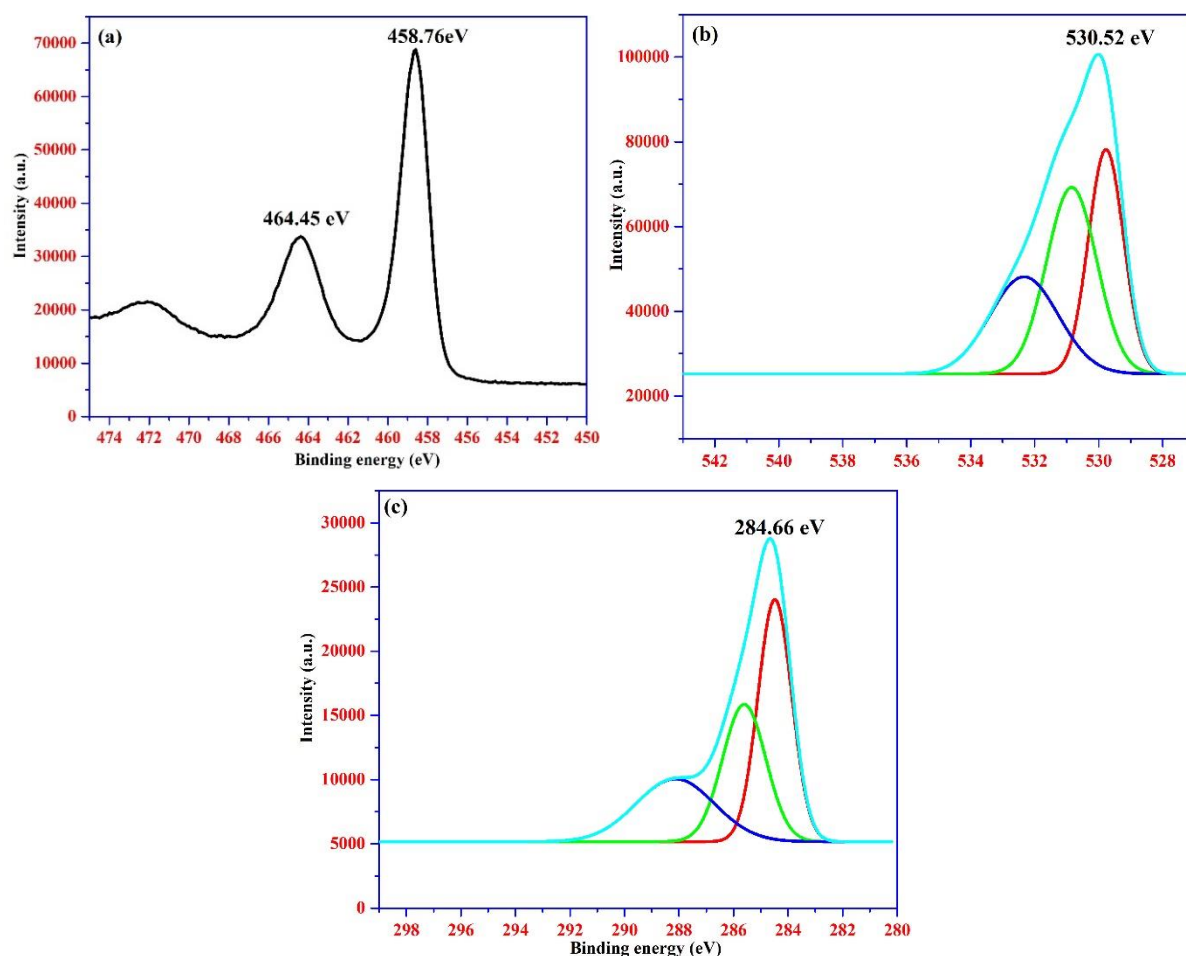


**Figure 4.5** High resolution core level XPS spectrum of (a) Ti 2p, (b) O 1s, and (c) C 1s

#### (d) FT-IR analysis

FT-IR spectra of the  $\text{TiO}_2$  and FDT/PAC nanocomposite are shown in Figure 4.6. The peaks of the  $\text{TiO}_2$  and FDT/PAC nanocomposite at  $3500\text{ cm}^{-1}$  and  $1600\text{ cm}^{-1}$  are assigned to the stretching and bending vibrations of the O-H and H-O-H bond which can be attributed to the physically and chemically absorbed surface water. The peak at around  $550\text{ cm}^{-1}$  is related to the stretching vibration of the Ti-O bond [34]. A new peak at  $1060\text{ cm}^{-1}$  appeared for the FDT/PAC

nanocomposite which confirms the presence of stretching vibration of the Ti-O-C bond [8]. This suggests that the TiO<sub>2</sub> nanoparticles were attached chemically with the C surface and hence Ti cannot be easily separated from the C surface.

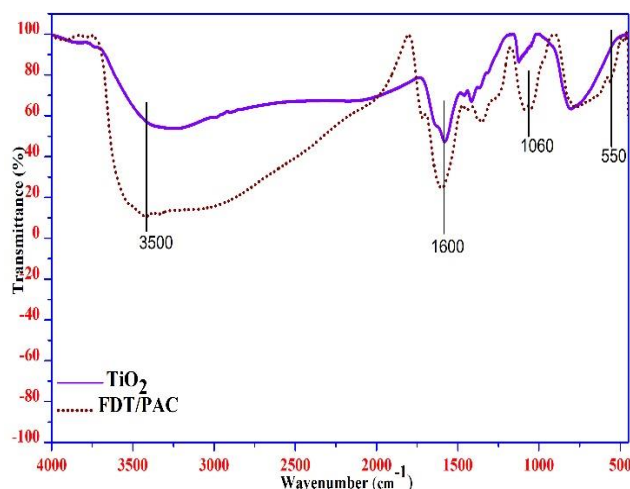


**Figure 4.6** FT-IR spectra of TiO<sub>2</sub> and FDT/PAC nanocomposite

#### (e) UV-Vis DRS analysis

The UV-Vis DRS spectra of Fe-doped nanocomposite (FDT/PAC) and TiO<sub>2</sub> are shown in Figure 4.7 (a), and the results are compared with TiO<sub>2</sub>-NP/PAC [25]. From Figure 4.7 (a), it can be observed that the absorption peak of TiO<sub>2</sub> and TiO<sub>2</sub>-NP/PAC appears in the wavelength range of the ultra-violet light region. On the other hand in the FDT/PAC nanocomposite, the absorption edge shifts towards the visible light region due to the doping of Fe ion. The absorption peak of TiO<sub>2</sub> in the UV range appears due to the transition from the 2p level of O to the 3d level of Ti. With Fe doping, the absorption peak of FDT/PAC nanocomposite shifts to a longer wavelength due to the excitation of the 3d electron of Fe<sup>3+</sup> ion to the conduction band of TiO<sub>2</sub> [8]. The optical bandgap energy was calculated using Tauc's equation given below [35]:

$$\alpha h\nu = K (h\nu - E_g)^n \quad (4.3)$$

where  $E_g$  = optical bandgap,  $h\nu$  = photon energy,  $\alpha$  = molar extinction coefficient,  $K$  is the proportionality constant, and  $n$  depends on the type of transition.

From the  $(\alpha h\nu)^2$  vs  $h\nu$  curve, the  $E_g$  values of the FDT/TiO<sub>2</sub> nanocomposite and TiO<sub>2</sub> were found to be 2.3 and 3.1 eV as compared to, TiO<sub>2</sub>-NP/PAC i.e. 3.2 eV. It can be seen from Figure 4.7 (b) that the  $E_g$  value of the TiO<sub>2</sub> decreased from 3.1 to 2.3 eV with the addition of Fe ions in the FDT/PAC nanocomposite which improved the absorption of light in the visible region.



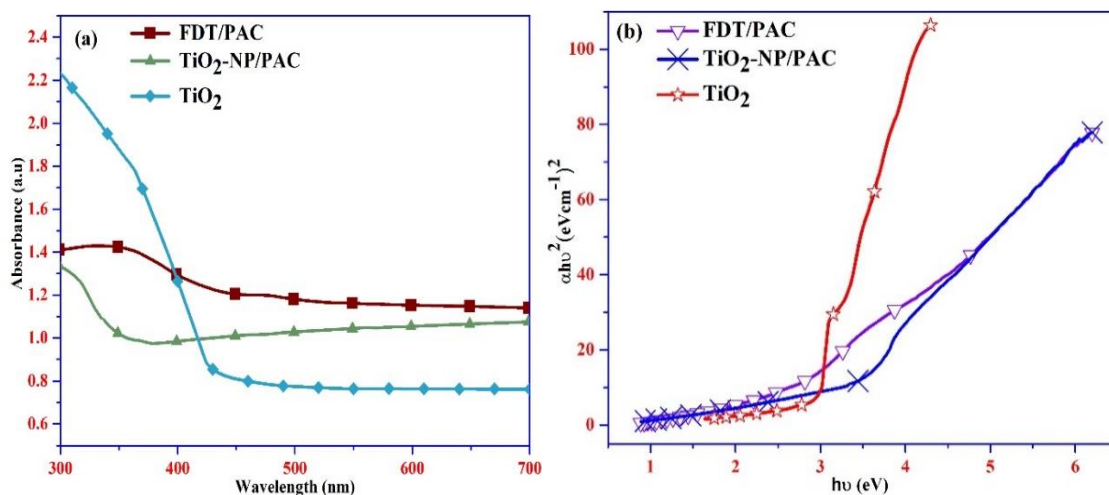


**Figure 4.7** (a) UV-Visible DRS spectra and (b) Tauc's plot for the determination of optical bandgap for TiO<sub>2</sub>, TiO<sub>2</sub>-NP/PAC, and FDT/PAC nanocomposite (plot for TiO<sub>2</sub>-NP/PAC is shown for comparison only) [25]

#### (f) PL analysis

The efficiency of the separation of photogenerated electron-hole pairs can be investigated using photoluminescence (PL) spectra. The lesser the PL peak intensity, the lesser the affinity to recombine the electron-hole pair which leads to more electron-hole pair participation in the photochemical reaction thus increasing the photocatalytic activity of the nanocomposite. In this present study, the PL spectra of TiO<sub>2</sub> and FDT/PAC nanocomposite are analyzed in the wavelength range from 450-750 nm (Figure 4.8). The sharp emission peak at 468 nm for TiO<sub>2</sub> is due to the transition of charge from Ti 3d to the O 2p level and signifies the recombination of the electron-hole pair [36]. Similar results have also been observed by Hasibur *et al.* [30] which showed that the PL emission peak of TiO<sub>2</sub> appears at around 477 nm wavelength indicating the bandgap recombination of electron-hole pair. The PL peak intensity for FDT/PAC nanocomposite was found to decrease as compared to TiO<sub>2</sub> which confirms the fact that the recombination of the electron-hole pair reduced significantly in the nanocomposite as compared to TiO<sub>2</sub>. This is due to the formation of a dopant energy level (Fe<sup>3+</sup>/Fe<sup>4+</sup>) within the bandgap of TiO<sub>2</sub> (nearer the valence band), which results in the excitation of Fe<sup>3+</sup> 3d-electrons from the dopant energy level to the TiO<sub>2</sub> conduction band (CT transition) [31]. Hence, the presence of Fe ions in the composite decreases the probability of electron-hole recombination by increasing the lifetime of the charge carrier which is expected to improve the photocatalytic activity.



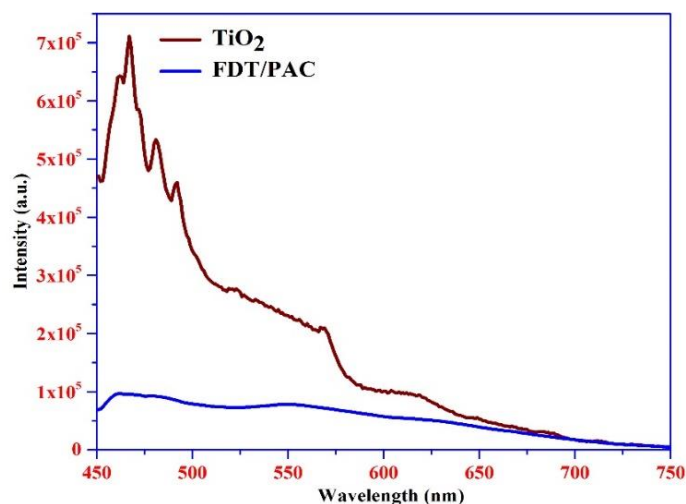


**Figure 4.8** Photoluminescence spectra of TiO<sub>2</sub> and FDT/PAC nanocomposite

#### (g) BET surface area analysis

BET surface area and pore volume of a nanocomposite can provide information about the structural properties, pore distribution, and active site availability for the adsorption of pollutants. The larger the surface area and pore volume of a nanocomposite the better will be its photocatalytic and adsorption performance. The results for proximate analysis of FDT/PAC nanocomposite are given in Table 4.1. From the table, it is evident that the FDT/PAC nanocomposite has a large BET surface area compared to pure TiO<sub>2</sub>. An increase in the surface area could be due to the incorporation of Fe ions to the TiO<sub>2</sub> complex which is likely to enhance the stress of the TiO<sub>2</sub> complex [32] and also because of the use of PAC as the supporting surface for the synthesis of FDT/PAC nanocomposite [26]. The total pore volume of 0.156 cm<sup>3</sup>g<sup>-1</sup> and pore radius of 4.4624 nm gives an idea about the formation of mesoporous material. Thus higher surface area/active sites are expected to enhance the photocatalytic performance of hybrid nanocomposite.

<b>Table 4.1</b> BET surface area and pore size of TiO <sub>2</sub> , FDT/PAC nanocomposite	
<b>Proximate analysis (wt %)</b>	
BET surface area (FDT/PAC)	82.779 m <sup>2</sup> g <sup>-1</sup>
BET surface area (TiO <sub>2</sub> )	60.21 m <sup>2</sup> g <sup>-1</sup>
BET surface area (PAC)	878.07 m <sup>2</sup> g <sup>-1</sup>
Total pore volume	0.156 cm <sup>3</sup> g <sup>-1</sup>
Pore radius	4.4624 nm

#### (h) pH<sub>zpc</sub> analysis

The zero point charge (pH<sub>zpc</sub>) of the FDT/PAC nanocomposite is found to be 6.02 (Figure 4.9), indicating that the surface charge of the nanocomposite will be positive when pH is less than 6.02 and negative when pH is greater than 6.02 [40].

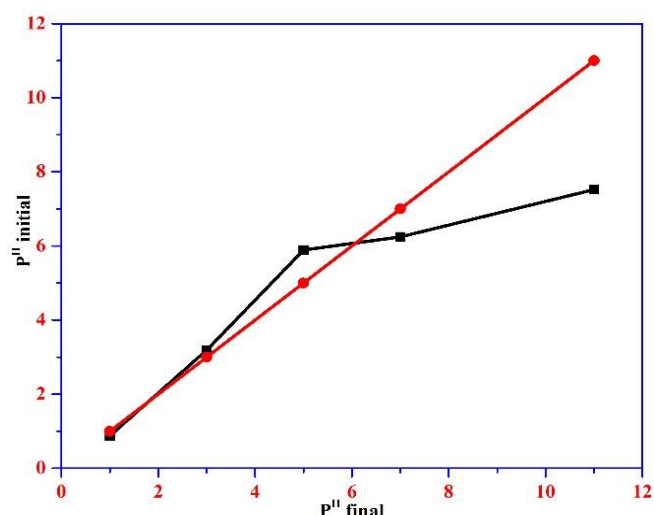


**Figure 4.9** Zero-point charge plot for FDT/PAC nanocomposite

### 4.3.2 Photocatalytic activity

#### (a) Effect of FDT/PAC nanocomposite amount

The photocatalytic activity of the FDT/PAC nanocomposite on the degradation of CR dye solution was studied with different dosages of the nanocomposite for different concentrations of CR dye solution. The FDT/PAC nanocomposite dosages were ranged from 0.02-0.10 g for 20, 60, and 100 ppm of CR solutions (Figure 4.10). It can be seen that the percentage degradation of CR increases with the increase of nanocomposite dosages till 0.06 g of the nanocomposite dose and beyond that saturation was observed. The maximum percentage of degradation (100%) was achieved for 20 ppm CR solution with 0.06 g of FDT/PAC nanocomposite after exposure to visible light irradiation for 60 minutes. There could be several reasons for this result: (i) The addition of PAC increases the surface area of the nanocomposite, helping more CR molecules gather around FDT/PAC nanocomposite, (ii) The recombination of electron-hole pair decreases due to the introduction of impurity Fe ions on the  $TiO_2$  matrix. However, when the dose becomes higher than 0.06 g, it serves as a recombination center for the photogenerated electron-hole species resulting in the decrease in the photocatalytic activity of the nanocomposite. One of the possible explanations could be: when the nanocomposite dose increases beyond a certain dose, the visible light penetration through the reaction mixture becomes lesser due to visible light scattering, hence CR dye degradation efficiency decrease [41]. Thus, for further studies, 0.06 g of FDT/PAC nanocomposite was taken as the optimum dose amount.

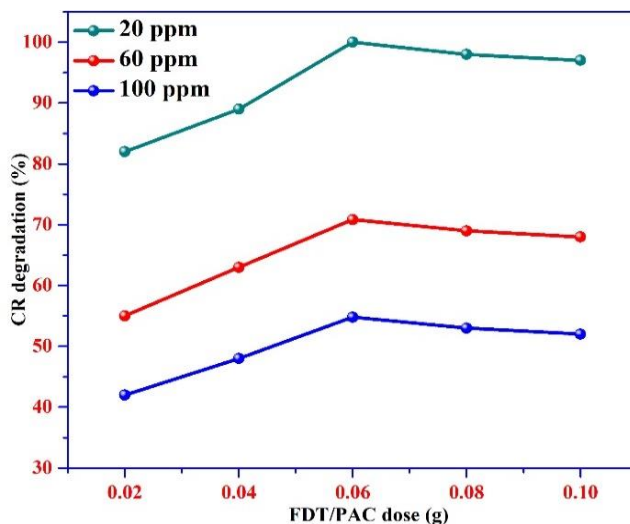


**Figure 4.10** Effect of FDT/PAC nanocomposite loading in the degradation of CR solution

### (b) Effect of pH

The photocatalytic degradation of CR dye was conducted with 0.06 g FDT/PAC nanocomposite with 20 ppm CR dye solution in the pH range of 1-11. From Figure 4.11, it is clear that at pH lower than 5; the percentage of CR degradation is quite high having maximum degradation at pH 1. This could be due to the positive surface characteristics of the nanocomposite below its pHzpc (pHzpc value is 6.02). At lower pH (pH < pHzpc 6.02), the nanocomposite surface becomes positively charged i.e.,  $(Fe - TiOH - PAC + H^+ \leftrightarrow Fe - TiOH_2^+ - PAC)$  thus the positively charged nanocomposite surface has more electrostatic attraction affinity to bind with negatively charged CR dye which leads to the maximum degradation of CR dye [42].

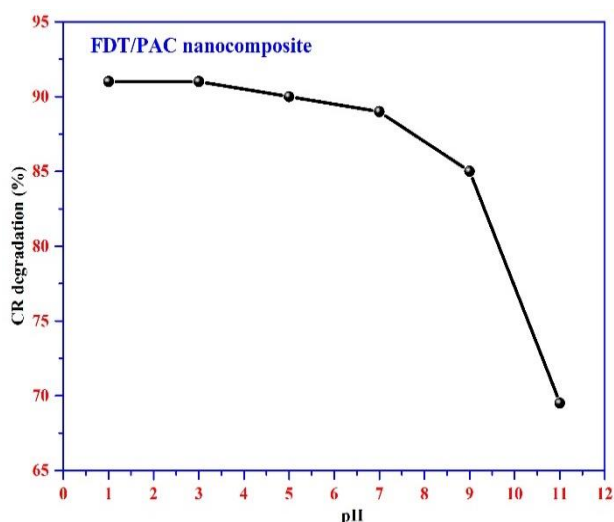


**Figure 4.11** Effect of pH in the degradation of CR solution

**(c) Effect of initial CR dye concentration and light irradiation time**

The initial CR dye concentration affects the degradation rate and nanocomposite efficiency. Figure 4.12 (a) shows the degradation pattern for different concentrations of CR dye when photo catalyzed with 0.06 g of FDT/PAC nanocomposite at pH = 1. The maximum degradation of 100% was observed for 20 ppm CR solution at 60 minutes; on the other hand, 88% and 75% degradation was observed for 60 and 100 ppm solution of the dye after 120 minutes irradiation. With the increase in the initial CR dye concentration, the adsorbed negatively charged CR dye molecules on the positive surface of FDT/PAC nanocomposite deactivate the active sites of the nanocomposite and consequently prevent the formation of reactive hydroxyl radicals. Furthermore, at higher CR dye concentration more dye molecules are available for adsorption on the surface of nanocomposite; hence photons get trapped by the CR molecules and are not able to reach the surface of the nanocomposite. Therefore, the rate of formation of hydroxyl and dioxygen radicals decreases, and thereby photocatalytic activity is decreased. From Figure 4.12 it can also be seen that the percentage degradation of CR dye increased with irradiation time and became saturated after exposure to light for 60 minutes, and no further degradation of dye took place with a further increase in exposure time. This may be due to the formation of a large quantity of small organic molecules produced due to degradation [43]. These small organic molecules adsorb on the surface of the nanocomposite resulting in the decreased formation of hydroxyl radicals that attack the dye molecules.

For understanding the effect of Fe doping in TiO<sub>2</sub>-NP/PAC nanocomposite, experiments had been carried out with TiO<sub>2</sub>/activated carbon sample without Fe doping under similar sets of conditions (under visible light) and the results are shown in Figure 4.12 (b). The degradation of 20 ppm CR dye solution was found to be 33.50%, for 60 ppm it was 20%, and for 100 ppm it was 15% as compared to FDT/PAC nanocomposite in which case it was 100% degradation for 20 ppm, 70.84% degradation for 60 ppm and 54.80% degradation for 100 ppm of CR dye solution. This partial degradation without Fe doping was probably due to the photosensitive nature of the dye in the visible region. The very high degradation of dye in presence of FDT/PAC catalyst confirms the fact that Fe doping increases the photocatalytic efficiency under visible light. Several researchers [44–46] also reported that some dyes having benzene, naphthalene, anthracene-like structures are photosensitive in the visible region. Even though TiO<sub>2</sub> is not activated by visible light, the dye can also absorb visible light photons which results in minor degradation of the dye. Further presence of activated carbon which contains some

structures similar to the dye enhances the visible light absorption which leads to partial degradation of the dye without TiO<sub>2</sub> activation with Fe ions [47].

Degradation of dye with bare TiO<sub>2</sub> was conducted under similar sets of conditions (under visible light) and are represented in Figure 4.12 (c). From this observation, the bare TiO<sub>2</sub> degradation of 20 ppm CR dye solution was 25%, for 60 ppm it was 18% and for 100 ppm it was 12%. Even though TiO<sub>2</sub> does not show optical response in the visible light region, the dye itself can also absorb visible light photons which results in partial degradation of the dye at 520 nm due to the photosensitive nature of the bare dye.

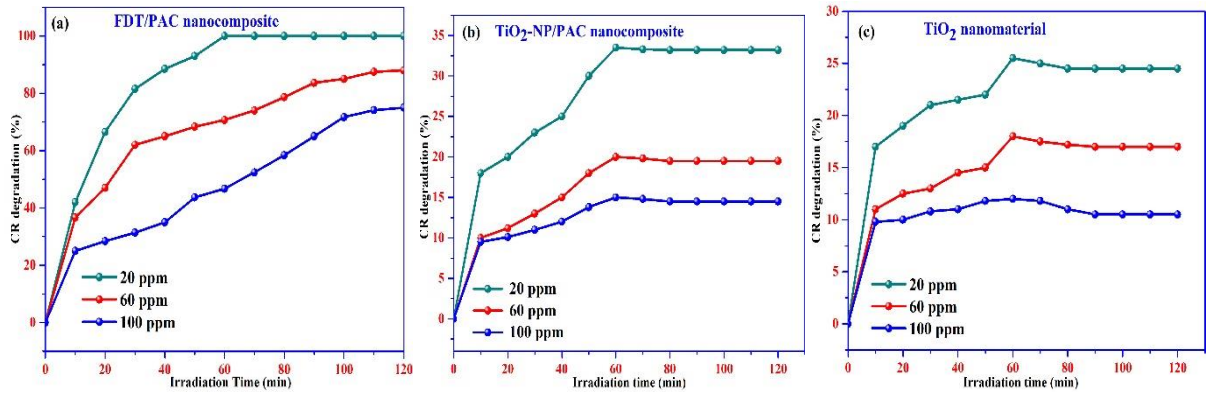


**Figure 4.12** Effect of degradation of CR dye solutions by (a) FDT/PAC, (b) TiO<sub>2</sub>-NP/PAC, and (c) TiO<sub>2</sub> catalyst for degradation of different concentrations of dye solutions for different contact times under visible light (520 nm)

### 4.3.3 Kinetic studies

The kinetic studies were conducted at optimum conditions i.e., CR dye concentration of 20 ppm, pH 1, catalyst dose of 0.06 g to understand the rate constant value and efficiency of the nanocomposite in the CR degradation using the Langmuir-Hinshelwood model. The kinetic study was represented using the pseudo-first-order rate equation 4.4 and the half lifetime ( $t_{1/2}$ ) by equation 4.5:

$$\ln\left(\frac{C_i}{C_e}\right) = K_{app} t \quad (4.4)$$

$$t_{1/2} = \frac{\ln 2}{K_{app}} \quad (4.5)$$

where  $C_i$  is the initial CR concentration (20 ppm);  $C_e$  is the CR concentration at equilibrium;  $K_{app}$  is the apparent rate constant.

The linear plot of  $\ln (C_i/C_e)$  versus irradiation time gives a high correlation coefficient ( $R^2$ : 0.999) which signifies that the degradation follows first-order rate kinetics (Figure 4.13). From the slope of the curve, the photocatalytic rate constant  $K_{app}$  value was calculated to be 0.05341 min<sup>-1</sup>. Using equation 4.5 the half-life period was found to be 12.97 minutes.

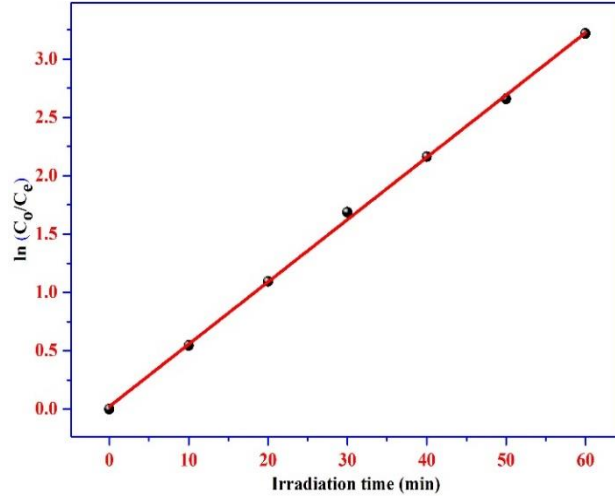


**Figure 4.13** Pseudo-first-order rate kinetics of CR degradation loaded on FDT/PAC nanocomposite

#### 4.3.4 Thermodynamic studies

In the present study, four temperatures i.e., 298 K, 308 K, 318 K, and 328 K were used to understand the relationship between changes in temperature with respect to heat and energy. The thermodynamics parameters such as standard entropy ( $\Delta S^\circ$ ), enthalpy ( $\Delta H^\circ$ ), free energy ( $\Delta G^\circ$ ) of the CR degradation were related to the distribution coefficient ( $K_d$ ) by:

$$\ln K_d = \frac{\Delta S^\circ}{R} - \frac{\Delta H^\circ}{RT} \quad (4.6)$$

$$\Delta G^\circ = -RT \ln K_d \quad (4.7)$$

where  $T$  is the absolute temperature,  $K_d$  is the distribution coefficient,  $R$  ( $8.314 \text{ J mol}^{-1} \text{ K}^{-1}$ ),  $\Delta H^\circ$ , and  $\Delta S^\circ$  are obtained from the slope and intercept by plotting  $\ln K_d$  vs  $1/T$  (Figure 4.14).

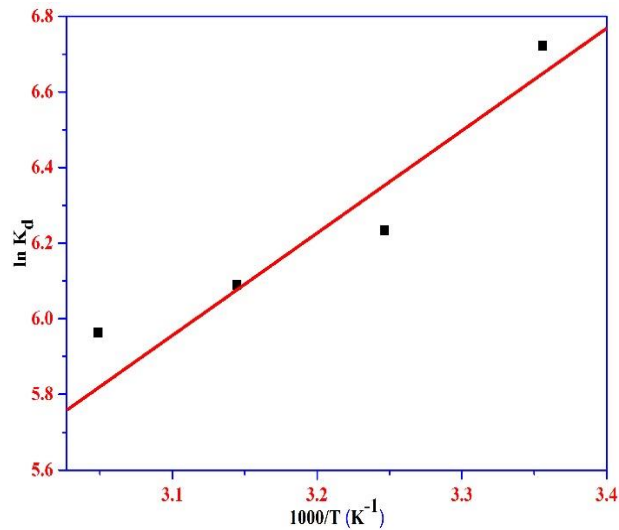


**Figure 4.14**  $\ln K_d$  as a function of  $1/T$  (CR concentration = 20 ppm, pH = 1, Nanocomposite dose = 0.06 g, and Contact time = 60 minutes)

Table 4.2 presents the derived thermodynamics parameters. The negative value of  $\Delta G^\circ$  signifies the spontaneity and feasibility of the photocatalytic reaction. Also, the negative values of  $\Delta S^\circ$  and  $\Delta H^\circ$  signify the randomness in the reaction system justifying the affinity of FDT/PAC nanocomposite towards CR degradation which is exothermic in nature.

<b>Table 4.2</b> Thermodynamic parameters calculated for the degradation of CR dye using FDT/PAC nanocomposite			
<b>T (K)</b>	<b>Thermodynamic parameters</b>		
	<b><math>\Delta G^\circ</math> (kJ mol<sup>-1</sup>)</b>	<b><math>\Delta H^\circ</math> (kJ mol<sup>-1</sup>)</b>	<b><math>\Delta S^\circ</math> (kJ mol<sup>-1</sup>K)</b>
298	-16.415	-19.835	-11.475
308	-16.301		
318	-16.186		
328	-16.071		

#### 4.3.5 Effect of interfering ions on CR photocatalytic degradation

In the industrial wastewater matrix, CR is found in combination with several ions such as sodium chloride, zinc chloride, copper sulphate, glycine, oxalic acid, sodium nitrite, cadmium nitrate, and EDTA. Hence, to investigate the applicability of FDT/PAC nanocomposite in the industrial wastewater matrix containing CR with several interfering ions a study was conducted by taking 20 ppm interfering ions with an initial CR concentration of 20 ppm, pH at 1, contact time for 60 minutes, the temperature at 298 K and 0.06 g of FDT/PAC nanocomposite. The percent degradation of CR as a function of different interfering ions is presented in Figure 4.15. From the figure, it can be seen that the degradation efficiency of the dye decreases from 100% to 56.0% in presence of Glycine, to 64.5% in presence of EDTA, to 66.0% in presence of CuSO<sub>4</sub>, to 85.0% in presence of NaNO<sub>3</sub>, to 77.0% in presence of ZnCl<sub>2</sub>, to 77.5% in presence of NaCl, to 68.5% in presence of Cd (NO<sub>3</sub>)<sub>2</sub>, and to 92.0% in presence of oxalic acid. In the presence of glycine (Gly), EDTA, CuSO<sub>4</sub> the percentage of degradation of CR decreases significantly and this could be due to the presence of different scavenging effects like glycine acting as a  $\cdot\text{OH}$  scavenger, EDTA as a hole scavenger, SO<sub>4</sub><sup>2-</sup> as an electron scavenger [48,49]. The presence of chloride ions inhibits the photocatalytic activity of the nanocomposite by scavenging both the  $\cdot\text{OH}$  radical and hole, and also blocks the active sites on FDT/PAC nanocomposite [50]. The nitrate ion can absorb light in the UV and visible region; hence there will be fewer photons available towards the pollutant molecules and therefore the degradation rate of CR is reduced with the increase of nitrate ion concentration [51]. From this result, it can be observed that the photocatalytic degradation of CR in the presence of interfering ions follows the order:

Oxalic acid < NaNO<sub>3</sub> < NaCl < ZnCl<sub>2</sub> < Cd (NO<sub>3</sub>)<sub>2</sub> < CuSO<sub>4</sub> < EDTA < Glycine.



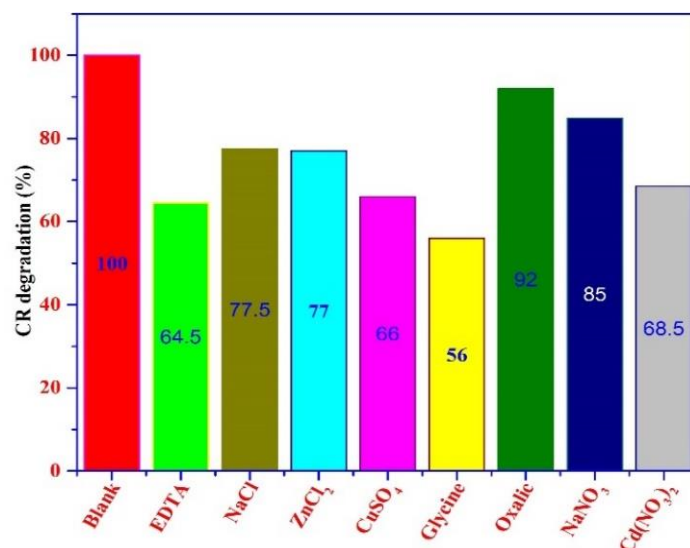


**Figure 4.15** Photocatalytic degradation of CR in the presence of interfering ions using FDT/PAC nanocomposite

#### 4.3.6 Reusability and photostability of the nanocomposite

The degradation efficiency of FDT/PAC nanocomposite was studied by reusing the catalyst for several cycles and the results are presented in Figure 4.16. After each photoreaction, the catalyst was collected from the reaction system by centrifugation and washed with distilled water then it was dried in an oven at mild temperature. When reused, in the first cycle of the degradation process, the nanocomposite degraded 93% of the CR which slowly reduced to 85% in the second cycle, to 76% in the third cycle, and the fourth cycle degraded 70% of the dye. In the fifth cycle also, the catalyst degraded around 64% of the dye signifying the fact that the present catalyst can be successfully used several times for photodegradation of CR.

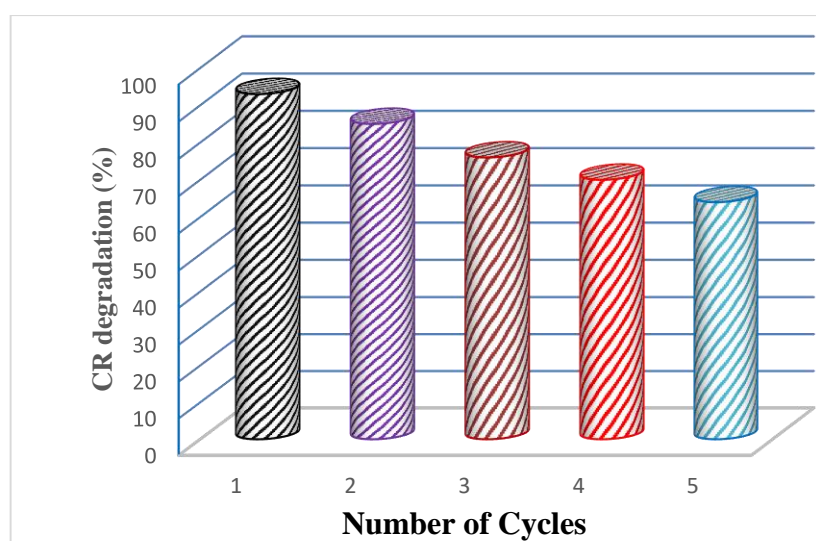


**Figure 4.16** CR degradation efficiency of FDT/PAC nanocomposite up to five cycles

To understand the photostability of the FDT/PAC nanocomposite, FT-IR spectra of the pristine FDT/PAC nanocomposite were compared with the recycled composite at the end of the fifth cycle of degradation of CR (Figure 4.17). From the figure, it can be seen that all the characteristic peaks that remain in both samples confirm that the nanocomposite had retained its original structure.

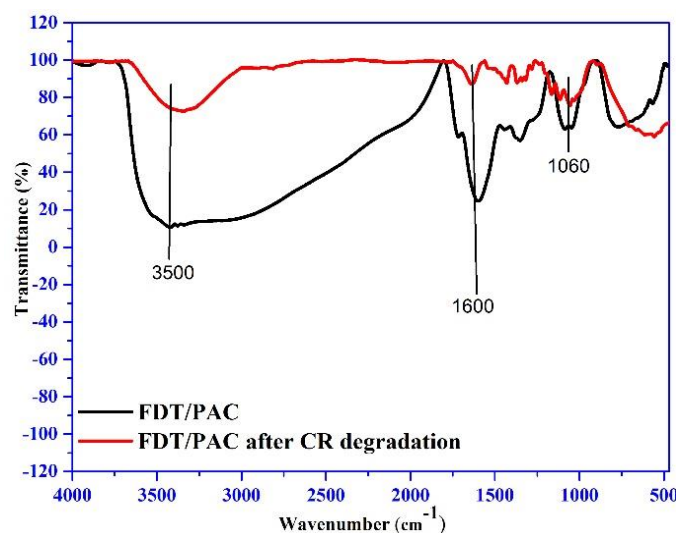


**Figure 4.17** FT-IR spectra of FDT/PAC before and after CR degradation

#### 4.3.7 GC-MS analysis

The degraded end products of the CR dye were analysed using GC-MS and the results are presented in Figure 4.18. Some major and minor product peaks are detected in the GC-MS spectra. The major products corresponding to peak position at  $m/z = 207$  is sodium (4-amino-3-diazenyl)-1 naphthoxide, at  $m/z = 191$  is 2-diazoniumnaphthalene-1, 4-diol, at  $m/z = 133$  is succinic acid radical, and at  $m/z = 96$  is 2-methyl benzyl cation. The minor products corresponding to peak position at  $m/z = 177$  is 3-diazonium naphthalene-1-ol, at  $m/z = 105.5$  is 2-ethyl benzyl cation (IV), and at  $m/z = 77$  is phenyl cation (VI) [52,53].

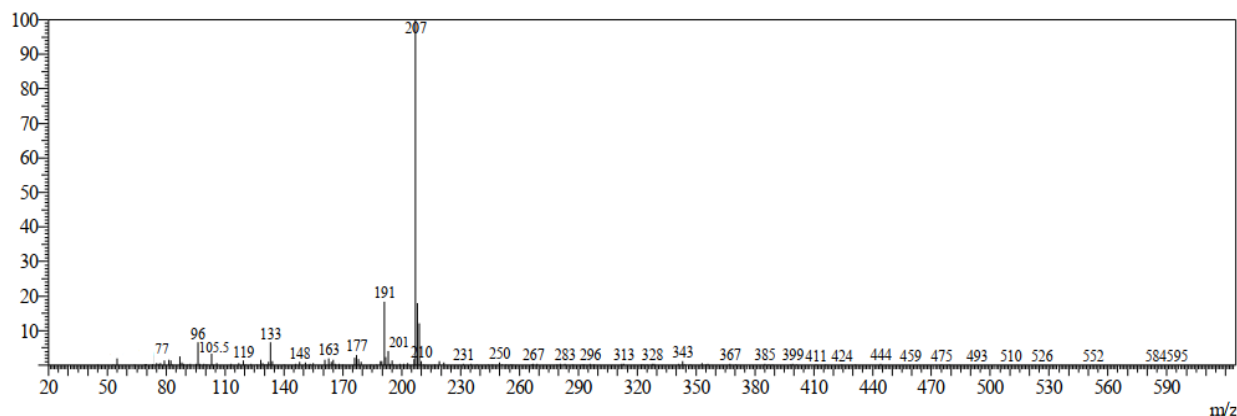


**Figure 4.18** Mass spectra of the metabolite of CR dye

The proposed degradation pathway of congo red is shown in Figure 4.19. Congo red dye mainly undergoes asymmetric cleavage producing sodium (4-amino-3-diazenyl naphthalene)-1-sulfonate (2 molecules) and diaminophenyl benzene (one molecule). Sodium (4-amino-3-diazenyl naphthalene)-1-sulfonate undergoes further dissociation to form compound-sodium (4-amino-3-diazenyl)-1 naphthaoxide (I) ( $m/z = 207$ ), 3-diazonium naphthalene-1-ol (II) ( $m/z = 177$ ), and succinic acid radical ( $m/z = 133$ ). Compound (II) transforms to form 2-diazoniumnaphthalene-1, 4-diol (III) ( $m/z = 191$ ), which further transforms to compound 2-ethyl benzyl cation (IV) ( $m/z = 105.5$ ) and 2-methyl benzyl cation (V) ( $m/z = 96$ ). In addition, diaminophenyl benzene transforms to form an intermediate compound aniline ( $m/z = 93$ ) which further dissociate to phenyl cation (VI) ( $m/z = 77$ ). Further, these compounds are transformed into smaller molecules such as carbon dioxide and water molecule.

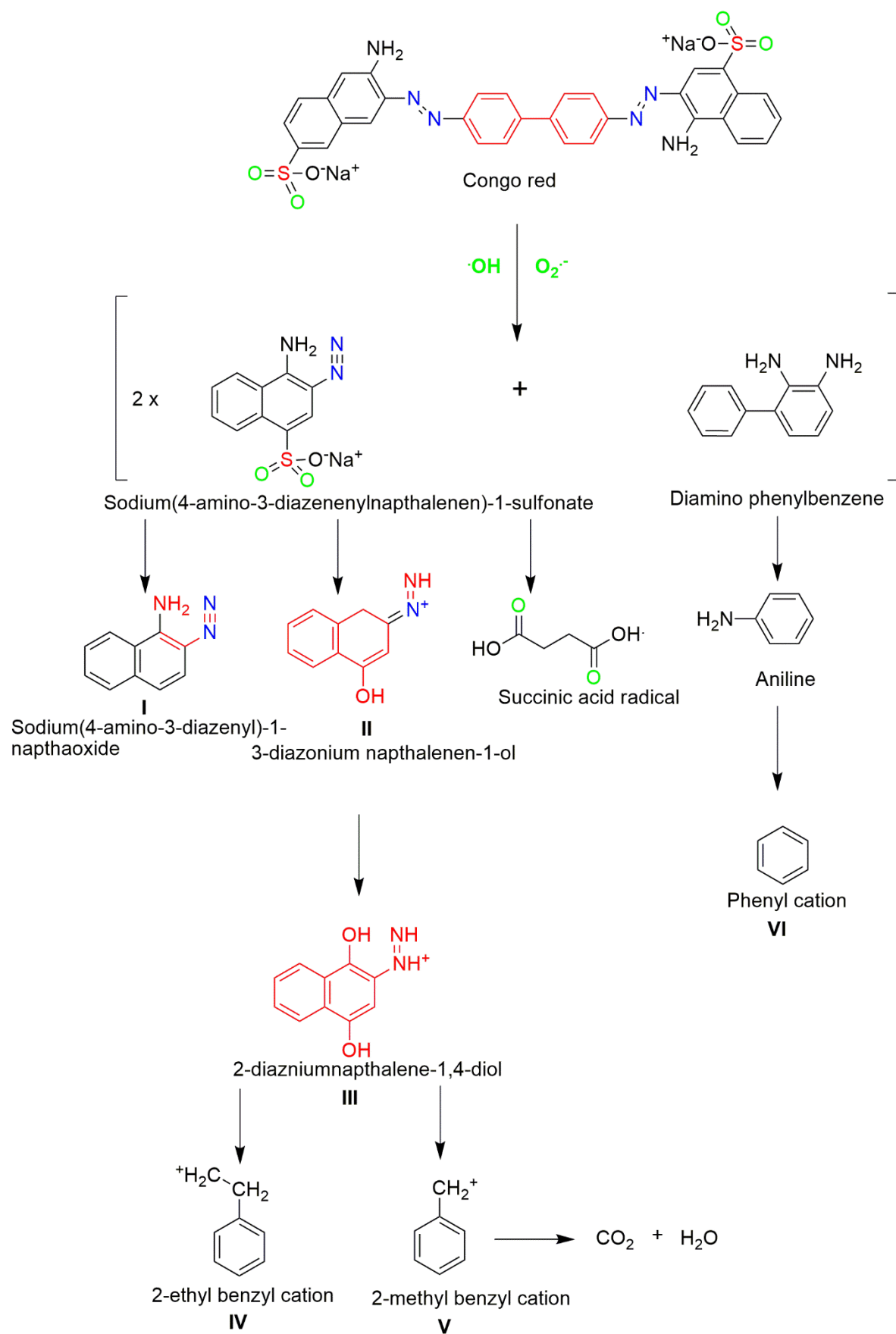


**Figure 4.19** Proposed degradation pathway for the degradation of CR over FDT/PAC nanocomposite [54]

### 4.3.8 Photocatalytic inactivation

Over the past two decades, photocatalytic inactivation of microorganisms has led to immense applications of this technique for the elimination of microbial contaminants from water [16,55,56]. In the present study, the activity of FDT/PAC, and bare  $\text{TiO}_2$  nanomaterial were evaluated for the inactivation of *E. coli* and *S. aureus* under visible light irradiation. Two control experiments were performed, which included: light control (visible light alone without nanocomposite), dark control (0.05 g nanocomposite alone without visible light), and the results are shown in Figure 4.20 (a) and (b).

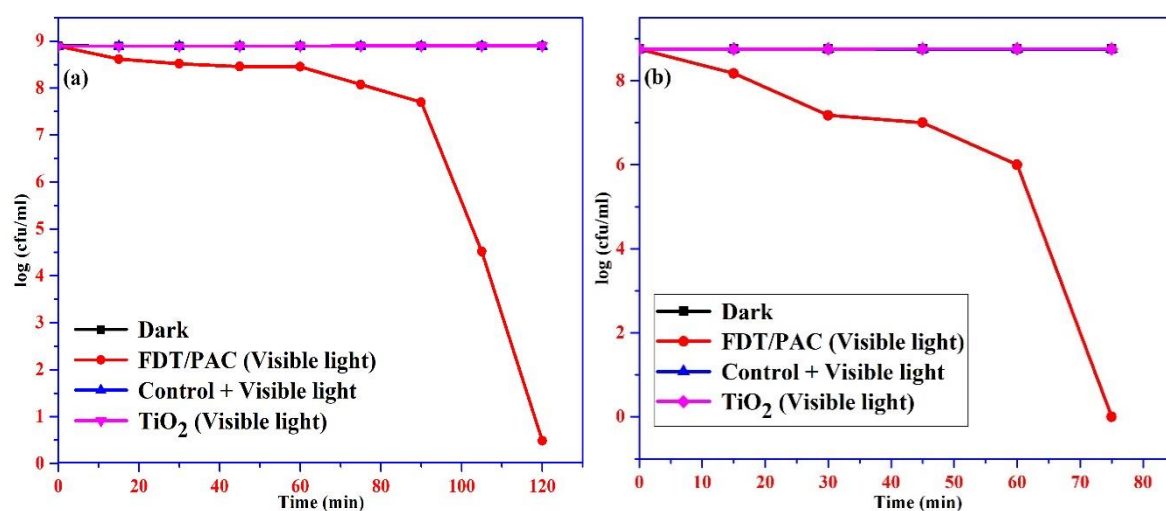


**Figure 4.20** Photocatalytic inactivation of (a) *E. coli*, (b) *S. aureus* as a function of time

From the graph, it is evident that only light (without the nanocomposite) or nanocomposite (without light) cannot inactivate the concerned bacteria [57]. Also, bare  $\text{TiO}_2$  nanomaterial did not show any antibacterial activity in presence of visible light irradiation. But the inactivation of *E. coli* and *S. aureus* were observed with the FDT/PAC nanocomposite in the presence of light as shown in Figures 4.21 and 4.22.



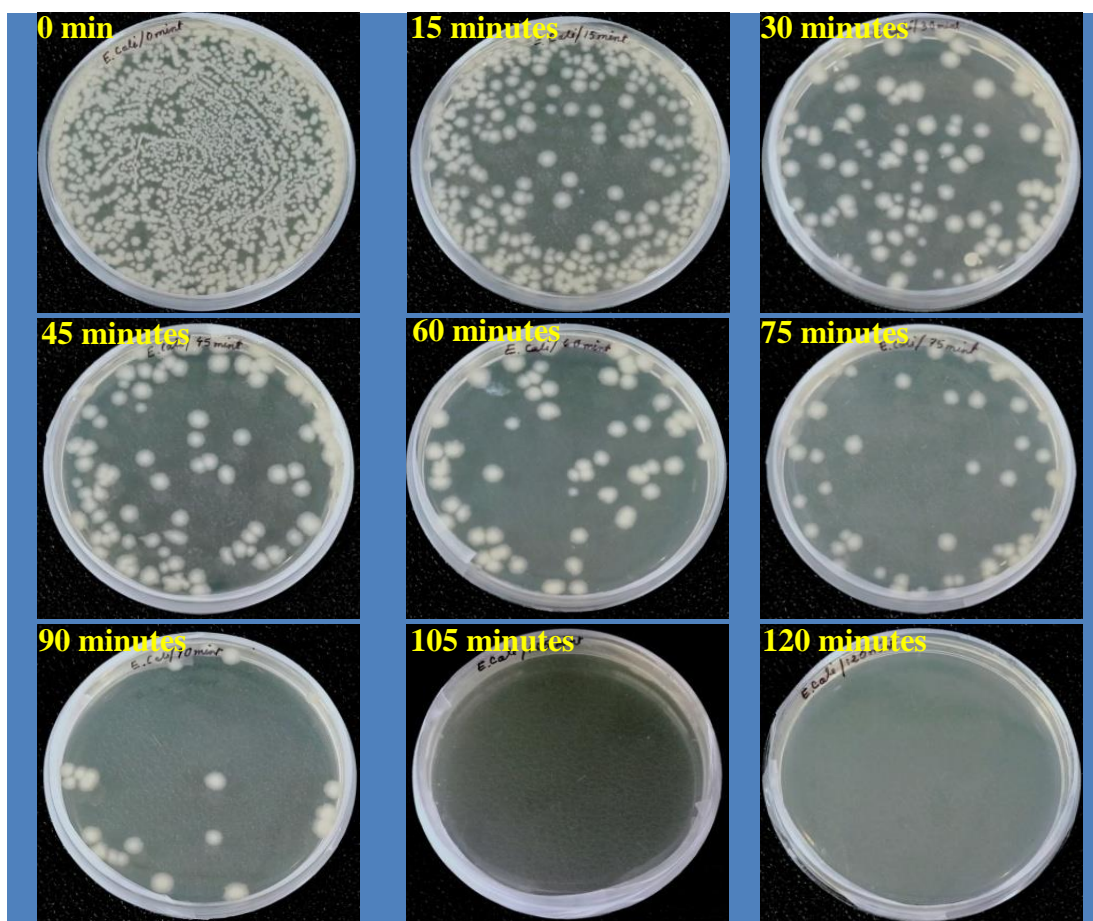


**Figure 4.21** Photographs of photocatalytic inactivation of *E. coli* at different light exposure times

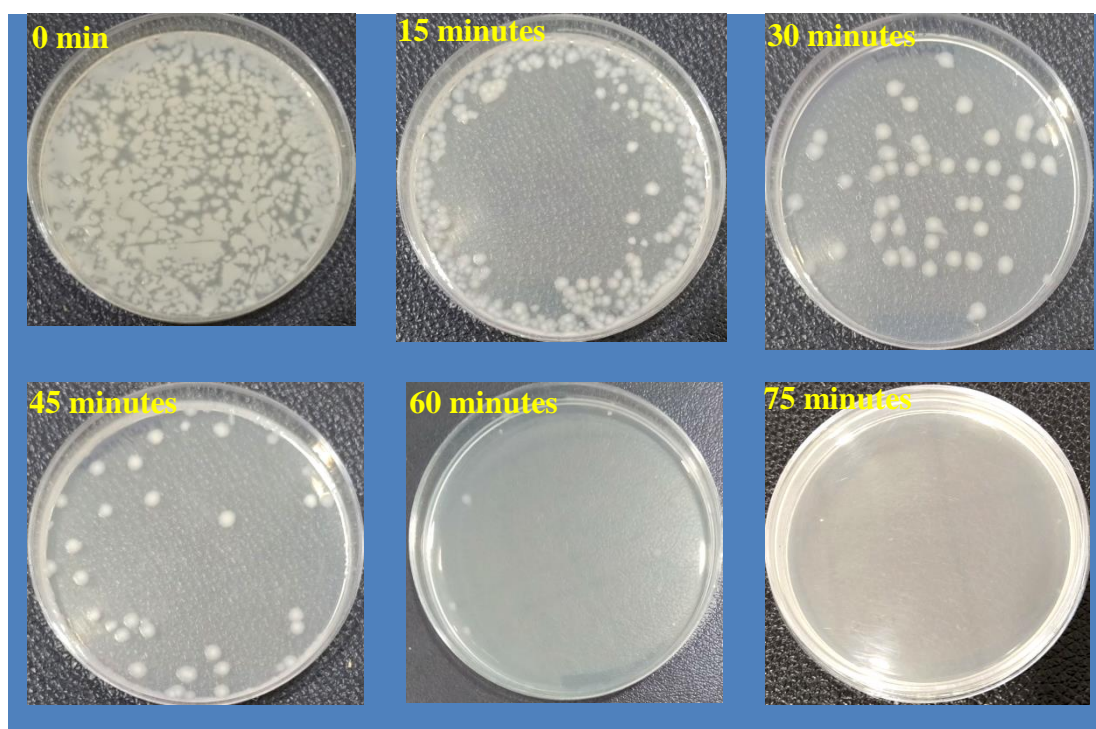


**Figure 4.22** Photographs of photocatalytic inactivation of *S. aureus* at different light exposure times

The figures show that 100% inactivation of *E. coli* and *S. aureus* occurs within 120 minutes and 75 minutes. In the photocatalytic process, irradiation of light on the catalyst creates electrons and holes pairs, which initiate the bacterial inactivation process [58]. The Fe-doped nanocomposite produces a new higher energy level on the conduction band of TiO<sub>2</sub> and the photogenerated electrons (e<sup>-</sup>) are then excited from the Fe defect state to the TiO<sub>2</sub> conduction band. Due to the efficient trapping of electron-hole pairs, more holes (h<sup>+</sup>) are formed in the valance band. The photogenerated h<sup>+</sup> can then react with adsorbed water molecules and hydroxide ions to form hydroxyl radicals (·OH). Thereafter, the electron on the conduction band of TiO<sub>2</sub> combines with the adsorbed water molecules and oxygen ions to produce dioxygen radical (·O<sub>2</sub><sup>-</sup>) and this reacts with hydrogen (H<sup>+</sup>) ions to form hydrogen peroxide (H<sub>2</sub>O<sub>2</sub>) and this further generates hydroxyl radicals (·OH). The in-situ generated hydroxyl radicals and dioxygen radicals are highly reactive and react with the *E. coli* and *S. aureus* and degrade the cell walls and membranes of the bacteria, leading to the inactivation of bacteria in the manner, which has been explained by several authors earlier (Figure 4.23) [59–63].

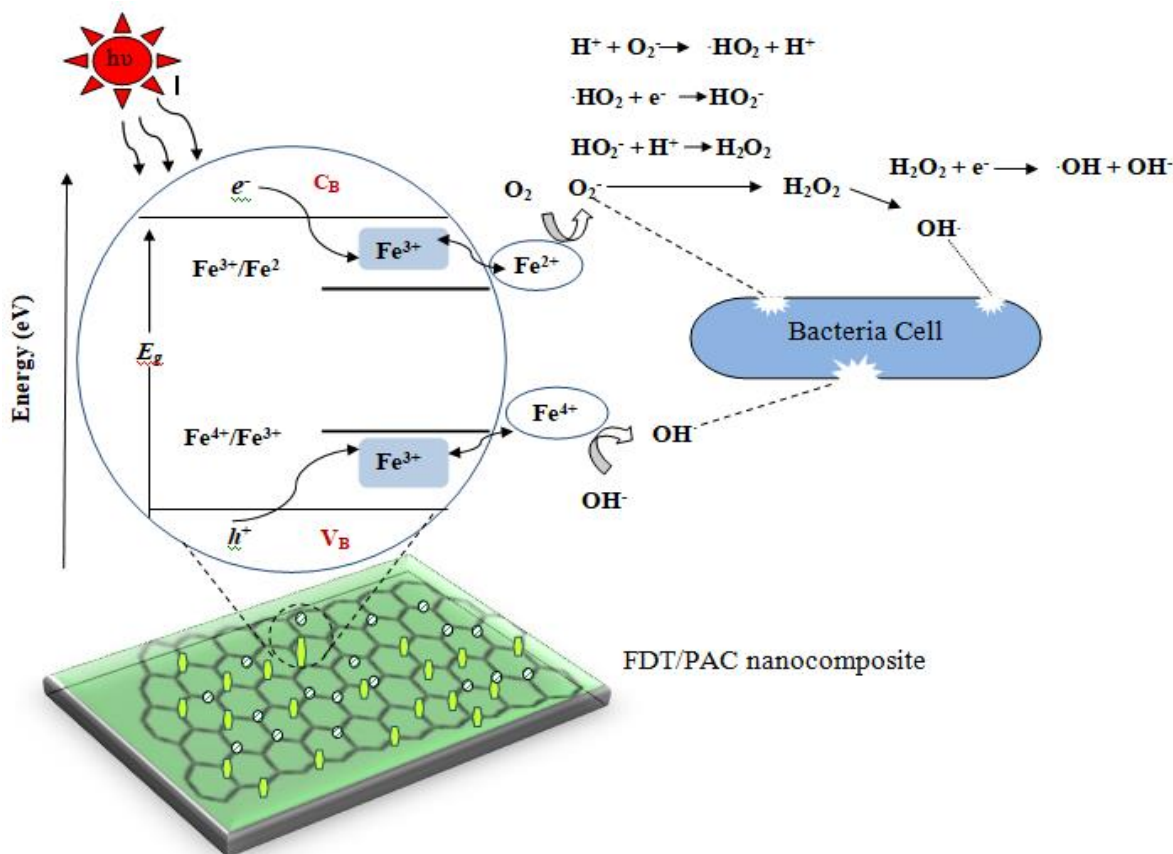


**Figure 4.23** A schematic diagram showing the mechanism of photocatalytic inactivation of bacteria using FDT/PAC nanocomposite



The Weibull inactivation model was employed to understand the bacterial inactivation mechanism and is given as equation 4.8:

$$\frac{N_t}{N_0} = e^{-Kt} \quad (4.8)$$

where  $N_0$  is the initial number of bacteria and  $N_t$  is the number of surviving bacteria at time  $t$  (min).  $K$  is the bacterial disinfection rate constant ( $\text{min}^{-1}$ ) and it is calculated from the slope of the curve [64] and presented in Table 4.3.

<b>Table 4.3</b> Rate constant of bacterial photocatalytic inactivation of <i>E. coli</i> and <i>S. aureus</i>		
<b>Nanocomposite</b>	<b><i>E. coli</i></b>	<b><i>S. aureus</i></b>
	Rate constant [ $k \times 10^{-3} (\text{min}^{-1})$ ]	Rate constant [ $k \times 10^{-3} (\text{min}^{-1})$ ]
FDT/PAC + Visible light	66.67	92.2

As seen from Table 4.3, the inactivation rate constant for *S. aureus* is 1.3 times more than that for *E. coli*. This indicates that gram-positive *S. aureus* was more sensitive to photocatalytic inactivation than gram-negative *E. coli* and this is in agreement with the previously published reports [65–68]. This could be due to the more complex cell wall structure of *E. coli* than gram-positive *S. aureus* as proposed by Yadav *et al.* [18]. Gram-positive bacteria have cell walls with thick layers of peptidoglycan while gram-negative bacteria have cell walls with thin layers of peptidoglycan and contain an outer cell membrane with lipopolysaccharide molecules. Due to the presence of an extra outer cell membrane in gram-negative bacteria, the penetration of species through the cell layer is difficult [67]. Therefore, a more number of hydroxyl radicals are required to attack the gram-negative bacteria as compared with the gram-positive bacteria for bacterial inactivation.

### 4.3.9 Energy consumption and cost analysis

#### (a) Electrical energy determination

The photocatalytic degradation of congo red dye using visible light irradiated FDT/PAC nanocomposite is an electrical energy-driven process, accordingly operating costs are involved. The electrical energy consumed while running the experiment is a major source of operating costs. Therefore, measuring the electric energy per order ( $E_{EO}$ ) for CR degradation can be a useful and informative way to calculate the expenses during the reaction and it can be calculated as [69]:

$$E_{EO} = \frac{P \times t \times 1000}{V \times 60 \times \log\left(\frac{C_i}{C_e}\right)} \quad (4.9)$$

where  $P$  = input power (kW),  $V$  = volume of CR (L),  $C_i$  = initial CR concentration,  $C_e$  = final CR concentration,  $t$  = irradiation time (minute).

By combining the Langmuir-Hinshelwood pseudo-first-order rate equation 4.4 with equation 4.9, the  $E_{EO}$  for a pseudo-first-order reaction can be written as [70]:

$$E_{EO} = \frac{38.4 \times P}{V \times K_{app}} \quad (4.10)$$

where  $K_{app}$  = pseudo-first-order rate constant ( $\text{min}^{-1}$ ). The above equation 4.10 was used to calculate the model of electric energy per order for the pseudo-first-order batch reactor. Table 4.4 represents the  $E_{EO}$  (experimental) and  $E_{EO}$  (model) derived values for CR degradation using FDT/PAC nanocomposite. From the table, it can be observed that the consumption of electrical energy was more for higher CR concentrations. Experimental  $E_{EO}$  value accurately coincides with the kinetic model  $E_{EO}$  value which confirms that the photocatalytic degradation of CR follows pseudo-first-order rate kinetics.

<b>Table 4.4</b> Effect of CR dye concentration on electrical energy consumption						
<b>Experimental conditions</b>			<b>Apparent rate constant (<math>K_{app}</math>) (<math>\text{min}^{-1}</math>)</b>	<b><math>R^2</math></b>	<b><math>E_{EO}</math> experimental (<math>\text{kWh m}^{-3}\text{order}^{-1}</math>)</b>	<b><math>E_{EO}</math> model (<math>\text{kWh m}^{-3}\text{order}^{-1}</math>)</b>
<b>Initial Conc. (ppm)</b>	<b>FDT/PAC Conc. (<math>\text{g L}^{-1}</math>)</b>	<b>pH</b>				
20	0.06	1	0.05341	0.99	1764.69	1797.41
60	0.06	1	0.01854	0.98	5175.40	5177.99
100	0.06	1	0.01594	0.94	6007.85	6022.58

#### (b) Total operating cost

Cost estimation is an important parameter to understand the efficiency of the applied method. It can be measured by adding the total maintenance cost, operating cost, and capital cost. In this study, the total operating cost and energy consumed in CR degradation were calculated using the equations 4.11 and 4.12 [71]:

$$\text{Total operating cost} = \frac{\text{Energy consumed per mg of CR degradation (kWh)} \times \text{unit cost (INR/kWh)} \times 10^6}{\text{CR degradation (mg)}} \quad (4.11)$$

$$\text{Energy consumed per mg of CR degradation (kWh)} = \frac{\text{Power input (kW)} \times \text{Reaction time (min)}}{1000 \times 60} \quad (4.12)$$

Table 4.5 represents the total operating cost involved in the degradation of CR from wastewater. It is observed that a total of 312.50, 236.74, and 166.67 INR (Indian rupee) operating costs were utilized for 20 ppm, 60 ppm, and 100 ppm CR dye degradation using 0.06 g FDT/PAC nanocomposite. These operating costs are mainly dependent on the concentration of CR, amount of nanocomposite, and total electric cost in the photocatalytic reactor without considering the cost involved in capital cost and maintenance cost.

<b>Table 4.5</b> Cost analysis of CR degradation in the photocatalytic reactor under different operating conditions						
<b>Congo red Conc. (ppm) <math>C_1</math></b>	<b>FDT/PAC Conc. (<math>\text{g L}^{-1}</math>) <math>C_2</math></b>	<b>Congo red Degradation Efficiency (%) <math>C_4</math></b>	<b>Congo red degradation (mg) <math>C_5 = [(C_1 \times C_4/100) \times \text{working volume}]</math></b>	<b>Reaction time (minute) <math>C_6</math></b>	<b>Energy consumed per mg of Congo red degradation (kWh) <math>C_7 = [(P \times C_6)/(1000 \times 60)]</math></b>	<b>Total operating cost (INR/kg of Congo red degradation) <math>C_8 = [(C_7 \times \text{unit cost} \times 10^6)/C_5]</math></b>
20	0.06	100	4	60	0.0005	312.50
60	0.06	88	10.56	120	0.001	236.74
100	0.06	75	15	120	0.001	166.67

(a) Total energy consumed (P) 0.5 kW [includes energy for electronic magnetic stirrer (50W), water pump (50W), exhaust fan (50W) and Visible lamp (350 W)] (b) Working volume of reactor 0.2 L and (c) Unit cost of power 2.5 INR ( $\text{kWh}^{-1}$ ).

### 4.3.10 Comparison studies

In the present study, the efficiency of the present FDT/PAC nanocomposite for photocatalytic degradation of CR is compared with other Fe-doped nanocomposites and is reported below in Table 4.6. Although different parameters were used by different authors, yet from the comparative study it can be observed that the present nanocomposite i.e., Fe-doped  $\text{TiO}_2$  supported on pine cone activated carbon shows an efficient activity towards congo red degradation with maximum degradation of 100% in 60 minutes using 0.06 g of the nanocomposite.

<b>Table 4.6</b> Comparison of catalytic activity of previous works in the literature with FDT/PAC nanocomposite							
<b>Nanocomposite</b>	<b>Pollutant</b>	<b>Mass (<math>\text{g L}^{-1}</math>)</b>	<b>Volume (ml)</b>	<b><math>C_i</math></b>	<b>Contact time (minute)</b>	<b>% degradation</b>	<b>Source</b>
Fe- $\text{TiO}_2$ /coconut shell AC	Dye wastewater	6.00	300	-	60	-	[7]
Fe- $\text{TiO}_2$ /commercial AC	Reactive Red 198	1.00	1000	-	-	-	[8]
Fe- $\text{TiO}_2$ /reduced graphene oxide	Rhodamine B	0.60	-	20 ppm	120	91.00	[28]
Fe- $\text{TiO}_2$ /zeolite	Methylene blue	1.00	1000	20 ppm	60	98.00	[72]
Fe- $\text{TiO}_2$ /walnut shells AC	Azo dye	0.25	-	4 mM	240	87.50	[73]
Fe- $\text{TiO}_2$ /Zeolites	Methylene blue	1.00	-	25 ppm	90	92.00	[74]
Fe-commercial AC/ $\text{TiO}_2$	Methylene blue	0.10	-	$1 \times 10^{-4}$ M	120	-	[75]
Fe- $\text{TiO}_2$ /coconut shell AC	Reactive brilliant red K2G	0.50	200	20 ppm	180	100.00	[76]
Mn, Mo, La/ $\text{TiO}_2$ /AC	Reactive Red 198	2.00	-	20 ppm	240	91.00	[77]
<b>FDT/PAC</b>	<b>Congo red</b>	<b>0.06</b>	<b>200</b>	<b>20 ppm</b>	<b>60</b>	<b>100.00</b>	<b>Present study</b>

#### 4.4 Conclusion

Fe-doped TiO<sub>2</sub> nanocomposite supported on activated carbon was synthesized using an ultrasonic-hydrothermal method. The characterization results confirmed the presence of Fe ions on the TiO<sub>2</sub> activated carbon nanocomposite. It is observed that doping of Fe<sup>3+</sup> ions reduced the optical bandgap of the nanocomposite from 3.2 to 2.3 eV. Additionally, activated carbon enhanced the surface area and separates the photo-induced electrons and electrons-holes thus inhibiting their rapid recombination which extends the electron's lifetime and increases the photocatalytic efficiency. The FDT/PAC nanocomposite could be effectively used for 100% degradation of 20 ppm congo red dye solution within 60 minutes. The photocatalytic degradation of CR followed the pseudo-first-order rate kinetics with an apparent rate constant of 0.05341 min<sup>-1</sup> and a half-life period of 12.97 minutes. The thermodynamics study revealed that the degradation process is exothermic and spontaneous. The presence of interfering ions such as glycine, EDTA, copper sulphate, cadmium nitrate, and zinc chloride affects mostly the degradation of CR by FDT/PAC, indicating that hydroxyl radicals are the dominant reactive species in the CR degradation process. The FDT/PAC nanocomposite has excellent regeneration properties and it degrades around 64% CR at the fifth cycle of use. The GC-MS analysis showed the formation of low molecular weight less harmful and green products such as phenyl cation, carbon dioxide, and water by the attack of hydroxyl radical on CR. The FDT/PAC nanocomposite was very effective in photocatalytic inactivation of bacteria *E. coli* and *S. aureus*. The maximum inactivation of *E. coli* was achieved within 120 minutes and *S. aureus* within 75 minutes under visible light irradiation. Experimental E<sub>EO</sub> and model E<sub>EO</sub> were found to accurately coincide with each other thereby confirming that the photocatalytic degradation of CR follows pseudo-first-order kinetics. The total operating cost was found to be 312.50, 236.74, and 166.67 INR for 20 ppm, 60 ppm, and 100 ppm CR dye degradation using 0.06 g FDT/PAC nanocomposite. Thus the Fe-doped TiO<sub>2</sub> activated carbon nanocomposite can be a promising photocatalyst for future environmental applications.

**References**

- [1] K. Kumar, A. Chowdhury, Use of Novel Nanostructured Photocatalysts for the Environmental Sustainability of Wastewater Treatments, *Encycl. Renew. Sustain. Mater.* (2018) 949–965. doi:10.1016/b978-0-12-803581-8.11149-x.
- [2] A. Omo Ibadon, P. Fitzpatrick, Heterogeneous Photocatalysis: Recent Advances and Applications, *Catalysts*. 3 (2013) 189–218. doi:10.3390/catal3010189.
- [3] M.M. Khan, S.F. Adil, A. Al-Mayouf, S.F. Adil, Metal Oxides as Photocatalysts, *J. Saudi Chem. Soc.* 19 (2015) 462–464. doi:10.1016/j.jscs.2015.04.003.
- [4] J. Ma, H. He, F. Liu, Effect of Fe on the photocatalytic removal of NO<sub>x</sub> over visible light responsive Fe/TiO<sub>2</sub> catalysts, *Appl. Catal. B Environ.* 179 (2015) 21–28. doi:10.1016/j.apcatb.2015.05.003.
- [5] K. Kumar Mandari, A. Kumar Reddy Police, J. Yeon Do, M. Kang, C. Byon, Rare earth metal Gd influenced defect sites in N doped TiO<sub>2</sub>: Defect mediated improved charge transfer for enhanced photocatalytic hydrogen production, *Int. J. Hydrogen Energy*. 43 (2018) 2073–2082. doi:10.1016/j.ijhydene.2017.12.050.
- [6] M. Khairy, W. Zakaria, Effect of metal-doping of TiO<sub>2</sub> nanoparticles on their photocatalytic activities toward removal of organic dyes, *Egypt. J. Pet.* 23 (2014) 419–426. doi:10.1016/j.ejpe.2014.09.010.
- [7] Y. Li, J. Chen, J. Liu, M. Ma, W. Chen, L. Li, Activated carbon supported TiO<sub>2</sub>-photocatalysis doped with Fe ions for continuous treatment of dye wastewater in a dynamic reactor, *J. Environ. Sci.* 23 (2011) 1129–1134. doi:10.1016/S1001-0742(10)60524-4.
- [8] A. Eshaghi, H. Moradi, Optical and photocatalytic properties of the Fe-doped TiO<sub>2</sub> nanoparticles loaded on the activated carbon, *Adv. Powder Technol.* 29 (2018) 1879–1885. doi:10.1016/j.appt.2018.04.026.
- [9] K. Katrina P. Rivera, M. Daniel G. de Luna, T. Suwannaruang, K. Wantala, Photodegradation of Alachlor Over Fe-TiO<sub>2</sub> on Granular Activated Carbon Support under UV and Visible Light, in: *Int. Conf. Biol. Civ. Environ. Eng.*, 2014: pp. 208–210. doi:10.15242/iicbe.c0314179.
- [10] A. Nishimura, N. Ishida, D. Tatematsu, M. Hirota, A. Koshio, F. Kokai, E. Hu, Effect of Fe Loading Condition and Reductants on CO<sub>2</sub> Reduction Performance with Fe/TiO<sub>2</sub> Photocatalyst, *Int. J. Photoenergy*. 2017 (2017) 1–11. doi:10.1155/2017/1625274.
- [11] M. J. Valero-Romero, J. G. Santaclara, L. Oar-Arteta, L. van Koppen, D. Y. Osadchii, J. Gascon, F. Kapteijn, Photocatalytic properties of TiO<sub>2</sub> and Fe-doped TiO<sub>2</sub> prepared by metal organic framework-mediated synthesis, *Chem. Eng. J.* 360 (2019) 75–88. doi:10.1016/j.cej.2018.11.132.
- [12] W. Zhou, P. Zhang, W. Liu, Anatase TiO<sub>2</sub> nanospindle/activated carbon (AC) composite photocatalysts with enhanced activity in removal of organic contaminant, *Int. J. Photoenergy*. 2012 (2012) 28–30. doi:10.1155/2012/325902.

- [13] S. Mohammad, M. Alam, S. Katun Sela, A.K.M. Nayab-ul-hossain, M. Masud, K. Sajib, M.R. Hasan, Fully natural garment dyeing using tamarind leaves as mordant, *J. Text. Eng. Fash. Technol.* 3 (2017) 666–669. doi:10.15406/jteft.2017.03.00103.
- [14] E. Routoula, S. V Patwardhan, Degradation of Anthraquinone Dyes from Effluents : A Review Focusing on Enzymatic Dye Degradation with Industrial Potential, *Environ. Sci. Technol.* 54 (2020) 647–664. doi:10.1021/acs.est.9b03737.
- [15] J.L. Harry-asobara, I. Kamei, Characteristics of White-rot Fungus *Phlebia brevispora* TMIC33929 and Its Growth-Promoting Bacterium *Enterobacter* sp. TN3W-14 in the Decolorization of Dye-Contaminated Water, *Appl. Biochem. Biotechnol.* 189 (2019) 1183–1194. doi:10.1007/s12010-019-03062-6.
- [16] J. Wang, C. Li, H. Zhuang, J. Zhang, Photocatalytic degradation of methylene blue and inactivation of Gram-negative bacteria by TiO<sub>2</sub> nanoparticles in aqueous suspension, *Food Control.* 34 (2013) 372–377. doi:10.1016/j.foodcont.2013.04.046.
- [17] N. KrishnaRao Eswar, P. C Ramamurthy, G. Madras, Novel synergistic photocatalytic degradation of antibiotics and bacteria using V-N doped TiO<sub>2</sub> under visible light: State of nitrogen in V-doped TiO<sub>2</sub>, *New J. Chem.* 40 (2016) 3464–3475. doi:10.1039/C5NJ02861B.
- [18] H. M. Yadav, S. V. Otari, V. B. Koli, S. S. Mali, C. Kook Hong, S. H. Pawar, S. D. Delekar, Preparation and characterization of copper-doped anatase TiO<sub>2</sub> nanoparticles with visible light photocatalytic antibacterial activity, *J. Photochem. Photobiol. A Chem.* 280 (2014) 32–38. doi:10.1016/j.jphotochem.2014.02.006.
- [19] B. Zhang, S. Zou, R. Cai, M. Li, Z. He, Highly-efficient Photocatalytic Disinfection of *Escherichia coli* under Visible Light Using Carbon Supported Vanadium Tetrasulfide Nanocomposites, *Appl. Catal. B, Environ.* 224 (2018) 383–393. doi:10.1016/j.apcatb.2017.10.065.
- [20] G. Veréb, L. Manczinger, G. Bozsó, A. Sienkiewicz, L. Forró, K. Mogyorósi, K. Hernádi, A. Dombi, Comparison of the photocatalytic efficiencies of bare and doped rutile and anatase TiO<sub>2</sub> photocatalysts under visible light for phenol degradation and *E. coli* inactivation, *Appl. Catal. B Environ.* 129 (2013) 566–574. doi:10.1016/j.apcatb.2012.09.045.
- [21] S. Mathew, P. Ganguly, S. Rhatigan, V. Kumaravel, C. Byrne, S. J. Hinder, J. Bartlett, M. Nolan, S. C. Pillai, Cu-Doped TiO<sub>2</sub>: Visible light assisted photocatalytic antimicrobial activity, *Appl. Sci.* 8 (2018) 1–20. doi:10.3390/app8112067.
- [22] H. Teng, S. Xu, D. Sun, Y. Zhang, Preparation of Fe-doped TiO<sub>2</sub> nanotubes and their photocatalytic activities under visible light, *Int. J. Photoenergy.* 2013 (2013) 1–7. doi:10.1155/2013/981753.
- [23] B.M. Babić, S.K. Milonjić, M.J. Polovina, B. V. Kaludierović, Point of zero charge and intrinsic equilibrium constants of activated carbon cloth, *Carbon N. Y.* 37 (1999) 477–481. doi:10.1016/S0008-6223(98)00216-4.
- [24] M. Thakur, G. Sharma, T. Ahamad, A.A. Ghfar, D. Pathania, M. Naushad, Efficient

- photocatalytic degradation of toxic dyes from aqueous environment using gelatin-Zr(IV) phosphate nanocomposite and its antimicrobial activity, *Colloids Surfaces B Biointerfaces*. 157 (2017) 456–463. doi:10.1016/j.colsurfb.2017.06.018.
- [25] M. Baruah, A. Supong, P. Chandra, B. Rituparna, K. Chubaakum, Batch sorption-photodegradation of Alizarin Red S using synthesized TiO<sub>2</sub>/activated carbon nanocomposite: an experimental study and computer modelling, *Nanotechnol. Environ. Eng.* 3 (2020) 1–13. doi:10.1007/s41204-020-00071-3.
- [26] S.H. Othman, S.A. Rashid, T. Idaty, M. Ghazi, N. Abdullah, Fe-Doped TiO<sub>2</sub> Nanoparticles Produced via MOCVD : Synthesis, Characterization, and Photocatalytic Activity, *J. Nanomater.* 2011 (2011) 1–8. doi:10.1155/2011/571601.
- [27] K. Song, S. Lee, C.Y. Suh, W. Kim, K.S. Ko, D. Shin, Synthesis and characterization of Iron Oxide nanoparticles prepared by Electrical Explosion of Fe Wire in Ar-O<sub>2</sub> gas Mixtures, *Mater. Trans.* 53 (2012) 2056–2059. doi:10.2320/matertrans.M2012186.
- [28] A.A. Isari, A. Payan, M. Fattahi, S. Jorfi, B. Kakavandi, Photocatalytic degradation of rhodamine B and real textile wastewater using Fe-doped TiO<sub>2</sub> anchored on reduced graphene oxide (Fe-TiO<sub>2</sub>/rGO): Characterization and feasibility, mechanism and pathway studies, *Appl. Surf. Sci.* 462 (2018) 549–564. doi:10.1016/j.apsusc.2018.08.133.
- [29] S. Sood, A. Umar, S. Kumar, S. Kumar, Highly effective Fe-doped TiO<sub>2</sub> nanoparticles photocatalysts for visible- light driven photocatalytic degradation of toxic organic compounds, *J. Colloid Interface Sci.* 450 (2015) 213–223. doi:10.1016/j.jcis.2015.03.018.
- [30] J. Shi, G. Chen, G. Zeng, A. Chen, K. He, Z. Huang, L. Hu, J. Zeng, J. Wu, W. Liu, Hydrothermal synthesis of graphene wrapped Fe-doped TiO<sub>2</sub> nanospheres with high photocatalysis performance, *Ceram. Int.* 44 (2018) 7473–7480. doi:10.1016/j.ceramint.2018.01.124.
- [31] M. Anwar Ismail, M. N. Hedhili, D. H. Anjum, V. Singaravelu, S. Ho Chung, Synthesis and Characterization of Iron-Doped TiO<sub>2</sub> nanoparticles Using Ferrocene from Flame Spray Pyrolysis, *Catalysts*. 11 (2021) 1–16. doi:10.3390/catal11040438.
- [32] C. Bathula, I. Rabani, S. Sekar, H.-K. Youi, J.-Y. Choy, A. Kadam, N.K. Shretha, Y.-S. Seo, H.-S. Kim, Enhanced removal of organic dye by activated carbon decorated TiO<sub>2</sub> nanoparticles from *Mentha Aquatica* leaves via ultrasonic approach, *Ceram. Int.* 47 (2021) 8732–8739. doi:10.1016/j.ceramint.2020.12.282.
- [33] N. Ramesh Reddy, U. Bharagav, M. Mamatha Kumari, K. K. Cheralathan, P. K. Ojha, M. V. Shankar, S. Woo Joo, Inclusion of low cost activated carbon for improving hydrogen production performance of TiO<sub>2</sub> nanoparticles under natural solar light irradiation, *Ceram. Int.* 47 (2021) 10216–10225. doi:10.1016/j.ceramint.2020.10.187.
- [34] H. Belayachi, B. Bestani, N. Benderdouche, M. Belhakem, The use of TiO<sub>2</sub> immobilized into grape marc-based activated carbon for RB-5 Azo dye photocatalytic degradation, *Arab. J. Chem.* 12 (2015) 3018–3027. doi:10.1016/j.arabjc.2015.06.040.



- [35] P.R. Chowdhury, K.G. Bhattacharyya, Synthesis and characterization of Mn/Co/Ti LDH and its utilization as a photocatalyst in visible light assisted degradation of aqueous Rhodamine B, *RSC Adv.* 6 (2016) 112016–112034. doi:10.1039/c6ra24288j.
- [36] T. Daimon, H. Naruse, H. Watanabe, H. Oda, A. Yamanaka, Study of blue photoluminescence in titanium doped Al<sub>2</sub>O<sub>3</sub> Single-Crystals, *IOP Conf. Ser. Mater. Sci. Eng.* 18 (2011) 1–4. doi:10.1088/1757-899X/18/10/102012.
- [37] R.K. Hasibur, K.A. Kumar, Titanium-di-oxide (TiO<sub>2</sub>) concentration-dependent optical and morphological properties of PANi-TiO<sub>2</sub> nanocomposite, *Mater. Sci. Semicond. Process.* 105 (2020) 1–11. doi:10.1016/j.mssp.2019.104745.
- [38] H. Moradi, A. Eshaghi, S.R. Hosseini, K. Ghani, Fabrication of Fe-doped TiO<sub>2</sub> nanoparticles and investigation of photocatalytic decolorization of reactive red 198 under visible light irradiation, *Ultrason. Sonochem.* 32 (2016) 314–319. doi:10.1016/j.ultsonch.2016.03.025.
- [39] X. Li, R. Shen, S. Ma, X. Chen, J. Xie, Graphene-based heterojunction photocatalysts, *Appl. Surf. Sci.* 430 (2018) 53–107. doi:10.1016/j.apsusc.2017.08.194.
- [40] P. Chandra Bhomick, A. Supong, M. Baruah, C. Pongener, D. Sinha, Pine Cone biomass as an effecient precursor for the synthesis of activated biocarbon for adsorption of anionic dye from aqueous solution: Isotherm, kinetic, thermodynamic and regeneration studies, *Sustain. Chem. Pharm.* 10 (2018) 41–49. doi:10.1016/j.scp.2018.09.001.
- [41] J.M.C. Robertson, P.K.J. Robertson, L.A. Lawton, A comparison of the effectiveness of TiO<sub>2</sub> photocatalysis and UVA photolysis for the destruction of three pathogenic micro-organisms, *J. Photochem. Photobiol. A Chem.* 175 (2005) 51–56. doi:10.1016/j.jphotochem.2005.04.033.
- [42] Z. Ghasemi, H. Younesi, A.A. Zinatizadeh, Kinetics and thermodynamics of photocatalytic degradation of organic pollutants in petroleum refinery wastewater over nano-TiO<sub>2</sub> supported on Fe-ZSM-5, *J. Taiwan Inst. Chem. Eng.* 65 (2016) 357–366. doi:10.1016/j.jtice.2016.05.039.
- [43] K. Mamun Reza, R. ASW, G. Fahmida, Parameters affecting the photocatalytic degradation of dyes using TiO<sub>2</sub>: a review, *Appl. Water Sci.* 7 (2017) 1569–1578. doi:10.1007/s13201-015-0367-y.
- [44] S. Sood, S. Kumar Mehta, Aa. Umar, S. Kumar Kansal, The visible light-driven photocatalytic degradation of Alizarin red S using Bi-doped TiO<sub>2</sub> nanoparticles, *New J. Chem.* 38 (2014) 3127–3136. doi:10.1039/c4nj00179f.
- [45] S. Kaur, V. Singh, Visible light induced sonophotocatalytic degradation of Reactive Red dye 198 using dye sensitized TiO<sub>2</sub>, *Ultrason. Sonochem.* 14 (2007) 531–537. doi:10.1016/j.ultsonch.2006.09.015.
- [46] E. -tae Yun, H. -Young Yoo, W. Kim, H. -Eun Kim, G. Kang, H. Lee, S. Lee, T. Park, C. Lee, J. -Hong Kim, J. Lee, Visible-light-induced activation of periodate that mimics dye-sensitization of TiO<sub>2</sub>: Simultaneous decolorization of dyes and production of oxidizing radicals, *Appl. Catal. B, Environ.* 203 (2017) 475–484.

- doi:10.1016/j.apcatb.2016.10.029.
- [47] A. E. Eliyas, L. Ljutzkanov, I. D. Stambolova, V. N. Blaskov, S. V. Vassilev, E. N. Razkazova-velkova, D. R. Mehandjiev, Visible light photocatalytic activity of TiO<sub>2</sub> deposited on activated carbon, *Cent. Eur. J. Chem.* 11 (2013) 3–5. doi:10.2478/s11532-012-0183-2.
- [48] S. Jothivel, R. Velmurugan, K. Selvam, B. Krishnakumar, M. Swaminathan, Preparation, characterization and photocatalytic activity of acidic sulfated nano titania for the degradation of Reactive Orange 4 under UV light, *Sep. Purif. Technol.* 77 (2011) 245–250. doi:10.1016/j.seppur.2010.12.014.
- [49] Gunture, A. Singh, A. Bhati, P. Khare, K. Malika Tripathi, S. Kumar Sankar, Soluble Graphene Nanosheets for the Sunlight-Induced Photodegradation of the Mixture of Dyes and its Environmental Assessment, *Sci. Rep.* 9 (2019) 1–12. doi:10.1038/s41598-019-38717-1.
- [50] P. Zheng, Z. Pan, H. Li, B. Bai, W. Guan, Effect of different type of scavengers on the photocatalytic removal of copper and cyanide in the presence of TiO<sub>2</sub>@yeast hybrids, *J. Mater. Sci. Mater. Electron.* 26 (2015) 6399–6410. doi:10.1007/s10854-015-3229-3.
- [51] N. Zhang, G. Liu, H. Liu, Y. Wang, Z. He, G. Wang, Diclofenac photodegradation under simulated sunlight: Effect of different forms of nitrogen and Kinetics, *J. Hazard. Mater.* 192 (2011) 411–418. doi:10.1016/j.jhazmat.2011.05.038.
- [52] U. O. Bhagwat, J. J. Wu, A. M. Asiri, S. Anandan, Sonochemical Synthesis of MgTiO<sub>2</sub> nanoparticles for persistent Congo red dye degradation, *J. Photochem. Photobiol. A Chem.* 336 (2017) 559–569. doi:10.1016/j.jphotochem.2017.06.043.
- [53] D. Iark, A. Júlia dos Reis Buzzo, J. Amanda Andrade Garcia, V. Gesser Corrêa, C. Vieira Helm, R. Carvalho Gomes Corrêa, R. A. Peralta, R. de Fátima Peralta Muniz Moreira, A. Bracht, R. Marina Peralta, Enzymatic degradation and detoxification of azo dye Congo red by a new laccase from *Oudemansiella canarii*, *Bioresour. Technol.* 289 (2019) 1–7. doi:10.1016/j.biortech.2019.121655.
- [54] U. O. Bhagwat, J. J. Wu, A. M. Asiri, S. Anandan, Photocatalytic Degradation of Congo Red Using PbTiO<sub>3</sub> Nanorods Synthesized via a Sonochemical Approach, *Chem. Sel.* 3 (2018) 11851–11858. doi:10.1002/slct.201802303.
- [55] N.R. Srinivasan, P.A. Shankar, R. Bandyopadhyaya, Plasma treated activated carbon impregnated with silver nanoparticles for improved antibacterial effect in water disinfection, *Carbon N. Y.* 57 (2013) 1–10. doi:10.1016/j.carbon.2013.01.008.
- [56] S. Boonyod, W. Sutthisripok, L. Sikong, Antibacterial Activity of TiO<sub>2</sub> and Fe<sup>3+</sup> doped TiO<sub>2</sub> Nanoparticles Synthesized at Low Temperature, *Adv. Mater. Res.* 214 (2011) 197–201. doi:10.4028/www.scientific.net/AMR.214.197.
- [57] H.M. Yadav, S. V Otari, R.A. Bohara, S.H. Pawar, S.D. Delekar, Synthesis and visible light photocatalytic antibacterial activity of nickel-doped TiO<sub>2</sub> nanoparticles against gram-positive and gram-negative bacteria, *J. Photochem. Photobiol. A Chem.* 294 (2014) 130–136. doi:10.1016/j.jphotochem.2014.07.024.

- [58] H.M.M. Ibrahim, Photocatalytic degradation of methylene blue and inactivation of pathogenic bacteria using silver nanoparticles modified titanium dioxide thin films, *World J. Microbiol. Biotechnol.* 31 (2015) 1049–1060. doi:10.1007/s11274-015-1855-9.
- [59] W. Wang, J. C. Yu, P. Keung Wong, Photocatalysts for Solar-Induced Water Disinfection: New Developments and Opportunities, *Mater. Sci. Forum.* 734 (2013) 63–89. doi:10.4028/www.scientific.net/MSF.734.63.
- [60] Q. Chen, J. Li, Y. Wu, F. Shen, M. Yao, Biological responses of Gram-positive and Gram-negative bacteria to nZVI ( $\text{Fe}^0$ ),  $\text{Fe}^{2+}$  and  $\text{Fe}^{3+}$ , *RSC Adv.* 3 (2013) 13835–13842. doi:10.1039/c3ra40570b.
- [61] S. Huang, Y. Xu, M. Xie, Y. Ma, J. Yan, Y. Li, Y. Zhao, H. Xu, H. Li, Multifunctional C-Doped  $\text{CoFe}_2\text{O}_4$  Material as Cocatalyst to Promote Reactive Oxygen Species Generation over Magnetic Recyclable C– $\text{CoFe}/\text{AgACS}$ – $\text{AgX}$  Photocatalysts, *ACS Sustain. Chem. Eng.* 6 (2018) 11968–11978. doi:10.1021/acssuschemeng.8b02279.
- [62] J. Jeong, J.E.E. Yeon Kim, J. Yoon, The Role of Reactive Oxygen Species in the Electrochemical Inactivation of Microorganisms, *Environ. Sci. Technol.* 40 (2006) 6117–6122. doi:10.1021/es0604313.
- [63] R. Oxygen, S. Ros, Insights into the Photocatalytic Bacterial Inactivation by Flower-Like  $\text{Bi}_2\text{WO}_6$  under Solar or Visible Light, Through in situ Monitoring and Determination of Reactive Oxygen Species (ROS), *Water.* 12 (2020) 1–19. doi:10.3390/w12041099.
- [64] M.T. Taghizadeh, V. Siyahi, H. Ashassi-Sorkhabi, G. Zarrini,  $\text{ZnO}$ ,  $\text{AgCl}$  and  $\text{AgCl}/\text{ZnO}$  nanocomposites incorporated chitosan in the form of hydrogel beads for photocatalytic degradation of MB, *E. coli* and *S. aureus*, *Int. J. Biol. Macromol.* 147 (2020) 1018–1028. doi:10.1016/j.ijbiomac.2019.10.070.
- [65] H.A. Foster, I.B. Ditta, S. Varghese, Photocatalytic disinfection using titanium dioxide: spectrum and mechanism of antimicrobial activity, *Appl Microbiol Biotechnol.* 90 (2011) 1847–1868. doi:10.1007/s00253-011-3213-7.
- [66] G. Fu, P.S. Vary, C. Lin, Anatase  $\text{TiO}_2$  Nanocomposites for Antimicrobial Coatings, *J. Phys. Chem. B.* 109 (2005) 8889–8898. doi:10.102/jp0502196.
- [67] L. Caballero, K. A. Whitehead, N. S. Allen, J. Verran, Inactivation of *Escherichia coli* on immobilized  $\text{TiO}_2$  using fluorescent light, *J. Photochem. Photobiol. A Chem.* 202 (2009) 92–98. doi:10.1016/j.jphotochem.2008.11.005.
- [68] L.K. Adams, D.Y. Lyon, P.J.J. Alvarez, Comparative eco-toxicity of nanoscale  $\text{TiO}_2$ ,  $\text{SiO}_2$ , and  $\text{ZnO}$  water suspensions, *Water Res.* 40 (2006) 3527–3532. doi:10.1016/j.watres.2006.08.004.
- [69] N. Daneshvar, A. Aleboyeh, A. R Khataee, The evaluation of electrical energy per order ( $E_{\text{EO}}$ ) for photooxidative decolorization of four textile dye solutions by the kinetic model, *Chemosphere.* 59 (2005) 761–767. doi:10.1016/j.chemosphere.2004.11.012.

- [70] M.A. Behnajady, H. Eskandarloo, M. Shokri, Influence of the chemical structure of organic pollutants on photocatalytic activity of TiO<sub>2</sub> nanoparticles: Kinetic analysis and evaluation of electrical energy per order (E<sub>EO</sub>), Dig. J. Nanomater. Biostructures. 6 (2011) 1887–1895.
- [71] M. A Vishnuganth, N. Remya, M. Kumar, N. Selvaraju, Photocatalytic degradation of carbofuran by TiO<sub>2</sub>-coated activated carbon: Model for kinetic, electrical energy per order and economic analysis, J. Environ. Manage. 181 (2016) 201–207. doi:10.1016/j.jenvman.2016.06.016.
- [72] G. Foura, N. Chouchou, A. Soualah, K. Kouachi, M. Guidotti, D. Robert, Fe-doped TiO<sub>2</sub> supported on HY zeolite for solar photocatalytic treatment of dye pollutants, Catalysts. 7 (2017) 1–16. doi:10.3390/catal7110344.
- [73] R. Nagargoje, S. Atalay, G.A. Ersoz, B. Palas, Photo-Fenton Oxidation of Azo Dyes in Textile Wastewaters in the Presence of Fe/AC and Fe-TiO<sub>2</sub>/AC Catalysts, Bombay Technol. 64 (2014) 45–53.
- [74] H. Taghvaei, M. Farhadian, N. Davari, S. Maazi, Preparation, characterization and photocatalytic degradation of methylene blue by Fe<sup>3+</sup> doped TiO<sub>2</sub> supported on natural zeolite using response surface methodology, Adv. Environ. Technol. 3 (2017) 205–216. doi:10.22104/aet.2018.2462.1124.
- [75] Z.-D. Meng, K. Zhang, W.-C. Oh, Preparation of Fe-AC/TiO<sub>2</sub> composites and pH dependence of their Photocatalytic activity for methylene blue, J. Korean Cryst. Growth Cryst. Technol. 19 (2009) 268–276.
- [76] L.I. Youji, L.I. Jing, M.A. Mingyuan, O. Yuzhu, Y.A.N. Wenbin, Preparation of TiO<sub>2</sub>/activated carbon with Fe ions doping photocatalyst and its application to photocatalytic degradation of reactive brilliant red K2G, Sci China Ser B-Chem. 52 (2009) 1113–1119. doi:10.1007/s11426-009-0169-x.
- [77] S. Jorfi, S. Mirali, A. Mostoufi, M. Ahmadi, Visible Light Photocatalytic Degradation of Azo Dye and a Real Textile Wastewater Using Mn, Mo, La/TiO<sub>2</sub>/AC Nanocomposite, Chem. Biochem. Eng. Q. 32 (2018) 215–227. doi:10.15255/CABEQ.2017.1261.

## CHAPTER 5

### **PHOTOCATALYTIC DEGRADATION OF ANTHRACENE USING Ni-DOPED TiO<sub>2</sub>/ACTIVATED CARBON NANOCOMPOSITE**

---

This chapter deals with the preparation of Ni-doped titanium dioxide nanocomposite supported on activated carbon using the hydrothermal synthesis method. The physicochemical characterization of the nanocomposite was done by different analytical methods like SEM-EDX, XRD, FT-IR, photoluminescence (PL), pH<sub>ZPC</sub>, and UV-Visible diffuse reflectance spectroscopy (DRS). The visible light active nanocomposite was used for the photocatalytic degradation of anthracene (ANT) from an aqueous solution. The degradation efficacy of the nanocomposite was evaluated by varying nanocomposite dosages, contact time, ANT concentrations, and pH of the solution. Kinetics and thermodynamics studies were carried out to understand the photocatalytic degradation behaviour of ANT. The effect of different interfering ions on photocatalytic degradation of ANT and also the reusability of the nanocomposite were studied. The photodegradation mechanism of ANT was studied using GC-MS analysis. The total electrical energy consumed and operating cost involved in the degradation process was also measured.

## 5.1 Introduction

The impact of Nanotechnology has expanded enormously over the years towards improving the performance of environmental technologies. Semiconductor metal oxide nanomaterials operating in advanced oxidation processes typically involve the formation of hydroxyl radicals ( $\cdot\text{OH}$ ), which are very strong oxidizing agents associated with the complete degradation of contaminants in wastewater [1]. Some examples of semiconductor-based metal oxide photocatalysts used for the same are  $\text{ZrO}_2$ ,  $\text{MgO}$ ,  $\text{TiO}_2$ ,  $\text{ZnO}$ ,  $\text{SiO}_2$ ,  $\text{CuCr}_2\text{O}_4$ , etc. [2]. Among the semiconductor metal oxides,  $\text{TiO}_2$  is the most broadly utilized photocatalyst because of its physicochemical stability, optical activity, cost-effectiveness, photostability, and low toxicity [3]. However, the use of  $\text{TiO}_2$  is limited predominantly because of the large energy barrier of anatase  $\text{TiO}_2$  (3.2 eV), which allows it to absorb only 3-5% of solar energy. The high recombination rate of photogenerated electron-hole pairs also further confines the photo quantum efficiency of  $\text{TiO}_2$  [4]. Hence, to resolve these problems it is preferred to modify the band energy of  $\text{TiO}_2$  either by doping metal/non-metal elements or by dye photosensitization [5–7]. To increase the photocatalytic efficiency of  $\text{TiO}_2$ , transition metal doping is one of the most efficient methods which decreases the energy barrier from 3.2 eV to below 3.0 eV [8]. This decrease in the energy gap shifts the photocatalytic activities from UV light to the visible light region. Among different transition metals, nickel (Ni) has been used as a dopant for  $\text{TiO}_2$ . Due to similar ionic radii of Ni with Ti (0.72 Å for Ni and 0.68 Å for Ti), it can be a substitute for the lattice structure of  $\text{TiO}_2$ . Doping  $\text{TiO}_2$  with Ni creates an impurity energy level on the conduction band of  $\text{TiO}_2$  which separates the electron-hole pair and lowers the energy barrier of  $\text{TiO}_2$ , and thereby enhancing the photocatalytic performance of  $\text{TiO}_2$  in the visible light region [9]. Application of Ni-doped  $\text{TiO}_2$  has widely been reported for the degradation of water pollutants [10–12], photochemical water splitting [13], hydrogen sensing [14], and solar cell applications [15]. It was reported that the Ni-doped  $\text{TiO}_2$  decreases the bandgap energy, and separates electron-hole pairs of  $\text{TiO}_2$ . Also, to avoid the separation and recovery difficulties of Ni-doped  $\text{TiO}_2$ , the catalyst is loaded on different support systems which restricts the agglomeration property of  $\text{TiO}_2$  nanomaterial [16].

Activated carbon (AC) containing lignocellulosic materials with highly developed surface area, porosity, and excellent adsorption characteristics enable AC the most suitable support system for catalysts. Such characteristics of AC have the potential to accumulate pollutant molecules present in the water around the photocatalyst surface. Thus,  $\text{TiO}_2$ -AC nanocomposite materials improve photocatalytic reaction rates towards pollutants degradation [17]. Contamination of



water with various toxic chemicals such as polychlorinated biphenyls, pentachlorophenols, hexachlorophenols, furans, and, polycyclic aromatic hydrocarbons, etc. has a major impact on human health and the environment [18]. Out of these toxic chemicals, polycyclic aromatic hydrocarbon (PAHs) is one of the most widely used organic compounds in industries. The contamination of water by PAHs might be due to low aqueous solubility, high volatility, high stability, and slow biodegradation capability [19]. Anthracene is the highly concentrated PAHs having low molecular weight with tricyclic aromatic hydrocarbon. Anthracene is a very toxic and allergenic, mutagenic, carcinogenic substance which is easily found in water. On exposure to anthracene into our body, it can directly affect the blood, intestines, stomach, skin, and lymph system, and swell the stomach and intestine [20]. Thus, the removal of this hazardous substance from water is of high concern.

Keeping in mind these environmental concerns, the present study aimed to synthesize nickel-doped  $\text{TiO}_2$  loaded on activated carbon (NDT/PAC) for possible application in the degradation of anthracene from water. The synergistic relationship between the surface adsorption and photocatalytic activity of the synthesized NDT/PAC was studied and compared with  $\text{TiO}_2$  loaded on activated carbon and also with  $\text{TiO}_2$  nanomaterial. The schematic illustration of the photodegradation of anthracene using NDT/PAC nanocomposite is reflected in Figure 5.1. This could be one of the first pieces of work to focus the use of nickel-doped  $\text{TiO}_2$  loaded on activated carbon nanocomposite for degradation of anthracene from wastewater.

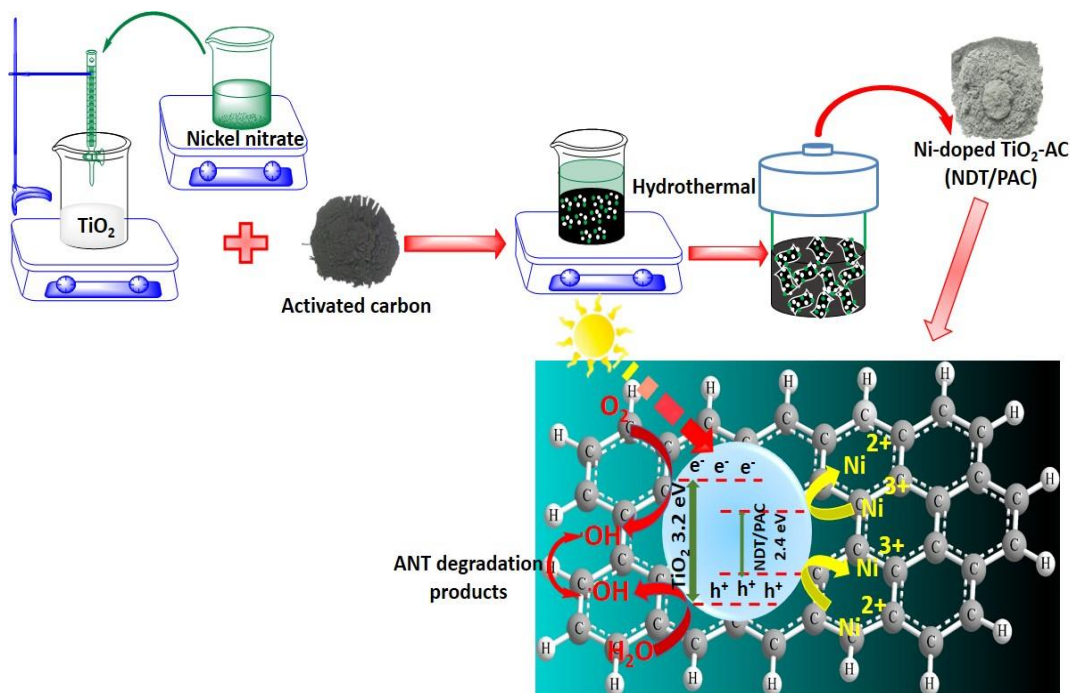


**Figure 5.1** A schematic representation of photocatalytic degradation of anthracene using NDT/PAC nanocomposite



## 5.2 Materials and method

### 5.2.1 Materials

Nickel nitrate hexahydrate ( $\text{Ni}(\text{NO}_3)_2 \cdot 6\text{H}_2\text{O}$ , 99.99%), titanium tetrachloride ( $\text{TiCl}_4$ , 99.10%), sulphuric acid ( $\text{H}_2\text{SO}_4$ , 98%), ammonia ( $\text{NH}_3$ , 25%), zinc chloride ( $\text{ZnCl}_2$ , 99%), and anthracene (ANT, 99%) were procured from Sigma-Aldrich and used without additional purifications. Silver nitrate ( $\text{AgNO}_3$ , 99%), ethylenediaminetetraacetic acid ( $\text{C}_{10}\text{H}_{16}\text{N}_2\text{O}_8$ , 99%), sodium nitrate ( $\text{NaNO}_3$ , 98%), sodium chloride ( $\text{NaCl}$ , 99.5%), copper sulphate ( $\text{CuSO}_4$ , 98.5%), glycine ( $\text{C}_2\text{H}_5\text{NO}_2$ , 99%), oxalic acid ( $\text{C}_2\text{H}_2\text{O}_4$ , 95%), and cadmium nitrate ( $\text{Cd}(\text{NO}_3)_2 \cdot 4\text{H}_2\text{O}$ , 98%) were obtained from Himedia, India.

### 5.2.2 Synthesis of NDT/PAC nanocomposite

Pine cone activated carbon (PAC) and  $\text{TiO}_2$  were used as a precursor for the synthesized NDT/PAC nanocomposite. PAC was prepared using the bio-waste of pine cones and  $\text{TiO}_2$  nanoparticles were synthesized using the sol-gel method. Synthetic pathways for PAC,  $\text{TiO}_2$ , and  $\text{TiO}_2$  supported on PAC nanocomposite were reported in our previous study [17].

Preparation of NDT/PAC nanocomposite was carried out as follows: The prepared  $\text{TiO}_2$  nanoparticles (0.15 g) were slowly mixed with 1.0 g of  $\text{Ni}(\text{NO}_3)_2 \cdot 6\text{H}_2\text{O}$  in 100 mL distilled water with continuous stirring for 30 minutes. The mixture was then slowly poured into a beaker containing 0.3 g of the PAC and the final mixture was ultrasonicated in an ultrasonic bath for 1h. Later, the mixture was kept inside a Teflon-lined stainless steel autoclave for hydrothermal treatment and heated at a temperature of  $150^\circ\text{C}$  for 24 h. The resultant solution was washed thoroughly with double distilled water followed by centrifugation until the neutral pH was attained. It was then dried overnight at  $65^\circ\text{C}$  and grounded to powder to obtain NDT/PAC nanocomposite [21].

### 5.2.3 Characterization

The following instrumental techniques were used to characterize the synthesized NDT/PAC nanocomposite: (i) the surface morphology was observed with a scanning electron microscopy (SEM) (Sigma-300; Zeiss device), (ii) the elemental compositions were analysed using Energy-dispersive X-ray spectroscopy (EDX) in conjunction with SEM, (iii) the crystal structures were analysed by X-ray diffractometer using PANalytical X'Pert Pro device ( $\text{Cu } K_\alpha$  radiation at 40 kV and 40 mA), (iv) the presence of different functional groups were studied by Fourier transformed Infra-red (FT-IR) spectrometer using Perkin Elmer instrument (Model: Spectrum Two), (v) the bandgap was determined using Shimadzu diffuse reflectance spectrophotometer

(DRS), (vi) the emission spectra were determined by a photoluminescence spectrophotometer using Horiba Fluoromax-4CP spectrofluorometer (150 W Xenon Lamp), (vii) the surface area, total pore volume and pore radii were determined using Brunauer–Emmett–Teller (BET) surface analyser (Quantachrome instrument) by measuring N<sub>2</sub> adsorption-desorption isotherm, (viii) the zero-point charge (pHzpc) of the NDT/PAC nanocomposite was determined using the batch equilibrium method as described in Chapter 2 section 2.3.

#### 5.2.4 Photocatalytic degradation experiment

The photocatalytic degradation of anthracene (ANT) was performed inside a photocatalytic reactor. The reactor was a black box with a high-pressure mercury visible light having a maximum wavelength of 520 nm with 350 W powers. Inside the reactor, a Pyrex glass vessel (capacity: 250 ml) containing pollutant and the nanocomposite mixture was placed above a magnetic stirrer and light irradiation was done by placing a high-pressure mercury lamp above (distance 10 cm) the reaction mixture. A continuous flow of cold water was circulated using a water pump through the outer jacket of the reactor to maintain the temperature of 25°C. Also, the continuous circulation of air was carried out using an exhaust fan [16].

ANT had been dissolved in acetone to prepare the standard solution (250 ppm). The standard solution was further diluted to various concentrations of 20, 40, 60, 80, and 100 ppm using double distilled water. For the batch degradation study, at first 150 ml of a particular concentration of ANT solution and 0.05 g of the nanocomposite were poured together in the photoreactor, and continuously stirred for 30 minutes in dark conditions to establish adsorption-desorption equilibrium inside the reaction system. After reaching the equilibrium condition, visible light was passed through the reaction medium to study the effect of light in the degradation of the ANT. At every 10 minutes interval, 3.5 ml of the ANT solution was taken out and the concentration of ANT was measured using a Lambda-365 UV-Vis spectrophotometer at an absorbance of 252 nm.

The ANT degradation percentage was calculated using equation 5.1.

$$\text{ANTdegradation (\%)} = \frac{C_i - C_e}{C_i} \times 100 \quad (5.1)$$

where C<sub>i</sub> represents initial concentration of ANT (ppm), and C<sub>e</sub> represents final concentrations of ANT (ppm).

### 5.3 Results and discussion

#### 5.3.1 Characterization of NDT/PAC nanocomposite

##### (a) XRD analysis

The XRD data of NDT/PAC nanocomposite were analyzed and compared with both TiO<sub>2</sub> nanoparticles and TiO<sub>2</sub> supported on AC (TiO<sub>2</sub>-NP/PAC) nanocomposite [17] (Figure 5.2). The average value of the crystallite sizes (*d*) was calculated by using Debye-Scherrer's equation 5.2 [22].

$$D = \frac{\kappa\lambda}{\beta \cos\theta} \quad (5.2)$$

where *k* = Scherer constant (0.9), *λ* = wavelength of the Cu K<sub>α</sub> X-ray radiation (0.15418 nm), *θ* = diffraction angle, and *β* = full-width at half-maximum (FWHM) of highest intensity peak [23].

XRD plot for all the three samples which contains TiO<sub>2</sub> have diffraction peaks at 25.281°, 38.576°, 48.050°, 53.891°, 55.062°, 62.690°, 68.762°, 70.311° and 75.032°, and miller indices at (1 0 1), (1 1 2), (2 0 0), (1 0 5), (2 1 1), (2 0 4), (1 1 6), (2 2 0) and (2 1 5) planes. This result suggested that the phase of TiO<sub>2</sub> is an anatase crystalline form [JCPDS card No. 21-1272]. In the XRD pattern of NDT/PAC nanocomposite, the diffraction peak for the NiO phase was not detected this might be possible due to the fine dispersion of Ni<sup>2+</sup> ions on the TiO<sub>2</sub>-NP/PAC nanocomposite surface. The average crystallite size for the NDT/PAC nanocomposite was observed to be in the range of 5-10 nm.

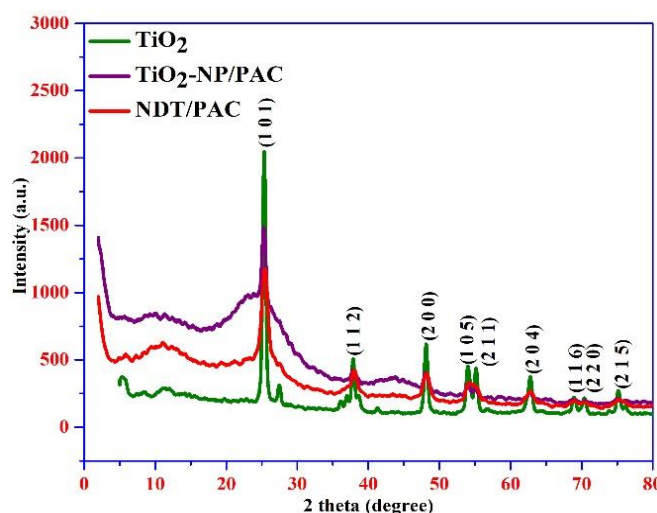


**Figure 5.2** XRD patterns of NDT/PAC nanocomposite in contrast with TiO<sub>2</sub>, TiO<sub>2</sub>-NP/PAC [17]

**(b) SEM and EDX analysis**

The SEM micrograph obtained for NDT/PAC nanocomposite is displayed in Figure 5.3 (a). As seen from the Figure, the white spherical  $\text{TiO}_2$  particles accumulating with Ni ions were aggregated on the PAC surface, and their particle sizes ranged from 5-20 nm.

The EDX spectra of the NDT/PAC nanocomposite are shown in Figure 5.3 (b). The spectra confirm the presence of Ni (0.34%), Ti (4.18%), O (12.31%), and C (83.17%) in the nanocomposite. These results reveal that the amounts of Ni dopants are less compared to Ti and O; this might be due to the loss of nickel nitrate during the hydrothermal synthesis of the nanocomposite.

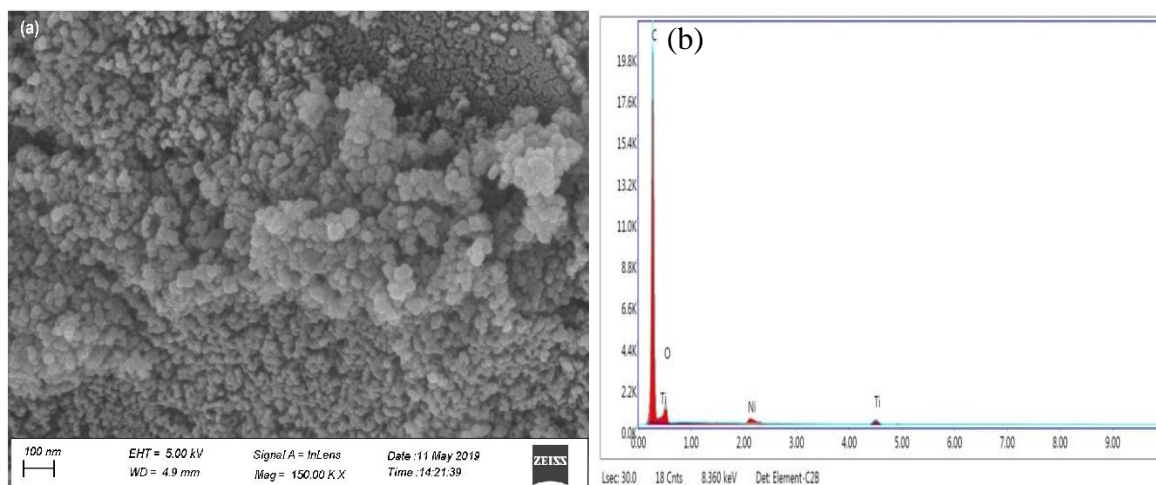


**Figure 5.3** (a) SEM image and (b) EDX pattern of NDT/PAC nanocomposite

**(c) FT-IR analysis**

The FT-IR data of the as-prepared NDT/PAC nanocomposite is shown in Figure 5.4. The broad peaks centered at 3767 and 3064  $\text{cm}^{-1}$  are assigned to  $\text{sp}^2$  C-H and -OH stretching vibrations. These two peaks confirm the surface functionalization of AC and the presence of surface hydroxyl groups. The peak at 1596  $\text{cm}^{-1}$  is attributed to the H-O-H bending vibration, which corresponds to the water molecules adsorbed on the surface and the interlayer space of the nanocomposite [12]. The absorption peak at 1277 and 1116  $\text{cm}^{-1}$  is due to the presence of C-O stretching vibration in the NDT/PAC nanocomposite. The bands at 787 and 620  $\text{cm}^{-1}$  account for the Ti-O stretching vibration of the Ti-O bond in the nanocomposite [16]. The band at 463  $\text{cm}^{-1}$  accounts for Ni-O stretching vibrations in the Ni-doped  $\text{TiO}_2$  nanocomposite [24].

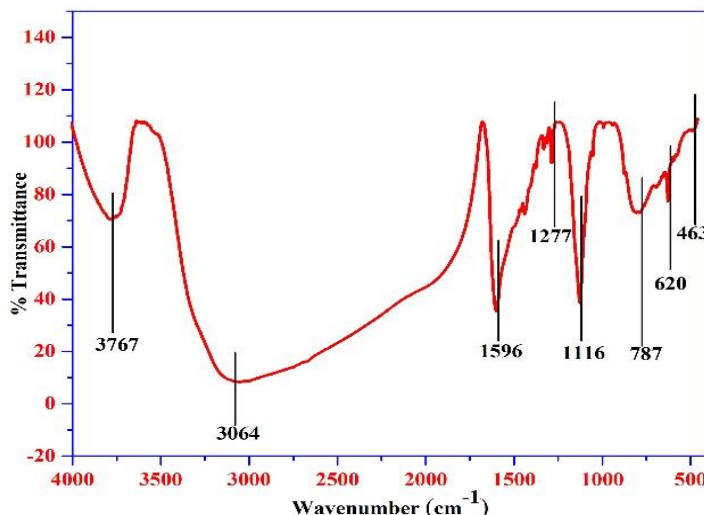


**Figure 5.4** FT-IR spectra of NDT/PAC nanocomposite

#### (d) UV-Vis DRS analysis

The DRS spectra of prepared NDT/PAC nanocomposite are shown in Figure 5.5 (a), and it is compared with the DRS spectra of  $\text{TiO}_2$  and  $\text{TiO}_2\text{-NP/PAC}$  nanocomposite [16]. The spectra of  $\text{TiO}_2$  and  $\text{TiO}_2\text{-NP/PAC}$  nanocomposite exhibited optical absorbance in the ultra-violet region (wavelength 200-380 nm), this might be attributed due to the migration of charge from O 2p to the Ti 3d level. In the case of Ni-doped  $\text{TiO}_2$ , a red-shifted absorption peak arises through the transition of the  $\text{Ni}^{2+}$  3d electron to the conduction band of  $\text{TiO}_2$  [25]. The bandgap energy of the Ni-doped  $\text{TiO}_2$  nanocomposite was calculated by following the classical Tauc's equation represented by equation 5.3 [26].

$$\alpha h\nu = K (h\nu - E_g)^n \quad (5.3)$$

where  $\alpha$  is the absorption coefficient,  $E_g$  represents the bandgap energy,  $h\nu$  is the photon energy,  $K$  is a proportionality constant, and  $n$  depends on the nature of transition ( $n = 1/2$ , for direct allowed charge transitions).

From the Tauc's plot, the bandgap energy for NDT/PAC nanocomposite was found to be 2.4 eV, which is much lower than  $\text{TiO}_2$  (3.1 eV) and  $\text{TiO}_2\text{-NP/PAC}$  (3.2 eV) (Figure 5.5 (b)) [17]. The bandgap energy for  $\text{TiO}_2$  reduces from 3.1 to 2.4 eV with the doping of  $\text{Ni}^{2+}$  ions in the  $\text{TiO}_2$  structure and this reduction in the bandgap shifts the optical absorbance to the visible light region. Thus, doping of  $\text{Ni}^{2+}$  ions in the  $\text{TiO}_2\text{-NP/PAC}$  shifts the photodegradation of ANT in the visible light region.

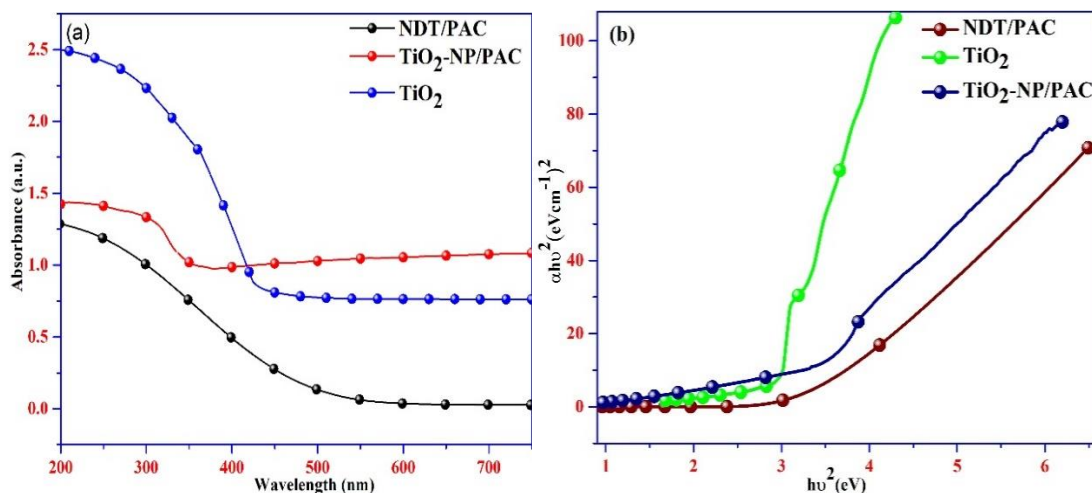


**Figure 5.5** (a) DRS spectra and (b) Tauc's plot for TiO<sub>2</sub>, TiO<sub>2</sub>-NP/PAC, and NDT/PAC nanocomposite (plot for TiO<sub>2</sub>, TiO<sub>2</sub>-NP/PAC is shown for comparison only) [16]

### (e) PL analysis

The effect of electron-hole pair recombination on photocatalysis can be studied using photoluminescence (PL) analysis. The luminescence emissions of TiO<sub>2</sub> and NDT/PAC nanocomposite were performed in the wavelength range from 450-750 nm (Figure 5.6). The high intense emission peak is observed for TiO<sub>2</sub> at around 464 nm, which signifies that the electron-hole pair's recombination is more. However, the PL intensity decreases after doping Ni ions on TiO<sub>2</sub>. This decrease in PL intensity could be due to the generation of an impurity energy level within the bandgap of TiO<sub>2</sub> from which electron transfer to the conduction band of TiO<sub>2</sub>. The low-intense peak of the NDT/PAC nanocomposite indicates a decreased recombination of charge carriers, which is expected to enhance the photocatalytic activity of the NDT/PAC nanocomposite.

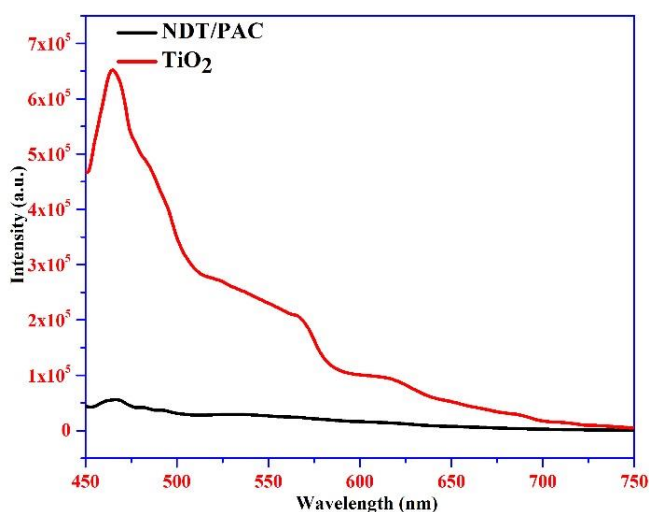


**Figure 5.6** PL spectra of TiO<sub>2</sub>, and NDT/PAC nanocomposite

### (f) BET surface area and pore structure analysis

Results of proximate analysis of NDT/PAC,  $\text{TiO}_2$ , and PAC are shown in Table 5.1. From the table, it is observed that the BET surface area of PAC is reduced from  $878.07 \text{ m}^2\text{g}^{-1}$  to  $84.13 \text{ m}^2\text{g}^{-1}$  in NDT/PAC. The decreased surface area may be attributed due to the covering of PAC pores by Ni and  $\text{TiO}_2$  nanoparticles, confirming that Ni and  $\text{TiO}_2$  nanoparticles had occupied a large surface area of PAC. It is also observed that the NDT/PAC has a higher BET surface area than that of bare  $\text{TiO}_2$  nanoparticles ( $60.21 \text{ m}^2\text{g}^{-1}$ ). The improvement of NDT/PAC nanocomposite surface area might be due to the addition of Ni ions to the  $\text{TiO}_2$  complex [27] and also the presence of PAC as catalytic support [28]. The pore diameter of  $8.70 \text{ nm}$  and total pore volume of  $0.08 \text{ cm}^3\text{g}^{-1}$  give information about the formation of mesoporous material (2-50 nm).

<b>Table 5.1</b> BET surface area and pore size of $\text{TiO}_2$ , PAC, and, NDT/PAC nanocomposite	
<b>Proximate analysis (wt %)</b>	
BET surface area (NDT/PAC)	$84.13 \text{ m}^2\text{g}^{-1}$
BET surface area ( $\text{TiO}_2$ ) [16]	$60.21 \text{ m}^2\text{g}^{-1}$
BET surface area (PAC) [16]	$878.07 \text{ m}^2\text{g}^{-1}$
Total pore volume	$0.08 \text{ cm}^3\text{g}^{-1}$
Pore radius	$8.70 \text{ nm}$

### (g) Zero-point charge analysis

The zero point charge (pHzpc) of the NDT/PAC nanocomposite corresponds to 6.75 (Figure 5.7), indicating that the nanocomposite surface becomes positively charged when  $\text{pH} < 6.75$  and negatively charged when  $\text{pH} > 6.75$  [16].

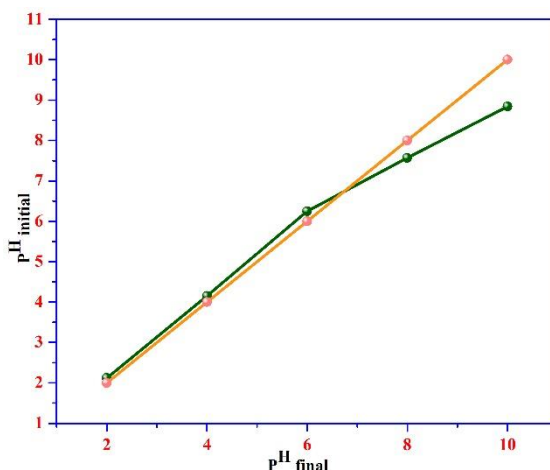


**Figure 5.7** pHzc plot for NDT/PAC nanocomposite

### 5.3.2 Photocatalytic activity

To confirm that the photocatalytic degradation for the present nanocomposite takes place only under visible light, ANT degradation was initially carried out under ultra-violet light (325 nm).



Since, the high-pressure mercury lamps also emit intense ultra-violet light, the same set of photocatalytic experiments using NDT/PAC nanocomposite was carried out using mercury UV lamp of wavelength 325 nm and it showed negligible degradation of ANT (20 ppm = 0.9%, 40 ppm = 0.85%, 60 ppm = 0.7%, 80 ppm = 0.5%, and 100 ppm = 0.0%) occurred after 3h of reaction under UV light (Figure 5.8). Subsequently, the visible light photocatalytic degradation experiments of ANT with NDT/PAC, TiO<sub>2</sub>-NP/PAC, and TiO<sub>2</sub> nanomaterial were evaluated following the procedure discussed in experimental section 5.2.4.

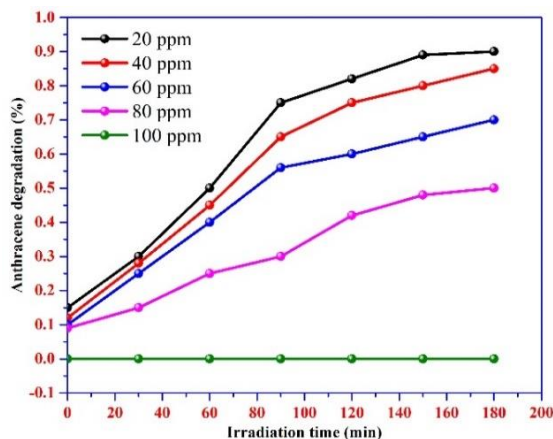


**Figure 5.8** Effect of NDT/PAC (0.05 g) with irradiation time in the degradation of ANT solution under UV light (325 nm)

#### (a) Effect of NDT/PAC nanocomposite amount

Degradation experiments of ANT with different doses of NDT/PAC, TiO<sub>2</sub>-NP/PAC, and TiO<sub>2</sub> were conducted in the presence of visible light. Different concentrations of ANT varying from 20-100 ppm was studied for different doses (0.01-0.09 g) of the NDT/PAC, TiO<sub>2</sub>-NP/PAC, and TiO<sub>2</sub> nanomaterial (Figure 5.9). It can be seen from the figure that NDT/PAC showed significantly higher photocatalytic degradation as compared to TiO<sub>2</sub>-NP/PAC and TiO<sub>2</sub>. The maximum percent degradation (99.9%) was attained for 20 ppm of ANT using 0.05 g of NDT/PAC nanocomposite under visible light exposure of 50 minutes. The very high degradation of ANT by NDT/PAC nanocomposite confirms the fact that introducing Ni dopant into TiO<sub>2</sub> inhibits the electron-hole recombination and shifts the optical response of TiO<sub>2</sub> from UV to visible light as evident from UV-Vis (DRS) and PL spectra (Figure 5.5 and 5.6) respectively [29]. Also, the use of PAC as a support material increases the surface area of the nanocomposite assisting a higher concentration of pollutant molecules to accumulate around the surface of the photocatalyst, which assists in improving the photocatalytic reaction rates. However, under a similar set of conditions, the maximum percentage degradation of ANT solution with TiO<sub>2</sub>-NP/PAC and TiO<sub>2</sub> were 31% and 22.5% respectively. This minor

degradation is due to the visible light-responsive behaviour of ANT which results from the degradation of ANT without  $\text{TiO}_2$  being doped with Ni ions [30]. Further, it is observed that by increasing the nanocomposite dose above 0.05 g, the percent degradation of ANT shows a decreasing trend. This could be due to the reduced visible light penetration as a result of light scattering, and higher recombination of the electron-hole pairs. Thus, in the present study, 0.05 g of NDT/PAC nanocomposite was considered to be the optimal amount for ANT degradation studies.

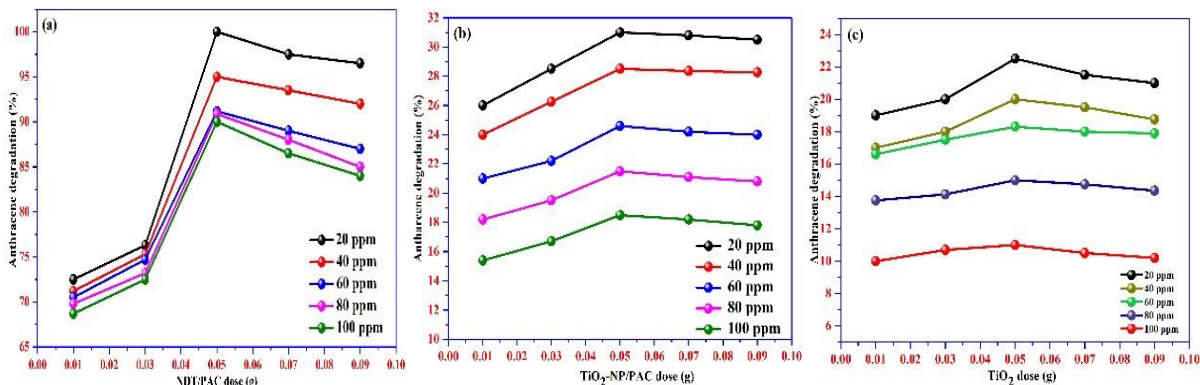


**Figure 5.9** Effect of nanocomposite (a) NDT/PAC, (b)  $\text{TiO}_2$ -NP/PAC, and (c)  $\text{TiO}_2$  amount in the degradation of ANT solution under visible light

### (b) Effect of pH

In photocatalysis, the effect of pH is an important parameter that gives information about the mechanism involved at the surface of the nanocomposite. Degradation of 150 ml of 20 ppm ANT solution in the pH range from 2-10 was studied with 0.05 g dose of the NDT/PAC,  $\text{TiO}_2$ -NP/PAC, and  $\text{TiO}_2$  nanomaterial (Figure 5.10). The highest percentage degradation of ANT was observed at pH = 2 then started decreasing with an increase in the pH of the solution. A similar trend of results was observed by Gupta *et al.* [31] and Zango *et al.* [32] where the highest degradation of ANT occurred in acidic media rather than under basic conditions. Since the  $\text{pH}_{\text{zpc}}$  of the NDT/PAC,  $\text{TiO}_2$ -NP/PAC, and  $\text{TiO}_2$  nanomaterial are 6.75, 6.45, and 6.25 respectively; thus the surface of the nanocomposite becomes positive at  $\text{pH} < \text{pH}_{\text{zpc}}$ . Hence, at lower pH ( $\text{pH} 2 < \text{pH}_{\text{zpc}}$ ), there will be a stronger interaction between the  $\pi$ -electron cloud of the ANT molecule and the positive charge on the nanocomposite surface [33]. On the other hand, with increasing pH or in alkaline media, availability of the  $\text{OH}^-$  ions increases which compete with the positive surface charge on the nanocomposite; hence the degradation of ANT decreases at higher pH [34].

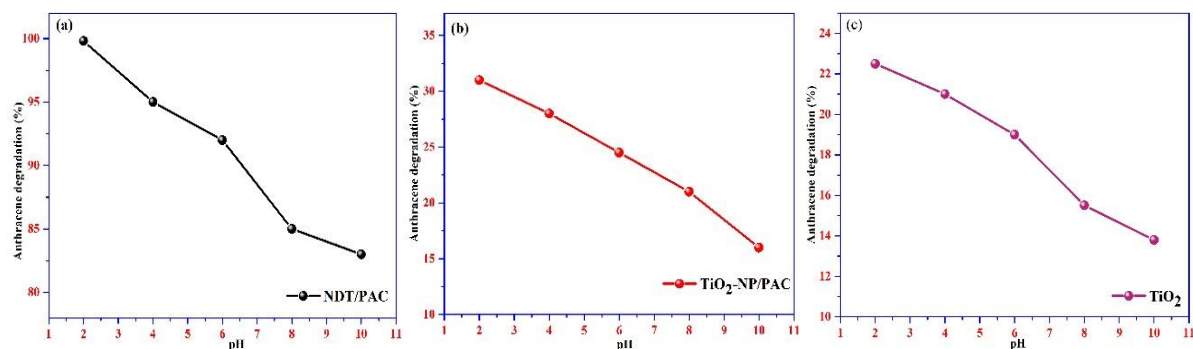


**Figure 5.10** Effect of (a) NDT/PAC, (b) TiO<sub>2</sub>-NP/PAC, and (c) TiO<sub>2</sub> (0.05 g) with pH in the degradation of ANT solution under visible light

### (c) Effect of initial anthracene concentration and light irradiation time

The photocatalytic degradation was studied for nanocomposite dosage of 0.05 g at an optimum pH (pH=2) for different concentrations of ANT solution, under visible light irradiation for different periods. The results (Figure 5.11) reveal that the ANT degradation initially increases with irradiation time till 50 minutes for all the concentrations. Once the exposure time reaches around 50 minutes, the saturation points are reached and the curve starts flattening. Interestingly maximum degradation of 99.9% was observed for 20 ppm solution, which reduces to 84.5%, 73%, 64%, and 53% for 40, 60, 80, and 100 ppm solution at 50 minutes irradiation time.

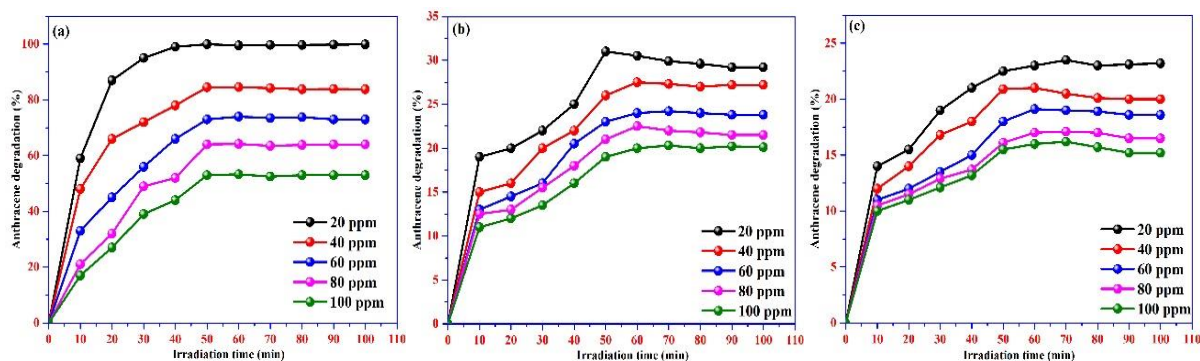


**Figure 5.11** Effect of (a) NDT/PAC, (b) TiO<sub>2</sub>-NP/PAC, and (c) TiO<sub>2</sub> (0.05 g) with contact time in the degradation of ANT solution under visible light

The possible explanation for less degradation of the ANT could be due to the lower availability of hydroxyl radical species in the reaction medium. Photocatalytic degradation is initiated by reactive hydroxyl radicals which are formed due to exposure to light and the degradation reaction mainly undergoes on the surface of the nanocomposite. When the concentration of ANT is more, light particles get captured between the ANT particles, and hence light particles are not able to reach the nanocomposite surface [34]. Thus, the production of reactive hydroxyl radical decreases, and consequently, the degradation of ANT is reduced.

### 5.3.3 Kinetic studies

The kinetic studies of degradation were conducted at optimum conditions of pH 2 for 20 ppm solution with 0.05 g nanocomposite dose. The rate of the reaction ( $K_{app}$ ), and the half-life time ( $t_{1/2}$ ) were determined using equations 5.4 and 5.5.

$$\ln\left(\frac{C_i}{C_e}\right) = K_{app} t \quad (5.4)$$

$$t_{1/2} = \frac{\ln 2}{K_{app}} \quad (5.5)$$

where  $C_i$  = Initial ANT concentration (20 ppm);  $C_e$  = Final ANT concentration at equilibrium;  $K_{app}$  = Apparent rate constant.

The linear plot of  $\ln(C_i/C_e)$  against irradiation time shows a high correlation coefficient ( $R^2$ : 0.998). This implies that the degradation of ANT concentration follows Langmuir-Hinshelwood pseudo-first-order rate kinetics (Figure 5.12). The  $K_{app}$  value and the  $t_{1/2}$  were measured from the slope and were found to be  $0.11449 \text{ min}^{-1}$  and 6.05 minutes.

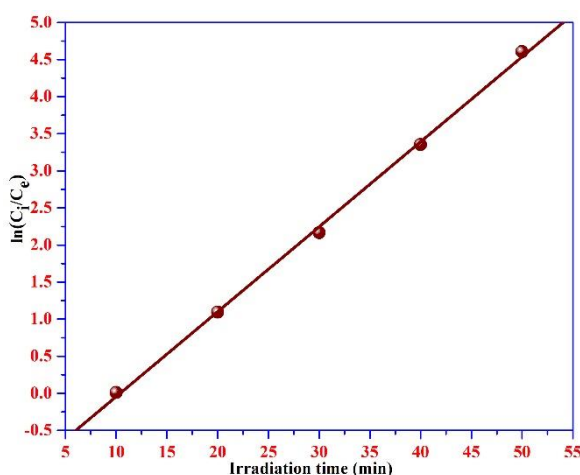


**Figure 5.12** Pseudo-first-order rate kinetics of ANT degradation loaded on NDT/PAC nanocomposite

### 5.3.4 Thermodynamic studies

Thermodynamic studies considered different temperatures (298 K, 308 K, 318 K, and 328 K) for photocatalytic degradation of ANT using NDT/PAC nanocomposite. The different thermodynamics parameters were calculated using the equations 5.6 and 5.7.

$$\ln K_d = \frac{\Delta S^\circ}{R} - \frac{\Delta H^\circ}{RT} \quad (5.6)$$

$$\Delta G^\circ = -RT \ln K_d \quad (5.7)$$

where  $T$  is the absolute temperature,  $K_d$  is the distribution coefficient,  $R$  ( $8.314 \text{ J mol}^{-1} \text{ K}^{-1}$ ).

The plot of  $\ln K_d$  vs  $1/T$  (Figure 5.13) gives the slope and intercept value from where  $\Delta H^\circ$  and  $\Delta S^\circ$  values were calculated.

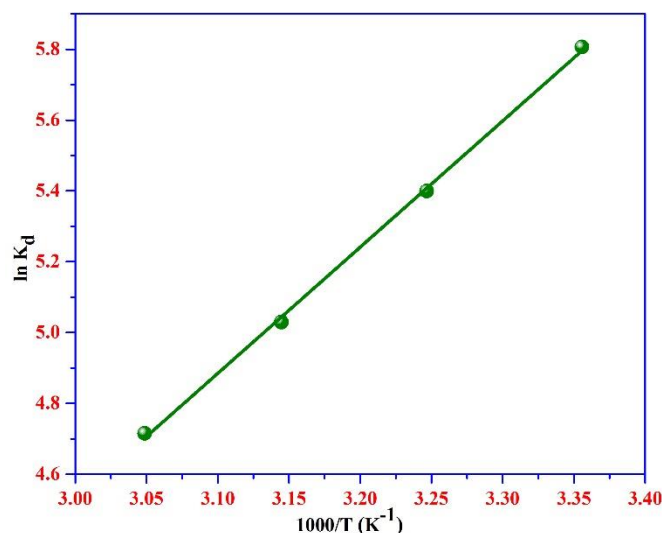


**Figure 5.13**  $\ln K_d$  as a function of  $1/T$  (Using 20 ppm ANT concentration, 0.05 g NDT/PAC, pH 2, and 50 minutes visible light irradiation)

The results of different thermodynamics parameters are listed in Table 2. The negative values of  $\Delta S^\circ$  (-51.2593) and  $\Delta H^\circ$  (-29.6355) signify the degradation of ANT using NDT/PAC nanocomposite was an exothermic process. Also, the negative value of  $\Delta G^\circ$  suggests that the photocatalytic reaction is spontaneous and feasible.

**Table 5.2** Values of enthalpy ( $\Delta H^\circ$ ), entropy ( $\Delta S^\circ$ ), and Gibbs free energy ( $\Delta G^\circ$ ) calculated for the photocatalytic degradation of ANT using NDT/PAC nanocomposite

T (K)	Thermodynamic parameters		
	$\Delta G^\circ$ (kJ mol <sup>-1</sup> )	$\Delta H^\circ$ (kJ mol <sup>-1</sup> )	$\Delta S^\circ$ (kJ mol <sup>-1</sup> K)
298	-14.3603	-29.6355	-51.2593
308	-13.8477		
318	-13.3351		
328	-12.8225		

### 5.3.5 Effect of interfering ions on ANT photocatalytic degradation

In industrial sewages, anthracene may be present in combination with different dissolved oxygen matter, organic solvents, humic substances, and acidic and basic species. Therefore the applicability of the NDT/PAC nanocomposite in the degradation of anthracene combined with different interfering ions such as EDTA, NaCl, ZnCl<sub>2</sub>, CuSO<sub>4</sub>, glycine, oxalic acid, NaNO<sub>3</sub>, and Cd(NO<sub>3</sub>)<sub>2</sub> was analysed. For this study, optimum NDT/PAC nanocomposite dose of 0.05 g, pH of 2, light irradiation dose of 50 minutes, and interfering ion concentration of 20 ppm were used and the degradation percentage as a function of different interfering ions are plotted in Figure 5.14. From the figure it can be evaluated that the degradation percentage decreases from 99.9% to 63% (EDTA), 79% (NaCl), 72% (ZnCl<sub>2</sub>), 64% (CuSO<sub>4</sub>), 49% (Glycine), 82% (oxalic acid), 78% (NaNO<sub>3</sub>), and 65% (Cd(NO<sub>3</sub>)<sub>2</sub>).

The decrease in degradation percentages is due to the scavenging properties of the cations or anions of interfering ions, as the photocatalytic degradation processes were predominantly driven by the highly oxidizing species, photogenerated valence band holes ( $h^+$ ), or hydroxyl radicals ( $\cdot OH$ ) [35].

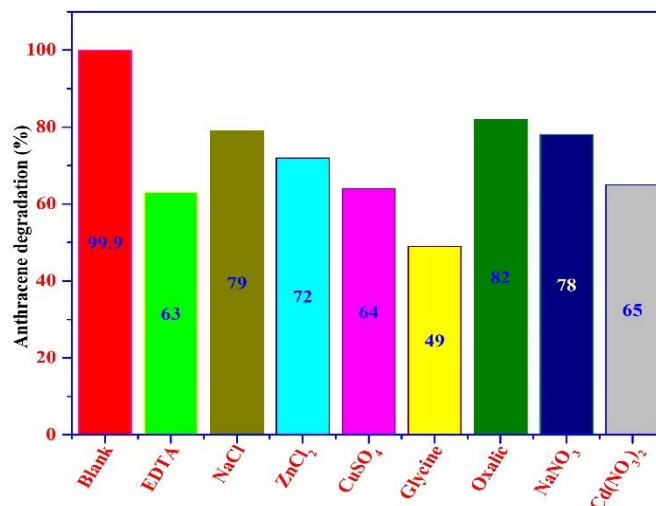


**Figure 5.14** Photocatalytic degradation of ANT in the presence of interfering ions using NDT/PAC nanocomposite

### 5.3.6 Nanocomposite reusability and photostability

The reusability of the prepared nanocomposite for the photocatalytic degradation of ANT was carried out for five cycles of usages. For reuse of the nanocomposite, every time after completion of the photocatalytic reactions, the nanocomposite remaining in the reaction medium was separated by centrifuging the solution. The obtained nanocomposite was then rinsed with double distilled water and dried in an oven. The dried nanocomposite was then again used for photocatalytic degradation of ANT (Figure 5.15). In the first cycle, the ANT degradation was 98.50% which reduced to 90.60% for the second cycle, became 85% for the third cycle, and degraded upto 79% in the fourth cycle. The degradation efficiency of the nanocomposite decreases marginally with increasing usages. This decrease in degradation efficiency could be due to the reduction of vacant adsorption sites on NDT/PAC nanocomposite for ANT adsorption. It could also be due to the release of the photoactive compounds from the NDT/PAC nanocomposite during the recycling process [36]. In the fifth cycle, the degradation efficiency of the nanocomposite was found to be around 73%, which establishes the fact that NDT/PAC nanocomposite still shows excellent usage capability after running it through several cycles.



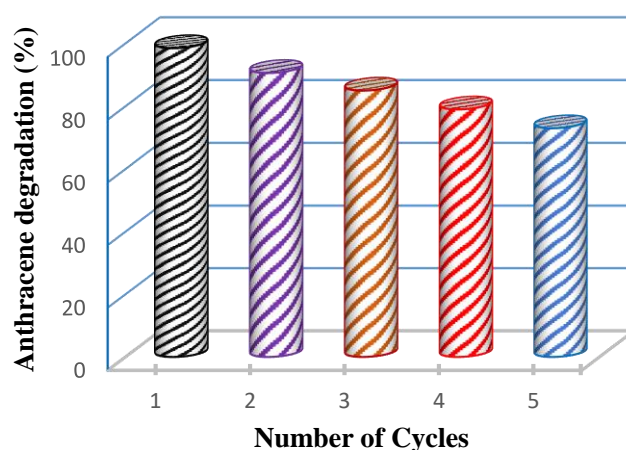


**Figure 5.15** ANT degradation efficiency of NDT/PAC nanocomposite upto five cycles

To understand the photostability of the NDT/PAC nanocomposite, FT-IR spectra of the pristine NDT/PAC nanocomposite were compared with the recovered composite at the end of the fifth cycle of degradation of ANT (Figure 5.16). From the figure, it can be seen that all the characteristic peaks that remain in both samples confirm that the nanocomposite had retained its original structure.

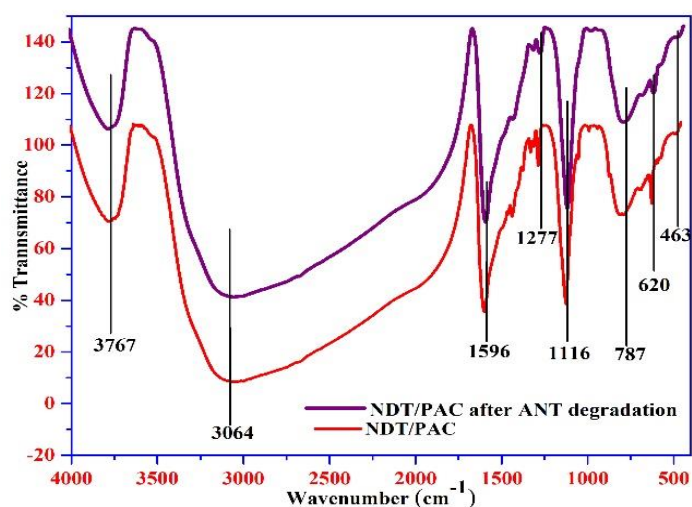


**Figure 5.16** FT-IR spectra of NDT/PAC before and after ANT degradation

### 5.3.7 GC-Mass analysis

GC-MS analysis was used to identify the degraded end products of the ANT and the results are presented in Figure 5.17. It can be observed from the mass spectra that the end products of ANT are degraded to less harmful carbon dioxide and water. The intermediate degraded products obtained are 9, 10-anthraquinone at  $m/z = 208$ , phthalic acid at  $m/z = 165$ , salicylic acid at  $m/z = 138$ , catechol at  $m/z = 110$ , and other smaller products.



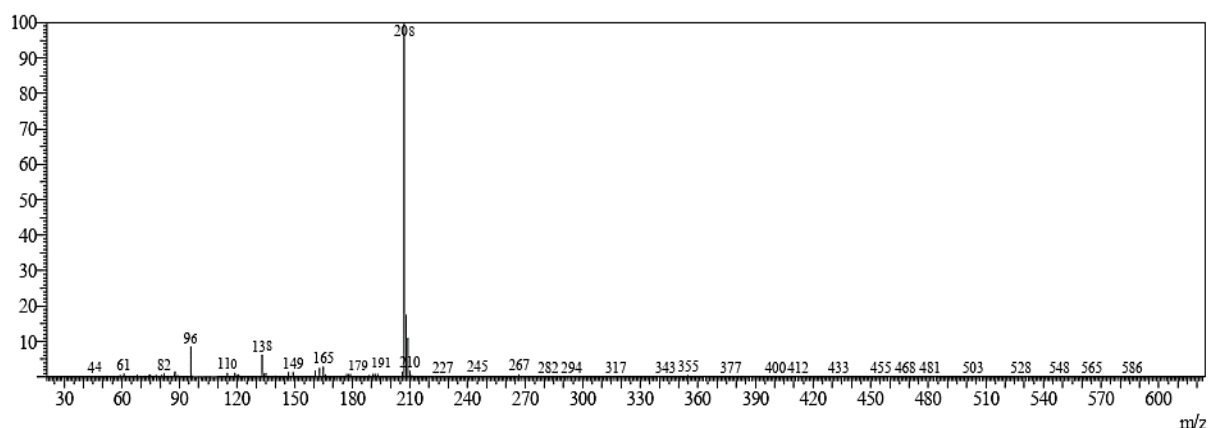


**Figure 5.17** Mass spectra of degradation products of ANT aqueous solution

The probable mechanism for degradation is reflected in Figure 5.18. Probably, ANT is initially degraded by an attack of hydroxyl radicals produced in the reaction medium generating 9, 10-anthraquinone (I). It then undergoes ring cleavage to form phthalic acid (II) and further oxidizes to yield salicylic acid (III) and catechol (IV). The ring-opening of catechol results in the formation of minor products like (1E, 3Z)-hexa-1,3,5-trien-1-ol (1a;  $m/z = 96$ ), and (1E, 3E)-penta-1,3-dien-1-ol (1b;  $m/z = 82$ ) [24,37]. Further, these compounds are transformed into smaller molecules such as carbon dioxide ( $m/z = 44$ ), and water.

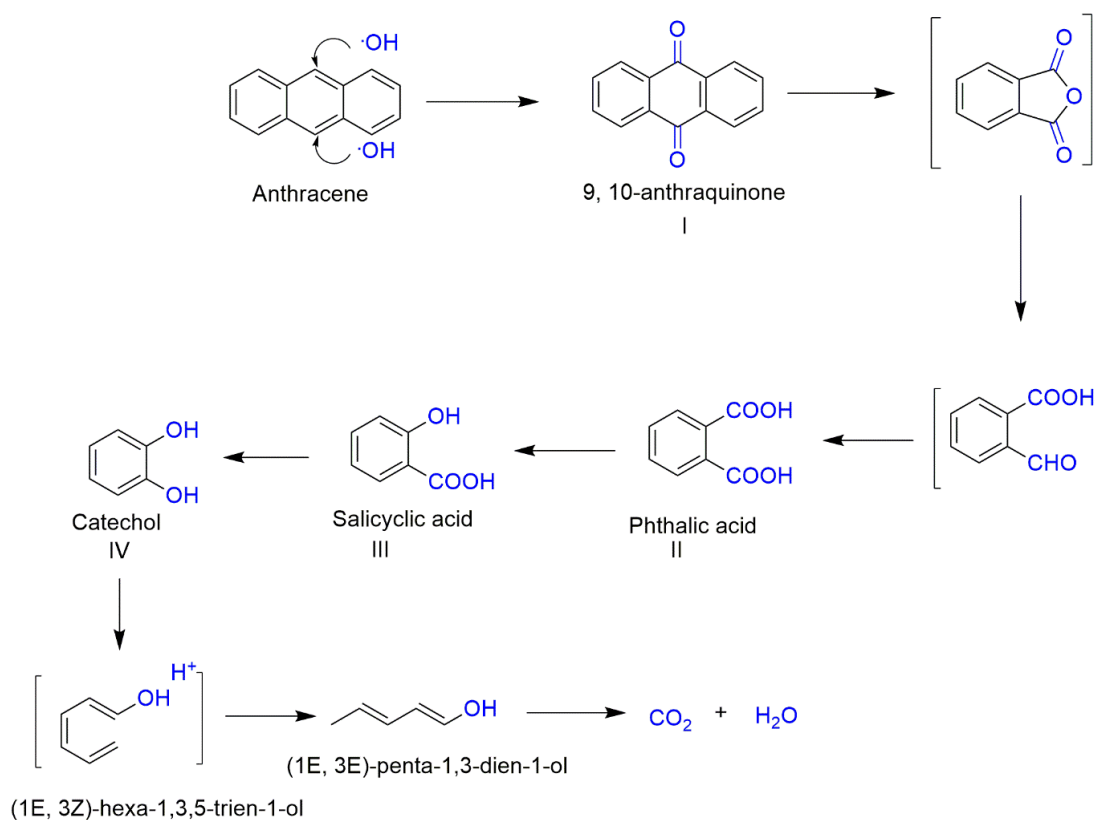


**Figure 5.18** Proposed degradation pathway for the degradation of ANT over NDT/PAC nanocomposite [24]

### 5.3.8 Energy consumption and cost analysis

Electrical energy consumption and total operating cost of the photocatalytic degradation of ANT using NDT/PAC nanocomposite were calculated and are discussed below in detail.

#### (a) Electrical energy determination

The electric energy per order ( $E_{EO}$ ) involved in the degradation of ANT is a useful and valuable approach for calculating the overall expenditure during the experimentation and can be calculated using equation 5.8 [38]:

$$E_{EO} = \frac{P \times t \times 1000}{V \times 60 \times \log\left(\frac{C_i}{C_e}\right)} \quad (5.8)$$

where  $V$  = volume of ANT (L),  $C_i$  = initial ANT concentration,  $C_e$  = final ANT concentration,  $t$  = irradiation time (min),  $P$  = input power (kW).

Combining Langmuir-Hinshelwood pseudo-first-order rate equation 5.4 and equation 5.8, the model of electric energy per order can be written as [39]:

$$E_{EO} = \frac{38.4 \times P}{V \times K_{app}} \quad (5.9)$$

where  $K_{app}$  = pseudo-first-order rate constant ( $\text{min}^{-1}$ ),  $V$  = volume of ANT (L),  $P$  = input power (kW).

Table 5.3 represents the  $E_{EO}$  (experimental) and  $E_{EO}$  (model) values for ANT degradation. The table shows higher electrical energy consumption at higher ANT concentrations. This could be due to the more visible light absorption with increased ANT concentrations. Furthermore, the value of the experimental  $E_{EO}$  is similar to that of the kinetic model  $E_{EO}$ , this result signifies that the degradation of ANT fits better with pseudo-first-order rate kinetics.

Table 5.3 Effect of ANT concentration on electrical energy consumption						
Experimental conditions			Apparent rate constant ( $K_{app}$ ) ( $\text{min}^{-1}$ )	$R^2$	$E_{EO}$ experimental ( $\text{kWh m}^{-3}\text{order}^{-1}$ )	$E_{EO}$ model ( $\text{kWh m}^{-3}\text{order}^{-1}$ )
Initial Conc. (ppm)	NDT/PAC Conc. ( $\text{g L}^{-1}$ )	pH				
20	0.05	1	0.1144	0.99	925.92	1118.88
40	0.05	1	0.0345	0.94	3424.82	3710.14
60	0.05	1	0.0251	0.98	4884.98	5099.60
80	0.05	1	0.0196	0.97	6260.52	6530.61
100	0.05	1	0.01467	0.99	8471.36	8725.28

#### (b) Total operating cost

Estimation of cost is an important factor in understanding the effectiveness of the applied method. It can be measured by adding up maintenance costs, operating costs, and capital costs.

In this study, the total operating costs and energy consumed during ANTs degradation were calculated using equations 5.10 and 5.11 [40].

$$\text{Total operating cost} = \frac{\text{Energy consumed per mg of ANT degradation (kWh)} \times \text{unit cost (INR/kWh)} \times 10^6}{\text{ANT degradation (mg)}} \quad (5.10)$$

$$\text{Energy consumed per mg of ANT degradation (kWh)} = \frac{\text{Power input (kW)} \times \text{Reaction time (min)}}{1000 \times 60} \quad (5.11)$$

Table 4 presents the total operating cost needed for the degradation of ANT from wastewater. The total operating cost in Indian rupees (INR) used during the ANT degradation using 0.05 g NDT/PAC nanocomposite were as follows: 347.56 (20 ppm), 205.45 (40 ppm), 158.54 (60 ppm), 135.63 (80 ppm), and 131.02 (100 ppm). These operating costs depend mainly on the ANT concentration, NDT/PAC nanocomposite dosages, and photocatalytic reactor configuration without considering the maintenance and capital cost.

**Table 5.4** Cost analysis of ANT degradation in the photocatalytic reactor under different operating conditions

ANT Conc. (ppm) C <sub>1</sub>	NDT/PAC Conc. (g L <sup>-1</sup> ) C <sub>2</sub>	ANT Degradation Efficiency (%) C <sub>4</sub>	ANT degradation (mg) C <sub>5</sub> = [(C <sub>1</sub> × C <sub>4</sub> /100) × working volume]	Reaction time (minute) C <sub>6</sub>	Energy consumed per mg of ANT degradation (kWh) C <sub>7</sub> = [(P × C <sub>6</sub> )/(1000 × 60)]	Total operating cost (INR/kg of ANT degradation) C <sub>8</sub> = [(C <sub>7</sub> × unit cost × 10 <sup>6</sup> )/C <sub>5</sub> ]
20	0.05	99.9	0.999	50	0.0004	347.56
40	0.05	84.5	1.69	50	0.0004	205.45
60	0.05	73.0	2.19	50	0.0004	158.54
80	0.05	64.0	2.56	50	0.0004	135.63
100	0.05	53.0	2.65	50	0.0004	131.02

(a) Total energy consumed (P) 0.5 kW [includes energy for electronic magnetic stirrer (50W), water pump (50W), exhaust fan (50W) and Visible lamp (350 W)] (b) Working volume of reactor 0.15 L and (d) Unit cost of power 2.5 INR (kWh)<sup>-1</sup>.

### 5.3.9 Comparison studies

A comparative study of current NDT/PAC nanocomposite with other nanomaterials was conducted to understand the relative efficiency of the NDT/PAC for ANT degradation in wastewater. The results of the comparison are shown in Table 5. It can be seen that the current NDT/PAC nanocomposite has relatively high degradation activity for ANT degradation compared to other nanomaterials in the literature. Thus, Ni-doped TiO<sub>2</sub> supported on activated carbon could be a potential photocatalyst for anthracene degradation in wastewater.

**Table 5.5** Comparison of catalytic activity of previous work in the literature with NDT/PAC nanocomposite

Nanocomposite	Pollutant	Mass	Volume (ml)	C <sub>i</sub>	Contact time (minute)	% degradation	Source
Fe <sub>3</sub> O <sub>4</sub> /MIL-101	Anthracene	5 mg	300	4 ppm	60	95	[41]
ZnO	Anthracene	1000 µg	1000	25 µg	240	96	[42]
NiO-ZnO ZnCo <sub>2</sub> O <sub>4</sub> MnCo <sub>2</sub> O <sub>4</sub> CoFe <sub>2</sub> O <sub>4</sub>	Anthracene	80 mg	1000	2 mg	720	98 95 92 88	[24]
n-ZnO/p-MnO	Anthracene	1.5 mg	3.5	20 ppm	60	-	[43]
MgO-carbon composite	Anthracene	6 g	1000	50 ppm	60	96.05	[44]
TiO <sub>2</sub>	Anthracene	175 mg	100	25 ppm	40320	70	[45]
Ag-TiO <sub>2</sub>	Anthracene	5 g	250	1000 ppm	360	100	[46]
<b>NDT/PAC</b>	<b>Anthracene</b>	<b>0.05 g</b>	<b>150</b>	<b>20 ppm</b>	<b>50</b>	<b>99.90</b>	<b>Present study</b>

## 5.4 Conclusion

Ni-doped TiO<sub>2</sub> supported on activated carbon nanocomposite was synthesized *via* a simple hydrothermal method. The XRD spectra confirmed the existence of the anatase phase of TiO<sub>2</sub> and also good dispersion of Ni<sup>2+</sup> ions on the surface of TiO<sub>2</sub>-activated carbon. The surface morphology of the nanocomposite confirmed that Ni-doped TiO<sub>2</sub> nanoparticles were isolated completely over the surface of the PAC and exhibited average particle size distribution of 5-20 nm. The UV-Vis DRS spectra indicated that the bandgap energy of TiO<sub>2</sub> reduces from 3.1 to 2.4 eV with the doping of Ni<sup>2+</sup> ions in the TiO<sub>2</sub> structure and this reduction in the bandgap shifts the optical absorbance to the visible light region. The prepared NDT/PAC nanocomposite showed very high performance towards photocatalytic degradation of ANT and a maximum of 99.9% degradation was observed for 20 ppm solution within 50 minutes. The photocatalytic degradation process was found to be in good agreement with the Langmuir-Hinshelwood pseudo-first-order rate kinetics having a rate constant of 0.11449 min<sup>-1</sup> and a half-life period of 6.05 minutes. The thermodynamic study indicated the temperature dependence, exothermic, and spontaneity of the degradation process. The effect of different interfering ions such as EDTA, NaCl, ZnCl<sub>2</sub>, CuSO<sub>4</sub>, glycine, oxalic acid, NaNO<sub>3</sub>, and Cd(NO<sub>3</sub>)<sub>2</sub> was analyzed, and it was observed that the presence of glycine, EDTA, CuSO<sub>4</sub>, NaNO<sub>2</sub> mostly affects in the degradation percentage of ANT. It was observed that the NDT/PAC nanocomposite can be

reused several times having good degradation efficiency till the fifth cycle. GC-MS analysis confirmed the generation of end products 9, 10-anthraquinone, phthalic acid, salicylic acid, catechol, (1E, 3Z)-hexa-1,3,5-trien-1-ol, (1E, 3E)-penta-1,3-dien-1-ol, and carbon dioxide after the photocatalytic degradation. Thus, it can be concluded from this work that the prepared nanocomposite can act as a good visible light-sensitive photocatalyst for degradation of ANT in water solution.

## References

- [1] P.S. Basavarajappa, S.B. Patil, N. Ganganagappa, K. Raghava, A. V Raghu, C. Venkata, Recent progress in metal-doped TiO<sub>2</sub>, non-metal doped/codoped TiO<sub>2</sub> and TiO<sub>2</sub> nanostructured hybrids for enhanced photocatalysis, *Int. J. Hydrogen Energy*. 45 (2020) 7764–7778. doi:10.1016/j.ijhydene.2019.07.241.
- [2] M.S.S. Danish, L.L. Estrella, I.M.A. Alemaida, A. Lisin, N. Moiseev, M. Ahmadi, M. Nazari, M. Wali, H. Zaheb, T. Senjyu, Photocatalytic Applications of Metal Oxides for Sustainable Environmental Remediation, *Metals (Basel)*. 11 (2021) 1–25. doi:10.3390/met11010080.
- [3] V. Binas, D. Venieri, D. Kotzias, G. Kiriakidis, Modified TiO<sub>2</sub> based photocatalysts for improved air and health quality, *J Mater*. 3 (2017) 3–16. doi:10.1016/j.jmat.2016.11.002.
- [4] S. Bagheri, Z. Adlan Mohd Hir, A. Termeh Yousefi, S. Bee Hamid Abd, Photocatalytic performance of activated carbon-supported mesoporous titanium dioxide, *Desalin. Water Treat*. 57 (2016) 10859–10865. doi:10.1080/19443994.2015.1038593.
- [5] J. Ma, H. He, F. Liu, Effect of Fe on the photocatalytic removal of NO<sub>x</sub> over visible light responsive Fe/TiO<sub>2</sub> catalysts, *Appl. Catal. B Environ*. 179 (2015) 21–28. doi:10.1016/j.apcatb.2015.05.003.
- [6] J. Huang, Y. Lei, T. Luo, Photocatalytic H<sub>2</sub> production from water by metal-free dye-sensitized TiO<sub>2</sub> semiconductors: The role and development process of organic sensitizers, *Chemistry-Sustainability-Energy-Materials*. 13 (2020) 5863–5895. doi:10.1002/cssc.202001646.
- [7] R. Marschall, L. Wang, Non-metal doping of transition metal oxides for visible-light photocatalysis, *Catal. Today*. 225 (2014) 111–135. doi:10.1016/j.cattod.2013.10.088.
- [8] R. Ramirez, C. Arellano, J. Varia, S. Martinez, Visible Light-Induced Photocatalytic Elimination of Organic Pollutants by TiO<sub>2</sub>: A Review, *Curr. Org. Chem*. 19 (2015) 540–555. doi:10.2174/138527281906150417094736.
- [9] R. Darvishi Cheshmeh Soltani, M. Safari, R. Rezaee, A. Maleki, R. Ghanbari, Y. Zandasalimi, Synthesis of immobilised Ni-doped TiO<sub>2</sub> nanoparticles through hydrothermal route and their efficiency evaluation in photodegradation of formaldehyde, *Int. J. Environ. Anal. Chem*. 1 (2020) 1–13. doi:10.1080/03067319.2020.1746777.
- [10] M. Shaban, A. M. Ahmed, N. Shehata, M. A. Betiha, A. M. Rabie, Ni-doped and Ni/Cr co-doped TiO<sub>2</sub> nanotubes for enhancement of photocatalytic degradation of methylene blue, *J. Colloid Interface Sci*. 555 (2019) 31–41. doi:10.1016/j.jcis.2019.07.070.
- [11] H. -Hsin Tseng, M. -Chi Wei, S. -Fan Hsiung, C. -Wei Chiou, Degradation of xylene vapor over Ni-doped TiO<sub>2</sub> photocatalysts prepared by polyol-mediated synthesis, *Chem. Eng. J*. 150 (2009) 160–167. doi:10.1016/j.cej.2008.12.015.
- [12] G.G. Nakhate, V.S. Nikam, K.G. Kanade, S. Arbuj, B.B. Kale, J.O. Baeg, Hydrothermally derived nanosized Ni-doped TiO<sub>2</sub>: A visible light driven photocatalyst for methylene blue degradation, *Mater. Chem. Phys*. 124 (2010) 976–981.

- doi:10.1016/j.matchemphys.2010.08.007.
- [13] Z. Dong, D. Ding, T. Li, C. Ning, Ni-doped TiO<sub>2</sub> nanotubes photoanode for enhanced photoelectrochemical water splitting, *Appl. Surf. Sci.* 443 (2018) 321–328. doi:10.1016/j.apsusc.2018.03.031.
- [14] Z. Li, D. Ding, Q. Liu, C. Ning, Hydrogen Sensing with Ni-Doped TiO<sub>2</sub> Nanotubes, *Sensors*. 13 (2013) 8393–8402. doi:10.3390/s130708393.
- [15] A. Ranjitha, N. Muthukumarasamy, M. Thambidurai, D. Velauthapillai, R. Balasundaraprabhu, S. Agilan, Fabrication of Ni-doped TiO<sub>2</sub> thin film photoelectrode for solar cells, *Sol. Energy*. 3 (2014) 159–165. doi:10.1016/j.solener.2014.02.034.
- [16] M. Baruah, S.L. Ezung, A. Supong, P.C. Bhomick, S. Kumar, D. Sinha, Synthesis, characterization of novel Fe-doped TiO<sub>2</sub> activated carbon nanocomposite towards photocatalytic degradation of Congo red, *E. coli*, and *S. aureus*, *Korean J. Chem. Eng.* 38 (2021) 1277–1290. doi:10.1007/s11814-021-0830-4.
- [17] M. Baruah, A. Supong, P. Chandra, B. Rituparna, K. Chubaakum, Batch sorption-photodegradation of Alizarin Red S using synthesized TiO<sub>2</sub>/activated carbon nanocomposite: an experimental study and computer modelling, *Nanotechnol. Environ. Eng.* 3 (2020) 1–13. doi:10.1007/s41204-020-00071-3.
- [18] W. Guo, B. Pan, S. Sakiah, G. Yavas, W. Ge, W. Zou, W. Tong, H. Hong, Persistent Organic Pollutants in Food: Contamination Sources, Health Effects and Detection Methods, *Environmental Res. Public Heal.* 16 (2019) 1–29. doi:10.3390/ijerph16224361.
- [19] H. I. Abdel-Shafy, M.S.M. Mansour, A review on polycyclic aromatic hydrocarbons: Source, environmental impact, effect on human health and remediation, *Egypt. J. Pet.* 25 (2016) 107–123. doi:10.1016/j.ejpe.2015.03.011.
- [20] A. Tarafdar, A. Sinha, R. E. Mastro, Biodegradation of anthracene by a newly isolated bacterial strain, *Bacillus thuringiensis* AT.ISM.1, isolated from a fly ash deposition site, *Appl. Microbiol.* 65 (2017) 327–334. doi:10.1111/lam.12785.
- [21] H. Teng, S. Xu, D. Sun, Y. Zhang, Preparation of Fe-doped TiO<sub>2</sub> nanotubes and their photocatalytic activities under visible light, *Int. J. Photoenergy*. 2013 (2013) 1–7. doi:10.1155/2013/981753.
- [22] Y. dong Liang, Y. jun He, Y. hang Zhang, Q. qian Zhu, Adsorption property of alizarin red S by NiFe<sub>2</sub>O<sub>4</sub> polyaniline magnetic composite, *J. Environ. Chem. Eng.* 6 (2018) 416–425. doi:10.1016/j.jece.2017.12.022.
- [23] A.A. Bunaciu, H.Y. Aboul-enein, X-Ray Diffraction: Instrumentation and Applications, *Crit. Rev. Analytical Chem.* 45 (2015) 289–299. doi:10.1080/10408347.2014.949616.
- [24] M. Rani, Rachna, U. Shanker, Mineralization of carcinogenic anthracene and phenanthrene by sunlight active bimetallic oxides nanocomposites, *J. Colloid Interface Sci.* 555 (2019) 676–688. doi:10.1016/j.jcis.2019.08.016.



- [25] A. Eshaghi, H. Moradi, Optical and photocatalytic properties of the Fe-doped TiO<sub>2</sub> nanoparticles loaded on the activated carbon, *Adv. Powder Technol.* 29 (2018) 1879–1885. doi:10.1016/j.appt.2018.04.026.
- [26] P.R. Chowdhury, K.G. Bhattacharyya, Synthesis and characterization of Mn/Co/Ti LDH and its utilization as a photocatalyst in visible light assisted degradation of aqueous Rhodamine B, *RSC Adv.* 6 (2016) 112016–112034. doi:10.1039/c6ra24288j.
- [27] X. Li, R. Shen, S. Ma, X. Chen, J. Xie, Graphene-based heterojunction photocatalysts, *Appl. Surf. Sci.* 430 (2018) 53–107. doi:10.1016/j.apsusc.2017.08.194.
- [28] A.A. Isari, A. Payan, M. Fattahi, S. Jorfi, B. Kakavandi, Photocatalytic degradation of rhodamine B and real textile wastewater using Fe-doped TiO<sub>2</sub> anchored on reduced graphene oxide (Fe-TiO<sub>2</sub>/rGO): Characterization and feasibility, mechanism and pathway studies, *Appl. Surf. Sci.* 462 (2018) 549–564. doi:10.1016/j.apsusc.2018.08.133.
- [29] X. Zou, X. Dong, L. Wang, H. Ma, X. Zhang, X. Zhang, Preparation of Ni Doped ZnO-TiO<sub>2</sub> Composites and Their Enhanced Photocatalytic Activity, *Int. J. Photoenergy.* 2014 (2014) 1–9. doi:10.1155/2014/893158.
- [30] Rachna, M. Rani, U. Shanker, Sunlight mediated improved photocatalytic degradation of carcinogenic benz[a]anthracene and benzo[a]pyrene by zinc oxide encapsulated hexacyanoferrate nanocomposite, *J. Photochem. Photobiol. A Chem.* 381 (2019) 1–12. doi:10.1016/j.jphotochem.2019.111861.
- [31] H. Gupta, R. Kumar, Removal of PAH Anthracene from Aqueous Media using Banana Peel Activated Carbon, *Int. J. Sci. Res. Environ. Sci.* 4 (2016) 109–114. doi:10.12983/ijres-2016-p0109-0114.
- [32] Z.U. Zango, K. Jumbri, N.S. Sambudi, N.H.H.A. Bakar, N.A.F. Abdullah, C. Basheer, B. Saad, Removal of anthracene in water by MIL-88(Fe), NH<sub>2</sub>-MIL-88(Fe), and mixed-MIL-88(Fe) metal–organic frameworks, *RSC Adv.* 9 (2019) 41490–41501. doi:10.1039/c9ra08660a.
- [33] Z. Ghasemi, H. Younesi, A.A. Zinatizadeh, Kinetics and thermodynamics of photocatalytic degradation of organic pollutants in petroleum refinery wastewater over nano-TiO<sub>2</sub> supported on Fe-ZSM-5, *J. Taiwan Inst. Chem. Eng.* 65 (2016) 357–366. doi:10.1016/j.jtice.2016.05.039.
- [34] Y. John, V. Emery David Jr, D. Mmerek, A Comparative Study on Removal of Hazardous Anions from Water by Adsorption: A Review, *Int. J. Chem. Eng.* 2018 (2018) 1–21. doi:10.1155/2018/3975948.
- [35] P. Zheng, Z. Pan, H. Li, B. Bai, W. Guan, Effect of different type of scavengers on the photocatalytic removal of copper and cyanide in the presence of TiO<sub>2</sub>@yeast hybrids, *J. Mater. Sci. Mater. Electron.* 26 (2015) 6399–6410. doi:10.1007/s10854-015-3229-3.
- [36] H. E. Emam, H. B. Ahmed, E. Gomaa, M. H. Helal, R. M. Abdelhameed, Recyclable photocatalyst composites based on Ag<sub>3</sub>VO<sub>4</sub> and Ag<sub>2</sub>WO<sub>4</sub> @MOF@cotton for effective discoloration of dye in visible light, *Cellulose.* 27 (2020) 7139–7155.

- doi:10.1007/s10570-020-03282-8.
- [37] T. Hadibarata, A.B. Khudhair, M.R. Salim, Breakdown Products in the Metabolic Pathway of Anthracene Degradation by a Ligninolytic Fungus *Polyporus* sp. S133, *Water Air Soil Pollut.* 223 (2012) 2201–2208. doi:10.1007/s11270-011-1016-1.
- [38] N. Daneshvar, A. Aleboyeh, A. R Khataee, The evaluation of electrical energy per order ( $E_{EO}$ ) for photooxidative decolorization of four textile dye solutions by the kinetic model, *Chemosphere*. 59 (2005) 761–767. doi:10.1016/j.chemosphere.2004.11.012.
- [39] M.A. Behnajady, H. Eskandarloo, M. Shokri, Influence of the chemical structure of organic pollutants on photocatalytic activity of  $TiO_2$  nanoparticles: Kinetic analysis and evaluation of electrical energy per order ( $E_{EO}$ ), *Dig. J. Nanomater. Biostructures*. 6 (2011) 1887–1895.
- [40] M. A Vishnuganth, N. Remya, M. Kumar, N. Selvaraju, Photocatalytic degradation of carbofuran by  $TiO_2$ -coated activated carbon: Model for kinetic, electrical energy per order and economic analysis, *J. Environ. Manage.* 181 (2016) 201–207. doi:10.1016/j.jenvman.2016.06.016.
- [41] A. Tirado-Guizar, W. González-Gómez, G. Pina-Luis, J. Trinidad Elizalde Galindo, F. Paraguay-Delgado, Anthracene removal from water samples using a composite based on metal-organic-frameworks (MIL-101) and magnetic nanoparticles ( $Fe_3O_4$ ), *Nanotechnology*. 31 (2020) 1–24. doi:10.1088/1361-6528/ab70fd.
- [42] S.S.M. Hassan, W.I.M. El Azab, H.R. Ali, M.S.M. Mansour, Green synthesis and characterization of ZnO nanoparticles for photocatalytic degradation of anthracene, *Adv. Nat. Sci. Nanosci. Nanotechnol.* 6 (2015) 1–11. doi:10.1088/2043-6262/6/4/045012.
- [43] B. L. Martínez-vargas, M. Cruz-ramírez, J. A. Díaz-real, J. L. Rodríguez-lópez, F.J. Bacame-valenzuela, R. Ortega-borges, Y. Reyes-vidal, L.O.- Frade, Synthesis and characterization of n-ZnO/p-MnO nanocomposites for the photocatalytic degradation of anthracene, *J. Photochem. Photobiol. A Chem.* 369 (2019) 85–96. doi:10.1016/j.jphotochem.2018.10.010.
- [44] A. Kumar Jagadeesan, J. Amarnath Duvuru, A. Jabasingh S, S. Kumar Ponnusamy, V. Anand Kabali, N. Gopakumaran, K. Raja Namasivayam Selvaraj, K. Thangavelu, S. Sunny, P. Pushkala Somasundaram, Y. Devarajan, One pot Green Synthesis of Nano magnesium oxide-carbon composite: Preparation, characterization and application towards anthracene adsorption, *J. Clean. Prod.* 237 (2019) 1–18. doi:10.1016/j.jclepro.2019.117691.
- [45] F.F. Karam, F.H. Hussein, S.J. Baqir, A.F. Halbus, R. Dillert, D. Bahnemann, Photocatalytic Degradation of Anthracene in Closed System Reactor, *Int. J. Photoenergy*. 204 (2014) 1–6. doi:10.1155/2014/503825.
- [46] F.C.S.M.R. Lopes, M. da G.C. da Rocha, P. Bargiela, H.S. Ferreira, C.A. de M. Pires,  $Ag/TiO_2$  photocatalyst immobilized onto modified natural fibers for photodegradation of anthracene, *Chem. Eng. Sci.* 227 (2020) 1–59. doi:10.1016/j.ces.2020.115939.

## CHAPTER 6

### **PHOTOCATALYTIC DEGRADATION OF PHENOL USING Co-DOPED TiO<sub>2</sub>/ACTIVATED CARBON NANOCOMPOSITE**

---

This chapter deals with the preparation of Co-doped titanium dioxide supported on activated carbon (CDT/PAC) nanocomposite using the hydrothermal synthesis method. The physicochemical characterization of the nanocomposite was done by different analytical methods like SEM-EDX, XRD, FT-IR, photoluminescence (PL), pH<sub>ZPC</sub>, and UV-Visible diffuse reflectance spectroscopy (DRS). The visible light active nanocomposite was used for the photocatalytic degradation of phenol from an aqueous solution. The efficacy of the nanocomposite was evaluated by varying nanocomposite dosage, contact time, phenol concentrations, and pH of the solution. Kinetics and thermodynamics studies were carried out to understand the photocatalytic degradation behaviour of phenol. The effect of different interfering ions on photocatalytic degradation of phenol and also the reusability of the CDT/PAC nanocomposite were studied. The photodegradation mechanism of phenol was studied using GC-MS analysis. The total electrical energy consumed and operating cost involved in the degradation process was also measured.

## 6.1 Introduction

In recent years, contamination of water resources due to rapid industrial development and modernization has stimulated significant concern worldwide [1]. From the pharmaceuticals industries, plastic plants, oil refiners, textile industries, and coal conversion industries, phenols are mainly discharged as waste products that largely contaminate water resources [2]. The bioaccumulative nature, persistence, widespread occurrence, and poor biodegradability of phenolic compounds create concern to the environment. Upon ingestion of phenol different health-related problems can arise such as metabolic acidosis, respiratory distress, renal failure, cardiovascular effects, neurological effects, necrosis of the skin, gastrointestinal irritation, abdominal pain, and paralysis [3]. Phenol retains its toxicity effects in our body even at a concentration lower than  $10 \text{ ng l}^{-1}$  [4]. Hence, the removal of phenol from water sources has become a major challenge for the research community. At present, several methods are applied for removing phenols from wastewater which include nanofiltration [5], adsorption [6], ion exchange [7], reverse osmosis [8], electrochemical degradation [9], membrane filtration [10], electrodialysis [11], electrocoagulation [12], wet oxidation [13], Fenton [14], and phytoremediation [15]. Although these methods successfully remove phenol from wastewater, there are some concerns related to secondary waste generation, operation difficulty, reliability, pre-treatment requirements, environmental impact, formation of toxic by-products, etc. [16]. In this regard, Advanced oxidation processes (AOPs) are getting attention due to their ability to degrade non-biodegradable pollutants in addition to their high treatment potential [17]. In the AOPs, upon exposure of light onto a photocatalyst having a particular wavelength, highly photo-reactive hydroxyl radicals ( $\cdot\text{OH}$ ) are generated. The reactive radicals perform a redox reaction with the electron-hole pairs of the photocatalyst and further degrade pollutant compounds to  $\text{CO}_2$  and  $\text{H}_2\text{O}$  [18]. In photocatalysis, numerous types of photocatalysts have been used such as  $\text{TiO}_2$ ,  $\text{Bi}_2\text{O}_3$ ,  $\text{SnO}_2$ ,  $\text{Fe}_2\text{O}_3$ ,  $\text{WO}_3$ , and  $\text{g-C}_3\text{N}_4$  [19]. To date,  $\text{TiO}_2$  in its anatase phase has gained much attention due to its unique properties that include photochemical stability, non-toxicity, biological and chemical inactivity, and environmental-friendly nature [20]. However, high quantity recombination between electron-hole pairs impedes their applicability in the visible light region [21].

Therefore, various strategies such as metal/non-metal doping [22,23], hydrogen treatment [24], photosensitization using dyes [25] have been employed to improve the photo-activity of  $\text{TiO}_2$  in the visible light. Among these alternatives, doping of  $\text{TiO}_2$  with transition metals can lead to catalysis degradation in the visible light region. Transition metal doping creates an intermediate

level in the lattice structure of  $\text{TiO}_2$  and also reduces the bandgap energy thus photocatalytic activity can take place in the visible light region [26]. Transition metal cobalt ( $\text{Co}^{2+}$ ) has been garnering more interest as a dopant for  $\text{TiO}_2$ . Due to similarity of the ionic radius of  $\text{Co}^{2+}$  ( $r = 0.65 \text{ \AA}$ ) to the ionic radius of  $\text{Ti}^{4+}$  ( $r = 0.68 \text{ \AA}$ ),  $\text{Co}^{2+}$  it can act as a substitute in the crystal structure of  $\text{TiO}_2$  [27]. However, the agglomerating property of  $\text{TiO}_2$  makes it difficult in separating it from the solution after photocatalytic reactions [28]. For these reasons,  $\text{TiO}_2$  is deposited on large surface area mesoporous materials and ultimately forms a novel material having properties of both materials. Activated carbon (AC) is widely used as catalyst support due to its high surface area, surface functionalities, and excellent porosity, which make it helpful in gathering pollutant molecules near the catalyst surface sites [29]. The synergistic effect between AC and  $\text{TiO}_2$  will also help in separating electron-hole pairs inhibiting their rapid recombination and thus prolonging the electron's lifetime, and thereby enhancing the photocatalytic activity [30]. The typical mechanism for the photodegradation of phenol is shown in Figure 6.1.

In this work, Co-doped  $\text{TiO}_2$  loaded on activated carbon (CDT/PAC) nanocomposite was obtained by hydrothermal method. CDT/PAC nanocomposite showed excellent catalytic properties in phenol degradation in the visible light region.

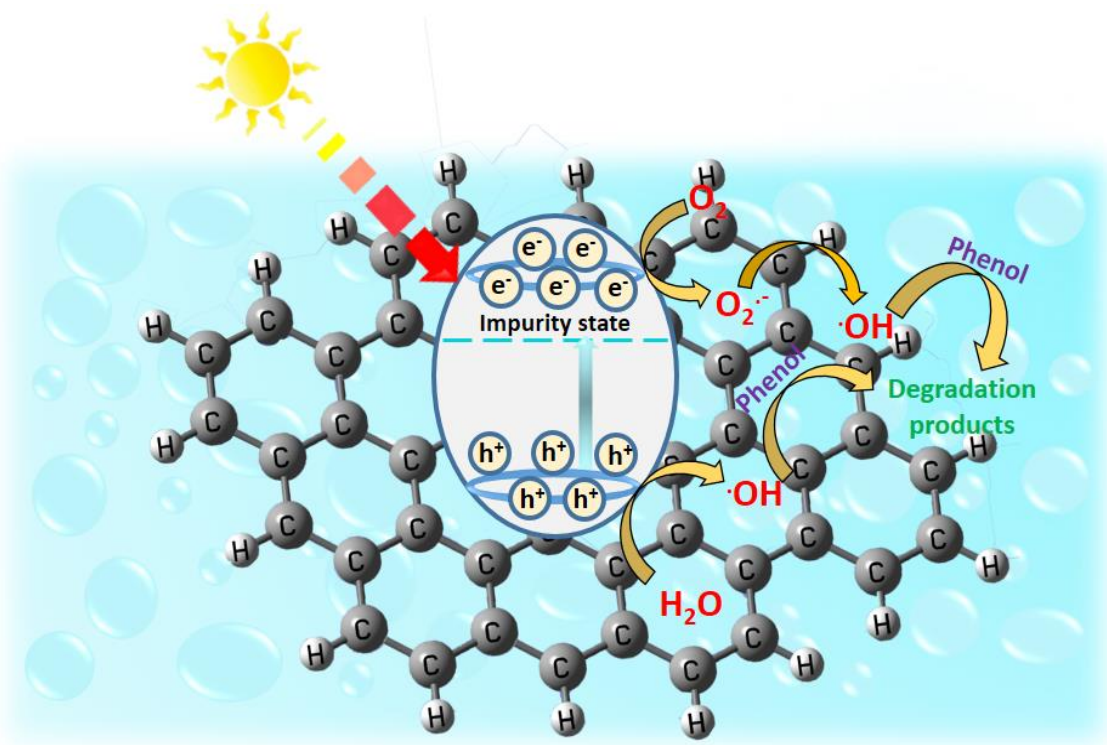


**Figure 6.1** Schematic illustration of photodegradation of phenol over CDT/PAC nanocomposite

## 6.2 Materials and methods

### 6.2.1 Materials

Cobalt nitrate hexahydrate ( $\text{Co}(\text{NO}_3)_2 \cdot 6\text{H}_2\text{O}$ , 99.90%), titanium tetrachloride ( $\text{TiCl}_4$ , 99.10%), sulphuric acid (98%), zinc chloride (99%), and ammonia (25%) were procured from Sigma-Aldrich. Co., India. Ethylenediaminetetraacetic acid ( $\text{C}_{10}\text{H}_{16}\text{N}_2\text{O}_8$ , 99%), sodium nitrate ( $\text{NaNO}_3$ , 98%), sodium chloride ( $\text{NaCl}$ , 99.5%), copper sulphate ( $\text{CuSO}_4$ , 98.5%), glycine ( $\text{C}_2\text{H}_5\text{NO}_2$ , 99%), oxalic acid ( $\text{C}_2\text{H}_2\text{O}_4$ , 95%), and cadmium nitrate ( $\text{Cd}(\text{NO}_3)_2 \cdot 4\text{H}_2\text{O}$ , 98%) were obtained from Himedia, India. Phenol ( $\text{C}_6\text{H}_6\text{O}$ , 99%) was procured from Merck, India. All chemicals utilized were of pure scientific grade and used without further purifications.

### 6.2.2 Synthesis of CDT/PAC nanocomposite

Activated carbon and  $\text{TiO}_2$  were used as the starting materials for CDT/PAC nanocomposite synthesis. Activated carbon was prepared using pine cones biomass and  $\text{TiO}_2$  nanoparticles using  $\text{TiCl}_4$  via the sol-gel method. The synthetic pathways for AC and  $\text{TiO}_2$  synthesis were described in sections 3.2.1.1 and 3.2.1.2 of Chapter 3. Synthetic methods to prepare  $\text{TiO}_2$ -pine cone activated carbon ( $\text{TiO}_2$ -NP/PAC) photocatalyst have been described in detail in section 3.2.1.3 of Chapter 3.

CDT/PAC nanocomposite was synthesized by a hydrothermal method. An amount of 0.15 g of the sol-gel prepared  $\text{TiO}_2$  nanoparticles were added to a beaker containing 1.0 g of  $\text{Co}(\text{NO}_3)_2 \cdot 6\text{H}_2\text{O}$  powder dispersed in 100 ml double distilled water. The resultant mixture was kept under stirring for 30 minutes. Subsequently, 0.3 g of PAC was slowly poured into the above mixture and it was subjected to ultrasonic agitation for 1 h. After ultrasonication, the solution was slowly transferred into a Teflon-lined autoclave and kept under hydrothermal treatment at  $150^\circ\text{C}$  for 24 h. After completion of the hydrothermal process, the product was centrifuged and washed with double distilled water to neutralize the pH of the solution, and finally, it was dried at  $65^\circ\text{C}$  for 12 h [31].

### 6.2.3 Characterization of CDT/PAC nanocomposite

The synthesized CDT/PAC nanocomposite was characterized by several analytical techniques. The catalyst phase and crystal structure were obtained using an X-ray diffractometer (XRD) (X'pert PRO Philips, Japan,  $\text{CuK}\alpha$  radiation). The surface morphology of the CDT / PAC was investigated using a scanning electron microscope (SEM, Zeiss, Sigma300) equipped with energy dispersive X-ray analysis (EDX). The presence of various functional groups was determined using a Fourier transform infrared (FT-IR) spectrometer (model: Perkin Elmer,



Spectrum Two). The light absorption performance was estimated using a diffuse reflection spectrophotometer (DRS, Shimadzu, and wavelength 200-600 nm). The emission spectrum was analyzed using a photoluminescence spectrophotometer (spectrofluorometer Horiba Fluoromax4CP, xenon lamp 150W). The BET surface area of the TiO<sub>2</sub>, TiO<sub>2</sub>-NP/PAC, and CDT/PAC nanocomposites was determined using a Quantachrome device (Autosorb iQ Station 1, 77 K). Total pore volume and pore radii were calculated using the Barrett-Joiner-Hallender (BJH) method. The zero point charge (pH<sub>zpc</sub>) of the catalyst was determined using the batch equilibration method as described in Chapter 2 section 2.3.

#### 6.2.4 Photocatalytic degradation experiment

Photocatalytic degradation of phenol was performed in a photocatalytic reactor consisting of a black box (dimension: 63 × 44 × 44 cm). A 250 ml Pyrex glass container containing 200 ml of phenol solution was placed on a magnetic stirrer and a fixed amount of CDT/PAC was mixed with this phenol solution. A visible light lamp (High-pressure mercury lamp, wavelength 520 nm, 350 W) was placed on the top of the reactor 10 cm away from the reaction solution. The photocatalytic reaction was triggered by the use of visible light radiation which reached the CDT/PAC photocatalyst through the phenol solution. The temperature of the reactor was maintained at 25°C using a constant flow of water from a water pump. In addition, a ventilation fan has been used inside the reactor for continuous air circulation.

Phenol stock solution (1000 ppm) was prepared by diluting 1 g of phenol in 1000 ml of double-distilled water. The stock solution was appropriately diluted to various concentrations of 20 ppm, 40 ppm, 60 ppm, 80 ppm, and 100 ppm to further obtain the desired concentration range. Afterward, 200 ml of phenol solution with different concentrations (20 ppm, 40 ppm, 60 ppm, 80 ppm, and 100 ppm) was mixed with the CDT/PAC nanocomposite without light exposure for a maximum of 30 minutes so that adsorption-desorption equilibrium can be established in the reaction system. When the equilibrium state was reached, the concentration of the phenol was measured and set as the initial concentration so that the adsorption of phenol by the nanocomposite did not interfere with the study of the overall photocatalytic effect. The final concentration of the phenol solution was then measured with a Lambda-365 UV-Vis spectrophotometer at a maximum wavelength of 269 nm by taking out 3.5 ml at every 10 minutes.

The degradation percentage was calculated by using equation 6.1.

$$\text{Phenol degradation (\%)} = \frac{C_i - C_e}{C_i} \times 100 \quad (6.1)$$

where C<sub>i</sub> and C<sub>e</sub> are the concentrations of phenol before and after the photocatalytic treatment.



### 6.3 Results and discussion

#### 6.3.1 Characterization of CDT/PAC nanocomposite

##### (a) XRD analysis

The XRD spectra of CDT/PAC are analysed and are matched with XRD spectra of  $\text{TiO}_2$ -NP/PAC, and  $\text{TiO}_2$  catalyst as shown in Figure 6.2. According to the figure, all the catalysts exhibited their characteristic peaks at 25.281 (1 0 1), 38.576 (1 1 2), 48.050 (2 0 0), 53.891 (1 0 5), 55.062 (2 1 1), 62.690 (2 0 4), 68.762 (1 1 6), 70.311 (2 2 0), and 75.032 (2 1 5) that correspond anatase phase of crystalline  $\text{TiO}_2$  with the miller indices (JCPDS file No. 21-1272) [32]. In the XRD spectra of CDT/PAC nanocomposite, no cobalt-rich oxides or  $\text{CoTiO}_x$  phases were observed which indicates that the concentration of  $\text{Co}^{2+}$  ions or  $\text{Co}_2\text{O}_3$  crystal was too small for peak detection, and also the  $\text{Co}_2\text{O}_3$  were well dispersed on the  $\text{TiO}_2$  surface. Moreover, the XRD peak of CDT/PAC nanocomposite at miler indice (1 0 1) was broader and slightly weaker in comparison with the single activated carbon support  $\text{TiO}_2$  nanocomposite, which suggests the effect of the  $\text{Co}^{2+}$  ions on CDT/PAC formation. There was no peak found for PAC due to its non-crystalline structure. The average crystalline size calculated for the CDT/PAC nanocomposite using the Debye-Scherrer equation was found to be 3.36 nm.

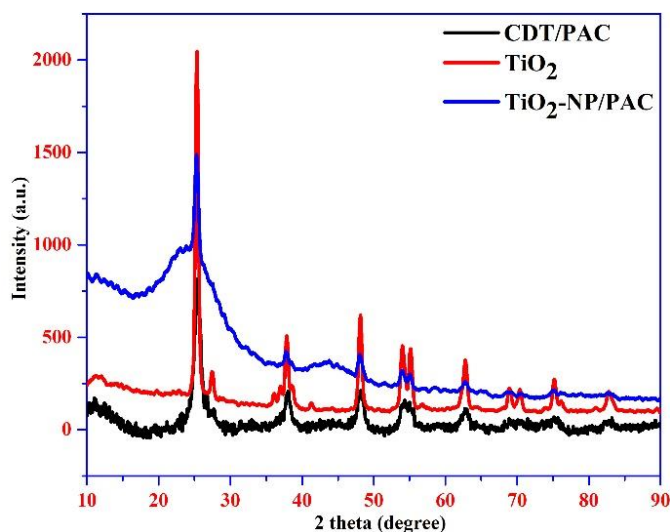


**Figure 6.2** XRD pattern of CDT/PAC nanocomposite and a comparison with  $\text{TiO}_2$ ,  $\text{TiO}_2$ -NP/PAC [24]

##### (b) SEM and EDX analysis

SEM image in Figure 6.3 (a) represents the surface morphology of CDT/PAC nanocomposite. It can be seen from the image that, white spherical  $\text{TiO}_2$  nanoparticles of different sizes were accumulated together with  $\text{Co}^{2+}$  ions and aggregated on the PAC surface. It was observed that the  $\text{Co}^{2+}$  ions were incorporated in lattice sites of  $\text{Ti}^{4+}$  ions and, these were filled and trapped inside the PAC pores. The average particle size of CDT/PAC nanocomposite is about 5 nm in

close agreement with the crystal sizes estimated from XRD (3.36 nm). Figure 6.3 (b) shows the EDX spectra of CDT/PAC nanocomposite which confirms that it is composed of Co, Ti, O, and C elements. It is clear from the EDX analyses that 75.38% Ti, 23.86% O, 0.28% Co, and 0.48% C are present in the CDT/PAC nanocomposite.

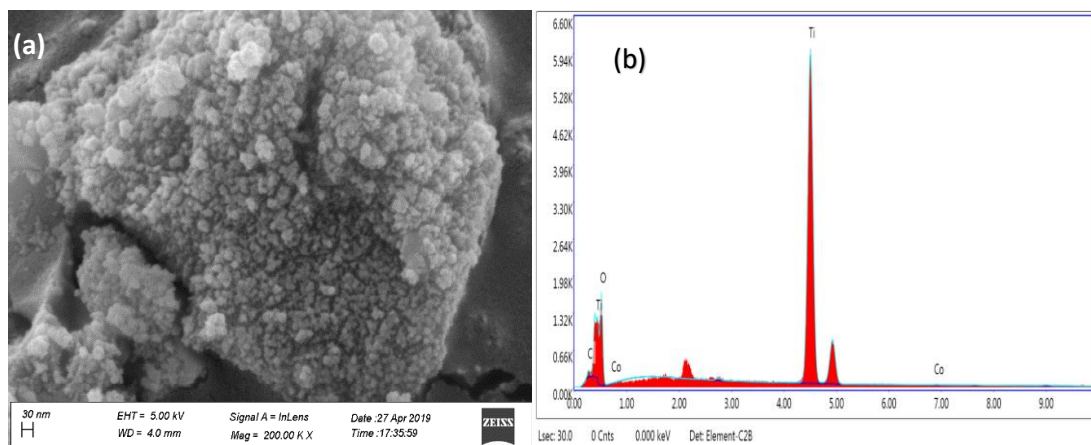


**Figure 6.3** (a) SEM image of CDT/PAC nanocomposite, (b) EDX spectra of CDT/PAC nanocomposite

### (c) FT-IR analysis

Figure 6.4 displays the FT-IR spectrum of CDT/PAC nanocomposite. The broadband at  $3394\text{ cm}^{-1}$  is assigned due to the superposition stretching vibration of the surface -OH radical or adsorbed water molecules. A resonance at  $1606\text{ cm}^{-1}$  corresponds to the -OH radical of water molecules adsorbed in the interlayer space [33]. A peak at  $1243\text{ cm}^{-1}$  resulted from the asymmetric stretching of ester and ether functional groups. The band at  $1048\text{ cm}^{-1}$  is attributed to the Ti-O-C stretching vibration, which suggests the formation of a bond between  $\text{TiO}_2$  and C, and is attached chemically making a strong Ti-O-C bond. The band at  $642\text{ cm}^{-1}$  is attributed to the Ti-O stretching vibration [27].

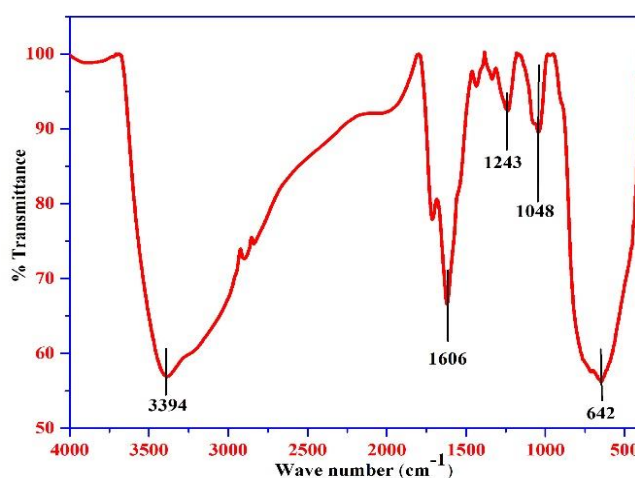


**Figure 6.4** FT-IR spectra of CDT/PAC nanocomposite

**(d) UV-Vis DRS analysis**

The UV-Vis diffuse reflectance spectra (DRS) of CDT/PAC are shown in Figure 6.5 (a), and the spectra of TiO<sub>2</sub>-NP/PAC, and TiO<sub>2</sub> are shown for comparison. From the figure, it can be seen that TiO<sub>2</sub> and TiO<sub>2</sub>-NP/PAC can well respond to ultraviolet light of wavelength (<400 nm), this characteristic is due to the excitation of O 2p electrons from valence band (VB) to Ti 3d conduction band (CB), hence these show photoabsorption only in the UV domain [34]. However, the addition of Co ion shifted the photoabsorption in the visible light of wavelength (>400nm), which was attributed due to the surface plasmon resonance effect of metallic Co ion [35]. Hence, CDT/PAC nanocomposite is a promising photocatalyst to use under visible light irradiation.

The optical bandgap energies were determined using Tauc's plot, and it is calculated using the equation:

$$\alpha h\nu = K (h\nu - E_g)^n \quad (6.2)$$

where  $E_g$  = energy of the bandgap (eV),  $h\nu$  = energy of photon,  $K$  = proportionality constant,  $\alpha$  = absorption coefficient, and  $n = 1/2$ , allowed direct transition.

A curve of  $(\alpha h\nu)^2$  vs  $h\nu$  was plotted, and from the curve, the  $E_g$  value was calculated. For CDT/PAC nanocomposite the  $E_g$  value was found to be 2.4 eV, which is much lower as compared to  $E_g$  values of TiO<sub>2</sub> (3.1 eV) and TiO<sub>2</sub>-NP/PAC (3.2 eV) [36]. As shown in Figure 6.5 (b), the Co doping reduces the bandgap energies of TiO<sub>2</sub> from 3.1 to 2.4 eV, this shift of bandgap energy is due to the excitation of VB Co ions (3d electrons) to the host TiO<sub>2</sub> CB [37]. These results suggest that the doping of Co ions affected the bandgap structure of TiO<sub>2</sub> as a result TiO<sub>2</sub> bandgap energy was reduced and this allowed it to become a visible light-sensitive photocatalyst.

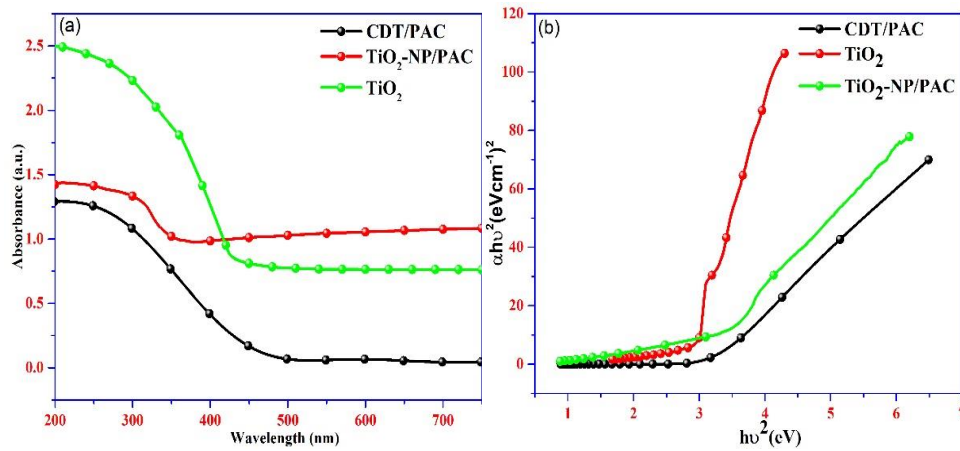


**Figure 6.5** (a) DRS spectra and (b) Tauc's plot for CDT/PAC nanocomposite (plot for TiO<sub>2</sub> and TiO<sub>2</sub>-NP/PAC is shown for comparison only) [24]

**(e) PL analysis**

Photoluminescence (PL) is used to study the separation efficiency of the electron-hole pairs formed in the photoreaction of the semiconductors [38]. The PL analysis of the bare  $\text{TiO}_2$ , Co-doped  $\text{TiO}_2$ , and Co-doped  $\text{TiO}_2/\text{PAC}$  nanocomposite was carried out with an excitation wavelength of 420 nm as shown in Figure 6.6. From the figure, it can be seen that a high-intensity emission peak at 466 nm was observed for  $\text{TiO}_2$  due to the high emission of a photon by  $e^-h^+$  recombination. However, after doping  $\text{TiO}_2$  with Co, the intensity of the PL spectra decreased. This decrease in the intensity of PL indicates that electron-hole pair recombination is significantly reduced compared to  $\text{TiO}_2$ , which may be due to the formation of the impurity energy level ( $\text{Co}^{2+}/\text{Co}^{3+}$ ) nearer the VB of  $\text{TiO}_2$ , and excitation of this charge to the CB of  $\text{TiO}_2$  [39]. In the Co-doped  $\text{TiO}_2$  supported on activated carbon, the emission peak intensity decreases more compared to Co-doped  $\text{TiO}_2$  which signifies more  $e^-h^+$  pair separation. This is mainly due to the high transportation and charge carrier mobility of activated carbon that leads to more photocatalytic activity.

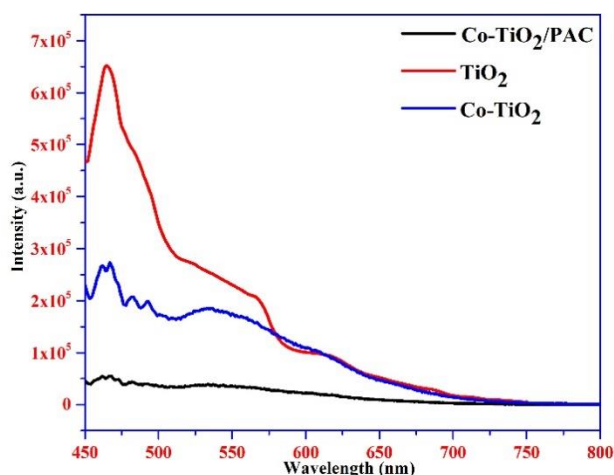


**Figure 6.6** Photoluminescence spectra of  $\text{TiO}_2$ , Co-doped  $\text{TiO}_2$ , and CDT/PAC nanocomposite

**(f) BET surface area and pore structure analysis**

The textural properties, namely BET surface area, pore radii, and total pore volume of the  $\text{TiO}_2$ , PAC, and CDT/PAC are given for comparison in Table 6.1. From the table, it is elucidated that the surface area of CDT/PAC nanocomposite is higher than that of bare  $\text{TiO}_2$  nanoparticles ( $60.21 \text{ m}^2\text{g}^{-1}$ ). This is due to the addition of Co ions to the  $\text{TiO}_2$  crystal structure [40] and also because the use of PAC as a support matrix enhances the surface area of the CDT/PAC [41]. It can be seen that the PAC surface area ( $878.07 \text{ m}^2\text{g}^{-1}$ ) is reduced to  $85.357 \text{ m}^2\text{g}^{-1}$  by the addition of Co-dopant in the CDT/PAC nanocomposite. This lowering of surface area may be due to the covering of PAC pores by Co and  $\text{TiO}_2$  nanoparticles, confirming that Co and  $\text{TiO}_2$

nanoparticles had occupied a large surface area of PAC. Furthermore, CDT/PAC has a total pore volume of  $0.121 \text{ cm}^3 \text{ g}^{-1}$  and a pore diameter of 4.148 nm which is within the mesoporous range. Thus, the higher surface area of mesoporous CDT/PAC nanocomposite will allow more photocatalytic performance.

<b>Table 6.1</b> BET surface area, pore-volume, and pore radii of $\text{TiO}_2$ , CDT/PAC nanocomposite	
<b>Proximate analysis (wt %)</b>	
BET surface area (CDT/PAC)	$85.357 \text{ m}^2 \text{ g}^{-1}$
BET surface area ( $\text{TiO}_2$ )	$60.21 \text{ m}^2 \text{ g}^{-1}$
BET surface area (PAC)	$878.07 \text{ m}^2 \text{ g}^{-1}$
Total pore volume	$0.121 \text{ cm}^3 \text{ g}^{-1}$
Pore radius	4.148 nm

### (g) Zero-point charge ( $\text{pH}_{\text{zpc}}$ ) analysis

The  $\text{pH}_{\text{zpc}}$  of the CDT/PAC nanocomposite was found to be 6.65 (Figure 6.7), which suggests that the nanocomposite surface acquires a positive charge when  $\text{pH} < 6.65$  and there will be a negative surface charge when  $\text{pH} > 6.65$  [24].

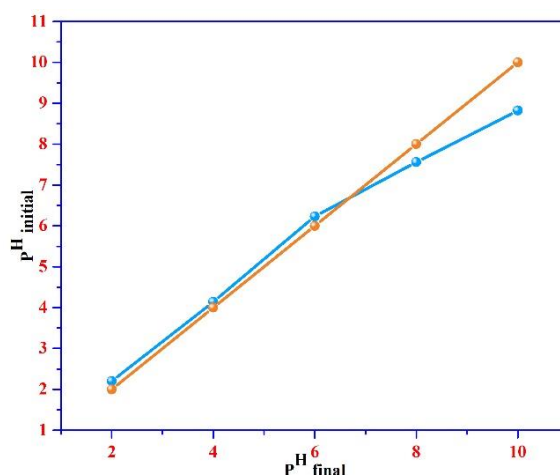


**Figure 6.7** Zero-point charge plot for CDT/PAC nanocomposite

### 6.3.2 Photocatalytic activity

The photocatalytic performance of the  $\text{TiO}_2$ ,  $\text{TiO}_2\text{-NP/PAC}$ , and CDT/PAC nanocomposite were evaluated by the degradation of phenol in an aqueous solution under visible light following the route as discussed in experimental section 6.2.4.

Initially, the degradation of the phenol was tested by irradiating the CDT/PAC nanocomposite under UV light (325 nm mercury lamp). Negligible percent of phenol degradation was observed under the same set of photocatalytic experiments and degradation of 0.85% (20 ppm), 0.8% (40 ppm), 0.72% (60 ppm), 0.4% (80 ppm), and 0.0% (100 ppm) occurred after 3h of reaction under

UV light (Figure 6.8). These results indicate that the CDT/PAC nanocomposite does not show its activity under UV light irradiation.

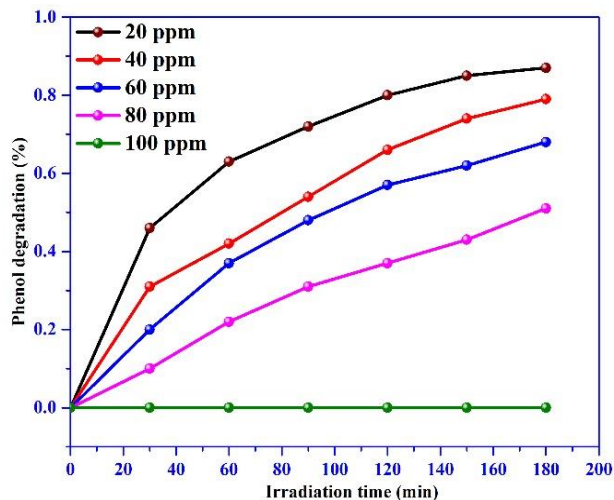


**Figure 6.8** Effect of CDT/PAC (0.35 g) with irradiation time in the degradation of phenol solution under UV light (325 nm)

#### (a) Effect of dosages of CDT/PAC nanocomposite

To investigate the effect of doses of  $\text{TiO}_2$ ,  $\text{TiO}_2\text{-NP/PAC}$ , and CDT/PAC nanocomposite on phenol degradation, varying dosages between 0.15–0.55 g were dispersed in 200 ml of 20, 40, 60, 80, and 100 ppm phenol solution (Figure 6.9). The degradation experiment was run according to the procedure as discussed in section 6.2.4. Among the nanocomposite, the CDT/PAC showed significantly higher photocatalytic degradation activity, and a maximum of 100% was achieved for 20 ppm phenol using 0.35 g of CDT/PAC at 60 minutes of visible light irradiation. This high degradation of phenol can be attributed to the doping of Co ions into  $\text{TiO}_2$  which separates the  $e^-h^+$  pair further, the addition of supporting material PAC enhances the surface area of the nanocomposite [24].

Under similar experimental conditions, the other catalyst  $\text{TiO}_2$  and  $\text{TiO}_2\text{-NP/PAC}$  degraded a maximum of 21.5% and 30.8% which is very less as compared to the CDT/PAC nanocomposite. This confirms that the high photocatalytic degradation of phenol using CDT/PAC nanocomposite is due to the doping of Co which shifts the light responses of  $\text{TiO}_2$  to the visible light region. The minor degradation of  $\text{TiO}_2$  and  $\text{TiO}_2\text{-NP/PAC}$  might be due to the phenol's light absorbance performance in the visible light region [42].

It can also be observed that for all the catalysts the phenol degradation was maximum till certain catalyst dosages and beyond this amount no significant degradation was achieved. The main reason could be due to the difficulty of light penetration through the reaction mixture when the catalyst amount increases and also the higher probability of the  $e^-h^+$  pair of the catalyst to



recombine [43]. From the figure, it can be observed that the maximum dose was 0.35 g which was taken as the optimum amount in further studies on phenol degradation.

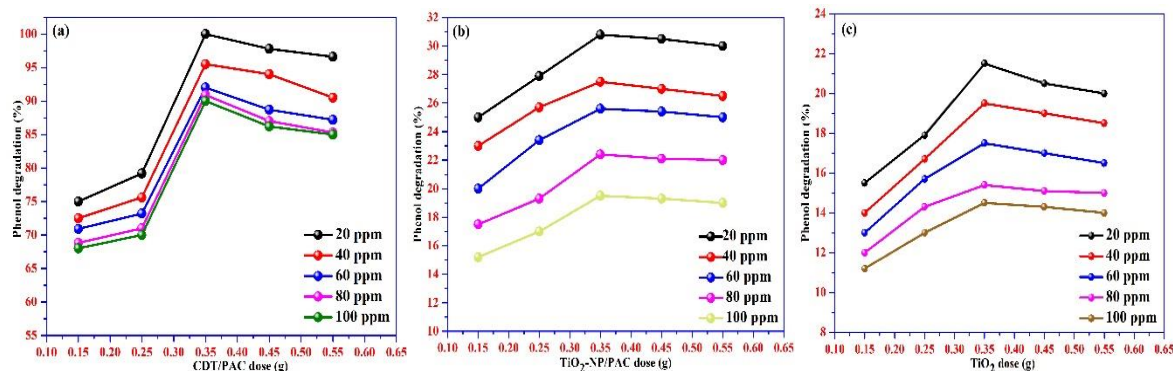


**Figure 6.9** Effect of nanocomposite (a) CDT/PAC, (b) TiO<sub>2</sub>-NP/PAC, and (c) TiO<sub>2</sub> amount in the degradation of phenol solution under visible light

### (b) Effect of pH

Several experiments were run to observe the effect of pH on the degradation of phenol. The pH of 20 ppm phenol solution was varied between 2-10 by adding HCl and NaOH solution and the solution was stirred with 0.35 g of catalysts (CDT/PAC, TiO<sub>2</sub>-NP/PAC, and TiO<sub>2</sub>). It can be observed that phenol degradation increased at the acidic pH (=2) region (Figure 6.10) and gradually decreased at the alkaline pH region for all three catalysts. This is because of the ionization state of phenol molecules and the surface chemical state of TiO<sub>2</sub> at this pH. Furthermore, the pH<sub>zpc</sub> of the CDT/PAC, TiO<sub>2</sub>-NP/PAC, and TiO<sub>2</sub> catalysts were 6.65, 6.45, and 6.25 respectively; at pH values lower than the pH<sub>zpc</sub>, the catalyst's surface becomes positively charged. Phenol with one hydroxyl group ionizes easily into anionic phenol in a strongly acidic solution which leads to electrostatic interaction between the positive surface of the nanocomposite and the negatively charged  $\pi$ -electron cloud of the phenol molecule [44]. However, at higher pH, the positive charge on the nanocomposite surface gradually diminishes, as a result, the intake of phenol ions decreases.

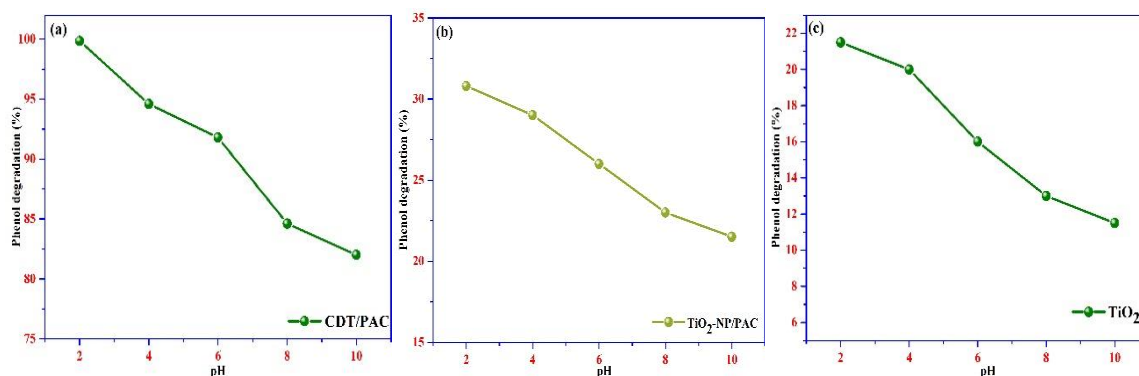


**Figure 6.10** Effect of (a) CDT/PAC, (b) TiO<sub>2</sub>-NP/PAC, and (c) TiO<sub>2</sub> (0.35 g) with pH in the degradation of phenol solution under visible light



### (c) Effect of initial phenol concentration and light irradiation time

The effect of initial phenol concentration and light irradiation time was studied using 0.35 g of nanocomposite at optimum pH 2 for phenol concentrations of 20, 40, 60, 80, and 100 ppm and varying visible light irradiation time (Figure 6.11). It can be seen from the figure that the degradation of phenol was initially increased with visible light irradiation time till 60 minutes for all the concentrations. The maximum degradation of 100% at 60 minutes was found for 20 ppm phenol solution, and for 40, 60, 80, and 100 ppm solution degradation percentage reduced to 82%, 75.5%, 63.9%, and 53% at 60 minutes irradiation time. This lesser degradation of phenol with the increase of initial concentration could be due to the lower availability of hydroxyl groups for photoreaction as the negatively charged phenol ions concentration increases it deactivate the positive surface active sites of catalysts. At higher phenol concentration, more phenol molecules are available for adsorption on the surface of the nanocomposite. Thus, photons get trapped between the phenolic particles, which prevent light particles from reaching the surface of the nanocomposite [45]. As a result, the production of reactive hydroxyl radical reduces, and consequently, the degradation of phenol is decreased. However, when the light exposure time reached beyond 60 minutes, the degradation became saturated and no further degradation occurred upon further increase in exposure time. This may be because the degradation resulted in the generation of a large amount of low molecular weight organic molecules, which hindered the formation of hydroxyl radicals and prevented further photodegradation [46].

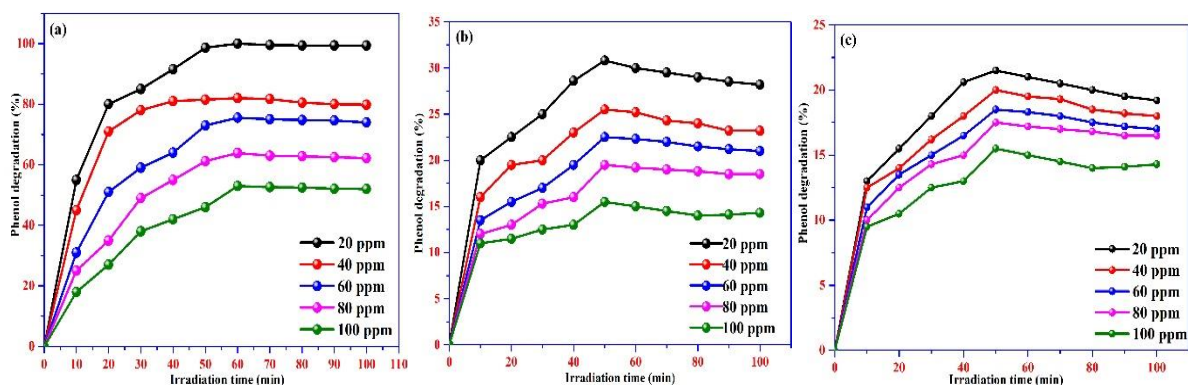


**Figure 6.11** Effect of (a) CDT/PAC, (b)  $\text{TiO}_2\text{-NP/PAC}$ , and (c)  $\text{TiO}_2$  (0.35 g) with contact time in the degradation of phenol solution under visible light

### 6.3.3 Kinetic studies

The reaction kinetics of the photocatalytic degradation of phenol (20 ppm) was studied under optimum operating conditions. The rate of the reaction ( $K_{\text{app}}$ ), and the half-life time ( $t_{1/2}$ ) were determined using equations 6.3 and 6.4.

$$\ln \frac{C_i}{C_t} = k_{app} t \quad (6.3)$$

$$t_{1/2} = \frac{\ln 2}{K_{app}} \quad (6.4)$$

where  $C_i$  is the initial phenol concentration (20 ppm);  $C_e$  is the equilibrium phenol concentration;  $K_{app}$  is the apparent reaction rate, and  $t_{1/2}$  is the half-life time [36].

The graph was plotted between  $\ln (C_i/C_e)$  against irradiation time ( $t$ ) as shown in Figure 6.12. The fitted curve gives a high correlation coefficient of  $R^2 = 0.999$ , and the reaction rate constant  $K_{app}$  and the half-life period  $t_{1/2}$  were found to be  $0.086 \text{ min}^{-1}$  and 7.981 minutes. This signifies that the phenol photodegradation follows the Langmuir-Hinshelwood pseudo-first-order rate kinetics.

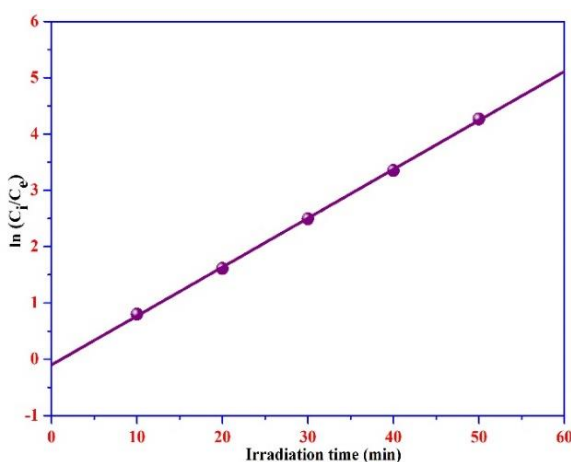


**Figure 6.12** Pseudo-first-order rate kinetics of phenol degradation loaded on CDT/PAC nanocomposite

### 6.3.4 Thermodynamics studies

In order to further understand the effect of temperature on the degradation process, degradation at four temperatures 298 K, 308 K, 318 K, and 328 K were analyzed. The different thermodynamics parameters including enthalpy change ( $\Delta H^\circ$ ), entropy change ( $\Delta S^\circ$ ), and Gibbs free energy ( $\Delta G^\circ$ ) were calculated using the equations:

$$\ln K_d = \frac{\Delta S^\circ}{R} - \frac{\Delta H^\circ}{RT} \quad (6.5)$$

$$\Delta G^\circ = -RT \ln K_d \quad (6.6)$$

where  $T$  is the absolute temperature,  $K_d$  is the distribution coefficient,  $R$  ( $8.314 \text{ J mol}^{-1} \text{ K}^{-1}$ ).

The values of  $\Delta H^\circ$  and  $\Delta S^\circ$  were calculated by slope and intercept of linear fitting from  $\ln K_d$  vs  $1/T$  (Figure 6.13).

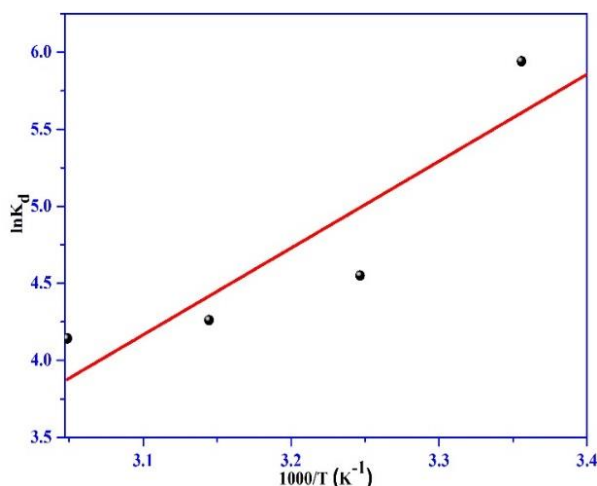


**Figure 6.13**  $\ln K_d$  vs  $1/T$  plot (phenol concentration = 20 ppm, pH = 2, Nanocomposite dose = 0.35 g and Contact time = 60 minutes)

The calculated thermodynamics parameters are shown in Table 6.2. From the table, it can be seen that the  $\Delta H^\circ$  and  $\Delta S^\circ$  values are  $-46.856$  and  $-0.1106$   $\text{kJ mol}^{-1}$ , respectively. The negative value of  $\Delta H^\circ$  indicates that the process of degrading phenol is exothermic, and the negative value of  $\Delta S^\circ$  indicates a slight reduction of randomness at the nanocomposite/phenol solution interface during the degradation of phenol on CDT/PAC. The negative  $\Delta G^\circ$  values indicate that the reaction involved in photocatalytic degradation of ANT using NDT/PAC is spontaneous [44]. Moreover, the decrease of  $\Delta G^\circ$  with the increase in temperature indicates that raising the temperature is unfavorable for phenol degradation.

<b>Table 6.2</b> Thermodynamic parameters calculated for the degradation of phenol using CDT/PAC nanocomposite			
<b>T (K)</b>	<b>Thermodynamic parameters</b>		
	<b><math>\Delta G^\circ</math> (kJ mol<sup>-1</sup>)</b>	<b><math>\Delta H^\circ</math> (kJ mol<sup>-1</sup>)</b>	<b><math>\Delta S^\circ</math> (kJ mol<sup>-1</sup>K)</b>
298	-13.891	-46.856	-0.1106
308	-12.785		
318	-11.678		
328	-10.572		

### 6.3.5 Effect of interfering ions on photocatalytic degradation of phenol

The effect of different interfering ions such as NaCl,  $\text{ZnCl}_2$ ,  $\text{CuSO}_4$ , glycine, oxalic acid,  $\text{NaNO}_3$ ,  $\text{Cd}(\text{NO}_3)_2$ , and EDTA were analyzed as their presence hinders the generation of hydroxyl radical ( $\cdot\text{OH}$ ), superoxide radical ( $\text{O}_2^{\cdot-}$ ), electron ( $\text{e}^-$ ), and holes ( $\text{h}^+$ ) [47]. In this regard, 20 ppm of these interfering ions were prepared and added to the phenol solution at optimum operating conditions. A graph showing the rate of phenol degradation for various interfering ions is shown in Figure 6.14. The figure shows that the degradation percent decreases from 99.9% to 91.2% (oxalic acid), 87.0% ( $\text{NaNO}_3$ ), 75.5% (NaCl), 72.0% ( $\text{ZnCl}_2$ ),

68.5% (EDTA), 65.8% ( $\text{Cd}(\text{NO}_3)_2$ ), 64.0% ( $\text{CuSO}_4$ ), 58.0% (Glycine), respectively. The addition of glycine,  $\text{CuSO}_4$ ,  $\text{Cd}(\text{NO}_3)_2$ , and EDTA significantly reduced the rate of phenol degradation. The reason for the decrease in the degradation rate is that Glycine acts as a  $\cdot\text{OH}$  absorber, the  $\text{SO}_4^{2-}$  ion of  $\text{CuSO}_4$  as electron absorber, the ion of nitrate  $\text{Cd}(\text{NO}_3)_2$  as photons absorber, and EDTA as a holes scavenger [48,49]. Likewise, the chloride ions of  $\text{ZnCl}_2$  and  $\text{NaCl}$  absorb holes and hydroxyl radicals [50]. [48]. However, the presence of other interfering ions (oxalic acid,  $\text{NaNO}_3$ ) had reduced the effects of the photocatalytic degradation process. From this result, it can be inferred that the photocatalytic degradation of phenol in the presence of interfering ions follows the order:

Oxalic acid <  $\text{NaNO}_3$  <  $\text{NaCl}$  <  $\text{ZnCl}_2$  < EDTA <  $\text{Cd}(\text{NO}_3)_2$  <  $\text{CuSO}_4$  < Glycine.

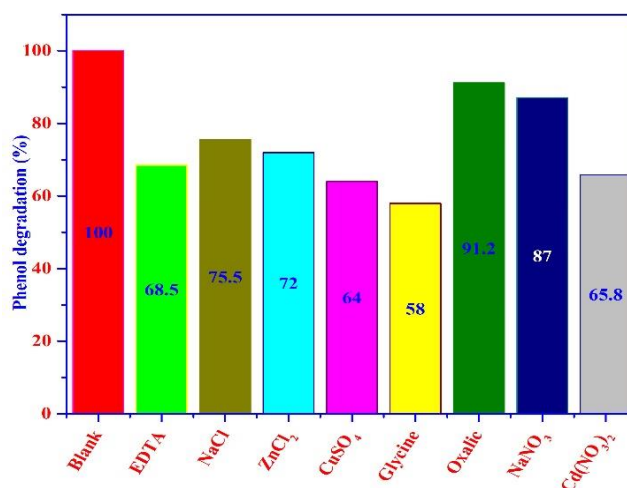


**Figure 6.14** Photocatalytic degradation of phenol in the presence of interfering ions using CDT/PAC nanocomposite

### 6.3.6 Nanocomposite reusability and photostability

The reusability and photostability of nanocomposite material were analyzed to visualize the effectiveness, sustainability, and economic benefits of the material. Hence, the photocatalytic degradation of phenol was carried out for five cycles of usages using the CDT/PAC nanocomposite as shown in Figure 6.15. For this, the nanocomposite which remained after the photocatalytic reactions were collected, washed with distilled water, and then dried in an oven [49]. The dried nanocomposite was then recycled for degradation of phenol and in the first cycle, the phenol degradation was 98.5%. Although, the degradation efficiency of the composite decreased for the phenol in the second (90.6%), third (85%), and fourth (79%) cycles by recycling the nanocomposite again. This decrease in degradation efficiency was due to the constant decrease of vacant adsorption sites within the CDT/PAC composite surface [50]. In the fifth cycle, the degradation efficiency of the nanocomposite was around 73%, signifying

that CDT/PAC nanocomposite still shows better reusability after running it through several times.

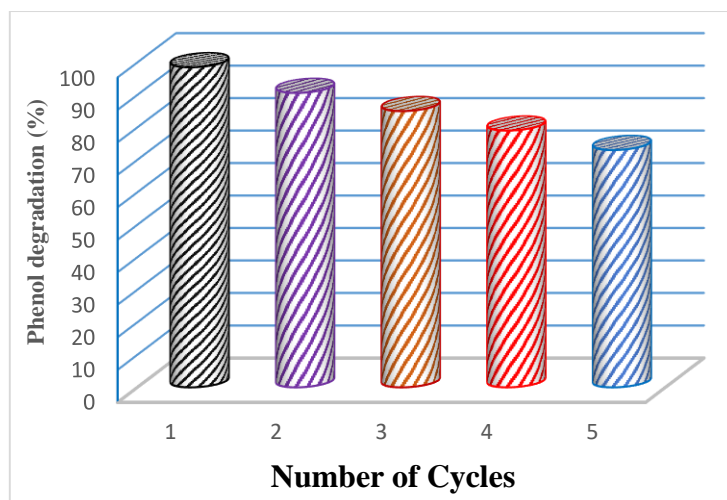


**Figure 6.15** Phenol degradation efficiency of CDT/PAC nanocomposite upto five cycles

In order to understand the photostability of the CDT/PAC nanocomposite, the nanocomposite retrieved after five-time reuse was characterized by FT-IR analysis, and the result was compared with that of the pristine CDT/PAC nanocomposite (Figure 6.16). Comparing the FT-IR peaks of CDT/PAC before and after phenol degradation, no significant change in the functional groups could be observed which indicates that the nanocomposite maintains the original structure during reuse.

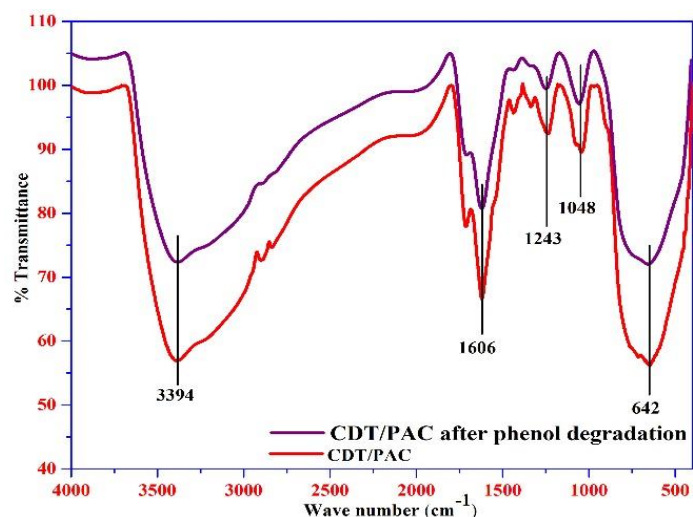


**Figure 6.16** FT-IR spectra of CDT/PAC before and after ANT degradation

### 6.3.7 GC-Mass analysis

Identification of the end phenol degradation products is confirmed through GC-Mass spectroscopic analysis as shown in Figure 6.17.

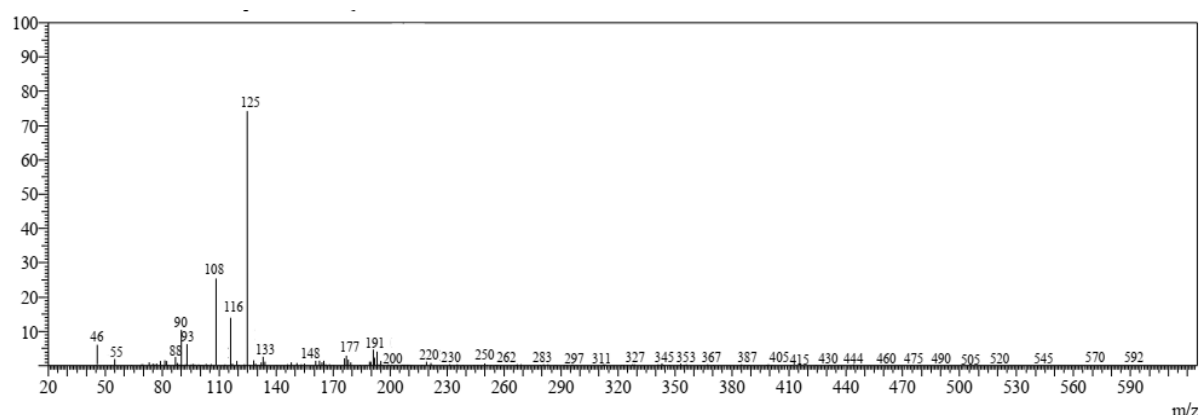


**Figure 6.17** Mass spectra of degradation products of phenol aqueous solution

The major intermediate products obtained were phenoxy radicals at  $m/z = 125$ , hydroquinone at  $m/z = 108$ , maleic acid at  $m/z = 116$ , phenoxide ion at  $m/z = 93$ , oxalic acid at  $m/z = 90$ , and formic acid at  $m/z = 46$ . The probable mechanism for degradation is reflected in Figure 6.18 [51]. Phenol is initially degraded by an attack of hydroxyl radicals produced in the reaction medium generating resonating phenoxy radicals. The phenoxy radicals oxidized to give intermediate benzoquinone and hydroquinone which further degraded and opened the rings to form maleic acid and phenoxide ion [52]. The generated phenoxide ion degraded to form oxalic acid and formic acid, which finally yielded harmless  $\text{CO}_2$  and water.

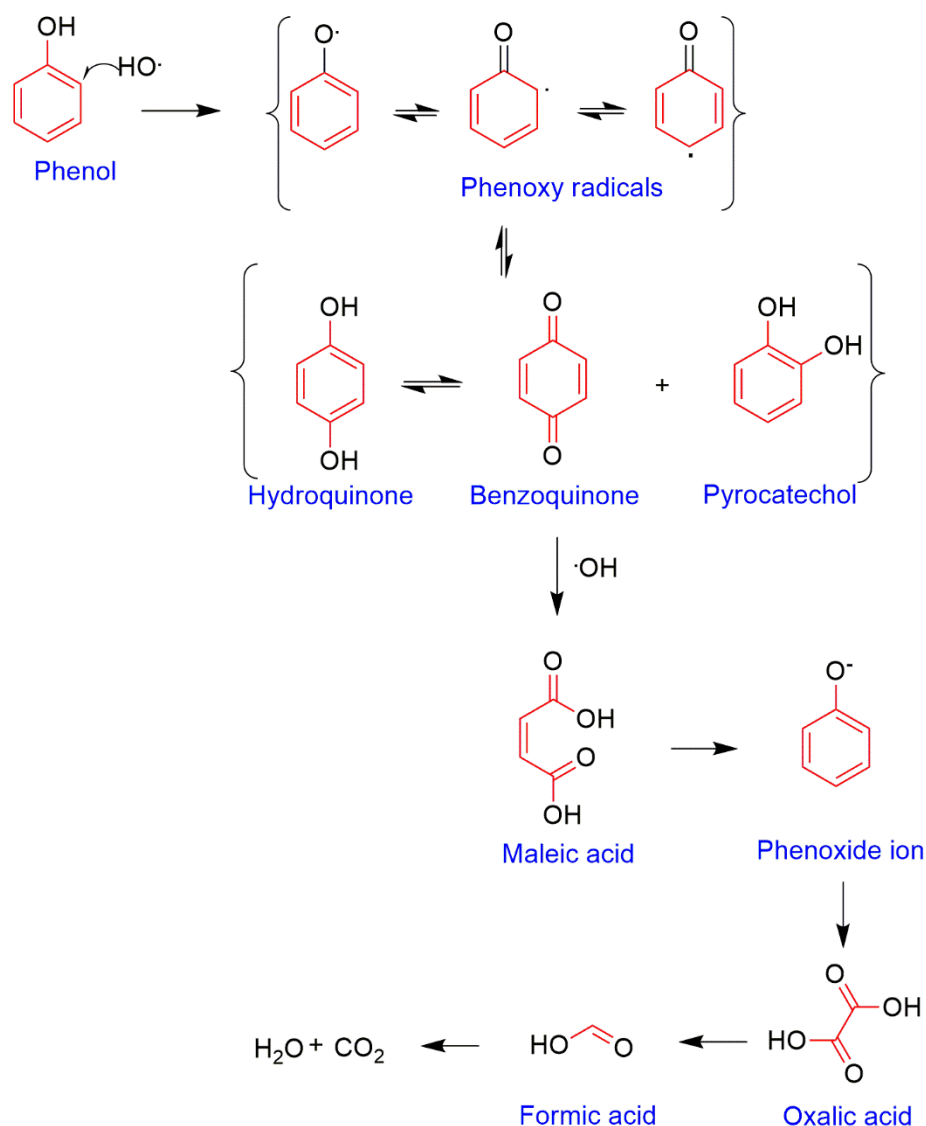


**Figure 6.18** Proposed degradation pathway for the degradation of phenol over CDT/PAC nanocomposite [51]

### 6.3.8 Energy consumption and cost analysis

#### (a) Electrical energy determination

In visible-light-driven photocatalytic degradation of phenol using the CDT/PAC nanocomposite process, electric energy consumption is one of the major contributors to the total operating costs [53]. Therefore figure-of-merit-based electric energy per order ( $E_{EO}$ ) calculation was used for a Langmuir-Hinshelwood pseudo-first-order kinetic model of advanced oxidation processes.

The  $E_{EO}$  ( $\text{kWhm}^{-3}\text{order}^{-1}$ ) can be calculated as [54]:

$$E_{EO} = \frac{P \times t \times 1000}{V \times 60 \times \log\left(\frac{C_i}{C_e}\right)} \quad (6.7)$$

where  $P$  represents total input power (kW),  $V$  represents the volume of phenol (L),  $C_i$



represents the initial concentration of phenol,  $C_e$  represents the final concentration of phenol, and  $t$  represents the light irradiation time (minute).

Combining the Langmuir-Hinshelwood pseudo-first-order rate equation 6.3 with equation 6.7, the model electric energy per order,  $E_{EO}$  (model) can be obtained, and can be written as [55]:

$$E_{EO} = \frac{38.4 \times P}{V \times K_{app}} \quad (6.8)$$

where  $K_{app}$  represents pseudo-first-order rate constant ( $\text{min}^{-1}$ ).

Table 6.3 shows the calculated experimental and model  $E_{EO}$  values for the degradation of phenol. According to this table, less electrical energy was consumed during the degradation of 20 ppm phenol solution as compared to higher concentrated phenol solution. This increase of electrical energy consumption value when the phenol concentration is high is attributed to the fact that higher concentrated phenol solution has a lower degradation rate. In addition, the experimental  $E_{EO}$  value exactly coincides with the model  $E_{EO}$  value which confirms that the photocatalytic degradation of phenol follows Langmuir-Hinshelwood pseudo-first-order rate kinetics [56].

<b>Table 6.3</b> Effect of phenol concentration on electrical energy consumption						
<b>Experimental conditions</b>			<b>Apparent rate constant (<math>K_{app}</math>) (<math>\text{min}^{-1}</math>)</b>	<b><math>R^2</math></b>	<b><math>E_{EO}</math> experimental (<math>\text{kWh m}^{-3}\text{order}^{-1}</math>)</b>	<b><math>E_{EO}</math> model (<math>\text{kWh m}^{-3}\text{order}^{-1}</math>)</b>
<b>Initial Conc. (ppm)</b>	<b>CDT/PAC Conc. (<math>\text{g L}^{-1}</math>)</b>	<b>pH</b>				
20	0.35	2	0.08683	0.99	1065.28	1105.60
40	0.35	2	0.05132	0.70	1856.26	1870.61
60	0.35	2	0.03956	0.96	2279.12	2426.69
80	0.35	2	0.03569	0.97	2401.63	2689.82
100	0.35	2	0.03326	0.97	2500.00	2886.34

### (b) Total operating cost

The total operating cost involved in a reaction is a very important feature to understand the efficiency of that method. The overall cost of a reaction is equal to the sum of the principal cost, maintenance cost, and operating cost. These costs depend on the reactor configuration, concentration of the pollutant, light irradiation time, and nanocomposite amount [57].

In this study, calculations for the total operating cost and energy consumed in the photocatalytic degradation of phenol was considered at optimum operating conditions, i.e., CDT/PAC nanocomposite dose of 0.35 g, light irradiation time of 60 minutes, pH 2, and phenol concentration (20, 40, 60, 80, and 100 ppm) using the equations 6.9 and 6.10.

$$\text{Total operating cost} = \frac{\text{Energy consumed per mg of phenol degradation (kWh)} \times \text{unit cost (INR/kWh)} \times 10^6}{\text{phenol degradation (mg)}} \quad (6.9)$$

$$\text{Energy consumed per mg of phenol degradation (kWh)} = \frac{\text{Power input (kW)} \times \text{Reaction time (min)}}{1000 \times 60} \quad (6.10)$$

The results obtained are represented in Table 6.4 and it can be noticed that a total of 312.50, 190.54, 137.96, 122.26, and 117.92 INR (Indian rupee) were utilized for 20 ppm, 40 ppm, 60 ppm, 80 ppm, and 100 ppm phenol degradation using 0.35 g of CDT/PAC nanocomposite. Furthermore, the value of operating costs was decreased with an increase in the initial phenol concentration i.e., from 312.50 to 117.92 INR [54].

**Table 6.4** Cost analysis of phenol degradation in the photocatalytic reactor under different operating conditions

Phenol Conc. (ppm) $C_1$	CDT/PAC Conc. (g L <sup>-1</sup> ) $C_2$	Phenol Degradation Efficiency (%) $C_4$	Phenol degradation (mg) $C_5 = [(C_1 \times C_4/100) \times \text{working volume}]$	Reaction time (minute) $C_6$	Energy consumed per mg of phenol degradation (kWh) $C_7 = [(P \times C_6)/(1000 \times 60)]$	Total operating cost (INR/kg of phenol degradation) $C_8 = [(C_7 \times \text{unit cost} \times 10^6)/C_5]$
20	0.35	100.0	4.00	60	0.0005	312.50
40	0.35	82.0	6.56	60	0.0005	190.54
60	0.35	75.5	9.06	60	0.0005	137.96
80	0.35	63.9	10.22	60	0.0005	122.26
100	0.35	53	10.60	60	0.0005	117.92

(a) Total energy consumed (P) 0.5 kW [includes energy for electronic magnetic stirrer (50W), water pump (50W), exhaust fan (50W), and Visible lamp (350 W)] (b) Working volume of reactor 0.2 L and (d) Unit cost of power 2.5 INR (kWh)<sup>-1</sup>.

### 6.3.9 Comparison studies

The efficiency of the CDT/PAC nanocomposite obtained in the present work for the degradation of phenol was compared with other nanocomposites which have been reported in the literature (Table 6.5). The amount of composite taken, contact time, and the degradation capacity of the nanocomposite were the parameters considered for comparison. The CDT/PAC nanocomposite shows very effective degradation efficiency of phenol in contrast with other reported literature and hence could be used as a better candidate for the nanocomposite preparation.

<b>Table 6.5</b> Comparison of catalytic activity of other work in the literature with CDT/PAC nanocomposite							
<b>Nanocomposite</b>	<b>Pollutant</b>	<b>Mass</b>	<b>Volume (ml)</b>	<b>C<sub>i</sub></b>	<b>Contact time (minute)</b>	<b>% degradation</b>	<b>Source</b>
GdVO <sub>4</sub> /FG	Phenol	50 mg	100	1 x 10 <sup>-4</sup> mol dm <sup>-3</sup>	180	98	[58]
EV/FG24	Phenol	50 mg	100	1 x 10 <sup>-4</sup> mol dm <sup>-3</sup>	180	96	[59]
RGO-TiO <sub>2</sub>	Phenol	1.5 g	1000	1.06 mM	20	94.70	[60]
ZnO@FeHCF	Phenol	20 mg	15	1x 10 <sup>-4</sup> M	1440	95	[61]
BiOBr/PSCN/Ag/AgCl BioBr/PSCN PSCN/Ag/AgCl BiOBr/Ag/AgCl Ag/AgCl BiOBr PSCN GCN	Phenol	50 mg	100	1 x10 <sup>-4</sup> mol dm <sup>-3</sup>	60	98 90 81 72 46 48 50 43	[47]
TiO <sub>2</sub> /AC	Phenol	2.5 mg	1000	10 ppm	90	80.60	[62]
TiO <sub>2</sub>	Phenol	1 g	1000	0.4 mmol	900	36.90	[63]
TiO <sub>2</sub> /SWP700	Phenol	1 g	150	50 ppm	720	69.30	[64]
<b>CDT/PAC</b>	<b>Phenol</b>	<b>0.35 g</b>	<b>200</b>	<b>20 ppm</b>	<b>60</b>	<b>99.90</b>	<b>Present study</b>

## 6.4 Conclusion

In this study, cobalt-doped TiO<sub>2</sub> supported on activated carbon was prepared successfully using the hydrothermal synthesis method. Characterization of the prepared nanocomposite confirmed the contribution of Co ions in reducing the bandgap of TiO<sub>2</sub>-PAC nanocomposite and transforming optical responses to the visible light region. The supporting material PAC has deducted the electron-hole recombination and agglomeration of TiO<sub>2</sub> nanoparticles thus increasing the photocatalytic activity. The CDT/PAC nanocomposite could be used effectively for the degradation of phenol from an aqueous solution with a maximum degradation percentage of 99.90% within 60 minutes for 20 ppm phenol solutions. The degradation of phenol using CDT/PAC nanocomposite followed the pseudo-first-order kinetic model according to the Langmuir-Hinshelwood model. The thermodynamic study has shown that the degradation process is exothermic and spontaneous. The presence of interfering ions glycine,

CuSO<sub>4</sub>, Cd(NO<sub>3</sub>)<sub>2</sub>, EDTA mostly affects the degradation of phenol solution. The nanocomposite is highly stable and can be used several times without any significant loss of inactivity. GC-MS analysis confirmed the generation of end products phenoxy radicals, hydroquinone, maleic acid, phenoxide ion, oxalic acid, and formic acid. The electrical energy consumed and total operating cost involved in the photocatalytic degradation of phenol using CDT/PAC nanocomposite were analyzed and very low amount of 312.50, 190.54, 137.96, 122.26, and 117.92 INR (Indian rupee) operating costs was found to have been incurred for 20 ppm, 40 ppm, 60 ppm, 80 ppm, and 100 ppm phenol solution. Thus the visible light active Co-doped TiO<sub>2</sub> supported on activated carbon nanocomposite can be a favorable photocatalyst for future environmental applications.

**References**

- [1] A. Boretti, L. Rosa, Reassessing the projections of the World Water Development Report, *Npj Clean Water*. 15 (2019) 1–6. doi:10.1038/s41545-019-0039-9.
- [2] H. I. Abdel-Shafy, M. S.M. Mansour, A review on polycyclic aromatic hydrocarbons: Source, environmental impact, effect on human health and remediation, *Egypt. J. Pet.* 25 (2016) 107–123. doi:10.1016/j.ejpe.2015.03.011.
- [3] R. M. Bruce, J. Santodonato, M. W. Neal, Summary review of the health effects associated with phenol, *Toxicol. Ind. Health*. 3 (1987) 535–568. doi:10.1177/074823378700300407.
- [4] WHO (World Health Organization), *Guidelines for Drinking-water Quality*, 3rd ed., 2008.
- [5] H. Koseoglu, B. Ilker Harman, N. O. Yigit, N. Kabay, M. Kitis, The impacts of operational conditions on phenol removal by nanofiltration membranes, *Desalin. Water Treat.* 26 (2011) 118–123. doi:10.5004/dwt.2011.2120.
- [6] L. Yu, D. P. Gamliel, B. Markunas, J. A. Valla, A Promising Solution for Food Waste: Preparing Activated Carbons for Phenol Removal from Water Streams, *ACS Omega*. 6 (2021) 8870–8883. doi:10.1021/acsomega.0c06029.
- [7] Z. M. Ahmed, S. Lyne, R. Shahrabani, Removal and recovery of phenol from phenolic wastewater via ion exchange and polymeric resins, *Environ. Eng. Sci.* 17 (2000) 245–255. doi:10.1089/ees.2000.17.245.
- [8] A. Mnif, D. Tabassi, M. Ben Sik Ali, B. Hamrouni, Phenol Removal from Water by AG Reverse Osmosis Membrane Amine, *Environ. Prog. Sustain. Energy*. 34 (2015) 982–989. doi:10.1002/ep.12078.
- [9] H. Luo, C. Li, C. Wu, W. Zheng, X. Dong, Electrochemical degradation of phenol by in situ electro generated and electro-activated hydrogen peroxide using an improved gas diffusion cathode, *Electrochim. Acta*. 186 (2015) 486–493. doi:10.1016/j.electacta.2015.10.194.
- [10] D. P. Zagklis, A. I. Vavouraki, M. E. Kornaros, C. A. Paraskeva, Purification of olive mill wastewater phenols through membrane filtration and resin adsorption/desorption, *J. Hazard. Mater.* 285 (2015) 69–76. doi:10.1016/j.jhazmat.2014.11.038.
- [11] D. Wu, G. Q. Chen, B. Hu, H. Deng, Feasibility and energy consumption analysis of phenol removal from salty wastewater by electro-electrodialysis, *Sep. Purif. Technol.* 215 (2019) 44–50. doi:10.1016/j.seppur.2019.01.001.
- [12] M. Uğurlu, A. Gürses, Ç. Doğar, M. Yalçın, The removal of lignin and phenol from paper mill effluents by electrocoagulation, *J. Environ. Manage.* 87 (2008) 420–428. doi:10.1016/j.jenvman.2007.01.007.
- [13] M. N. Timofeeva, S. Ts. Khankhasaeva, S. V. Badmaeva, A. L. Chuvilin, E. B. Burgina, A. B. Ayupov, V. N. Panchenko, A. V. Kulikova, Synthesis, characterization and

- catalytic application for wet oxidation of phenol of iron-containing clays, *Appl. Catal. B Environ.* 59 (2005) 243–248. doi:10.1016/j.apcatb.2005.01.013.
- [14] M. Luo, D. Bowden, P. Brimblecombe, Catalytic property of Fe-Al pillared clay for Fenton oxidation of phenol by H<sub>2</sub>O<sub>2</sub>, *Appl. Catal. B Environ.* 85 (2009) 201–206. doi:10.1016/j.apcatb.2008.07.013.
- [15] P. Rajasulochana, V. Preethy, Comparison on efficiency of various techniques in treatment of waste and sewage water-A comprehensive review, *Resour. Technol.* 2 (2016) 175–184. doi:10.1016/j.reffit.2016.09.004.
- [16] G. Crini, E. Lichtfouse, Advantages and disadvantages of techniques used for wastewater treatment, *Environ. Chem. Lett.* 17 (2019) 145–155. doi:10.1007/s10311-018-0785-9.
- [17] R.K. Gautam, M.C. Chattopadhyaya, Advanced Oxidation Process-Based Nanomaterials for the Remediation of Recalcitrant Pollutants, in: *Nanomater. Wastewater Remediat.*, 2016: pp. 33–48. doi:10.1016/B978-0-12-804609-8/00003-0.
- [18] N.N. Bahrudin, M.A. Nawi, W.I. Nawawi, Photocatalytic enhancement of immobilized TiO<sub>2</sub>-polyaniline bilayer (TiO<sub>2</sub>- PBL) system for decolorization of methyl orange dye, *Mater. Res. Bull.* 106 (2018) 388–395. doi:10.1016/j.materresbull.2018.06.023.
- [19] M.S.S. Danish, L.L. Estrella, I.M.A. Alemaida, A. Lisin, N. Moiseev, M. Ahmadi, M. Nazari, M. Wali, H. Zaheb, T. Senjyu, Photocatalytic Applications of Metal Oxides for Sustainable Environmental Remediation, *Metals (Basel)*. 11 (2021) 1–25. doi:10.3390/met11010080.
- [20] M. Pawar, S.T. Sando, P. Gouma, A Brief Overview of TiO<sub>2</sub> Photocatalyst for Organic Dye Remediation: Case Study of Reaction Mechanisms Involved in Ce-TiO<sub>2</sub> Photocatalysts System, *J. Nanomater.* 2018 (2018) 1–13. doi:10.1155/2018/5953609.
- [21] Z. Noorimotlagh, I. Kazeminezhad, N. Jaafarzadeh, M. Ahmadi, Z. Ramezani, S.S. Martinez, The visible-light photodegradation of Nonylphenol in the presence of carbon-doped TiO<sub>2</sub> with Rutile/Anatase ratio coated on GAC: Effect of parameters and degradation mechanism, *J. Hazard. Mater.* 350 (2018) 108–120. doi:10.1016/j.jhazmat.2018.02.022.
- [22] V. Kumaravel, S. Mathew, J. Bartlett, S.C. Pillai, Photocatalytic hydrogen production using metal doped TiO<sub>2</sub>: A review of recent advances, *Appl. Catal. B Environ.* 244 (2019) 1021–1064. doi:10.1016/j.apcatb.2018.11.080.
- [23] R. Marschall, L. Wang, Non-metal doping of transition metal oxides for visible-light photocatalysis, *Catal. Today*. 225 (2014) 111–135. doi:10.1016/j.cattod.2013.10.088.
- [24] M. Baruah, S.L. Ezung, A. Supong, P.C. Bhomick, S. Kumar, D. Sinha, Synthesis, characterization of novel Fe-doped TiO<sub>2</sub> activated carbon nanocomposite towards photocatalytic degradation of Congo red, *E. coli*, and *S. aureus*, *Korean J. Chem. Eng.* 38 (2021) 1277–1290. doi:10.1007/s11814-021-0830-4.
- [25] J. Huang, Y. Lei, T. Luo, Photocatalytic H<sub>2</sub> production from water by metal-free dye-sensitized TiO<sub>2</sub> semiconductors: The role and development process of organic

- sensitizers, *Chemistry-Sustainability-Energy-Materials*. 13 (2020) 5863–5895. doi:10.1002/cssc.202001646.
- [26] O. Ola, M.M. Maroto-valer, Review of material design and reactor engineering on TiO<sub>2</sub> photocatalysis for CO<sub>2</sub> reduction, *J. Photochem. Photobiol. C Photochem. Rev.* 24 (2015) 16–42. doi:10.1016/j.jphotochemrev.2015.06.001.
- [27] B. Choudhury, A. Choudhury, Luminescence characteristics of cobalt doped TiO<sub>2</sub> nanoparticles, *J. Lumin.* 132 (2012) 178–184. doi:10.1016/j.jlumin.2011.08.020.
- [28] Y.Y. Gurkan, E. Kasapbasi, N. Turkten, Z. Cinar, Influence of Se/N Codoping on the Structural, Optical, Electronic and Photocatalytic Properties of TiO<sub>2</sub>, *Molecules*. 2 (2017) 1–17. doi:10.3390/molecules22030414.
- [29] M. Iwanow, T. Gärtner, V. Sieber, B. König, Activated carbon as catalyst support: precursors, preparation, modification and characterization, *Beilstein J. Org. Chem.* 16 (2020) 1188–1202. doi:10.3762/bjoc.16.104.
- [30] H. Atout, A. Bouguettoucha, D. Chebli, J.M. Gatica, H. Vidal, M.P. Yeste, A. Amrane, Integration of Adsorption and Photocatalytic Degradation of Methylene Blue Using TiO<sub>2</sub> Supported on Granular Activated Carbon, *Arab. J. Sci. Eng.* 42 (2017) 1475–1486. doi:10.1007/s13369-016-2369-y.
- [31] H. Teng, S. Xu, D. Sun, Y. Zhang, Preparation of Fe-doped TiO<sub>2</sub> nanotubes and their photocatalytic activities under visible light, *Int. J. Photoenergy*. 2013 (2013) 1–7. doi:10.1155/2013/981753.
- [32] G. Sadanandam, K. Lalitha, V. Durga Kumari, M. V. Shankar, M. Subrahmanyam, Cobalt doped TiO<sub>2</sub>: A stable and efficient photocatalyst for continuous hydrogen production from glycerol: Water mixtures under solar light irradiation, *Int. J. Hydrogen Energy*. 38 (2013) 9655–9664. doi:10.1016/j.ijhydene.2013.05.116.
- [33] G.G. Nakhate, V.S. Nikam, K.G. Kanade, S. Arbuj, B.B. Kale, J.O. Baeg, Hydrothermally derived nanosized Ni-doped TiO<sub>2</sub>: A visible light driven photocatalyst for methylene blue degradation, *Mater. Chem. Phys.* 124 (2010) 976–981. doi:10.1016/j.matchemphys.2010.08.007.
- [34] M. Humayun, F. Raziq, A. Khan, W. Luo, Modification strategies of TiO<sub>2</sub> for potential applications in photocatalysis: a critical review, *Green Chem. Lett. Rev.* 11 (2018) 86–102. doi:10.1080/17518253.2018.1440324.
- [35] A. Mittal, B. Mari, S. Sharma, V. Kumari, S. Maken, K. Kumari, N. Kumar, Non-metal modified TiO<sub>2</sub>: a step towards visible light photocatalysis, *J. Mater. Sci. Mater. Electron.* 30 (2019) 3186–3207. doi:10.1007/s10854-018-00651-9.
- [36] M. Baruah, A. Supong, P. Chandra, B. Rituparna, K. Chubaakum, Batch sorption-photodegradation of Alizarin Red S using synthesized TiO<sub>2</sub>/activated carbon nanocomposite: an experimental study and computer modelling, *Nanotechnol. Environ. Eng.* 3 (2020) 1–13. doi:10.1007/s41204-020-00071-3.
- [37] S. Gu, X. Zhao, X. Zhou, F. Xie, X. Wang, Z. Tang, Nickel-Doped Porous ZnO



- Nanosheets Functionalized with CuInS<sub>2</sub> Nanoparticles: An Efficient Photocatalyst for Chromium (VI) Reduction, *Chempluschem*. 85 (2019) 1–31. doi:10.1002/cplu.201900664.
- [38] L. Shi, F. Wang, Y. Wang, D. Wang, B. Zhao, L. Zhang, D. Zhao, D. Shen, Photoluminescence and photocatalytic properties of rhombohedral CuGaO<sub>2</sub> nanoplates, *Sci. Rep.* 6 (2016) 1–10. doi:10.1038/srep21135.
- [39] M. H. Mangrola, V. G. Joshi, B. H. Parmar, A. S. Pillai, Optical and dielectric properties of the Cobalt doped TiO<sub>2</sub> nanoparticles, *Int. J. Mod. Phys. Conf. Ser.* 22 (2013) 332–335. doi:10.1142/S2010194513010313.
- [40] X. Li, R. Shen, S. Ma, X. Chen, J. Xie, Graphene-based heterojunction photocatalysts, *Appl. Surf. Sci.* 430 (2018) 53–107. doi:10.1016/j.apsusc.2017.08.194.
- [41] A.A. Isari, A. Payan, M. Fattahi, S. Jorfi, B. Kakavandi, Photocatalytic degradation of rhodamine B and real textile wastewater using Fe-doped TiO<sub>2</sub> anchored on reduced graphene oxide (Fe-TiO<sub>2</sub>/rGO): Characterization and feasibility, mechanism and pathway studies, *Appl. Surf. Sci.* 462 (2018) 549–564. doi:10.1016/j.apsusc.2018.08.133.
- [42] W. Wang, P. Serp, P. Kalck, J. Luis Faria, Visible light photodegradation of phenol on MWNT-TiO<sub>2</sub> composite catalysts prepared by a modified sol–gel method, *J. Mol. Catal. A Chem.* 235 (2005) 194–199. doi:10.1016/j.molcata.2005.02.027.
- [43] A. Gnanaprakasam, V.M. Sivakumar, M. Thirumarimurugan, Influencing Parameters in the Photocatalytic Degradation of Organic Effluent via Nanometal Oxide Catalyst: A Review, *Indian J. Mater. Sci.* 2015 (2015) 1–16. doi:10.1155/2015/601827.
- [44] P. Chandra Bhomick, A. Supong, M. Baruah, C. Pongener, D. Sinha, Pine Cone biomass as an effecient precursor for the synthesis of activated biocarbon for adsorption of anionic dye from aqueous solution: Isotherm, kinetic, thermodynamic and regeneration studies, *Sustain. Chem. Pharm.* 10 (2018) 41–49. doi:10.1016/j.scp.2018.09.001.
- [45] Y. John, V. Emery David Jr, D. Mmereki, A Comparative Study on Removal of Hazardous Anions from Water by Adsorption: A Review, *Int. J. Chem. Eng.* 2018 (2018) 1–21. doi:10.1155/2018/3975948.
- [46] K. Mamun Reza, R. ASW, G. Fahmida, Parameters affecting the photocatalytic degradation of dyes using TiO<sub>2</sub>: a review, *Appl. Water Sci.* 7 (2017) 1569–1578. doi:10.1007/s13201-015-0367-y.
- [47] P. Raizada, P. Thakur, A. Sudhaik, P. Singh, A. Aslam, P. Khan, V.K. Thakur, A. Hosseini-Bandegharai, Fabrication of dual Z-scheme photocatalyst via coupling of BiOBr/Ag/AgCl heterojunction with P and S co-doped g-C<sub>3</sub>N<sub>4</sub> for efficient phenol degradation, *Arab. J. Chem.* 13 (2019) 4538–4552. doi:10.1016/j.arabjc.2019.10.001.
- [48] Gunture, A. Singh, A. Bhati, P. Khare, K. Malika Tripathi, S. Kumar Sankar, Soluble Graphene Nanosheets for the Sunlight-Induced Photodegradation of the Mixture of Dyes and its Environmental Assessment, *Sci. Rep.* 9 (2019) 1–12. doi:10.1038/s41598-019-38717-1.

- [49] S. Moosavi, R. Yi Man Li, C.W. Lai, Y. Yusof, S. Gan, O. Akbarzadeh, Z.Z. Chowhury, X. -GuangYue, M.R. Johan, Methylene Blue Dye Photocatalytic Degradation over Synthesised  $\text{Fe}_3\text{O}_4/\text{AC}/\text{TiO}_2$  Nano-Catalyst: Degradation and Reusability studies, *Nanomaterials*. 10 (2020) 1–15. doi:10.3390/nano10122360.
- [50] H. E. Emam, H. B. Ahmed, E. Gomaa, M. H. Helal, R. M. Abdelhameed, Recyclable photocatalyst composites based on  $\text{Ag}_3\text{VO}_4$  and  $\text{Ag}_2\text{WO}_4$  @MOF@cotton for effective discoloration of dye in visible light, *Cellulose*. 27 (2020) 7139–7155. doi:10.1007/s10570-020-03282-8.
- [51] P. Jin, R. Chang, D. Liu, K. Zhao, L. Zhang, Y. Ouyang, Phenol degradation in an electrochemical system with  $\text{TiO}_2$ /activated carbon fiber as electrode, *J. Environ. Chem. Eng.* 2 (2014) 1040–1047. doi:10.1016/j.jece.2014.03.023.
- [52] Y. Tao, Z.L. Cheng, K.E. Ting, X.J. Yin, Photocatalytic Degradation of Phenol Using a Nanocatalyst: The Mechanism and Kinetics, *J. Catal.* 2013 (2013) 1–7. doi:10.1155/2013/364275.
- [53] M. A Vishnuganth, N. Remya, M. Kumar, N. Selvaraju, Photocatalytic degradation of carbofuran by  $\text{TiO}_2$ -coated activated carbon: Model for kinetic, electrical energy per order and economic analysis, *J. Environ. Manage.* 181 (2016) 201–207. doi:10.1016/j.jenvman.2016.06.016.
- [54] N. Daneshvar, A. Aleboyeh, A. R Khataee, The evaluation of electrical energy per order ( $E_{EO}$ ) for photooxidative decolorization of four textile dye solutions by the kinetic model, *Chemosphere*. 59 (2005) 761–767. doi:10.1016/j.chemosphere.2004.11.012.
- [55] M.A. Behnajady, H. Eskandarloo, M. Shokri, Influence of the chemical structure of organic pollutants on photocatalytic activity of  $\text{TiO}_2$  nanoparticles: Kinetic analysis and evaluation of electrical energy per order ( $E_{EO}$ ), *Dig. J. Nanomater. Biostructures*. 6 (2011) 1887–1895.
- [56] S. A. Parsons, M. Williams, *Advanced oxidation processes for water and wastewater treatment*, 4th ed., IWA publishing, 2015. doi:10.2166/9781780403076.
- [57] R. C. Asha, M. A. Vishnuganth, N. Remya, N. Selvaraju, M. Kumar, *Livestock Wastewater Treatment in Batch and Continuous Photocatalytic Systems: Performance and Economic Analyses*, *Water Air Soil Pollut.* 226 (2015) 1–13. doi:10.1007/s11270-015-2396-4.
- [58] P. Shandilya, D. Mittal, A. Sudhaik, M. Soni, P. Raizada, A.K. Saini, P. Singh,  $\text{GdVO}_4$  modified fluorine doped graphene nanosheets as dispersed photocatalyst for mitigation of phenolic compounds in aqueous environment and bacterial disinfection, *Sep. Purif. Technol.* 210 (2018) 804–816. doi:10.1016/j.seppur.2018.08.077.
- [59] P. Shandilya, D. Mittal, M. Soni, P. Raizada, J. -ho Lim, D. Yong Jeong, R.P. Dewedi, A.K. Saini, P. Singh, Islanding of  $\text{EuVO}_4$  on high-dispersed fluorine doped few layered graphene sheets for efficient photocatalytic mineralization of phenolic compounds and bacterial disinfection, *J. Taiwan Inst. Chem. Eng.* 93 (2018) 528–542. doi:10.1016/j.jtice.2018.08.034.

- [60] W. Sang, C. Zhan, S. Hao, L. Mei, J. Cui, Q. Zhang, X. Jin, C. Li, Effect of the presence of inorganic anions on the degradation of phenol by dielectric barrier discharge plasma combined with RGO-TiO<sub>2</sub>, *J. Water Process Eng.* 41 (2021) 1–30. doi:10.1016/j.jwpe.2021.101997.
- [61] Rachna, M. Rani, U. Shanker, Sunlight Assisted Degradation of Toxic Phenols by Zinc Oxide Doped Prussian Blue Nanocomposite, *J. Environ. Chem. Eng.* 8 (2020) 1–12. doi:10.1016/j.jece.2020.104040.
- [62] N.N. Bahrudin, M.A. Nawi, Immobilized titanium dioxide/powdered activated carbon system for the photocatalytic adsorptive removal of phenol, *Korean J. Chem. Eng.* 35 (2018) 1–10. doi:10.1007/s11814-018-0062-4.
- [63] H. Ling, K. Kim, Z. Liu, J. Shi, X. Zhu, J. Huang, Photocatalytic degradation of phenol in water on as-prepared and surface modified TiO<sub>2</sub> nanoparticles, *Catal. Today.* 258 (2015) 96–102. doi:10.1016/j.cattod.2015.03.048.
- [64] P. Lisowski, J.C. Colmenares, O. Mašek, W. Lisowskia, D. Lisovytskiya, A. Kamińska, D. Łomota, Dual functionality of TiO<sub>2</sub>/biochar hybrid materials: photocatalytic phenol degradation in liquid phase and selective oxidation of methanol in gas phase, *Sustain. Chem. Eng.* 5 (2017) 6274–6287. doi:10.1021/acssuschemeng.7b01251.

# CHAPTER 7

## SUMMARY AND CONCLUSIONS

---

This chapter presents the overall summary and conclusions of the thesis. The future scope of the work is also highlighted in this chapter.

Heterogeneous photocatalysis is emerging as an alternative wastewater treatment method for the degradation of hazardous pollutants. Semiconductor materials have the potential to perform photocatalysis when irradiated with light to generate powerful hydroxyl radicals ( $\cdot\text{OH}$ ). The semiconductor material like  $\text{TiO}_2$  is mainly used as a photocatalyst in the field of wastewater treatment, air purification, inactivation of microorganisms, smell elimination, anti-mist, and self-cleaning. However, powdered  $\text{TiO}_2$  has low exchange efficacy, high agglomeration ability, and also has a high quantity recombination rate between electron and hole pairs which limits the complete use of  $\text{TiO}_2$  in the highly available visible light region (400-750 nm). As a result, to overcome the agglomeration of  $\text{TiO}_2$ , it was immobilized on activated carbon, and to transfer the light absorption to the visible light region, it was doped with metal ions. Thus, the present thesis is focused on doping  $\text{TiO}_2$  with transition metal ions, and impregnating it on activated carbon adsorbent to enhance the photocatalytic activity of  $\text{TiO}_2$  in the visible light region. The summary of the overall thesis work is presented below:

1. Photocatalyst  $\text{TiO}_2$  was successively synthesized using the sol-gel method. The synthesized  $\text{TiO}_2$  was immobilized on chemically activated pine cone activated carbon (PAC) using the hydrothermal method. SEM and XRD results of the nanocomposite revealed that  $\text{TiO}_2$  nanoparticles are placed inside the PAC pores and the  $\text{TiO}_2$  particles are in anatase form with a crystal size of 2.35 nm. The prepared nanocomposite showed a maximum of 99.10% degradation of 20 ppm alizarin red S (ARS) dye after 80 minutes of Ultra-Violet light exposure using 0.05 g of the nanocomposite. The Langmuir-Hinshelwood pseudo-first-order rate kinetics described the photocatalytic degradation of ARS well with an apparent rate constant of  $0.02372 \text{ min}^{-1}$  and a half-life time of 29.30 minutes. According to the thermodynamic parameter, the degradation was exothermic and spontaneous. The presence of interfering ions such as glycine, copper sulphate, cadmium nitrate, and zinc chloride affects mostly the degradation of ARS which indicated that hydroxyl radicals are the dominant reactive species in the ARS degradation process. Regeneration studies indicated the reusability of the exhausted nanocomposite up to the fifth cycle with significant degradation efficacy. GC-MS analysis reveals that the end-products of ARS photodegradation leads to the formation of low molecular weight products such as cyclo 3,5-hexadiene 1,2-dienone, carbon dioxide, and water. The cost involved while running the experiment was found to be 672.72, 240.24, and 156.86 INR for 20 ppm, 60 ppm, and 100 ppm ARS degradation using 0.05 g of  $\text{TiO}_2$ -NP/PAC nanocomposite. Theoretical

investigation through DFT results suggested that the binding  $\text{TiO}_2$  with PAC increases the chemical reactivity of the nanocomposite as compared to  $\text{TiO}_2$  nanoparticles.

2.  $\text{TiO}_2$  supported on PAC nanocomposite doped with Fe ions shifts the light absorbance in the visible light region. The Fe-doped titanium dioxide nanocomposite supported on activated carbon was synthesized using an ultrasonic-hydrothermal method. The XRD spectra indicated that the Fe ions were incorporated into the crystal lattice of  $\text{TiO}_2$ . The surface morphology of the nanocomposite confirmed that Fe-doped  $\text{TiO}_2$  nanoparticles were well dispersed on the PAC surface and exhibited average particle size distribution of 2-20 nm. The doping of  $\text{Fe}^{3+}$  ions reduced the optical bandgap of the nanocomposite from 3.2 to 2.3 eV and shift the light absorption in the visible light region. The synthesized FDT/PAC nanocomposite was utilized as an efficient photocatalyst for the degradation of Congo red (CR) dye under visible light irradiation. FDT/PAC nanocomposite displayed much improved visible light active photocatalysis (100%) than bare  $\text{TiO}_2$  (25%) and  $\text{TiO}_2$ -NP/PAC (33.50%) nanocomposite towards CR degradation under optimum conditions (CR concentration = 20 ppm, pH = 1, Nanocomposite dose = 0.06 g, and Contact time = 60 minutes). The photocatalytic degradation of CR was satisfactorily described by the pseudo-first-order rate kinetics with an apparent rate constant of  $0.05341 \text{ min}^{-1}$  and a half-life period of 12.97 minutes. The FDT/PAC nanocomposite has excellent regeneration properties and it degrades around 64% CR at the fifth cycle of use. The GC-MS analysis showed the asymmetric cleavage of the CR forming low molecular products such as phenyl cation, carbon dioxide, and water. The FDT/PAC nanocomposite was very effective in photocatalytic inactivation of bacteria *E. coli* and *S. aureus*. The maximum inactivation of *E. coli* was achieved within 120 minutes and *S. aureus* within 75 minutes under visible light irradiation. The total operating cost was found to be 312.50, 236.74, and 166.67 INR for 20 ppm, 60 ppm, and 100 ppm CR dye degradation using 0.06 g FDT/PAC nanocomposite.

3. Ni-doped  $\text{TiO}_2$  supported on activated carbon nanocomposite was synthesized *via* a simple hydrothermal method. The XRD spectra confirmed the existence of the anatase phase of  $\text{TiO}_2$  and also good dispersion of  $\text{Ni}^{2+}$  ions on the surface of  $\text{TiO}_2$ -activated carbon. The white spherical  $\text{TiO}_2$  particles accumulating with Ni ions were aggregated on the PAC surface and their particle sizes range from 5-20 nm. The bandgap energy of  $\text{TiO}_2$  reduces from 3.1 to 2.4 eV with the doping of  $\text{Ni}^{2+}$  ions in the  $\text{TiO}_2$  structure and this reduction in the bandgap shifts the optical absorbance to the visible light region. The prepared NDT/PAC nanocomposite

seems to be very efficient towards photocatalytic degradation of anthracene (ANT) and a maximum of 99.9% degradation was observed for 20 ppm solution within 50 minutes. The photocatalytic degradation process was found to be in good agreement with the Langmuir-Hinshelwood pseudo-first-order rate kinetics having a rate constant of  $0.11449 \text{ min}^{-1}$  and a half-life period of 6.05 minutes. The thermodynamic study indicated the temperature dependence, exothermic, and spontaneity of the degradation process. The effect of different interfering ions such as EDTA, NaCl,  $\text{ZnCl}_2$ ,  $\text{CuSO}_4$ , glycine, oxalic acid,  $\text{NaNO}_3$ , and  $\text{Cd}(\text{NO}_3)_2$  was analyzed, and among them, the presence of glycine, EDTA,  $\text{CuSO}_4$ ,  $\text{NaNO}_2$  affects mostly in the degradation percentage of ANT as these have strong scavenging properties for the electron, hole, and hydroxyl radical. The NDT/PAC nanocomposite can be reused several times having good degradation efficiency till the fifth cycle. GC-MS analysis confirmed the generation of low molecular weight end products such as (1E, 3E)-penta-1,3-dien-1-ol, carbon dioxide, and water after the photocatalytic degradation. The total operating cost in Indian rupees (INR) used during the ANT degradation using 0.05 g NDT/PAC nanocomposite were as follows: 347.56 (20 ppm), 205.45 (40 ppm), 158.54 (60 ppm), 135.63 (80 ppm), and 131.02 (100 ppm). Thus, it can be concluded from this work that the prepared nanocomposite can act as a good visible light-sensitive photocatalyst for degradation of ANT in water solution.

4. Cobalt-doped  $\text{TiO}_2$  supported on activated carbon was prepared successfully using the hydrothermal synthesis method. Doping of Co ions reduces the bandgap of  $\text{TiO}_2$ -PAC nanocomposite and shifts the photocatalytic activity towards the visible light region. The CDT/PAC nanocomposite could be used effectively for the degradation of phenol from an aqueous solution with a maximum degradation percentage of 99.90% within 60 minutes for 20 ppm phenol solutions. The degradation followed pseudo-first-order kinetics with a rate constant of  $0.086 \text{ min}^{-1}$  and a half-life time of 7.981 minutes. The thermodynamic study revealed that the degradation process is exothermic and spontaneous. The presence of interfering ions glycine,  $\text{CuSO}_4$ ,  $\text{Cd}(\text{NO}_3)_2$ , EDTA affects mostly the degradation of phenol solution as they have electron and hole scavenging properties. The nanocomposite is highly stable and can be used several times without any significant loss in catalytic activity. GC-MS analysis confirmed the generation of low molecular weight end products such as formic acid, carbon dioxide, and water. A total of 312.50, 190.54, 137.96, 122.26, and 117.92 INR (Indian rupee) were utilized for 20 ppm, 40 ppm, 60 ppm, 80 ppm, and 100 ppm phenol degradation using 0.35 g of



CDT/PAC nanocomposite. Thus the Co-doped TiO<sub>2</sub> activated carbon nanocomposite using visible light irradiation can be a promising photocatalyst for the degradation of phenol.

### **Future Prospects**

In this thesis, TiO<sub>2</sub> and metal-doped TiO<sub>2</sub> supported on activated carbon are applied for the degradation of dyes and pharmaceuticals compounds. This work can be extended by incorporating TiO<sub>2</sub> and metal-doped TiO<sub>2</sub> with natural fibers, g-C<sub>3</sub>N<sub>4</sub>, or LDH using similar synthetic routes reported in this thesis. The synthesized photocatalysts can be used for dye-sensitized solar cells, hydrogen production, chemoselective reduction of nitroarenes, degradation of volatile aromatic pollutants, and debromination of polybrominated diphenyl ether.

1. Developing new visible-light hybrid photocatalyst by coupling TiO<sub>2</sub> with other metal oxides such as ZnO, ZrO<sub>2</sub>, CaO, Cu<sub>2</sub>O and supporting them on activated carbon to apply them in photo electrochemical water splitting reactions, photodegradation of herbicides, insecticides, and saturated hydrocarbon.
2. The photocatalytic performance can be further evaluated to degrade more water pollutants and the method can be used on an industrial scale.
3. In this thesis, TiO<sub>2</sub> is doped with transition metals, however, TiO<sub>2</sub> can also be co-doped with metal and non-metal, multi-element for higher visible active photocatalysis.
4. The technique of total organic carbon (TOC) can be employed to investigate the mineralization of pollutants used in this thesis.

**NAGALAND****UNIVERSITY**

(A Central University Estd. By the Act of Parliament No. 35 of 1989)

Headquarters: Lumami-798627, Nagaland, India

### Ph.D. Thesis Certificate on Plagiarism check

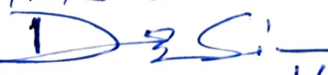
Name of the Research Scholar	Mridushmita Baruah
Ph.D. Registration Number	Ph.D./CHE/00001
Title of Ph.D. thesis	Photocatalytic degradation of water pollutants using activated carbon-TiO <sub>2</sub> /metal doped TiO <sub>2</sub> based nanocomposite
Name & Institutional Address of the Supervisor	Prof. Dipak Sinha Department of Chemistry, Nagaland University, Lumami
Name of the Department and School	Department of Chemistry, School of Sciences
Date of submission	03/12/2021
Date of plagiarism check	03/12/2021
Percentage of similarity detected by the URKUND software	1%

I. I hereby declare that/certify that the Ph.D. thesis submitted by me is complete in all respect as per the guidelines of Nagaland University (NU) for this purpose. I also certify that the Thesis (soft copy) has been checked for plagiarism using URKUND similarity checked software. It is also certified that the contents of the electronic version of the thesis re the same as the final hardcopy of the thesis. Copy of the report generated by the URKUND software is also enclosed.

Mridushmita Baruah  
(MRIDUSHMITA BARUAH)  
(Name & Signature of the Scholar)

Place: LUMAMI

Date: 14/12/2021










  
(DIPAK SINHA) 14/12/21  
Name & Signature of the Supervisor:  
With Seal

Dipak Sinha  
Department of Chemistry  
Nagaland University

## Document Information

<b>Analyzed document</b>	Photocatalytic degradation of water pollutants using activated carbon-TiO <sub>2</sub> metal doped TiO <sub>2</sub> based nanocomposite by Mridushmita Baruah.pdf (D120924197)
<b>Submitted</b>	2021-12-03T10:42:00.0000000
<b>Submitted by</b>	Dipak Sinha
<b>Submitter email</b>	dipaksinha@gmail.com
<b>Similarity</b>	1%
<b>Analysis address</b>	dipaksinha.naga@analysis.orkund.com

## Sources included in the report

<b>W</b>	URL: <a href="https://www.nature.com/articles/s41467-021-20977-z">https://www.nature.com/articles/s41467-021-20977-z</a> Fetched: 2021-12-03T10:45:00.0000000		<b>1</b>
<b>W</b>	URL: <a href="https://digitalcommons.mtech.edu/cgi/viewcontent.cgi?article=1249&amp;context=grad_rsch">https://digitalcommons.mtech.edu/cgi/viewcontent.cgi?article=1249&amp;context=grad_rsch</a> Fetched: 2021-12-03T10:45:00.0000000		<b>2</b>
<b>W</b>	URL: <a href="https://www.sciencedirect.com/science/article/pii/S266652392100009X">https://www.sciencedirect.com/science/article/pii/S266652392100009X</a> Fetched: 2021-12-03T10:45:00.0000000		<b>1</b>
<b>W</b>	URL: <a href="https://www.science.gov/topicpages/p/photocatalytic%2Bdegradation%2Bkinetics">https://www.science.gov/topicpages/p/photocatalytic%2Bdegradation%2Bkinetics</a> Fetched: 2021-08-14T08:04:06.7500000		<b>1</b>
<b>W</b>	URL: <a href="https://www.sciencedirect.com/science/article/pii/S1389556715000441">https://www.sciencedirect.com/science/article/pii/S1389556715000441</a> Fetched: 2021-12-03T10:45:00.0000000		<b>1</b>
<b>W</b>	URL: <a href="http://xlink.rsc.org/?DOI=c4ra10604k">http://xlink.rsc.org/?DOI=c4ra10604k</a> Fetched: 2021-12-03T10:45:00.0000000		<b>1</b>
<b>W</b>	URL: <a href="https://link.springer.com/content/pdf/10.1007/s11814-021-0830-4.pdf">https://link.springer.com/content/pdf/10.1007/s11814-021-0830-4.pdf</a> Fetched: 2021-07-17T18:54:19.4200000		<b>9</b>
<b>W</b>	URL: <a href="https://www.mdpi.com/1420-3049/21/11/1491/xml">https://www.mdpi.com/1420-3049/21/11/1491/xml</a> Fetched: 2021-12-03T10:45:00.0000000		<b>1</b>
<b>W</b>	URL: <a href="https://en.wikipedia.org/wiki/Cobalt%2528II%2529_nitrate">https://en.wikipedia.org/wiki/Cobalt%2528II%2529_nitrate</a> Fetched: 2021-12-03T10:45:00.0000000		<b>1</b>

## CURRICULUM VITAE

### Personal Details

Name in Full	<b>MRIDUSHMITA BARUAH</b>
Date of Birth	13 <sup>th</sup> October, 1993
Address of Correspondence	Department of Chemistry Nagaland University Lumami Campus-798627 Zunheboto, Nagaland
Permanent Address	Simaluguri, Ward No. 6, Dist-Sivasagar, Assam Pin-785686
Email ID	<a href="mailto:mridushmita13@gmail.com">mridushmita13@gmail.com</a>

### Academic qualifications

Exam Passed	Board/ University	Year Of Passing	Division	Percentage Of marks	Subjects
Matriculation (10 <sup>th</sup> )	SEBA, Assam	2009	1 <sup>st</sup> Div	66.00%	Assamese, English, General Science, Mathematics, Social Science, Hindi
Higher Secondary (10+2)	AHSEC, Assam	2011	1 <sup>st</sup> Div	70.00%	English, Assamese, Physics, Chemistry, Biology, Mathematics
B.Sc.	Gargaon College (Dibrugarh University)	2014	1 <sup>st</sup> Div	68.50%	Chemistry (Major)
M.Sc.	Mizoram University	2016	1 <sup>st</sup> Div	78.00%	Chemistry (Physical)
Ph.D.	Nagaland University	2021	Thesis Submitted		
Title of the Thesis: Photocatalytic Degradation of Water Pollutants using Activated Carbon-TiO <sub>2</sub> /Metal doped TiO <sub>2</sub> based Nanocomposite					

### Additional Courses Completed

Online certification course under SWAYAM

- |   |                        |                       |
|---|------------------------|-----------------------|
| • Nanotechnology, Science and Applications, | NPTEL (IIT Madras),    | <b>Total Credit-2</b> |
| • Surface Engineering of Nanomaterials,     | NPTEL(IIT Roorkee),    | <b>Total Credit-2</b> |
| • Soft Nano Technology,                     | NPTEL (IIT Kharagpur), | <b>Total Credit-2</b> |

## Research Area

- Synthesis and characterization of metal oxide nanomaterial and nanocomposite
- Development of biomass-based materials and their characterization
- Photocatalysis
- Adsorption studies
- Application of DFT on adsorption/photocatalysis studies
- Application of activated carbon and metal oxide nanomaterial for environmental remediation

## RESEARCH PUBLICATIONS

### A. Research Papers Published in Journals

1. Synthesis, characterization of novel Fe-doped TiO<sub>2</sub> activated carbon nanocomposite towards photocatalytic degradation of Congo red, *E. coli*, and *S. aureus*, *Korean Journal of Chemical Engineering*, 38, 1277-1290, 2021.

DOI: <https://doi.org/10.1007/s11814-021-0830-4>

**Mridushmita Baruah**, Soremo L Ezung, Aola Supong, Parimal Chandra Bhomick, Suraj Kumar, Dipak Sinha.

2. Batch sorption-photodegradation of Alizarin Red S using synthesized TiO<sub>2</sub>/activated carbon nanocomposite: an experimental study and computer modelling, *Nanotechnology for Environmental Engineering*, 3, 1–13, 2020.

DOI: <https://doi.org/10.1007/s41204-020-00071-3>

**Mridushmita Baruah**, Aola Supong, Parimal Chandra Bhomick, Rituparna Karmaker, Chubaakum Pongener, Dipak Sinha.

- Hydrothermally derived Ni-doped TiO<sub>2</sub> activated carbon nanocomposite: A visible light-driven photocatalyst for Anthracene degradation.

**Mridushmita Baruah**, Soremo L Ezung, Shisak Sharma, Upasana Bora Sinha, Dipak Sinha. (Manuscript submitted).

- Synthesis and characterization of Co-doped TiO<sub>2</sub> activated carbon nanocomposites for the photocatalytic degradation of phenol.

**Mridushmita Baruah**, Soremo L Ezung, Shisak Sharma, Upasana Bora Sinha, Dipak Sinha. (Manuscript submitted).

3. Alizarin Red S adsorption onto biomass-based activated carbon: optimization of adsorption process parameters using Taguchi experimental design.

*International Journal of Environmental Science and Technology*, 17, 1137-1148, 2020.

DOI: <https://doi.org/10.1007/s13762-019-02389-1>

Parimal Chandra Bhomick, Aola Supong, **Mridushmita Baruah**, Chubaakum Pongener, Champa Gogoi, Dipak Sinha.

4. Activated carbon synthesized from biomass material using single-step KOH activation for adsorption of fluoride: Experimental and theoretical investigation, *Korean Journal of Chemical Engineering*, 36, 551–562, 2019.

DOI: <https://doi.org/10.1007/s11814-019-0234-x>

Parimal Chandra Bhomick, Aola Supong, Rituparna Karmaker, **Mridushmita Baruah**, Chubaakum Pongener, Dipak Sinha.

5. Adsorptive removal of Bisphenol A by biomass activated carbon and insights into the adsorption mechanism through density functional theory calculations, *Sustainable Chemistry and Pharmacy*, 13, 1-13, 2019.

DOI: <https://doi.org/10.1016/j.scp.2019.100159>

Aola Supong, Parimal Chandra Bhomick, **Mridushmita Baruah**, Chubaakum Pongener, Upasana Bora Sinha, Dipak Sinha.

6. Pine Cone biomass as an efficient precursor for the synthesis of activated biocarbon for adsorption of anionic dye from aqueous solution: Isotherm, kinetic, thermodynamic and regeneration studies, *Sustainable Chemistry and Pharmacy*, 10, 41–49, 2018.

DOI: <https://doi.org/10.1016/j.scp.2018.09.001>

Parimal Chandra Bhomick, Aola Supong, **Mridushmita Baruah**, Chubaakum Pongener, Dipak Sinha. Upasana Bora Sinha, Dipak Sinha.

7. Adsorption of fluoride onto activated carbon synthesized from Manihot esculenta biomass—Equilibrium, kinetic and thermodynamic studies, *Journal of Environmental Chemical Engineering*, 6, 2382-23389, 2018. DOI: <https://doi.org/10.1016/j.jece.2018.02.045>

Chubaakum Pongener, Parimal Chandra Bhomick, Aola Supong, **Mridushmita Baruah**, Upasana Bora Sinha, Dipak Sinha.

## B. BOOK CHAPTERS PUBLISHED

1. Waste biomass for synthesis of porous activated carbon and its application in water treatment in the book titled “Climate Change and Sustainable Development (Perspectives from North East India)”, ISBN 978-93-88593-32-8, First Edition, Purbayon Publication, Guwahati, 2019, 170-190.

**Mridushmita Baruah**, Aola Supong, Parimal Chandra Bhomick, Chubaakum Pongener, Supongtoshi Jamir, Dipak Sinha.

2. Efficient Fluoride removal from contaminated water using the scale of Rohu fish (*Labeo rohita*) in the book titled “Environment: Climate Change and Natural Challenges”, ISBN 978-93-90919-60-4, First Edition, Gargaon College Publication cell, Simaluguri, Assam, 202, 171-186.

**Mridushmita Baruah**, Kikrusenuo Sanchu, Dipak Sinha.

## PAPERS PRESENTED

- **Oral presentation** on “Batch sorption-photodegradation of Alizarin Red S using synthesized TiO<sub>2</sub>/activated carbon nanocomposite: an experimental study and computer modelling”, at International E-conference on Advances in Science and Technology for Betterment of Health, Environment and energy, organized by Department of Chemistry, GITAM School of Science, Bengaluru, 1<sup>st</sup>-3<sup>rd</sup> December, 2020.

- **Oral presentation** on “Synchronous role of coupled adsorption and photocatalytic degradation on TiO<sub>2</sub>-NP/PAC nanocomposite generating excellent mineralization of Alizarin Red S dye on aqueous solution”, at National e-Seminar on Chemistry in emerging trends of interdisciplinary research, organised by Department of Chemistry, Nagaland University, 18<sup>th</sup>-20<sup>th</sup> November, 2020.



- **Oral presentation** on “Photocatalytic Degradation Of Alizarin Red S Dye In Aqueous Solutions: A Kinetic Approach” at International Seminar on Chemistry and Environmental Sustainability, organized by Department of Chemistry, Mizoram University, 19<sup>th</sup>-22<sup>nd</sup> February, 2019.
- **Oral presentation** on “Efficient use of Nano-TiO<sub>2</sub> materials in the degradation of Alizarin Red S from aqueous solution”, at National Seminar on Chemistry in Interdisciplinary Research, organised by Nagaland University, 9<sup>th</sup>-10<sup>th</sup> November, 2018.
- **Oral presentation** on “Efficient Application of Nano-TiO<sub>2</sub> Particles in the Photocatalytic removal of Dye”, at National Seminar on Bio-resource exploration and Utilization: Applications in modern Biology, organised by Bioinformatics Infrastructure facility, Nagaland University, 9<sup>th</sup>-10<sup>th</sup> October, 2018.
- **Oral presentation** on “Synthesis and characterization of Activated carbon Prepared from Sugarcane Bagasses by Chemical Activation”, at National Seminar on Climate change and sustainable development: With special focus on North EAST India, organised by NUTA, Nagaland University, 17<sup>th</sup>-18<sup>th</sup> May, 2017.
- **Poster presentation** on “Synthesis and characterization of activated carbon prepared from bio-waste by chemical activation” at National Seminar on Chemistry in Interdisciplinary Research, organised by Department of Chemistry, Nagaland University, 16<sup>th</sup>-17<sup>th</sup> March, 2017.

## CONFERENCES/SEMINARS/WEBINARS/WORKSHOPS ATTENDED

### Workshop Attended

- Attended International Virtual workshop on Recent Advances & Applications of Conducting Polymer Nanostructures & Nanocomposites, organised by IIT Mandi, 23<sup>rd</sup>-24<sup>th</sup> June, 2021.
- Attended Sensitization workshop on DST women Scientist Scheme, organised by DST, New-Delhi and Nagaland University, 4<sup>th</sup>-5<sup>th</sup> March, 2019.
- Attended Short term course on Analytical Techniques for Physical, Chemical and Bio-inspired materials, organised by NIT, Dimapur, 23<sup>rd</sup>-27<sup>th</sup> July, 2018.
- Attended one day workshop on Importance of IPR in Academic Institutions, organised by IPR cell, Nagaland University 29<sup>th</sup> May 2019.
- Attended Two-Day workshop on “Quality Enhancement in Research” organised by IQAC, Nagaland University, 22<sup>nd</sup>-23<sup>rd</sup> March, 2021.

### Webinar Attended

- Attended one day International Webinar on “ E-Learning Trends Today and Beyond 2021” organised by Manipur Institute of Management Studies, Manipur University, 12<sup>th</sup> May, 2021.
- Attended International E-Conference on “Recent Advances in Chemical, Physical and Biological Sciences” organised by Department of Chemistry, Nabira Mahavidyalaya, Katol, 29<sup>th</sup>-30<sup>th</sup> June, 2021.



- Attended International Webinar on “Sustainable Chemistry IWSC-2021” organised by ACT, Homi Bhabha Centre for Science Education Mumbai, 18<sup>th</sup> March 2021.
- Attended National Level Online Faculty Development Programme on “Effective Teaching Techniques and Skills for Career Advancement” organised by Faculties of Science Stream, Sao Chang College, Nagaland, 23<sup>rd</sup>-28<sup>th</sup> June, 2021.
- Attended Webinar on “Saga of Science from 13<sup>th</sup> to 21<sup>st</sup> Century”, organised by Department of Chemistry, Mizoram University, 25<sup>th</sup> August, 2020.
- Attended Three days National Online FDP on “ICT Tools for Effective Teaching Learning” organised by IQAC, Kamla Nehru Mahavidyalaya, Nagpur, 8<sup>th</sup>-10<sup>th</sup> June, 2021.
- Attended National Level One-Week Faculty Development Programme on “Research Methodology” organised by Kamla Nehru Mahavidyalaya, Nagpur, 26<sup>th</sup>-1<sup>st</sup> May, 2021.
- Attended National Webinar on “Recent Advances in Chemistry” organised by Department of Chemistry & IQAC, Govt. G.N.A. PG College, Bhatapara, 26<sup>th</sup> July, 2021.
- Attended Live Webinar on “Visions: How Science and Technology will Revolutionize the 21<sup>st</sup> Century” and “Fruit Juice Clarification Techniques Using Membrane Technology” organised by Mizoram University, 21<sup>st</sup> September, 2020.